

https://dspace.org/

Synthesis, properties and applications of Mn, Co, Ni and Cu chalogenide nanoparticles

Moloto, Nosipho

2011-03-07
http://hdl.handle.net/10539/9108

Downloaded from a DSpace repository. https://dspace.org/

SYNTHESES, PROPERTIES AND APPLICATIONS OF Mn, Co, Ni AND Cu CHALCOGENIDE NANOPARTICLES

By

Nosipho Moloto (MSc.)

A thesis submitted in fulfilment of the requirements for the degree of

Doctor of Philosophy in the Faculty of Science

School of Chemistry

University of the Witwatersrand

Private Bag X 03

WITS

2050

Supervisors: Prof. N. J. Coville

Dr. S. S. Ray

DECLARATION

I declare that "Syntheses, Properties and Applications of Mn, Co, Ni and Cu Chalcogenide Nanoparticles" is my own, unaided work submitted at the University of the Witwatersrand, Johannesburg. It has not been submitted for any degree or examination in any other university, and all sources I have used or quoted have been indicated and acknowledged with complete references.

Name: Nosipho Moloto Date: 2010

Signature:.....

ABSTRACT

Science and technology in the nanoscale level has shown tremendous potential over the past few decades. One of the emerging areas that is at the interface of chemistry, physics, engineering, biology and materials science is the field of semiconductor nanocrystals. The unique properties of semiconductor nanocrystals have attracted great attention. Different strategies of syntheses of semiconductor nanocrystals have been developed so that their composition, size, shape and surface protection can be controlled. These inherent properties have resulted in numerous potential applications of these materials. Herein we report on different synthetic strategies of magnetic semiconductor nanoparticles and we probe their optical, electrical and magnetic properties as well as review some of the possible application of these materials.

Metal sulfides and selenides of magnetic metal ions are of particular interest in our study as a result of their dual properties i.e. good optical properties (absorption in: UV for MnS/Se, visible for NiS/Se and IR for CoS/Se and CuS/Se and the ability to emit light)as well as their magnetic properties. The metal centres have shown to have magnetic characteristics due to the unpaired d-electrons. The oxide counterparts of these metals though possessing similar magnetic behaviour rarely luminescent and therefore have limited applications compared to the sulfides and selenides. Metal sulfides and selenides of other metals such as Cd are known to have excellent optical properties and strategies have been developed to dope them with magnetic ions in order to achieve dual applications but these strategies have proved to be challenging and minute amounts of the dopant are usually incorporated into the core metal chalcogenide thus resulting in very small magnetic moments. Other complicated assemblies have also been developed to achieve the same dual properties e.g. simultaneous encapsulation of luminescent nanoparticles such as CdSe and magnetic Fe_2O_3 by a polymer microsphere. These assemblies have disadvantages such as multiple synthesis steps and large particle sizes. Consequently magnetic metal chalcogenides are far more promising and we therefore embark on synthesizing these nanoparticles and exploring their properties.

The thesis is presented in the form of seven chapters. Chapter 1 gives the background to the physics, syntheses and growth mechanisms of the semiconductor nanoparticles. Chapter 2 is presented as the preliminary study to the synthesis and characterization of all the metal sulfides and selenides. Two methods of syntheses are identified as promising for the preparation of both the sulfides and selenides i.e. the single-source precursor and modified hydrothermal methods. These methods and variation of synthetic conditions are further explored in the successive chapters (3-6). The reported nanoparticles display good optical, magnetic and electrical properties and subsequently some of the applications relating to these properties are discussed. On the other hand though the synthetic methods are simplistic and inexpensive, further optimization of the reaction parameters is required and suggestions are proposed in chapter 7 as future work.

ACKNOWLEDGEMENTS

This thesis is an important milestone to my journey of becoming a scientist. It has been a difficult but fruitful journey. I have endured a lot of challenges but emerged victorious with the help and support of various people. My heartfelt gratitude goes to my hubby Justice who has been very supportive and understanding. He has been my source of strength, always keeping things under control and never complaining. I am especially grateful for the role he played while I was at MIT, he not only helped me cope emotionally but he looked after our family effortlessly playing the roles of both mom and dad. My kids (Tumi and Nhlanhla) and niece (Palesa) also deserve appreciation for always understanding that mommy is a student and might not always be around and for being brave and forever loving.

I would also like to thank my PhD advisors, Prof Neil Coville for his invaluable contribution and critic. His appreciation of high quality science and integrity has been a marvel and has made me to strive to be a better scientist. To Dr Justice Moloto for his insight to the project as well as endless discussions and critics that has ensured the success of this project. Thanks also go to the National Centre for Nano-Structured Materials, CSIR for managing the project. Particularly the nano students who have been a good bunch to bounce off ideas, to share what's happening in the world of nano as well as endless debates about relationships, money and politics. Special thanks go to Dr Lucky Sikhwivhilu who has been a good friend and collaborator on other side projects, to Gugu, Nonhlanhla, Wendy, Ntombi, Gebhu, Clive, Thomas, Sipho, Dr Sibusiso, Thabo, Dr Sabelo and Siyasanga for being good friends and always on the same page. I would also like to thank CATOMAT for always making me feel at home. Thanks also go to the quantum dots group Poslet, Nobathembu, Ben, Phindile and Thandeka for all the discussions and being in the same boat as me.

Appreciation also goes to Wits for giving me the opportunity to go to MIT for a year. It was a wonderful experience that will have impact far beyond the PhD. I will be forever grateful to Prof Moungi Bawendi for allowing me to work in his lab and for imparting his knowledge as well for the gained exposure. Thanks also go to Prof Hazel Sive and Karen Fosher for always ensuring my stay at MIT was pleasant. To the Bawendi group for their heart warming

welcome especially the devices' group who I have enjoyed working with immensely. Finally acknowledgments go to my extended family for always being the background source of strength that I know I could always count on as well to God almighty for all the blessings and for getting me through very tough situations.

LIST OF PUBLICATIONS

Publications Included as part of the thesis

- N. Moloto, M.J. Moloto, N.J. Coville, S.S. Ray, The study on the time dependency and the stability of cobalt sulphide nanoparticles under an electron beam, Journal of Nanoscience and Nanotechnology 10(9) (2010) 5594-5601.
- N. Moloto, M. J. Moloto, N.J. Coville, S.S. Ray, Optical and structural characterization nickel selenide nanoparticles synthesized by simple methods, Journal of Crystal Growth 311 (2009) 3924-3932.
- N. Moloto, S.S. Ray, M.J. Moloto, A facile route for the synthesis of poly(vinylcarbazole)/manganese sulphide quantum dots nanocomposites with enhanced optical properties, Journal of Nanoscience and Nanotechnology 8(11) (2009) 6031-6037.
- N. Moloto, N.J. Coville, S.S. Ray, M.J. Moloto, Morphological and optical properties of MnS/polyvinylcarbazole hybrid composite, Physica B 404 (2009) 4461-4465.
- N. Moloto, N.J. Coville, M.J. Moloto, Synthesis and characterization of nickel selenide nanoparticles: size and shape determine parameters, ***to be submitted***.
- N. Moloto, N.J. Coville, M.J. Moloto, Optical and magnetic properties of MS and MSe nanoparticles where M = Mn, Co, Ni and Cu, ***to be submitted***.

Additional publications

- N. Moloto, N. Revaprasadu, M.J. Moloto, P. O'Brien, M. Helliwell, *N*,*N*′-Diisopropyl- and *N*,*N*′-dicyclohexylthiourea cadmium(II) complexes as precursors for the synthesis of CdS nanoparticles, Polyhedron 26 (2007) 3947-3955.
- N. Moloto, N. Revaprasadu, M.L. Musetha, M.J. Moloto, The effect of precursor concentration, temperature and capping group on the morphology of CdS nanoparticles, Journal of Nanoscience and Nanotechnology 9(8) (2009) 4760-4766.
- N. Moloto, N. Revaprasadu, M.J. Moloto, P. O'Brien, J. Raftery, *N*,*N*′-Diisopropyl- and *N*,*N*′-dicyclohexylthiourea zinc(II) complexes as precursors for the synthesis of ZnS nanoparticles, South African Journal of Science 105 (2009) 258-263.

- S.K. Pillai, N. Moloto, S.S. Ray, One-step synthesis of quantum dots decorated carbon nanotube heterostructure, Journal of Nanoscience and Nanotechnology, 10(7) (2010) 4279-4285.
- L.M. Sikhwivhilu, S. Mpelane, N. Moloto, S.S. Ray, Hydrothermal synthesis of TiO_2 nanotubes: microwave heating versus conventional heating, Journal of American Chemical Society (2010), ***submitted***.

RESEARCH VISITS

- Visiting scholar at Massachusetts Institution of Technology, US in Prof M. G. Bawendi laboratory from September 2009 to July 2010.

PRESENTATIONS

- Oral presentation: Department of Chemistry Seminar (University of Zululand) (03/2007): Quantum dots incorporated polymer nanocomposites.
- Oral presentation: National Centre for Nano-structured Materials Seminar (CSIR) (05/2007): Metal chalcogenide nanoparticles.
- Poster presentation: Held (29/07-01/08/2007), ICMR-University of Zululand 2007, Richards Bay: Incorporation of MnS nanoparticles into Poly(vinylcarbazole).
- Attended a workshop on thermal analysis and possess a certificate (10/2007).
- Oral presentation: National Centre for Nano-structured Materials Seminar (CSIR) (11/2007): Quantum dots polymer nanocomposites.
- Oral presentation: Department of Chemistry Seminar (University of the Witwatersrand) (02/2008): Fabrication and characterization of quantum dots-polymer nanocomposites.
- Attended a workshop. Electrochemistry in nanotechnology (SA-UK Network) CSIR Pretoria (05/2008).
- Poster presentation: Held (11/05-16/05/2008). The 5th International Conference on Semiconductor Quantum Dots. Gyeongju South Korea: Influence of MnS quantum dots on the optical and physical properties poly(N-vinylcarbazole).
- Attended the 1^{St} South African PhD Project. 05/2008 Kempton Park.

- Oral presentation: Held (09-12/07/2008) 53rd SAIP, University of Limpopo: Quantum dots: An aid to improve organic solar cells efficiency.
- Oral presentation: Department of Chemistry Seminar (University of the Witwatersrand) (07/2008): Synthesis and characterization of dilute magnetic semiconductors and their application as fillers in polymer-nanocomposites.
- Oral presentation: National Centre for Nano-structured Materials Seminar (CSIR) (08/2008): Quantum dots for potential application in polymer semiconductor devices.
- Department of Chemistry Seminar (University of the Witwatersrand) (06/2008): Optical properties and morphology of nickel selenide nanoparticles.
- Oral presentation: Held (23-27/03/2009) SACPM 2009, Mabula Game Lodge: Application of quantum dots in optoelectronic devices.
- Oral presentation: Department of Chemistry (Massachusetts Institute of Technology) (10/2009): Syntheses and characterization of QDs and QD heterostructures.
- Oral presentation: Held (30/11-4/12/2009) MRS Fall Meeting, Boston MA: Quantum dots polymer-nanocomposites.
- Oral presentation: Department of Chemistry (Massachusetts Institute of Technology) (07/2010): Determination of the refractive index of PbS/polymer thin films.

For my family

TABLE OF CONTENTS

Declaration **2**

Abstract **3**

Acknowledgements **5**

List of publications **7**

Research visits **8**

Presentations **8**

Appendix **15**

List of figures 15

List of tables 19

List of schemes 20

List of abbreviations **20**

Chapter 1: introduction to metal chalcogenide semiconductor nanocrytsals **22**

1. Background on semiconductor nanocrystals 23

1.1. Introduction 23

1.2. Properties of semiconductor nanocrystals 26

1.2.1. Electronic structure of semiconductor nanocrystals 26

1.2.2. Optical properties of semiconductor nanocrystals 31

1.2.3. Electrical properties of semiconductor nanoparticles 35

1.2.4. Magnetic properties 45

1.2.4.1. Basic concepts in magnetism 46

1.2.4.2. Magnetic anisotropy and domains in small particles 51

1.2.4.3. Super-paramagnetism 52

1.3. Synthetic routes to semiconductor nanocrystals 53

1.4. General growth mechanism of semiconductor nanocrystals 61

1.5. References 69

Chapter 2: syntheses of magnetic metal sulfide and selenide nanoparticles for potential biomedical applications **79**

2.1. Introduction 79
2.2. Potential biomedical applications 80
2.2.1. In vivo applications 80
2.2.1.1. Therapeutic applications 80
2.2.1.2. Diagnostic applications 81
2.2.2. In vitro applications 82
2.2.2.1. Diagnostic applications 82
2.2.3. Future applications 84
2.3. Syntheses of magnetic nanoparticles 84
2.3.1. Syntheses of ms nanoparticles 85
2.3.1.1. Materials 85
2.3.1.2. Syntheses of the precursors 86
2.3.1.3. Syntheses of the nanoparticles 86
2.3.2. Syntheses of mse nanoparticles 86
2.3.2.1. Materials 86
2.3.2.2. Syntheses of the nanoparticles 87
2.4. Characterization techniques 87
2.5. Results and discussion 88
2.5.1. Manganese sulfide and manganese selenide nanoparticles 88
2.5.2. Cobalt sulfide and cobalt selenide nanoparticles 94
2.5.3. Nickel sulfide and nickel selenide nanoparticles 100
2.5.4. Copper sulfide and copper selenide nanoparticles 104
2.6. Conclusions 109
2.7. References 110

Chapter 3: time and temperature dependency of cobalt sulfide nanocrystals: a stability study 114

3.1. Introduction 114
3.2. Experimental 115
3.2.1. Materials 115
3.2.2. Synthesis of the precursor 115
3.2.3. Synthesis of cobalt sulfide nanocrystals 115

3.2.3.1. The reaction time study 115
3.2.3.2. Annealing of the nanoparticles 116
3.2.3.3. Temperature study 116
3.3. Characterization techniques 116
3.4. Results and discussion 117
3.5. Conclusions 135
3.6. References 136

Chapter 4: optical and structural characterization of nickel selenide nanocrystals synthesized by simple methods 139

4.1. Introduction 139
4.2. Experimental 140
4.2.1. General 140
4.2.2. Synthetic methods 140
4.2.2.1. Synthesis of [nicl2(sec6h5)2] 140
4.2.2.2. Synthesis of nickel selenide nanoparticles 141
4.3. Characterization techniques 142
4.3.1. Microanalysis 142
4.3.2. Nuclear magnetic resonance and fourier transformed-infrared spectroscopy 142
4.3.3. Optical characterization 142
4.3.4. X-ray diffraction 142
4.3.5. Electron microscopy 142
4.4. Results and discussion 143
4.4.1. Optical properties 144
4.4.2. Structural properties 146
4.5. Conclusions 154
4.6. References 154

Chapter 5: synthesis and characterization of nickel selenide nanoparticles: size and shape determining parameters 156

5.1. Introduction 156
5.2. Experimental 157
5.2.1. Materials 157

5.3. Characterization techniques 159
5.3.1. Optical characterization 159
5.3.2. X-ray diffraction 159
5.3.3. Electron microscopy 159
5.4. Results and discussion 160
5.4.1. The effect of molar ratio on the size and shape of nickel selenide nanocrystals ... 160
5.4.2. The effect of reaction time on the size and shape of nickel selenide nanocrystals 165
5.4.3. The effect of ph on the size and shape of nickel selenide nanocrystals 171
5.4.4. The effect of solvent on the size and shape of nickel selenide nanocrystals 174
5.5. Conclusions 178
5.6. References 179

Chapter 6: syntheses and characterization of qd-polymer nanocomposites for potential opto-electronic applications 181

6.1. Introduction 181
6.2. Application of qd/pnc in opto-electronic devices 182
6.2.1. Photovoltaics based on quantum dots-polymer nanocomposites 182
6.2.2. Light emitting diodes based on the quantum dots-polymer nanocomposites 183
6.3. Experimental 184
6.3.1. Materials 184
6.3.2. Synthesis of the precursor 185
6.3.3. Synthesis of mns nanoparticles 185
6.3.4. Synthesis of the nanocomposites 185
6.3.4.1. Route 1 185
6.3.4.2. Route 2 185
6.3.4.3. Route 3 186
6.3.4.4. Route 4 186
6.4. Characterization 188
6.5. Results and discussion 189
6.6. Conclusions 198
6.7. References 199

Chapter 7: conclusions and recommendations 201

7.1. Conclusions 201
7.2. Future work and recommendations 205
7.3. References 205

APPENDIX

LIST OF FIGURES

Fig. 1-1: (a) Band diagram for a simple two-band model for direct-gap semiconductors. (b) Optical transitions in finite-size semiconductor nanocrystals are discrete due to the quantization of the bulk bands [71]. 26
Fig. 1-2: (a) Simple model of a nanocrystal (quantum dot) as a semiconductor inclusion embedded in an insulating matrix. (b) Potential well formed in any one dimension (x, y, or z) in the conduction and valence bands. The energy levels of the excited carriers (electrons and holes) become quantized due to the finite size of the semiconductor nanocrystal [72]. 28
Fig.1-3: Size dependent optical properties due to quantum confinement [83]..... 32
Fig. 1-4: Fluorescence in a bulk semiconductor..... 33
Fig. 1-5: Schematic representation of a typical structure for electrical characterization of nanocrystalline films..... 36
Fig. 1-6: Schematic cross-sectional structure for (a) a photovoltaic device and (b) a light-emitting diode containing both nanocrystals and a conjugated polymer. 37
Fig. 1-7: Energy as a function of configuration co-ordinate for the initial and final states in an electron transfer reaction. The reorganization energy, k, and the free energy change for the reaction, $\Delta \boldsymbol{G0}$ are shown [98]..... 38
Fig. 1-8: Schematic diagram of the evolution of electronic bands of an itinerant ferromagnet with increasing dimensionality (atom to bulk) for nickel [134]..... 50
Fig. 1-9: Illustration of the overall free energy $\Delta \boldsymbol{G}$ as a function of the growth particle size r [207]..... 62
Fig. 1-10: A series of different clusters formed by addition of closed shells in the fccstructure. Each of the presented clusters represents the core of the subsequent cluster. Starting from a single atom, cubo octahedra of 13, 55 and 147 Au atoms can be built [223]. 65

Fig. 1-11: Sketch of the potential landscape in the growth of CdSe magic size clusters. For simplicity it is sketched only in one-dimension. The model is to be understood as a modification to the classical nucleation potential as shown in Fig. 1-9 [225]. 66
Fig. 2-1: Schematic representation of the magnetically driven transport of drugs to a specific region. A catheter is inserted into a arterial feed to the tumour and a magnetic stand is positioned over the targeted site. 81
Fig. 2-2: Schematic representation of the magnetically assisted separation of substances. In this case a magnetic nanosphere to which an antibody has been anchored is dispersed in a liquid medium containing the antigen (substance to be analysed)..... 83
Fig. 2-3: Absorption and photoluminescence spectra (λ_{exc} = 250 nm) of (a) MnS and (b) MnSe. 89
Fig. 2-4: (a, c and d) are the SEM, HRTEM micrographs and size distribution curve of MnS and (b, d and e) are the SEM, HRTEM micrographs and size distribution curve of MnSe. 91
Fig. 2-5: X-ray diffraction patterns of (a) MnS and (b) MnSe (₸ denotes HDA, ¥ denotes elemental Se). 93
Fig. 2-6: ESR spectra of (a) MnS and (b) MnSe taken at 298 K. 94
Fig. 2-7: Absorption and photoluminescence spectra (λ_{exc} = 250 nm) of (a) Co_3S_4 and (b) Co_3Se_4. 96
Fig. 2-8: SEM micrographs of (a) Co_3S_4, (b) Co_3Se_4 and HRTEM micrographs of (c) Co_3S_4 and (d) Co_3Se_4. 98
Fig. 2-9: X-ray diffraction patterns of (a) CoS and (b) Co_3Se_4 (₸ denotes HDA, ¥ denotes elemental Se). 99
Fig. 2-10: ESR spectra of (a) Co_3S_4 and (b) Co_3Se_4 taken at 298 K..... 100
Fig. 2-11: Absorption and photoluminescence spectra (λ_{exc} = 250 nm) of (a) NiS and (b) Ni_3Se_4. 101
Fig. 2-12: SEM micrographs of (a) NiS, (b) Ni_3Se_4 and HRTEM micrographs of (c) NiS and (d) Ni_3Se_4. 102
Fig. 2-13: X-ray diffraction patterns of (a) NiS and (b) Ni_3Se_4 (₸ denotes HDA). 103
Fig. 2-14: ESR spectra of (a) NiS and (b) Ni_3Se_4 taken at 298 K..... 104
Fig. 2-15: Absorption and photoluminescence spectra (λexc = 250 nm) of (a) CuS and (b) CuSe. 105

Fig. 2-16: SEM micrographs of (a) CuS, (b) CuSe and HRTEM micrographs of (c) CuS and (d) CuSe. 107
Fig. 2-17: X-ray diffraction patterns of (a) CuS and (b) CuSe (₸ denotes HDA, ¥ denotes elemental Se). 108
Fig. 2-18: ESR spectra of (a) CuS and (b) CuSe taken at 298 K. 109
Fig. 3-1: Absorption spectra of cobalt sulfide nanoparticles collected from tetramethylthiuram disulfide at 160 °C in HDA for various times (5 min, 15 min, 30 min, 45 min and 60 min). Inset: colour of the particles dispersed in toluene ranges from green (5 minutes) to dark brown (60 min). 119
Fig. 3-2: Photoluminescence spectra of cobalt sulfide nanoparticles collected from tetramethylthiuram disulphide at 160°C in HDA for various times (5 min, 15 min, 30 min, 45 min and 60 min). 120
Fig. 3-3: XRD patterns of cobalt sulfide nanoparticles collected from the reaction mixture after: (a) 5 min and (b) 60 min († denote HDA peaks) 122
Fig. 3-4: FESEM images (at 5 kV) and size distribution histograms of cobalt sulfide nanoparticles collected from the reaction mixture after: (a) 5 min: $\mu = 9 \pm 1$ nm and (b) 60 min: $\mu = 17 \pm 2$ nm. 123
Fig. 3-5: TEM images (at 200 kV) and the size distribution of cobalt sulfide nanoparticles collected from the reaction mixture after: (a) 5 min: $\mu = 15 \pm 4$ aspect ratio and (b) 60 min: $\mu = 16 \pm 1$ aspect ratio. 125
Fig. 3-6: HRTEM micrographs of cobalt sulfide (5 min sample) depicting the growth mechanism of nanowires where the electron beam was focused on a single sphere for (a) 30 sec, (b) 1 min, (c) 5 min and (d) 10 min. 126
Fig. 3-7: Successive photon bombardment of cobalt sulfide nanoparticles synthesized for 5 min (a), photoluminescence intensity profile with 0.05 % instrument error (b) (curve to guide the eye). 127
Fig. 3-8: TGA of the cobalt sulfide nanocrystals synthesized after 5 min. 129
Fig. 3-9: (a) SEM image at low magnification, (b)-(d) SEM images at the same magnification depicting $CoS_{1.097}$ of different sizes, (e)-(f) TEM images showing different sizes of $CoS_{1.097}$ and (g)-(h) HRTEM images at different magnification. 130
Fig. 3-10: Absorption spectra of cobalt sulfide synthesized for 1hr in HDA at different temperatures. 131

Fig. 3-11: Photoluminescence spectra of cobalt sulfide synthesized for 1hr in HDA at different temperatures. 132
Fig. 3-12: X-ray diffractograms of cobalt sulfide synthesized for 1hr in HDA at (a) 120 °C, (b) 160 °C, (c) 200 °C and (d) 240 °C († denotes HDA) 133
Fig. 3-13: FESEM micrographs of cobalt sulfide synthesized for 1hr in HDA at (a) 120 °C, (b) 160 °C, (c) 200 °C and (d) 240 °C. 135
Fig. 4-1: Absorption and photoluminescence spectra of nickel selenide prepared by method 1 - a, 2 - b, 3 - c in CH_3OH and 3 - d in H_2O. 146
Fig. 4-2: X-ray diffraction patterns of nickel selenide prepared by method 1 - a, 2 - b, 3 – c in CH_3OH and 3 – d in H_2O 146
Fig. 4-3: FE-SEM micrographs (a), TEM (b) and HRTEM (c) of nickel selenide prepared by method 1 148
Fig. 4-4: FE-SEM micrographs (a), and HRTEM (b) of star-shaped nickel selenide prepared by method 2 149
Fig. 4-5: FE-SEM micrographs (a), TEM (b) and HRTEM (c) of nickel selenide prepared by method 3 in CH_3OH. 150
Fig. 4-6: EDX spectrum of particles prepared by method 3 in CH_3OH. 151
Fig. 4-7: FE-SEM micrographs (a), TEM (b) and HRTEM (c) of nickel selenide prepared by method 3 in H_2O. 152
Fig. 5-1: Absorption and photoluminescence spectra of nickel selenide nanoparticles synthesized at various times. 162
Fig. 5-2: SEM and HRTEM micrographs of nickel selenide particles synthesized in a 1:1, 1:2, 2:1 and 1:3 Ni:Se ratio respectively. 164
Fig. 5-3: XRD patterns of nickel selenide synthesized at different Ni:Se molar ratios. 165
Fig. 5-4: Absorption and photoluminescence spectra of nickel selenide nanoparticles synthesized at various times. 167
Fig. 5-5: SEM and HRTEM micrographs of nickel selenide particles synthesized after 1h, 3h, 6h and 24h respectively 169
Fig. 5-6: XRD patterns of nickel selenide synthesized at different times. 170
Fig. 5-7: Absorption and photoluminescence spectra of nickel selenide nanoparticles synthesized at differentpH values. 171
Fig. 5-8: XRD patterns of nickel selenide synthesized at different pH values. 172

Fig. 5-9: SEM micrographs of nickel selenide nanocrystals synthesized at different values of pH. 173
Fig. 5-10: UV-Vis absorption and photoluminescence spectra of nickel selenide synthesized using different solvents; (a) water, (b) ethylenediamine and (c) pyridine. *Toluene and #second order excitation..... 175
Fig. 5-11: SEM and HRTEM micrographs of nickel selenide nanocrystals synthesized in different solvents. 176
Fig. 5-12: XRD patterns of nickel selenide nanoparticles synthesized in ethylenediamine and pyridine. 177
Fig. 6-1: Illustration of the bulk hetero-junction hybrid solar cells and the charge transfer mechanism [27]. 183
Fig. 6-2: Typical configuration of a hybrid polymer light emitting diode. 184
Fig. 6-3: XRD pattern of MnS quantum dots. 190
Fig. 6-4: Absorption and photoluminescence spectra of (a) MnS nanoparticles, (b) pure PNVC, (c) MnS/PNVC prepared by route 1, (d) MnS/PNVC prepared by route 2, (e) MnS/PNVC prepared by route 3 and (f) MnS/PNVC prepared by route 4. 191
Fig. 6-5: SEM micrographs of (a) MnS quantum dots, (b) PNVC, (c) MnS/PNVC synthesized by route 1, (d) MnS/PNVC synthesized by route 2, (e) MnS/PNVC synthesized by route 3 and (f) MnS/PNVC synthesized by route 4. 193
Fig. 6-6: FT-IR spectra of (a) pure PNVC, (b)MnS/PNVC synthesized by route 1, (c) MnS/PNVC synthesized by route 2, (d) MnS/PNVC synthesized by route 3 and (e)MnS/PNVC synthesized by route 4. 194
Fig. 6-7: AFM images of a MnS/PNVC synthesized by route 2, (a) cross-section, (b) 3D view and (c) line scan. 195
Fig. 6-8: EDX spectrum of MnS/PNVC nanocomposites synthesized by route 4. 196

LIST OF TABLES

Table 2-1: Summary of the optical and morphological properties of the nanocrystals. 109
Table 4-1: Summary of nickel selenide particle's data from all methods 153
Table 5-1: Reaction parameters for the molar ratio experiments. 158
Table 5-2: Reaction parameters of the time experiments 158

Table 5-3: Reaction parameters for the pH experiments..... 158
Table 5-4: Reaction parameters for the solvent experiments..... 159
Table 5-5: Summary of the optical properties observed at different reaction time. 168
Table 6-1: Practical examples of QD-polymer devices..... 184
Table 6-1: Electrical properties of the QD and QD/PNC..... 197

LIST OF SCHEMES

Scheme 2-1: Schematic showing excess HDA ligands. 92
Scheme 3-1: Formation of cobalt chloride tetramethylthiuram disulphide complex. 118
Scheme 3-2: Growth mechanism of high voltage irradiation induced nanowires. 128
Scheme 4-1: Preparation of nickel selenide using method 1. 143
Scheme 6-1: Schematic diagram of the synthetic routes of MnS/PNVC nanocomposites... 187
Scheme 6-2: Schematic diagram of the set-up for the electrical measurements of the powders, (A) sample holder, (B) stainless steel pistons,(C, D) stainless steel casings, (E) micrometer, (J) weight, (K) Pressure gauge, (I, F, G, H) iron metal pieces..... 189

LIST OF ABBREVIATIONS

QD: Quantum dots

0D: 0 dimensional

1D: 1 dimensional

2D: 2 dimensional

3D: 3 dimensional

LED: Light emitting diodes

TOP: Trioctylphosphine

TOPO: Trioctylphosphine oxide

IR: Infra-red spectroscopy

NMR: Nuclear magnetic resonance spectroscopy

AC: Alternating current

SPE: Solid-phase extraction

HIV: Human immunodeficiency virus

Tat: Trans-activator of transcription

MSPE: Magnetic solid-phase extraction

DMS: Dilute magnetic semiconductors

MS: Metal sulfides

MSe: Metal selenides

UV-VIS-NIR: Ultraviolet-visible-near infrared spectroscopy

RS: Rock salt

ZB: Zinc blend

W: Wurtzite

MBE: Molecular beam epitaxy

UV-VIS: Ultraviolet-visible spectroscopy

JCPDS: Joint committee on powder diffraction standards

OMVPE: Organometallic vapour phase epitaxy

PL: Photoluminescence spectroscopy

FE-SEM: Field emission scanning electron microscopy

SEM: Scanning electron microscopy

TEM: Transmission electron microscopy

HRTEM: High resolution transmission electron microscopy

EDX: Energy dispersive x-ray spectroscopy

XRD: X-ray diffraction spectroscopy

LAB6: Lathanum boride

ESR: Electron spin resonance spectroscopy

HDA: Hexadecylamine

AACVD: Aerol assisted chemical vapour deposition

CIDS: Copper indium diselenide

VLS: Vapour liquid solid

PNVC: Poly-N-Vinylcarbazole

PNC: Polymer nanocomposites

PV: Photovoltaic

Py: Pyridine

en: Ethylenediamine

RT: Room temperature

FT-IR: Fourier transformed infrared

AFM: Atomic force microscopy

PMMA: Polymethyl methacrylate

MMA: Methyl methacrylate

MPS: Methacryeoxypropyltrimethoxysilane

SQUID: Superconducting quantum interference devices

CHAPTER 1: INTRODUCTION TO METAL CHALCOGENIDE SEMICONDUCTOR NANOCRYSTALS

1. Background on semiconductor nanocrystals

1.1. Introduction

The enormous potential of science and technology on the nanoscale to impact on industrial output has been recognised throughout the world. One of the emerging areas of nanotechnology that is at the interface of chemistry, biology, physics, materials science and engineering is the field of semiconductor nanocrystals, whose unique properties have attracted much attention in the past few decades. The drive and the interest on the study of semiconductor nanocrystals is as a result of their novel properties. The main goal of nanotechnology is to develop economically and environmentally efficient methods for the design of novel nanostructured materials and highly dispersed systems, preparation of films and coatings and the fabrication of functional nanostructures that are promising for applications in various fields. These vary from information and telecommunication systems, optoelectronics, and catalysis to medicine and bioengineering.

Semiconductor materials are basic to modern electronic devices. A characteristic trend of progress in electronics is continuous miniaturization of functional elements and the corresponding increase in the degree of integration of integrated circuits and other devices [1]. Miniaturization of functional elements of integrated circuits down to the nano level using conventional technologies faces two serious problems. First, electronic, optical, magnetic and other properties of nanomaterials can be significantly different from the properties of the same materials with corresponding bulk phases [2]. The nano level is also characterized by manifestation of novel physical effects, *e.g.*, electron tunneling, size quantization of energy levels, *etc*. Second, traditionally used methods of fabrication of functional elements for planar technologies, which involve a number of lithographic processes, approach the physical limit of the resolution of lithographic systems and cause economic problems due to exponential increase in the cost of production of more and more miniature sized devices [3-5].

It is believed that the advancement of technologies to the nano level and the development of real nanotechnologies requires economically efficient, simple (as simple as possible), and environmentally friendly approaches [6]. Chemical synthesis, functionalization, ordered spatial organization of nanoparticles, and design of nanomaterials and devices based on them meet these common requirements. Methods of synthesis as well as the structure and properties of nanoparticles have been considered in a monographand in a collection of works [7-11]. Researchers first became interested in semiconductor nanocrystals in the 1980s [12-16]. At that time, the concept of size quantization was formulated; it has been developed in more recent studies [17-19]. Since then, considerable progress has been achieved in this field. However, the results obtained in studies of the optical properties and in other physical experiments were difficult to interpret owing to polydispersity, presence of surface defects, and a low degree of crystallinity of the synthesized nanoparticles [20,21]. This was only improved upon recently [22-25]. Progress in this field was stimulated by the possibility of using semiconductor nanocrystals as materials for field effect transistors, light emitting diodes, photocatalysts, biological labels, and sensors. As the size of semiconductor nanoparticles decreases, a threshold value characteristic of each type of semiconductor is reached [26-28].

At smaller nanoparticle sizes, the energy gap (band-gap) increases and the optical spectrum is shifted toward the short wavelength region [29-32]**.** At a sufficiently small semiconductor size i.e. in the so called "quantum" state, the density of states of conduction electrons can take only particular discrete values. This is responsible for the quantum size effect, *i.e*., transition from a continuous to discrete energy spectrum of conduction electrons [29-35]. As a result, nanoparticles possess unique optical and electronic properties not observed for corresponding bulk samples. Owing to a substantial increase in the fraction of surface atoms and to an increasing role of the surface effects not only the optical properties but also other characteristics of materials (structure of electronic energy levels and transitions, electron affinity, conductivity, phase transition temperatures, *etc*.) also become dependent on the nanoparticle size and shape; these changes are usually called the “size effect’ [29-35].

A number of studies into the syntheses of semiconductor nanocrystals over the past few decades have been conducted with an emphasis on size control in order to determine the extent of quantum confinement [36-40]. Lately the development of semiconductor nanocrystals has extended from the pure adjustment of particle sizes to the more sophisticated properties such as their shape and composition [41-44]. The hope is that through control of these features, different fields of application might open up for the use of nanocrystals.The term "nanoparticles" as applied to semiconductor particles was first used in the literature only recently. Even as late as 1998, nanoscale CdSe particles were called "colloidal particles" or "semiconductor cluster molecules" [45]. Since then semiconductor nanoparticles have more and more often been called "quantum dots" and this term has now been commonly accepted [46-48]. If an electron-hole pair (exciton) is formed inside a spherical particle whose diameter is equal to or smaller than the natural electron-hole separation in the material (the Bohr exciton radius), no motion is possible for the exciton. This particle is called a "quantum dot" (QD) because the number of degrees of freedom of the exciton is zero (0D) [46-52]. An exciton formed inside a particle that extends in one direction (along, *e.g.*, the *z* axis) cannot move along the *x* and *y* axes, but can move along the *z* axis. This one dimensional (1D) situation is possible for nanorods, nanowires, and nanofibers. In two dimensional (2D) nanodisks, an exciton can move along two axes. It was initially assumed and then confirmed in numerous experiments that such changes in the shape of nanoparticles must affect their spectral and luminescence characteristics [53-58].

The II-VI and III-V semiconductor nanocrystals have been one of the most successfully synthesized and applicable materials made to date. CdSe has been one of the materials readily studied due to its reproducibility, monodispersity and size tuneable optical properties. These properties of CdSe give insight and understanding into the behaviour of nanocrystalline semiconductors and therefore most theories and models are formulated from this system [59-62].

1.2. Properties of semiconductor nanocrystals

1.2.1. Electronic structure of semiconductor nanocrystals

A major interest in studying semiconductor nanocrystals is to understand what happens when the semiconductor becomes small. This is a question that is imperative to ask, not only for the pure need to understand but also for the practical uses that emerge from this understanding. Because of the drive to miniaturize electronic and optoelectronic devices, it therefore becomes important to understand the properties of nanocrystalline semiconductors. To have an insight into understanding these properties, various semiconductor nanocrystals have been studied [63-70]. For these studies one of the most important and versatile tools has been spectroscopy. The usefulness of spectroscopy stems from the intrinsic properties of electron movement between quantum levels. Direct band-gap semiconductors can absorb a photon when an electron is promoted directly from the valance band to the conduction band [71]. During that process an electron and hole pair is created in the material, as shown in Fig 1-1(a).

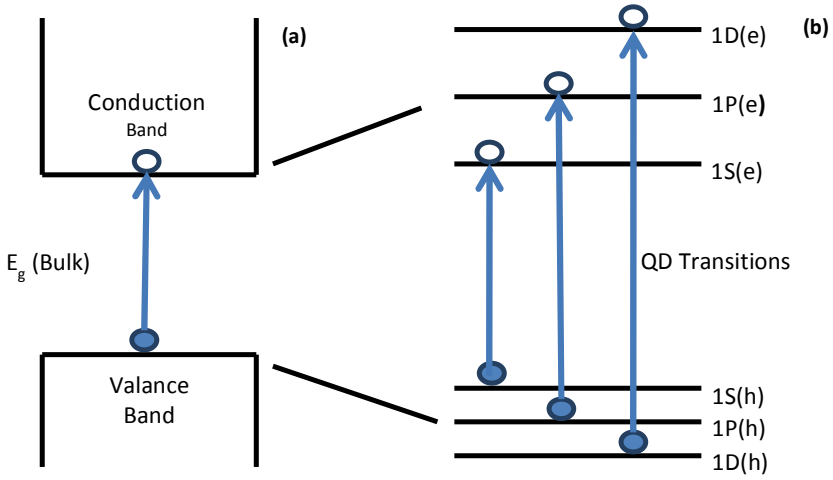

Fig. 1-1: (a) Band diagram for a simple two-band model for direct-gap semiconductors. (b) Optical transitions in finite-size semiconductor nanocrystals are discrete due to the quantization of the bulk bands [71].

However, if the size of the semiconductor becomes comparable or smaller than the Bohr exciton radius, then the carriers are confined by the boundaries depicted in equation (1)

$$l \ll R \ll a_B \quad (1)$$

where l is the lattice spacing, R is the radius of the particles and a_B is the Bohr exciton radius of a hydrogen atom.

This phenomenon is known as the quantum size effect and it leads to atomic like conduction and valance band as shown in Fig. 1-1(b) [71]. Regardless of the nature of the nanocrystal semiconductor, the material remains structurally identical to the bulk semiconductor; consequently this behaviour is solely due to the finite size.When the realization of such behaviour dawned upon scientists, endeavours to try and explain it were undertaken [72-74]. Various models were developed and one of the frequently used modelis that of a quantum dot semiconductor embedded in an insulating matrix as illustrated in Fig 1-2(a) [72].

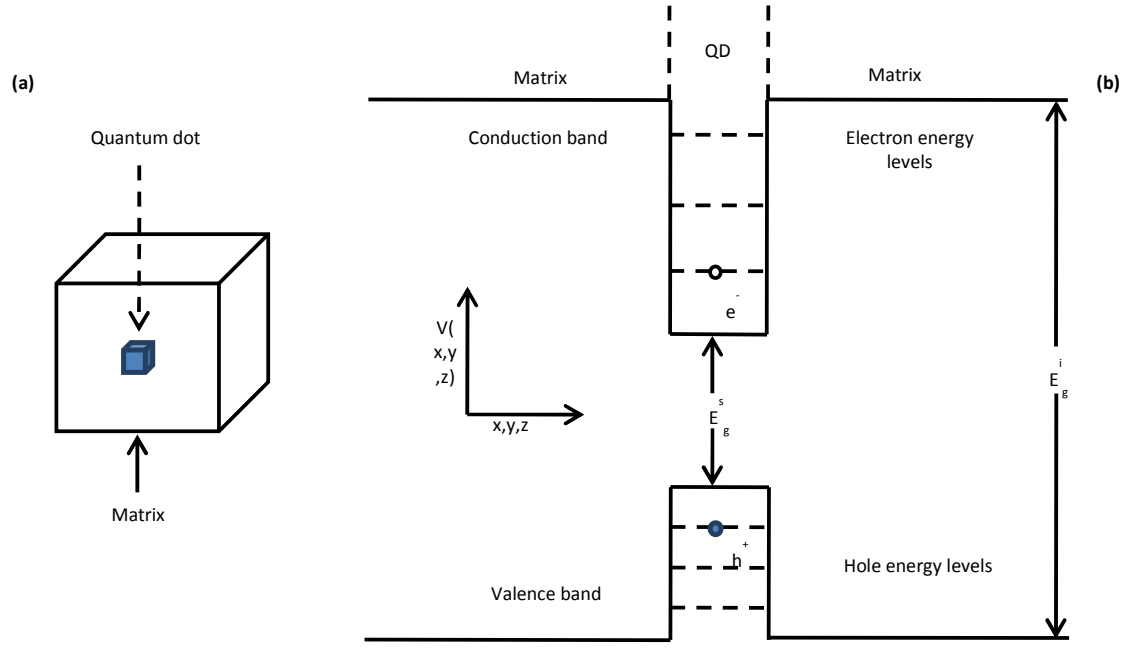

Fig. 1-2: (a) Simple model of a nanocrystal (quantum dot) as a semiconductor inclusion embedded in an insulating matrix. (b) Potential well formed in any one dimension (x, y, or z) in the conduction and valence bands. The energy levels of the excited carriers (electrons and holes) become quantized due to the finite size of the semiconductor nanocrystal [72].

Photo-excited carriers reside in a potential well as shown in Fig 1-2(b). This causes the valence and conduction band to be quantized into a ladder of hole and electron energy levels, respectively. Therefore in contrast to the bulk absorption spectrum which potrays a continuum above the band-gap of the semiconductor (E^s_g), the spectrum of the semiconductor nanocrystals exhibits a series of discrete electronic transitions between the quantized energy levels [72]. In order to appreciate and comprehend the quantum size effect, a close comparison of the theory of the electronic structure of the bulk semiconductor to the nanocrystal semiconductor is required.

There are two factors; both related to the size of the individual nanocrystal that differentiates their behaviour from that of macrocrystalline semiconductors. The first is the high dispersity (large surface/volume ratio) associated with the particles, with both physical and chemical properties of the semiconductor being sensitive to the surface structure. The second factor is the actual size of the particle, which can determine the electronic and

physical properties of the material. The absorption and scattering of light in larger particles is described by Mie's theory [73]. However the optical spectra of nanocrystalline compound semiconductors which show a blue shift in absorption band edges as the size decreases cannot be explained by classical theory. Such size dependent optical properties are as a result of the size quantization effect, which occurs when the size of the nanoparticle is smaller than the bulk Bohr radius (*eq. 2*),

$$a_B = \varepsilon \frac{m}{m^*} a_0 \quad (2)$$

where ε is the dielectric constant of the material, $\mathrm{m}^*$is the mass of the electron or hole, m is the rest mass of the electron, and a_0 is the Bohr radius of the hydrogen atom [74]. For the nanocrystal, it is convenient to consider three different Bohr radii: one for the electron ($\mathrm{a_e}$), one for the hole ($\mathrm{a_h}$), and one for the electron–hole pair or exciton (a_{exc}). The latter is a hydrogenic-like bound state that forms in bulk crystals due to the Coulombic attraction between an electron and hole. Using *eq. (2)*, each of these Bohr radii can be easily calculated. In the case of the exciton, the reduced mass of the electron–hole pair is used for m^*. With these values; three different limits can be considered [75].

First, when the nanocrystal radius, $a$is much smaller than a_e, a_h, a_{exc} (i.e., when $a < a_e$, a_h , a_{exc}), the electron and hole are each strongly confined by the nanocrystal boundary. This is referred to as the strong confinement regime. Second, when a is larger than both a_e, and a_h, but is smaller than a_{exc} (i.e., when a_e, $a_h < a < a_{exc}$ only, the center-of-mass motion of the exciton is confined. This limit is called the weak confinement regime. Finally, when a is between a_e and a_h (e.g., when $a_h < a < a_e$, a_{exc}), one entity (e.g., the electron) is strongly confined and the other (e.g., the hole) is not. This is referred to as the intermediate confinement regime [76-78]. The confinement regime which is accessed in the experiment depends on the nanocrystal material and its size. For example, because the exciton Bohr radius in InAs is 36 nm and nanocrystals are typically much smaller than this size, InAs nanocrystals are in the strong confinement regime. In contrast, CuCl has an exciton Bohr radius of 0.7 nm.

Accordingly, CuCl nanocrystals are in the weak confinement regime. CdSe nanocrystals can be in either the strong confinement or the intermediate confinement regime, depending on the size of the nanocrystal, because a_{exc} is 6 nm [79]. Considering that the charge carriers in spherical semiconductor nanocrystals are confined within three dimensions by the crystallite, in the case of quantum confinement, it therefore follows that the wave function given in *eq. 3*:

$$\psi(r) = \Phi(kr)u(r)(\psi(r \geq R) = 0) \qquad (3)$$

with

$$u(r+n) = u(r) \qquad (4)$$

has to satisfy the boundary conditions. In semiconductor nanocrystals when compared to their bulk counterparts, the electrons and holes are closer together; as such the Coulombic interaction between the electron and hole cannot be neglected. Brus [80,81] showed, on the basis of the effective mass approximation, that for CdE (E = S or Se) nanocrystals the size dependence on the energy of the first electronic transition of the exciton (or the band gap shift with respect to the typical bulk value) can be approximated using the equation,

$$\Delta E \cong \left(\frac{\hbar^2\pi^2}{2R^2}\right)\left[\frac{1}{m_e^*} + \frac{1}{m_h^*}\right] - \left(\frac{1.8e^2}{\varepsilon R}\right) \qquad (5)$$

where ΔE is the change in energy, $\hbar$ is Planc's constant, R is the radius of the particles, m_e^* and m_h^* are the effective masses of the electron and hole respectively and ε is the dielectric constant of the material.

The dependence of eq. 5 on R is dependent on the two terms containing R. The Coulomb term $\left(\frac{1.8e^2}{\varepsilon R}\right)$ shifts the first excited electronic state to lower energy (R^{-1}), while the quantum localization term $\left(\frac{\hbar^2\pi^2}{2R^2}\right)$ shift the state to higher energy (R^{-2}). Consequently, the first excitonic transition (band gap) increases in energy with decreasing particle diameter. This prediction has been confirmed experimentally for a wide range of semiconductor

nanocrystals [82-87] with a blue shift in the onset of the absorption of light being observed with decreasing particle diameter. Moreover, the valence and conduction bands in nanocrystalline materials consist of discrete sets of electronic levels and can be viewed as a state of matter between that of molecules and a bulk material. However eq. 5 does not account for other important factors observed in real nanocrystals and therefore might not accurately predict the particle size relationship. Other theoretical methods have been established, but none are accurate when it comes to predicting energy transitions for very small particles [83-87].

1.2.2. Optical properties of semiconductor nanocrystals

(a) Absorption

Absorption of a photon by the nanocrystal occurs if its energy exceeds the band-gap. As a result of quantum confinement; decreasing the size of the semiconductor to nanoscale results in a hypsochromic (blue-) shift of the absorption onset as shown in Fig. 1-3 [83]. A relatively sharp absorption feature near the absorption onset corresponds to the excitonic peak, i.e. the lowest excited state exhibiting large oscillator strength. While its position depends on the band-gap and, consequently, on the size of the nanoparticles, its form and width is strongly influenced by the size distribution, as well as the type and stoichiometry of the nanocrystals. Therefore polydispersed samples typically exhibit only a shoulder in the absorption spectrum at the position of the excitonic transition. Less pronounced absorption features in the shorter wavelength range correspond to excited states of higher energy [84]. As a rule of thumb, it can be asserted that the larger the number of such spectral features and the more distinctly they are resolved in the absorption spectrum, the smaller is the size dispersion of the sample.

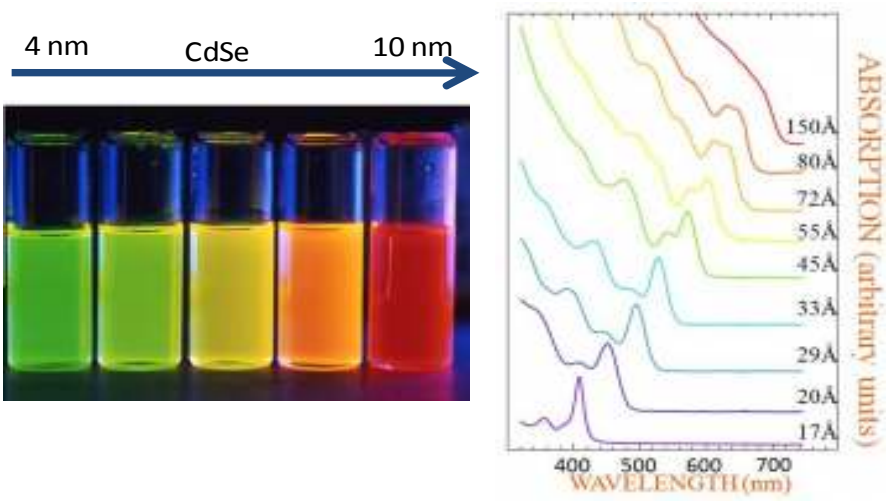

Fig.1-3: Size dependent optical properties due to quantum confinement [83].

(b) Photoluminescence

Photoluminescence, i.e. the generation of luminescence through excitation by photons, is formally divided into two categories, fluorescence and phosphorescence, depending upon the electronic configuration of the excited state and the emission pathway. Fluorescence occurs when a semiconductor absorbs photons with an energy hv_e superior to its band-gap, and after charge carrier relaxation via phonons to the lowest excited state emits light of a higher wavelength (lower energy hv_f) after a brief interval. The process is called the fluorescence (Fig. 1-4).

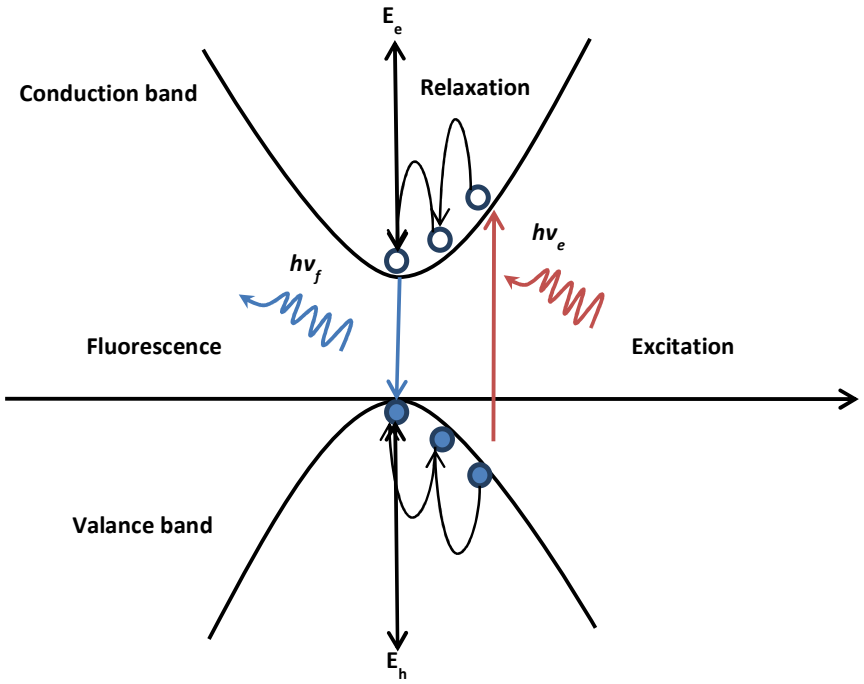

Fig. 1-4: Fluorescence in a bulk semiconductor.

The process of phosphorescence occurs in a similar manner, but with a much longer excited state lifetime. This is related to the symmetry states of the crystal. The emitted photons have an energy corresponding to the band gap of the nanocrystals and for this reason the emission colour can be tuned by changing the particle size. It should be noted that efficient room temperature band edge emission requires proper surface passivation, otherwise charge carriers are very likely to be trapped in surface states, enhancing non-radiative recombination. For CdSe, due to spectral diffusion and the size distribution of the nanocrystals, the room temperature luminescence line-widths of ensembles lie in the range of 20–25 nm (full width at half maximum, FWHM). This phenomenon is usually referred to as a Stokes-shift and has its origin in the particular structure of the exciton energy levels inside the nanocrystal.The absorption of electromagnetic radiation by nanocrystallite materials is relatively straightforward. However, the luminescent behaviour of such particles is more complicated and the ideas that have emerged for explaining these phenomena illustrate an interesting interplay between experiment and theory. Brus, in his keynote paper [81], explained, on the basis of theoretical and experimental studies, the features expected in the luminescence spectra of quantum confined semiconductors and successfully

anticipated the results of many subsequent experiments. The luminescence of materials such as CdSe, CdS, CdTe and other nanocrystalline particles show a typical red shift in emission relative to the corresponding absorption spectrum.

The luminescent behaviour of nanocrystalline semiconductors is very complicated and is often controversial. There are two models which attempt to explain the origin of this effect. Brus, *et. al.* [81] investigated the luminescence properties of nanocrystalline semiconductors. The investigation was based on cadmium sulfide, which is usually sulfur deficient due to S^{2-} vacancies. The S^{2-} vacancy (V_s^+) is a deep trap for electrons and exothermically extracts an electron from the valence band. The hole localizes away from the defect and the V_s^+ state cannot energetically remove another electron. The V_s^+ vacancy sets a deep (ca. 0.07 eV) trap for a conduction electron, in which they combine forming the V_s^0 state. Luminescence is attributed to the emission from the recombination of the electron in the V_s^0 state and a pre-existing trapped hole. The distribution of the electron-transfer distance, R, is determined by the density of trapped holes and is independent of the diameter of the cluster. In surface-passivated nanocrystalline materials, the 'plugging' of the surface states by the passivating material minimizes the transfer of electrons to the S^{2-} defects. As a result, electron-hole recombination leads to near band edge emission. This has been confirmed experimentally when the surface of nanoparticles are passivated with organic ligands such as tri-n-octylphosphine oxide (TOPO), inorganic phases and/or oxidation of surface molecules, resulting in a narrow band edge emission with increased quantum yields.

The second model attributes the red shifted band edge emission observed in luminescence studies on surface passivated CdSe quantum dots to the existence of a "dark exciton" [85-87]. The lowest electron-hole pair state or band edge exciton ($1S_{3/2}1Se$) in spherical CdSe quantum dots is eightfold degenerate. However, in non-spherical CdSe quantum dots this degeneracy is split further into five sublevels. This is due to the distortion of the wurtzite lattice of CdSe as a result of crystal field splitting, the non-spherical shape of the particles and the exchange interaction between electron and hole. Of the five sublevels that exist for this system, the levels $|N_m| = 1^U$, 1^L and 0^U are optically active ('bright excitons') and the $|N_m| = 2$ and 0^L states are optically forbidden ('dark excitons'). Transitions from the dark

states are forbidden because decay to the ground state requires two units of momentum. This optically forbidden nature of the $|N_m| = 2$ state explains the emission behaviour in CdSe. Excited electrons that occupy the $|N_m| = 1^L$ state relax into the $|N_m| = 2$ state.

The energy difference between those two levels accounts for the observed Stokes shift in the luminescence spectrum, which increases as particle size decreases. Emission from the dark state to the ground state occurs when an additional unit of momentum is provided by a phonon. This mechanism also explains the relatively long radiative lifetimes. Photoluminescence studies on a single quantum dot of CdSe with continuous excitation have recently revealed intermittent light emission [85], which is attributed to an Auger electron photoionization mechanism. The "on-state" emission occurs from radiative recombination from single electron-hole pairs after photoexcitation. The "off-state" is formed when the particle absorbs two photons, generating two electron-hole pairs and through Auger photoionization there is an ejection of charge (e^- or h^+) outside the dot. Subsequent emission is non-radiative, with the energy being transferred to the carriers, which accounts for the off-state. When the CdSe particles are passivated by another semiconductor, such as ZnS, the average on/off times increases relative to the unpassivated CdSe. This confirms the sensitivity of luminescence to changes at the nanoparticle-matrix interface [86].

1.2.3. Electrical properties of semiconductor nanoparticles

In a nanocrystal, the electronic states are typically confined within the nanocrystal by significant potential barriers. Transport between nanocrystals can, therefore, be considered as a problem of hopping between localized states [87]. For small nanocrystals in the strong confinement regime, charge transport is limited by inter-particle electron transfer, rather than by the transport of electrons within a single particle. Therefore, the physics has more in common with that of charge transport in molecular systems, rather than with traditional semiconductor transport theory [88]. In nanocrystals, changing the size allows the electron affinity and ionization potential of the nanocrystal to be tuned, which may, in principle, affect the rate of charge transfer. The disorder and surface trap states associated with small particles may dominate the charge transport properties of nanocrystalline systems.

One of the major motivations for the study of nanocrystals is the possibility that they may be useful in device applications. Some of the devices which have been demonstrated in the laboratory include light-emitting diodes (LEDs) [89], photovoltaic devices [90], and single-electron transistors [91]. For large-area applications such as LEDs and photovoltaics, nanocrystals have the advantages of being processable from solution and having size-tunable absorption and emission. Despite these advantages, nanocrystals have not yet found their way into commercial devices.

In order to illustrate some of the charge transport and charge transfer processes important in nanocrystal-based devices, the method of operation of LEDs and photodiodes will be briefly introduced. The simplest device in which light emission can occur is a thin film of nanocrystals sandwiched between metal electrodes, as illustrated in Fig. 1-5. One of the electrodes must be semitransparent; hence, indium–tin oxide (ITO) is typically used as the anode. When a positive voltage is applied to the anode, holes are injected from the anode and electrons from the cathode. These carriers can then move through the device under the action of the applied field by hopping from nanocrystal to nanocrystal.

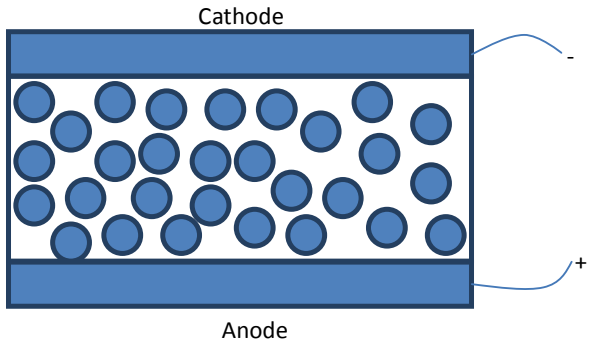

Fig. 1-5: Schematic representation of a typical structure for electrical characterization of nanocrystalline films.

When an electron and hole arrive on the same nanocrystal, an exciton can be formed, which can then decay radiatively giving emission at an energy characteristic of the size of the nanocrystal. It has been found that this simple type of a device does not work well as a LED because poor hole injection leads to low efficiencies and high turn-on voltages. A much

improved performance has been achieved using a layer of a hole-transporting conjugated polymer between the anode and the nanocrystal layer [92,93], as shown schematically in Fig. 1-6(a). Conjugated polymers have semiconducting properties due to delocalization of k-orbitals along the unsaturated polymer chain and are used in large-area LEDs and photodiodes in their own right [94,95]. In the nanocrystal LED, the polymer layer provides an intermediate energy level between the anode and the nanocrystals, which assists the overall rate of hole injection.

In a photodiode or photovoltaic device, the processes are opposite to those required in a LED. Light is absorbed in the device, producing excitons which must then be split up into free electrons and holes. These charge carriers must then be transported to opposite electrodes without recombination, thus producing a current in the external circuit. Again, conjugated polymers are useful as hole transporters in conjunction with nanocrystals [96]. By mixing nanocrystals with the polymer as shown in Fig. 1-6(b), dissociation of excitons created in the polymerinto electrons and holes can be facilitated by electron transfer from polymer to nanocrystal. Both electron and hole must then find a pathway to the appropriate electrode by hopping from polymer chain to polymer chain or from nanocrystal to nanocrystal, respectively.

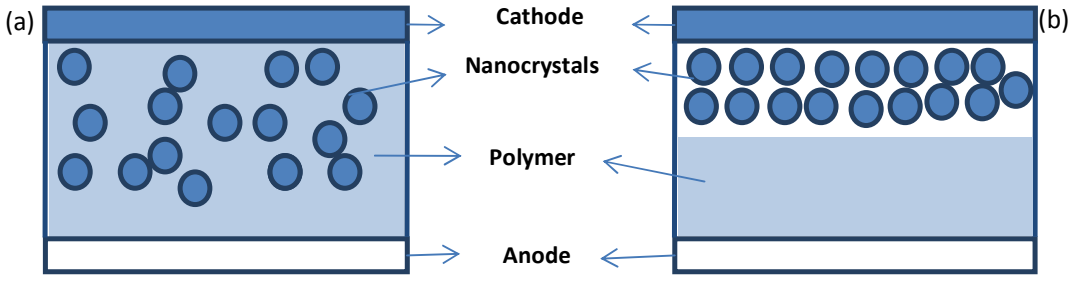

Fig. 1-6: Schematic cross-sectional structure for (a) a photovoltaic device and (b) a light-emitting diode containing both nanocrystals and a conjugated polymer.

The theory of electron transfer between localized states has been developed to predict rates of electron transfer in molecular systems and has been extended to treat electron transfer to and from molecules at a metallic or semiconductor surface [97]. In this model

the energy of the initial and final states are considered as a function of nuclear coordinates, as shown in Fig. 1-7. The nuclear coordinates cannot change during the electron tunneling process from initial to final state, and electron transfer must therefore occur at nuclear coordinates which correspond to an intersection of the initial and final potential energy surfaces.In Fig. 1-7, ΔG^0represents the free-energy change between initial and final states and λ is the reorganization energy required to change from initial to final equilibrium nuclear coordinates. For charge transport between nanocrystals, the tunneling rate is slow compared with typical vibrational frequencies and the system must, on average, sample the crossing point many times before transfer can occur.

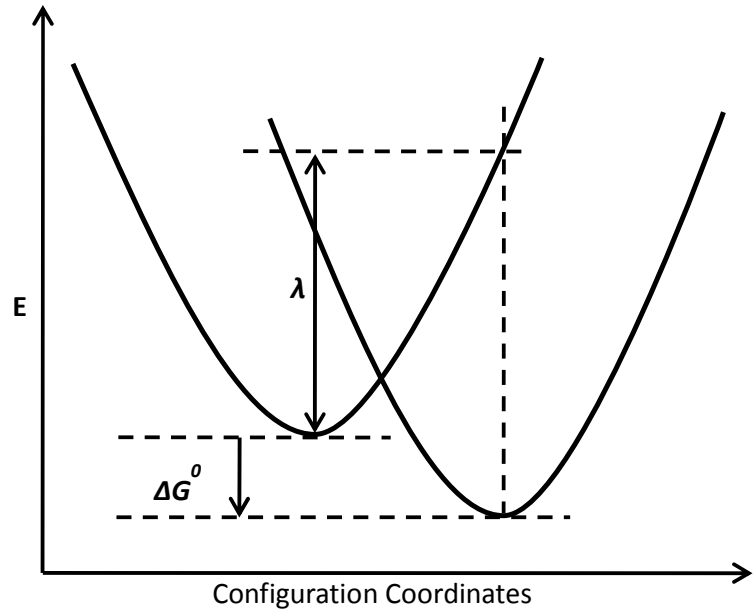

Fig. 1-7: Energy as a function of configuration co-ordinate for the initial and final states in an electron transfer reaction. The reorganization energy, k, and the free energy change for the reaction, ΔG^0 are shown [98].

In this non-adiabatic limit, the rate of electron transfer k is given by Eq. (6)

$$k = \left(\frac{2\pi}{\hbar}\right)|V_{12}|^2(FC) \quad (6)$$

where V_{12} is the electronic coupling matrix element between initial and final states on resonance and FC is the Frank–Condon factor, given by the sum of overlap integrals of the vibrational wave functions of the initial and final states, weighted by the Boltzmann probability of occupation of the initial vibrational state. At high temperatures, when the vibrational frequencies are all small compared with kT/h, the vibrations may be treated classically and Eq. (6) reduces to Eq. (7) [98].

$$k = \left(\frac{2\pi}{\hbar}\right)|V_{12}|^2(FC)(4\pi\lambda kT)^{-1/2}e^{-\Delta E^*/kT} \quad (7)$$

where

$$\Delta E^* = \frac{(\Delta G^0 - \lambda)^2}{4\lambda} \quad (8)$$

To calculate the total reorganization energy λin Eq. (8), both internal vibrations in the molecules and changes in the configuration of the solvent or dielectric surrounding the molecules must be taken into account.

$$\lambda = \lambda_i + \lambda_0 \quad (9)$$

where λ_i and λ_0 denote the internal and dielectric contributions respectively.

The contribution from the dielectric can be estimated using a dielectric continuum model, where the slow (non-electronic) part of the response is responsible for the reorganization barrier to electron transfer. For electron transfer between two spheres, $\lambda_0$is given by:

$$\lambda_0 = \frac{e^2}{4\pi\varepsilon_0}\left(\frac{1}{2r_1} + \frac{1}{2r_2} + \frac{1}{d}\right)\left(\frac{1}{\varepsilon_{op}} - \frac{1}{\varepsilon_s}\right) \quad (10)$$

where r_1 and r_2 are the radii of the two spheres, $d$is their center-to-center separation, and ε_{op} and $\varepsilon_s$are respectively the optical and static dielectric constants of the surrounding dielectric. For the specific case of charge transfer between two nanocrystals, an attempt to

identify the main contributions to $\lambda_i$andλ_0 can be made. This problem has been studied by Brus [99], who applied the Marcus theory of electron transfer to silicon nanocrystals surrounded by solvent. To calculate the internal reorganization energy, one must consider how the lattice in the nanocrystal responds to the addition (or removal) of an electron. In general, changing the charge state of the nanocrystal changes the equilibrium nuclear configuration. The energy associated with the change from the uncharged configuration to the charged configuration on a single nanocrystal is denoted as λ_s. Because reorganization is necessary in both nanocrystals for electron transfer to occur, the total value of λ_i in Eq. (9) is given by the sum of the deformation energies λ_s on both nanocrystals. To understand the origin of λ_s in more detail, the vibrational modes which transform between the charged and uncharged configurations must also be considered. These modes are the phonon modes of the nanocrystal, which may be either acoustic or optical. The strength of coupling of phonon modes to the electronic state of the nanocrystal is dependent on the chemical composition of the semiconductor and on the nanocrystal size [100].

In a non-polar material such as silicon, the relevant coupling is with acoustic phonons. Acoustic phonons connect to the energy of the system through the deformation potential (a change in the electronic energy due to strain in the lattice). In nanocrystals, the contribution to $\lambda_s$from coupling to acoustic phonons through the deformation potential is expected to scale approximately as r^{-3}, where r is the nanocrystal radius [101]. Brus estimated a value of λ_s= 12 meV in silicon nanocrystals of diameter 2 nm [99]. In polar nanocrystals such as CdSe, the situation is more complicated because optical phonons may also couple to the electronic state through the Fr$\ddot{o}$hlich interaction [102]. This interaction involves a polarization of the crystal lattice in response to an internal electric field. The Fr$\ddot{o}$hlich interaction is responsible for the vibrational structure seen in emission spectra of CdSe nanocrystals, although, in this case, the scaling of coupling strength with nanocrystal size is complicated because both an electron and hole are present in the nanocrystal and partially compensate each other's charge [102].

The simpler case of coupling of optical phonons to a change in the overall charge state of the nanocrystal (polaron formation) has been modelled in CdSe by Oshiro *et al.* [103], who found that the relaxation energy associated with polaron formation increases rapidly as the

nanocrystal size becomes less than the exciton Bohr radius, reaching a value of ≈30 meV for a diameter of 2 nm. An accurate estimation of the additional reorganization energy due to deformation potential coupling in CdSe nanocrystals could not be made; however the contribution from the Fr*ö*hlich interaction is expect to dominate. Because the longitudinal optical (LO) phonon energy in CdSe (26.5 meV) is comparable with thermal energies at room temperature, the high temperature approximation made in Eq. (7) is unlikely to be valid even at room temperature.

In this case, it is necessary to use more detailed theories which account for quantization of vibrational energy and allow nuclear tunnelling between different vibrational states [104]. As explained earlier, additional reorganization energy arises when the nanocrystals are surrounded by a dielectric which relaxes in response to the change in charge state of the nanocrystal. For the case considered by Brus, where silicon nanocrystals are surrounded by water, the highly polar nature of the solvent leads to a value of λ_0 as large as 400 meV for transfer between touching nanocrystals of 2 nm diameter [99]. In a close-packed film of CdSe nanocrystals coated with tri-n-octylphosphine oxide (TOPO), the TOPO ligands (and the surrounding nanocrystals) play the role of the solvent. For example, Eq. (10) can be used to estimate a value of λ_0= 100 meV for 2 nm diameter CdSe particles with a center-to-center separation of 3.3 nm (corresponding to the separation of close-packed TOPO-coated particles [105]). In this estimate, it has been assumed that the local effective dielectric constant is dominated by the TOPO, which has a static dielectric constant ε_s= 2.61 [106], and the optical frequency dielectric constant has been approximated with that of TOPO, which is ε_{op} = 2.07 [107]. The $|V_{12}|^2$ tunneling term in Eq. (6) can be treated in a simple approximation as tunneling through a one-dimensional potential barrier in the presence of an applied field.

This approach was used by Leatherdale *et al.* in the context of electron transfer from a photo-excited nanocrystal containing an electron and a hole [108]. Using the Wentzel–Kramer–Brillouin (WKB) approximation to obtain the tunnelling probability through a square tunnel barrier of height$\emptyset$and width $d$in an applied field Egives a tunnelling probability, S,

$$S = \left[-\frac{4}{3}\sqrt{\frac{2m^*}{\hbar^2}}\frac{1}{eE}\left[\emptyset^{3/2} - (\emptyset - eEd)^2\right]\right] \quad (11)$$

where m^* is the effective mass of the carrier within the barrier. For thin, high barriers, the tunneling probability is found to decrease exponentially with increasing barrier width. It is often useful to describe the charge transport properties of an extended solid in terms of the carrier mobility, μ. For electron transport, for example, the electron mobility μ_e is defined by:

$$J_e = ne\mu_e E \quad (12)$$

where J_e is the electron drift current density, $n$is the number density of electrons, and $E$is the applied field. In systems where hopping transport dominates, the mobility is often field dependent. The mobility is related to the net hopping rate for individual carriers, $R(E)$, by:

$$\mu(E) = \frac{R(E)}{E}d \quad (13)$$

where d is a typical hopping distance in the direction of the applied field and $R(E) = R_{forward}\ (E) - R_{back}\ (E)$, the difference in forward and backwards hopping rates. In some materials, a significant proportion of the carriers may occupy trap states which are much less mobile than the ‘‘free’’ carriers. It is useful to define an effective mobility, μ_{eff}, such that:

$$J = n_{total}e\mu_{eff}E \quad (14)$$

where n_{total} is the sum of both trapped and free-charge carrier densities. Where the trapped carriers are completely immobile and the free carriers have mobility μ_{free}, we may define the effective mobility as:

$$\mu_{eff} = \mu_{free}\frac{n_{free}}{n_{total}} \quad (15)$$

In nanocrystalline systems it is well known that trap states exist at the surface of the particles and that the number and depth of traps is highly sensitive to the surface passivation. Because transport of both trapped carriers and ‘‘free’’ carriers (those occupying core states) involves tunnelling between particles, carriers in shallow traps may have mobilities which are not much less than those of ‘‘free’’ carriers.

It is therefore not possible to draw a clear distinction between mobile (free) and immobile (trapped) carriers. In this case, where there are populations of carrier n_i with different mobilitiesμ_i, the appropriate definition of effective mobility is:

$$\mu_{eff} = \frac{\sum_i \mu_i n_i}{\sum_i n_i} \quad (16)$$

In this simple model for electron transport between identical nanocrystals, one would expect the activation barrier to decrease with applied field until the transfer becomes activationless at $\Delta G = -\lambda$. At higher fields, the activation energy would then increase as the ‘‘inverted Marcus region’’ is entered. In practice, though, there is a series of quantum-confined electron levels in a nanocrystal, and at high fields, electrons are likely to be injected into higher-lying electronic states, followed by rapid relaxation to the lowest state [99]. The presence of these higher-lying states allows electron transfer to occur with smaller activation energy than would be necessary for direct transfer to the lowest electron state in the inverted region. Electron transfer in a nanocrystalline film is a local process sensitive to the electronic structure of an individual nanocrystal and to its immediate environment. Therefore, disorder can play an important role in determining electron transport through the film.

The first source of disorder in the electron energy levels arises from the distribution of particle sizes, leading to a distribution of quantum confinement energies. This disorder is also responsible for the inhomogeneous broadening observed in absorption and emission. For typical CdSe nanocrystals, this broadening is in the range 50–100 meV and is mostly due to variation in the electron confinement energy. At a given electric field, electron transfer will occur most readily from particles where the neighbouring particle has an electron affinity which gives the lowest activation energy. Further disorder arises from the

distribution in inter-particle separations in a solid film. Because the tunnelling rate is exponentially sensitive to the tunnelling distance, a distribution of distances will lead to a distribution of tunnelling rates. Also, the effective dielectric constant experienced by a charged particle will be sensitive to the exact arrangement of other particles around it.

Because the electron affinity depends not only on the electron- confinement energy but also on the local dielectric environment surrounding the nanocrystal [109] spatial disorder will give rise to additional disorder in the electron affinity of individual particles. The effects of disorder on the transport properties of nanocrystalline films have been studied for metallic particles [110], but they have not yet been modelled in detail for semiconducting particles. However, the results of work on charge transport in molecularly doped polymer films are particularly relevant because much of the physics is similar. Bassler and co-workers have used Monte Carlo simulations to model the field and temperature dependence of the mobility in systems with a Gaussian distribution of transport levels [111]. At low fields, electrons on nanocrystals with particularly low energies within the broadened distribution will find it more difficult to hop to a neighbouring nanocrystal, because the neighbours are likely to be higher in energy. The presence of these low-energy sites leads to behaviour which is in some ways analogous to the effect of traps. Bassler and co-workers assume microscopic hopping rates given by the simple Miller–Abrahams model [112] (activationless where the final state is lower in energy than the initial state and with an activation energy given by ΔG where the hop is ‘‘up hill’’ in energy). In its simplest form, their model predicts mobilities which follow:

$$\mu = \mu_0 exp\left[\left(-\frac{A}{kT}\right)^2\right] exp\left[\gamma(T)\sqrt{E}\right] \quad (17)$$

where the constant A and the temperature dependence of γ depend on the details of the disorder that is present. This model (for systems where the disorder has a Gaussian width of about 0.1 eV) corresponds well with experiments on molecularly doped polymers [113]. It is however difficult to measure over a large enough temperature range to distinguish the temperature dependence predicted by Eq. (17) from the simple Arrehnius behaviour which might be expected if structural reorganization energies controlled the transport. Similar behaviour to that predicted by Eq. (17) might be expected in nanocrystalline systems if

disorder is the dominant effect. In summary it has been shown that in addition to the electronic tunneling process, both internal and dielectric relaxation energies are likely to be important in determining electron transfer dynamics in nanocrystals. Both of these relaxation energies are size dependent and can be in the range 50–100 meV for small CdSe particles. It has also been identified that surface trapping, higher-lying states, and disorder are factors likely to complicate the transport in real samples.

1.2.4. Magnetic properties

When the object becomes so small that the number of surface atoms is a sizeable fraction of the total number of atoms then the surface effects become increasingly important. In magnetism a typical size of a magnetic domain is of the order of 1 μm and particles much smaller than that will be mono-domain [114]. Properties of very small metal particles have been extensively studied for the past 50 years and much is known about their electronic and geometrical structure [115]. Nevertheless, the field is still growing due to the vast number of different systems and properties which are magnetic and the complexity of material magnetism. While the interest in nanoscopic material is academic to a great extent, small magnetic materials are of industrial importance primarily stimulated by the recording industries' desire for ever denser and more reliable recording media [116]. The requirement of smaller particles which can be used for recording purposes continues since smaller particles imply higher data storage density [115]. Another area of importance relating to the use of nanoparticles that posses both the optical and magnetic properties has been in biomedicine for therapeutic as well as diagnostic applications [116]. However, there are limits to how small the magnetic particle can be and still be useful.

Magnetic nanocrystals are complex systems and often have complex electronic structures. Consequently it has become a computational challenge to determine even the ground state of the smallest ferromagnetic particles from first principles [117-119]. The complications mainly arise because the electronic spin (which is the carrier of the magnetic moment) cannot be ignored as it done for conventional materials. Many interesting magnetic properties are related to the dynamics of the spin system [120]. At low temperatures, the magnetic moment (total electronic spin) of the system may spontaneously change direction in a quantum tunneling process [121]. At higher temperatures, the spin direction will

fluctuate due to thermal agitation. At the same time the magnitude of the magnetic moment will reduce, and eventually vanish at high enough temperatures (at the Curie temperature) [122-124].

1.2.4.1. Basic concepts in magnetism

(a) Atomic magnetism

Most atoms have a net electronic angular momentum ***J*** which is a combination of the total spin ***S*** and the total angular momentum ***L***. These quantities can be determined for a specific atom using Hunds rules. The electronic structure of the partially occupied atomic shell is found by maximizing the spin ***S*** for the valance shell of the atom, while respecting Pauli's principle. The orbital angular momentum ***L*** is found by maximizing it without violating the Pauli's principle. The ***S*** and the ***L*** are then combined to give the total angular momentum ***J*** in such a way as to maximize the total $J = |L \pm S|$ in units of $\hbar$. The magnetic moment of the state ***(SLJ)*** is given by eq. 18 [125]:

$$\mu = -g(SLJ)\mu_B \boldsymbol{J} \quad (18)$$

where g is the Lande factor given by:

$$g = {}^{3}/_{2} + {}^{1}/_{2}\left(S(S+1)\right) - \frac{L(L+1)}{J(J+1)} \quad (19)$$

The energy of the paramagnetic atom$(\mu \neq 0)$in a magnetic field is:

$$E(B) = \mu \cdot \boldsymbol{B} \quad (20)$$

Which means its energy depends on its orientation. Consequently if it is subjected to a gradient, there will be a net force on it:

$$\boldsymbol{F} = -\nabla(\mu \cdot \boldsymbol{B}) \quad (21)$$

For, example if an atom is subjected to a field gradient $\delta {}^{B_z}/_{\delta_z}$, the force in the *z* direction is

$$F_z = g\mu_B m_J \delta {}^{B_z}/_{\delta_z} \quad (22)$$

where m_J is the *z* component of ***J*** (quantized in units of ħ) and μ_B is the Bohr magneton. A consequence of this effect is that the force due to a field gradient on an atom is quantized and is either attractive or repulsive depending on the orientation of ***J*** with respect to the field. This is the reason for the symmetric and quantized deflection pattern that is observed in Stern-Gerlach atomic beam deflection experiments. On the other hand if the atom is in contact with the heat bath then the angular momentum can relax in the direction of lowest energy which is aligned with the magnetic field, thereby causing a net attractive force towards the direction of increasing field strength. In other words paramagnetic atoms in a matrix are attracted to magnets. The magnetization *M* is the time average of the projection of the magnetic moment in the direction of the magnetic field ***B*** as given in eq. 23[126].

$$M = \sum m_J g_J \mu_B exp\left(m_J g_J \mu_B {}^{B}/_{kT}\right) / \sum exp\left(m_J g_J \mu_B {}^{B}/_{kT}\right) \quad (23)$$

when $x = Jg_J\mu_B {}^{B}/_{kT} = \mu {}^{B}/_{kT}$ we obtain the Brillouin function:

$$M = g_J\mu_B {}^{(2J+1)}/_{2J} \, coth\left\{{}^{(2J+1)x}/_{2J}\right\} - \left({}^{1}/_{2J}\right) coth\left({}^{x}/_{2J}\right) \quad (24)$$

For a large J this reduces to a well known Langevin function:

$$M = g_J\mu_B coth(x) - {}^{1}/_{x} \quad (25)$$

(b) Ferromagnetism

When the metal atoms are combined one at time to form a particle, they arrange in such a way so as to minimize the total energy [125]. The atomic bonding is mediated by the valance electrons which diffuse into the solid and are shared by several or in the case of conduction electrons by all the atoms in the solid [127-129]. To illustrate the bonding and its consequences to magnetism, a simple case of bonding of two hydrogen atoms is considered. The ground state spatial wave functions of a diatomic molecule can be approximated as linear combinations of the atomic ground state, following Heitler and London for the H_2 molecule (eq. 26).

$$\psi_{s/t}(r_1, r_2) = \emptyset_1(r_1)\emptyset_2(r_2) \pm \emptyset_1(r_1)\emptyset_2(r_2) \quad (26)$$

where $\emptyset(r)$ is the electronic ground state wave function of the hydrogen atom and ψ is the two electron wave function,ψ_s is symmetric under interchange of the electronic coordinates r_1 and r_2 and $\psi_t$is the anti-symmetric. This means that the two spins are oppositely aligned and hence in a singlet system, while the spin wave function of ψ_t must be symmetric (consequently the spins are aligned to give a triplet state). The energy difference between these two states is the exchange energy J_{st} given in eq. 27.

$$J_{st} = < \psi|H|\psi_s > - < \psi_t|H|\psi_t \quad (27)$$

where *H* is the total Hamiltonian.

The energy difference between the $S = 0$ and $S = 1$ state is essentially due to the electric Coulomb interaction. For most diatomic molecules, as for H_2, the singlet state is lower in energy than the triplet state (ψ_s is then the bonding state and ψ_t is the antibonding state of the molecule). Hund's rules dictates that the atoms with partially filled electronic shells will have relatively large spins. These rules can be traced to the exchange interaction which in atoms favours aligned spins, since anti-symmetry of associated spatial wave functions produces vanishing probabilities for both electrons to occupy the same place at the same time. Consequently the Coulomb energy is reduced compared with the symmetric case.

(c) Exchange

Several exchange type interactions are responsible for magnetism in materials. One is the intra-atomic exchange which causes atoms to attain a net spin that underlies Hunds rules. Exchange is also responsible for spin order (ferromagnetic or antferromagnetic behaviour). The interaction is an inter-atomic exchange coupling which can be either indirect or direct. Indirect exchange occurs, for example, in the rare earth metals where the localized spins (from partially filled f-shells) interact almost entirely via the mutually shared conduction electrons. Due to the small overlap of the f-wave functions, this interaction is more important than the direct exchange in these cases. The indirect exchange is described in theory by the Rudrman, Kittel, Kasuya and Yusida (the RKKY) [130-132] model which shows that the coupling between S_i and S_j is given by eq. 28:

$$V_{ij} = -J_{sd}^2 \left({}^{2mk_F^4}/_{\pi^3} \right) F_0(2k_F R_{ij}) S_i \cdot S_j \quad (28)$$

where,

$$F_0(x) = -{}^{cos(x)}/_{x^3} + {}^{sin(x)}/_{x^4} \quad (29)$$

and $J_{sd}$is the indirect (s-d) exchange coupling constant, m is the electron mass, k_F is the Fermi wavevector andR_{ij} is the distance between the localized spins S_i and S_j. The function $F_0(x)$ shows that for short distances the coupling is ferromagnetic however it reverses sign and oscillates as the distance increases. These RKKY oscillations in the exchange coupling are important for an understanding of the magnetic properties of surfaces and nanoparticles.

(d) Magnetism in nanocrystals

Surface magnetism

The magnetism at the surface of ferromagnets are significantly altered from the bulk for several reasons. For example since, the number of the nearest neighbours is reduced, a valence electron tends to spend more time at each ionic site, due to reduced coordination when compared with bulk. Weaker bonding to neighbouring sites causes the ions to have a more isolated atom character, i.e. the electrons (and hence the moments) are more

localized than bulk [133]. Fig 1-8 shows the evolution of the electronic structure as the dimensionality is increased from the atom to the surface to the bulk. In general, increasing the dimensionality causes a reduction of the spin imbalance as shown in Fig 1-8. Related considerations are important for ferromagnetic clusters and thin film [134].

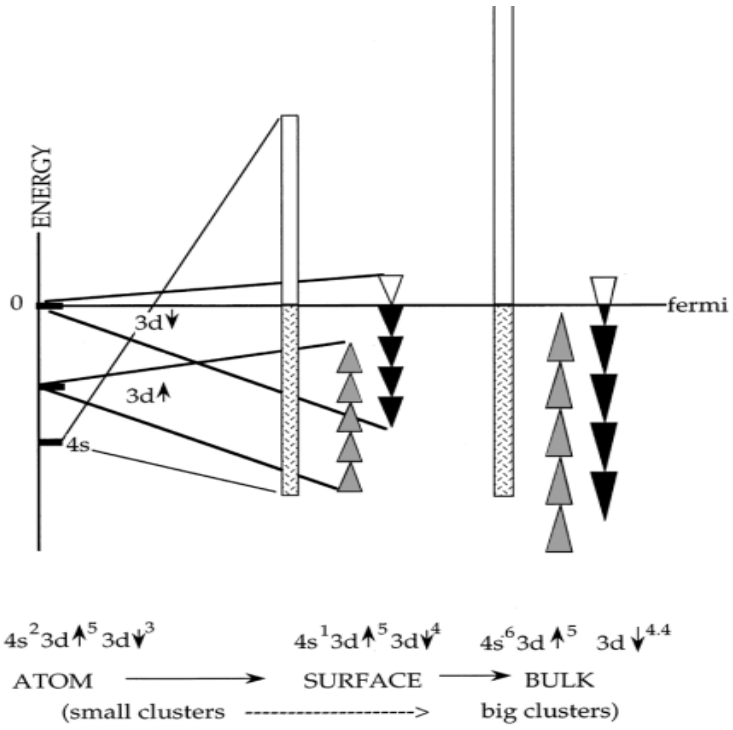

Fig. 1-8: Schematic diagram of the evolution of electronic bands of an itinerant ferromagnet with increasing dimensionality (atom to bulk) for nickel [134].

In the atom, the electronic system is organized into electronic shells with discrete energies. The 3d states are split by exchange interaction so that the minority (spin down) states are higher in energy than the spin up states as dictated by Hunds rules. The ground state configuration has a spin imbalance of 2. Further, increasing the coordination causes the discrete levels to broaden to continuous bands whose width is a measure of the frequency with which the electrons hop from one atom to the next. The band broadens most rapidly causing one electron to transfer to the d bands. Consequently the surface has a spin imbalance of 1. Increasing the coordination continues this trend so that ultimately the spin balance is reduced to 0.6 in the electronic configuration. The electronic structure of small particles follows similar trends due to the large surface to volume ratio.

1.2.4.2. Magnetic anisotropy and domains in small particles

In extended ferromagnetic systems, long range magnetic effects are important [128-130]. If the magnetic moment of the system is maximized i.e. all the spins are aligned, an extended magnetic field will result (as in permanent magnets). There is a substantial amount of magnetic field energy in this configuration. In the bulk, energy is significantly reduced through the formation of domains [135]. Within a domain, the magnetization is uniform in one direction, and the direction varies from one domain to the next. The net effect is a great reduction in the magnetic field strength and hence the magnetic field energy. Domain walls (Bloch walls) are however energetically costly, since in traversing a wall, the spin orientation changes at the expense of the exchange coupling which prefers aligned spins. Consequently domains tend to be relatively large (on the order of 1 μm). Small magnetic particles, therefore, are typically mono-domain, since the energy cost to form domain walls outweighs the reduction in magnetic energy. Typically, critical sizes for mono-domain particles are in the range of 20-2000 nm and depend on the ferromagnetic material under consideration.

The direction of the magnetic moment in the small particle is determined by both the shape and by its crystal structure through the anisotropy effect. Shape anisotropy accounts for the preferential orientation of the magnetic polarization (magnetization) along the axis for elongated particles. This is caused by the fact that the total magnetic field energy of the system is minimized for this polarization. The magnetization also prefers alignment along specific crystallographic axes. This is known as the crystalline anisotropy effect, which in fact dominates over the shape anisotropy effect in very small particles [128-130]. Physically the spin system couples to the crystal lattice via the spin orbit interaction. Axes of preferential magnetization are called the easy axes of magnetization. For example, if the z axis is the preferred axis then (to lowest order) the energy per unit volume will depend on the direction of magnetization and vary as:

$$E = K\cos^2\theta \quad (30)$$

where *K* is the anisotropy energy per unit volume and θ measures the angle between the z axis and the axis of magnetization.

1.2.4.3. Super-paramagnetism

Consider a single domain ferromagnetic particle without crystalline anisotropy [136]. The dynamics of the orientation of the spin system at temperature T (far below the Curie temperature), in a magnetic field B, is that of a single large spin system with spin S and magnetic moment μ in a magnetic field. The average magnetic moment in the direction of the applied field is given by the Langevin equation for atomic paramagnetism (eq. 23). The size of the spin can be many orders larger than the magnitude for a single atom. This situation is called super-paramagnetism. In particular:

$$M/\mu = coth\left(\mu \cdot B/kT\right) - kT/\mu \cdot B \quad (31)$$

where μ is the magnetic moment and M is the magnetization. Consequently,

$$M/\mu = \mu \cdot B/3kT \text{ for } \mu B \ll kT \quad (32)$$

$$M/\mu = 1 \text{ for } \mu B \gg kT \quad (33)$$

If an assembly of identical uniaxial super-paramagnetic particles is initially polarized along the easy axis, then the magnetization will reduce with increasing time:

$$M(t) = M_0 exp\left(-t/\tau\right) \quad (34)$$

The relaxation time τ is given by:

$$\tau = \tau_0 exp\left(kV/kT\right) \quad (35)$$

where τ_0 is of the order 10^{-10}-10^{-13} sec.

The approach to thermal equilibrium is due to random thermal effective torques or fields explained by Neel and Brown. The relaxation rate has an Arrhenius like behaviour, where $\tau_0{}^{-1}$is the attempt frequency and *KV* represents the barrier height, with V is the particle

volume, and Ka material constant (the anisotropy energy density). Estimates of the relaxation times for a 11.5 nm diameter spherical Fe particles at 300 K is 10^{-1} sec, while for a 15.0 nm particle it is 10^{9} sec, which demonstrates the extreme sensitivity to size in this case.Thesmaller particle instantly relaxes while the large one is stable for 30 years. The blocking temperature measures the temperature for which $\tau = 10^{2}$ sec which corresponds to an energy barrier $KV = 25kT$. An important property of super-paramagnetic particle systems is that they are non-hysteretic and their magnetization curves scale with H/T. These effects were first demonstrated by Bean and Jacobs for 2.2 nm Fe nanoparticles suspended in Hg at 77 K and 200 K.

1.3. Synthetic routes to semiconductor nanocrystals

(a) Colloidal routes

The first reported routes to such small particles involved the controlled precipitation of dilute colloidal solutions and the cessation of growth immediately after nucleation. La Mer, *et al.* [137] reported the synthesis of highly monodispersed micrometric colloids in which it was explained by nucleation and growth that are properly controlled. With this method particles with dimensions of the order of nanometres can be reproducibly synthesized. Small crystals, which are less stable, dissolve and then re-crystallize on larger more stable crystals, a process known as Ostwald ripening. For such methods to be effective for quantum dot synthesis the particles must have low solubility, which can be achieved by correct choice of the solvent, pH, temperature and passivating agent. Highly monodispersed samples are obtained if the process of nucleation and growth are distinctly separated to achieve fast nucleation and slow growth. The colloidal stability of these crystals has been improved by using solvents with low dielectric constants or by using stabilisers such as a styrene/maleic acid copolymer.

Henglein, Brus and co-workersas well as Weller [138-141] have made significant contributions to this field especially in studies of CdS. The control of the size of CdS nanocrystals was achieved by altering nucleation kineticrate using pH [139]. Despite its efficiency some of the most important semiconductors such as CdSe, GaAs, InP and InAs cannot be easily synthesised by this method. This method is a problem as it involves low

temperature, producing poorly crystalline material. Such colloidal particles prepared in aqueous media are not sufficiently stable at higher temperature for annealing to occur without agglomeration. CdS and ZnS have also been produced from methanolic solutions without the use of an organic ligand for stabilisation, using the repulsion of the electrostatic double layer to stop agglomeration [141].Zn_3P_2 and Cd_3P_2 have both been produced by aqueous methods, by the injection of phosphine gas into a solution of the relevant metal perchlorate [142,143]. The control of the particle size was achieved by varying the phosphine concentration and the temperature of the reaction. Samples of both Zn_3P_2 and Cd_3P_2 showed remarkable quantum size effects as observed by changes in the colour of the products. Their colours varied from white in small Cd_3P_2 particles to brown for the bulk material.

Surface modifications of semiconductors nanocrystallites can lead to electro- and photoluminescence systems, which may have applications in light emitting devices. One possibility for the preparation of this type of material is the growth of a solid on the surface of another, with the latter acting as a seed for the heterogeneous nucleation of the former. Examples for the use of this method include TiO_2/Cd_3P_2 [144], HgS/CdS [145], PbS/CdS [146], CdS/HgS [147], ZnS/CdSe [148], ZnSe/CdSe [149] and CdSe/ZnS [150]. Solution methods (using an aqueous media) provide a cheaper route to synthesis of many nanoparticle materials. However the low temperatures typically used in these methods mean that any defects formed in the early stages of the preparation are likely to be trapped and the crystallinity of the material will be poor. Also several semiconductors are not easily obtained using these methods, with some being air and/or moisture sensitive e.g. GaAs and InSb.

(b) Synthesis in confined matrices

A number of matrices have been used in the preparation of semiconductor nanoparticles and these include zeolites [151], layered solids [152], molecular sieves [153] micelles/microemulsions [154], gels [155], polymers [156] and glasses [157]. These matrices can be viewed as nanochambers, which limit the size to which crystallites can grow. Their properties are not only determined by the confinement of the host materials but also by the properties of the system, which include the internal/external surface properties of the zeolite and the lability of micelles. Growing particles in the internal cavities of zeolites limits

the particle size of materials, usually to less than 20 nm. CdS has been synthesised in two different zeolites by ion exchange from the sodium cationic form to the cadmium cationic form, followed by exposure to H_2S gas. Depending on the amount of cadmium ions utilised, different particle sizes were obtained [158].

Cadmium telluride nanoparticles have also been prepared in sodium or potassium zeolites. This involved the vapour deposition of tellurium to give CdTe clusters. The size of the cluster could be controlled by either a potassium or sodium resin, which altered the pore diameter [159]. PbS nanoparticles were obtained by exchanging Pb^{2+} into a ethylene/methacrylic acid copolymer followed by exposure to H_2S gas. The size of the particles was again controlled by the amount of Pb^{2+} ions resulting in sizes ranging from 13 nm to 125 nm [160]. A similar technique was used to grow particles in the interlamellar regions of the layered host, $Zr(O_3PCH_2CH_2COOH)_2$. Conversion of the host to different metals such as Pb, Cd, and Zn followed by treatment with H_2E (E = S, Se) resulted in the growth of metal sulfide and selenide nanoparticles [161]. Cole-Hamilton and co-workers [162] have developed an organo-metallic route to polymeric composites of CdSe and ZnSe. This involves use of the polymer 2-pyridyl-polybutadiene which was reacted with a group 2 metal alkyl, to give an adduct. A toluene solution of the polypyridine bound metal alkyl was exposed to H_2Se gas to give particles whose size was mainly controlled by both the solvent and reaction temperature. GaP nanoparticles have also been prepared in the pores of zeolite Y, in which the vapour transfer of Me_3Ga into a dry Na^+/H^+ exchange zeolite resulted in methane evolution and the formation of $Me_{3-x}Ga$ sites. Exposure of this material to excess PH_3 at various temperatures (200 – 400 °C) resulted in the growth of particles with a size range of 1 – 2 nm.

Steigerwald, *et al.* [163] prepared capped CdSe, ZnS, ZnS/CdSe, and CdSe/ZnS nanocrystallites from inverse micellar solutions. Silylchalcogenide reagents were added to the microemulsions containing the appropriate metal ions. The particle surfaces were subsequently capped with the phenyl groups or with other semiconductor materials such as ZnS.

$$CdCl_2 + Se(SiMe_3)_2 \xrightarrow{-2Me_3SiCl} CdSe \qquad (36a)$$

$$ZnEt_2 + Se(SiMe_3)_2 \xrightarrow{-2SiEtMe_3} ZnSe \qquad (36b)$$

$$CdMe_2 + Te(Si^iPrMe_2)_2 \xrightarrow{-2Si^iPrMe_3} CdTe \qquad (36c)$$

Silylchalcogenides react readily with metal salts or simple metal alkyls to form metal-chalcogenide bonds as shown in eq. 36(a), (b) and (c). Another approach to nanocrystallite synthesis in a matrix was developed by Choi and Shea [163,164] who reported using the porous inorganic-organic xerogel (polysilsesquioxanes) to produce cadmium sulfide and chromium nanoparticles. The chromium precursor used was a zero valent arene tricarbonyl chromium complex, introduced as a component of the xerogel matrix, which after heating under vacuum produced chromium nanoparticles.

(c) Metal-organic routes

A popular method of preparing high quality, crystalline monodispersed nanoparticles was first reported by Murray, *et al.* in 1993 [172]. In this method a volatile metal alkyl (dimethylcadmium) and a chalcogen source Se were mixed in tri-n-octylphosphine (TOP) to form TOPSe and injected into hot TOPO (tri-n-octylphosphine oxide), a polar co-ordinating Lewis base solvent. Nucleation of the nanoparticulate CdSe was achieved by the sudden introduction of the concentrated reagents resulting in abrupt supersaturation and the formation of nuclei, followed by slower growth and annealing, consistent with an Ostwald ripening process. The nanoparticles were passivated by a monolayer of the solvent ligands and hence could be isolated by solvent/non-solvent interactions.

The size distribution of the nanoparticles is controlled by the temperature at which the synthesis is undertaken, with larger particles being obtained at higher temperatures and lower temperatures yielding smaller particles. The combination of TOP/TOPO allowed for slow steady growth conditions above 280 °C. This method has the advantage over other methods including, near monodispersity ($\sigma \cong 5\%$ of particles) and high yields. For these methods the surface coverage is such that the percentage of surface sites bound to TOPO molecules, through a metal-oxygen dative bond, increases from 30% to 60% as the particle

size decreases from particle diameter of approximately 6 nm to 1.8 nm, respectively. Variations in surface coverage with particle size can be explained by steric effects; interactions between surface bound bulky neighbouring capping molecules (TOPO) predominates in larger particles, whereas smaller particles can accommodate higher percentage levels of TOPO, due to a lower steric hindrance in the latter particles.

One of the limitations of this method is the use of hazardous compounds such as dimethylcadmium, $[(CH_3)_2Cd]$, especially at high temperatures. An approach to overcome this problem involves the use of single molecule precursors, a single compound containing all the elements required to form the nanocrystallite, such as alkyldiseleno or alkyldithiocarbamato complexes [165,166]. The fabrication of semiconductor nanocrystals from single molecule precursors is a one step process, typically carried out at temperatures in the range 200 – 250 °C. A similar approach was used in which non-air sensitive lead(II) alkyldithio- or alkyldiselenocarbamates, led to the synthesis of cubic phase PbS and PbSe nanocrystallites respectively [167,168]. Related compounds can be used to prepare compound semiconductor nanoparticles, such as oligomeric $Cd(Se(C_2H_5)_2$ or metal dithiocarbamates in 4-ethylpyridine. The conventional TOPO method was reported by Alivisatos, *et al.* in the synthesis of capped InP nanocrystals [169-171]. The reaction involved dissolving $InCl_3$ in hot TOPO followed by addition of $P(SiMe_3)_3$ (Eq. 37) with annealing of the resulting InP nanocrystals.

$$InCl_3 + \text{TOPO} \xrightarrow{100\ ^\circ C,\ 12h} \text{In-TOPO} \xrightarrow{P(SiMe_3)_3,\ 265\ ^\circ C,\ \text{days}} \text{InP/TOPO} \xrightarrow{\text{surfactant (S), 100 °C, days}} \text{InP(TOPO + S)} \qquad (37)$$

The band gap for bulk InP is 1.28 eV, whereas InP particles produced above exhibit values in the range from 1.7 – 2.4 eV. The percentage surface coverage of InP particles with TOPO was found to be in the range of 30 to 70% depending on the size of the particles. Values of the band edge and deep trap emissions were reported to shift with the mean size of the nanocrystallites, with stronger emission observed for smaller InP particles and when oxidation on the surface had occurred. For InAs, prepared by a similar method using the dehalosilylation reaction between $As[(SiMe_3)_3]$ and $InCl_3$, surface oxidation does not change

the properties of the resulting particles [173]. GaAs nanoparticles have been prepared by reacting $GaCl_3$ with $As(SiMe_3)_3$ in boiling quinoline. However the quantum size effects were not properly determined as unidentified species masked the optical properties [174-177]. Another preparative method for the synthesis of GaAs and InP is by the methanolysis of organometallic compounds such as $[Cp^*(Cl)In(\mu\text{-}P(SiMe_3)_2]_2$ (where Cp is C_5H_5). A chemical route involving cadmiumin led to bulk, amorphous, Cd_3P_2 after rapid flocculation of nanoparticles [178](Eq. 38).

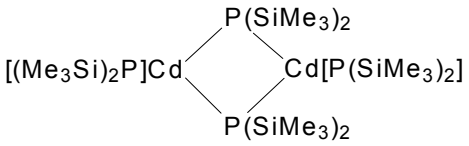

$$+ \quad 8\ MeOH \longrightarrow$$

$$2/3\ Cd_3P_2 \quad + \quad 8\ MeOSiMe_3 \ + \ 8/3\ PH_3$$

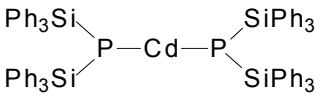

$$+ \qquad 4/3\ MeOH \longrightarrow$$

$$nano\text{-}Cd_3P_2 \quad + \quad 4/3\ HP(SiPh_3)_2 \ + \ 4/3\ MeOSiPh_3 \qquad (38)$$

To control the kinetics for the decomposition of molecular precursors, a single molecule precursor with bulkier substituents was used, $Cd[P(SiPh_3)_2]_2$[179]. The methanolysis gave soluble nanoparticles of Cd_3P_2 with diameters ranging from 3 nm to 4 nm; however the particles were not crystalline. There are a number of potential advantages of using the single-molecular precursor route over the other existing methods:

- The single source route avoids the use of volatile, sometimes toxic and/or pyrophoric precursors.
- Some of the semiconductor nanoparticles are air sensitive. The precursors of such nanoparticles can be synthesized under both aerobic and anaerobic conditions, with the resulting precursors being air and moisture stable.
- There is less chance of the incorporation of impurities into the nanoparticles when an involatile precursor is involved.

- Low temperature deposition routes are possible.
- Although there are theoretical models that predict the optical properties of semiconductor nanoparticles, the properties of nanoparticles obtained by these new synthetic routes are sometimes hard to anticipate and often lead to particles with unique and unanticipatedproperties.

Bis(alkyldithio/selenocarbamate)cadmium and zinc compounds have been used as single-molecular precursors in the growth of group II-VI thin films by low pressure and aerosol-assisted chemical vapour deposition (LPCVD and AACVD methods) [180,181]. These compounds have been shown to be good precursors for the preparation of nanoparticles, a process that involves their decomposition in a high boiling point coordinating solvent (Lewis base) such as TOPO or 4-ethylpyridine. The preparation of these compounds follows a simple procedure in which CSe_2 or CS_2 is reacted with an excess of an amine and NaOH or KOH at a temperature below 0 °C, to give the dithio/seleno carbamate as the dialkylammonium salt. This compound is reacted with a stoichiometric quantity of an aqueous solution of cadmium(II)chloride or zinc(II)chloride to give the bis(alkyldithio-/diselenocarbamato)cadmium(II)/zinc(II) compound as a precipitate. Nanoparticles from single-source precursors employ a "one-pot" synthesis in which there is rapid nucleation followed by slow particle growth which is essential to generate a narrow size distribution. The synthesis and use of novel single-molecular precursors that produce self-capped nanoparticles have also been explored. Organic group from the precursor should migrate upon thermolysis and act as a capping agent on the surface of the nanoparticle. The asymmetric complex dithiocarbamatecadmium, $[Cd\{(S_2CNMe(C_{18}H_{37})\}_2]$, is an example. It was used to prepare nanoparticles under a dynamic vacuum in the solid state at temperatures ranging between 150 – 300 °C, producing CdS capped nanoparticles [182].The spectroscopic analysis, IR and NMR spectral data, suggest that the capping group is principally $NHMe(C_{18}H_{37})$. Although capping agents such as TOPO and 4-ethylpyridine work well to passivate the surface of nanoparticles they are only weakly covalently coordinated to the surface and are relatively labile, which may be advantageous if the capping agent is to be exchanged for a different ligand. However the alternative method is to passivate the particles with a more robust capping agent, which is not labile. This process can be used to

grow a second material epitaxially on the surface of the nanoparticle. An example is to use another metal chalcogenide material (preferably with a wider band gap) on the surface of a secondmetal chalcogenide nanoparticle, to produce a core-shell nanoparticle such as CdSe-CdS e.g. using $[Cd(Se_2CNMe^nHex)_2]$ as a source for CdSe and $[Cd(S_2CNMe^nHex)_2]$ as the CdS source [183].

The high surface to volume ratio of nanocrystalline materials means that the surface plays an important role in the optical and electronic properties of the material. It is for this reason that surface modification of these particles has been a subject of investigation. Beside surface passivation being achieved by capping nanocrystallites with organic and inorganic groups, colloidal CdS has been passivated to remove surface defects using$Cd(OH)_2$. This give a marked increase in fluorescence in the surface modified samples [184]. Organic ligands such as thiopyridines and thiolates have been reported to reduce the surface defects and increase luminescent efficiencies. In the colloidal synthesis of these core-shell structures the core acts as a seed for the heterogeneous nucleation of the shell [185,186]. Core-shell systems reported include Si/SiO_2,$CdS/Cd(OH)_2$, CdSe/ZnS, CdSe/ZnSe and CdSe/CdSwhich account for improved luminescence quantum yields. Thisis desirable since decreased fluorescence lifetimes are related to tailoring of the band gap positions between the two materials [187-190]. These properties render these materials potentially useful in optoelectronic devices.

A number of cadmium complexes including dithiobiurea as well as ethylxanthate have been reported for their use as single-source precursors to prepare CdS nanoparticles. This follows the successful use of the cadmium complex of N,N′-bis(thiocarbamoyl)hydrazine as an efficient precursor for CdS nanoparticles [191-193]. The synthesis was carried out in TOPO as both capping agent and solvent medium for the reaction. Spherical particles with an average size of 4.2 nm were obtained from the ethylxanthate complex. Spherical aggregates of relatively uniform size (50 nm) were obtained at 240 °C while at 150 °C irregular non-spherical particles were observed from the dithiobiurea complex. Alkylxanthate compounds were have been used as capping agents [194].

(d) Hydrothermal synthesis

Hydrothermal synthesis is a common method used to synthesize zeolite/molecular sieve crystals. This method exploits the solubility of almost all inorganic substances in water at elevated temperatures and pressures and subsequent crystallization of the dissolved material from the fluid. Water at elevated temperatures plays an essential role in the precursor material transformation because the vapour pressure is much higher, and the structure of water at elevated temperatures is different from that obtained at room temperature. The properties of the reactants, including their solubility and reactivity, also change at high temperatures. The changes mentioned above provide more parameters to produce different high-quality nanoparticles and nanotubes, which are not possible at low temperatures. During the synthesis of nanocrystals, parameters such as water pressure, temperature, reaction time, and the respective precursor- product system can be tuned to maintain a high simultaneous nucleation rate and good size distribution. Different types of nanoparticles such as TiO_2, $LaCrO_3$, ZrO_2, $BaTiO_3$, $SrTiO_3$, $Y_2Si_2O_7$, Sb_2S_3, CrN, SnS_2, PbS, Ni_2P, and SnS_2 nanotubes, Bi_2S_3 nanorods, and SiC nanowires have been successfully synthesized in this way [195-200]. The solvent is not limited to water but also includes other polar or nonpolar solvents, such as benzene and the process is more appropriately called a solvothermal synthesis.

1.4. General growth mechanism of semiconductor nanocrystals

(a) Nucleation and growth

The chemical growth of bulk or nanosized materials inevitably involves the process of precipitation of a solid phase from solution. A good understanding of the process and parameters controlling the precipitation helps to improve the engineering of the growth of nanoparticles to the desired size and shape. For a particular solvent, there is a particular solubility for a solute, whereby addition of any excess solute will result in precipitation and formation of nanocrystals [201]. Thus, in the case of nanoparticle formation, for nucleation to occur, the solution must be supersaturated either by directly dissolving the solute at higher temperature and then cooling to low temperatures or by adding the necessary reactants to produce a supersaturated solution during the reaction [202,203]. The precipitation process then essentially consists of a nucleation step followed by particle growth stages [204,205].

In general, there are three kinds of nucleation processes: homogeneous nucleation, heterogeneous nucleation, and secondary nucleation [206]. Homogeneous nucleation occurs in the absence of a solid interface by combining solute molecules to produce nuclei. Homogeneous nucleation happens due to a thermodynamic driving force because the supersaturated solution is not stable. The overall free energy change, ΔG, is the sum of the free energy due to the formation of a new volume and the free energy due to the new surface created as shown in eq. 39 [207]. For spherical particles where V is the molecular volume of the precipitated species, r is the radius of the nuclei, k_B is the Boltzmann constant, S is the saturation ratio, and γ is the surface free energy per unit surface area. When $S > 1$, ΔG has a positive maximum at a critical size, r^*(Fig. 1-9). This maximum free energy is the activation energy for nucleation.

$$\Delta G = -\frac{4}{V}\pi r^3 k_B T In(S) + 4\pi r^2 \gamma \qquad (39)$$

Nuclei larger than the critical size will further decrease their free energy for growth and form stable nuclei that grow to form particles. The critical nuclei size r^* can be obtained by setting $d\Delta G/dr = 0$. For a given value of S, all particles with $r > r^*$ will grow and all particles with $r < r^*$ will dissolve.

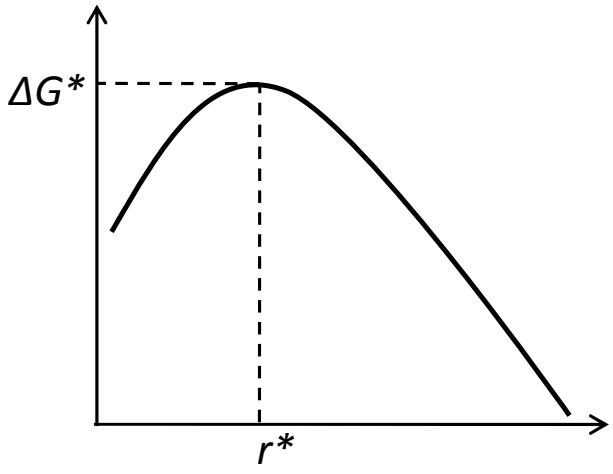

Fig. 1-9: Illustration of the overall free energy ΔG as a function of the growth particle size r [207].

From the eq. 40, it follows that the higher the saturation ratio *S*, the smaller the critical nuclei size $r^*$is. After the nuclei are formed from the solution, they grow via molecular addition, which relives the supersaturated step. When the concentration drops below the critical level, nucleation stops and the particles continue to grow by molecular addition until the equilibrium concentration of the precipitated species is reached.

$$r^* = \frac{2V\gamma}{3k_BTln(S)} \qquad (40)$$

Uniformity of the size distribution is achieved through a short nucleation period that generates all of the particles obtained at the end of the reaction followed by a self-sharpening growth process. At this stage, the smaller particles grow more rapidly than the larger ones because the free energy driving force is larger for smaller particles than for larger ones if the particles are slightly larger than the critical size. At this stage, focusing in size occurs [208]. Nearly monodispersed size distribution can be obtained at this stage by either stopping the reaction (nucleation and growth) quickly or by supplying reactant source to keep a saturated condition during the course of the reaction [209].

On the other hand, when the reactants are depleted due to particle growth, Ostwald ripening or defocusing will occur, where the larger particles continue to grow, and the smaller ones get smaller and finally dissolve. Because the saturation ratio (S) decreases and the corresponding critical nuclei size (r^*) increases according to *eq. 40* any particles smaller than this new critical size will dissolve [210]. If the reaction is quickly stopped at this stage, the particles will have a broad size distribution, which is featured by a distribution centering two size regimes, a bigger one and a smaller one, and the critical size, now at this saturation, is in between [211]. Once the reaction (mainly the growth of the particles) goes into this stage, it is difficult to get monodisperse particles unless the reaction is extended to long enough times to completely deplete the supersaturation and the smaller nuclei. In the latter case, the size of the particles gets relatively large and can extend into the micrometer size regime [212]. During an actual experiment, when there is no continuous supply of the reactants, the saturation ratio continues to decrease and the critical nuclei size continues to increase. To get a short burst of nucleation, a high saturation ratio (S) is suitable. In addition

to the growth by molecular addition, where soluble species deposit on the solid surface, particles can grow by aggregation with other particles, and this is called secondary growth. The rate of particle growth by aggregation is much larger than that by molecular addition. After the particles grow to a stable size, they will grow by combining with smaller unstable nuclei and not by collisions with other stable particles [213].

Because of their small size resulting in instability, these nanoparticles must be arrested during the reaction either by adding surface protecting reagents, such as organic ligands or inorganic capping materials [214], or by placing them in an inert environment such as an inorganic matrix or polymers [215]. The nanocrystal dispersions are stable if the interaction between the capping groups and the solvent is favourable, providing an energetic barrier to counteract the van der Waals and magnetic (if magnetic materials are being synthesized) attractions between nanoparticles [216]. To help arrest the nanoparticle growth, different solvents are also used to change the solubility or the reaction rate [217].

(b) Magic size clusters

Nanocrystals of various shapes have been successfully synthesized over the past years [218]. Because the properties of nanosized materials are strongly influenced by their shape, it therefore becomes imperative to explore the growth mechanism that leads to a particular shape. It is known that for a given monomer concentration there is a critical nanoparticle size that forms. The solubility of the particles of the critical size equals exactly the monomer concentration in the solution. On the other hand, when the nanocrystals present in the solution are larger than the critical size, narrowing of the size distribution occurs, whereby the smaller nanocrystals in the distribution grow more rapidly than the bigger ones. Upon the depletion of the monomer concentration, as a result of particle growth, the critical size becomes larger than the average size present. Consequently, Ostwald ripening occurs and the size distribution becomes broader. The distribution can be refocused by the injection of additional monomer, which shifts the critical size back to a smaller value. It can therefore be seen that the focusing time as well as the critical size can change with different initial monomer concentrations.

The nucleation stage for the growth of anisotropic shape therefore plays a crucial role in determining the size/shape of the resulting nanocrystal. The initial nuclei are usually much smaller than the ones used for the synthesis of isotropic nanocrystals. In the extremely small size range, the relative chemical potential is highly size dependent and very sensitive to the configuration of the nuclei [219]. Thermodynamically, all the nanocrystals will grow towards the shape having the lowest energy at equilibrium, which is governed by classical theory. However, the formation of nanocrystals is a kinetics driven process [220]. In principle, before the reaction reaches the equilibrium stage, any metastable nanocrystal shape can be arrested from the reaction by tuning the reaction conditions [221]. Even spherical shaped particles are not thermodynamically stable unless they are capped by protecting ligands.

This essentially means that at lower monomer concentration or larger growth times, all nanocrystals grow towards the lowest chemical potential and this leads to the formation of dots. At the median concentration three dimensional isotropic growth is supported resulting in formation of spindle-shaped nanocrystals. At higher monomer concentrations, then magic-sized nanoclusters promote the formation of rods or other elongated structures that are metastable. The magic size clusters could be considered as those clusters that possess complete shells of atoms [222]. A classical example is the series of truncated octahedra [223].

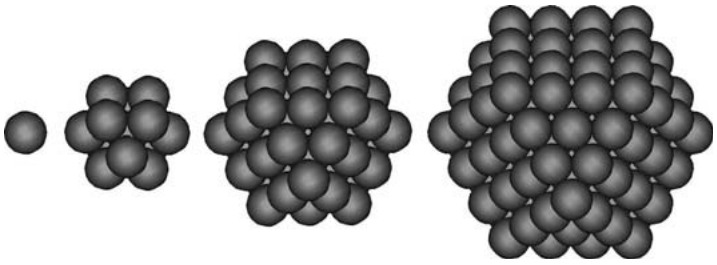

Fig. 1-10: A series of different clusters formed by addition of closed shells in the fccstructure. Each of the presented clusters represents the core of the subsequent cluster. Starting from a single atom, cubo octahedra of 13, 55 and 147 Au atoms can be built [223].

The first member of this series is a single atom along with its 12 nearest neighbours in the *fcc* structure. The larger structure can be constructed from the previous ones by covering each of the exposed facets with one layer of atoms. Thus the smaller cluster contains 13

atoms, the second 55 atoms and the third 147 atoms. These clusters differ little from a sphere and therefore minimize the contribution of the surface atoms in the entire structure. For the large clusters the facetted surface structure is obvious. Two types of facets are exposed. The (111) facets with triangular shape and the (100) facets with quadratic shape. Various examples of the synthesis of the magic size clusters for CdSe have been reported in the literature [224]. The size of the cluster is purely dependent on the reaction time.

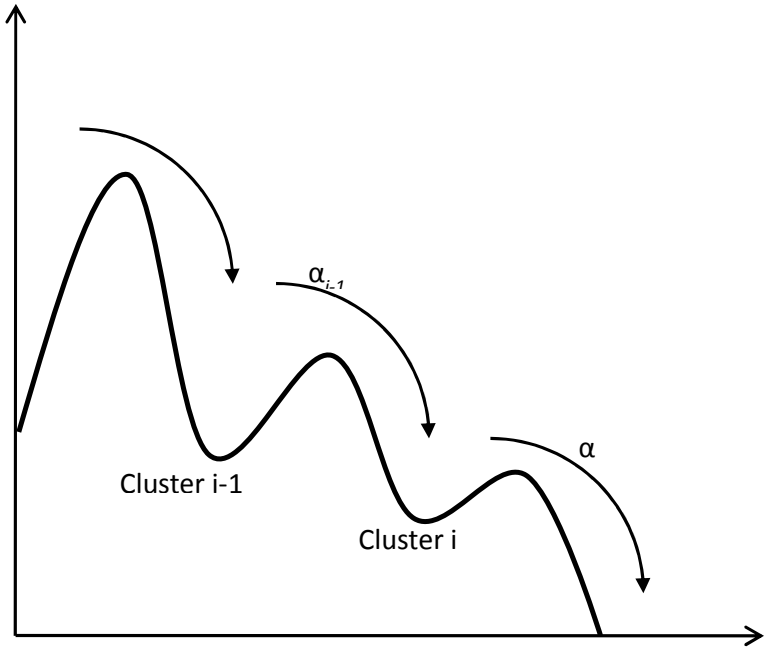

Fig. 1-11: Sketch of the potential landscape in the growth of CdSe magic size clusters. For simplicity it is sketched only in one-dimension. The model is to be understood as a modification to the classical nucleation potential as shown in Fig. 1-9 [225].

The growth mechanism of the magic size cluster can be thought of as a variation of the continuous growth model [225]. The growing nanocrystal is exposed to a flux of monomers. In the same way as in a normal growth model, the monomers dynamically bind and unbind on the surface of the nanocrystal. However, in the case of magic size clusters the ratio between the binding- and unbinding-rate depends on the size of the crystal [226]. The magic sizes represent sizes of extraordinary stability. If the crystal is slightly larger than a magic-size cluster, the release of the outer atoms is more probable than the deposition of other

monomers onto the nanocrystal. Accordingly, nanocrystals slightly smaller than a magic-size cluster have a high affinity for monomers to reach the closed-shell structure. In the normal growth model in contrast, the binding rate dominates for all crystal sizes above the critical size, so that all the crystals grow continuously [227].

A way to formally rationalize the stability of the magic size clusters is to introduce a slight modification to the energy landscape as sketched in Fig. 1-11. In this modified landscape the magic sizes represent local minima. The sketch is a simplified model for the one-dimensional case. In principle the modified growth model can be understood as a subsequent nucleation. The growth proceeds only through a series of jumps over potential barriers. In the potential a preferential direction is inscribed. A given magic size cluster can evolve only into a larger magic size cluster. The melting, i.e. the evolution to a smaller magic size cluster, is virtually suppressed. Clusters that grow leave their own family$i$and after they have overcome the potential barrier, they become part of the subsequent family $i + 1$. In the same way the depopulation of the preceding family $i - 1$ feeds the population of family$i$. Therefore, the evolution of the concentration $ci$of clusters of family $i$can be described by only two rate constants. The concentration of clusters of family$i$grows at the rate $a_{i-1}c_{i-1}$ and decreases at the rate $a_i c_i$:

$$\frac{dc_i}{dt} = \alpha_{i-1}\, c_{i-1} - \alpha_i c_i \qquad (41)$$

The differential equations for the individual families can be summarized in a vectorial form:

$$\frac{d}{dt}\begin{pmatrix} c_0 \\ c_1 \\ c_2 \\ \vdots \\ c_n \end{pmatrix} = \begin{pmatrix} -\alpha_0 & 0 & 0 & 0 \\ \alpha_0 & -\alpha_1 & 0 & 0 \\ 0 & \alpha_1 & -\alpha_2 & 0 \\ \vdots & \vdots & \ddots & \vdots \\ 0 & 0 & 0 & -\alpha_n \end{pmatrix}\begin{pmatrix} c_0 \\ c_1 \\ c_2 \\ \vdots \\ c_n \end{pmatrix} \qquad (42)$$

It is interesting to note the singular role of the families 0 and n in the coefficient matrix. Family n is exceptional only for a trivial reason. It represents the last family described by the matrix. Clusters that leave this family enter into a different growth regime. From the data found in the literature it can be deduced that this growth regime is continuous growth.

More interesting is family 0. It is not fed by any other family, thus the clusters of this family must exist from the beginning of the reaction. At the beginning only free monomers are found in the solution. Therefore the clusters of family 0 can at maximum be single atoms, which actually cannot be discerned from the other atoms. In this sense it is difficult to find a physical meaning for the number c_0. Only the rate of depopulation of family 0 can be interpreted nicely. It coincides with the rate at which clusters of family 1 appear. In other words the rate $\alpha_0 c_0$ can be interpreted as the nucleation rate of the system. This becomes evident when calculating the total concentration of magic size clusters:

$$c_{total} = \sum_{i=1}^{n} c_i \quad (43)$$

As long as the largest family n is not populated, this number is constant over time. A reasonable boundary condition to solve Eq. (42) is to set all concentrations to zero at $t = 0$, except for c_0, which will take a finite value. If we exclude family 0 from the sum, the total concentration of clusters would be zero at the beginning of the reaction and then increase until it reaches a saturation value. It would remain stable until the first clusters appear in family n. The exact shapes of the individual entities that are deposited as well as the atomic structure of the clusters produced in this synthesis scheme are still unknown. One could imagine that the growth proceeds through the deposition of either individual atoms or very small molecular units, such as rings of the form $(CdSe)_3$. The magic size clusters are merely interesting as they provide a means of observing the process of growth at a very low level. One can assume that between the individual steps of the growth single layers of atoms are deposited onto the clusters. Therefore it is very likely that the clusters have a pyramidal shape as seen also in clusters of CdSe [228]. This structure also provides a highly symmetric shape in the cubic zinc blende phase of clusters [229].

Generally this layer by layer growth is assumed to take place even at larger length scales. It has been observed in situ in a high-resolution TEM experiment for the growth of Al_2O_3 from a drop of liquid aluminium [230]. In that case the growth of layers of hundreds of atoms proceeded in a stepwise manner. Individual layers are deposited in time periods shorter

than 0.04 s. Magic-size clusters are of interest for various reasons. First, they extend the accessible spectrum for instance CdSe [228] and CdTe [229] towards lower wavelengths. One can assume that by this one procedure approaches a minimum. Smaller clusters would be in the range of atomic species. In that sense the clusters can also be understood as the molecular edge of the size spectrum of nanocrystals. A second reason for the interest in magic size clusters is their reproducibility. As the number of atoms in the clusters is well defined also the physical properties are also well defined. This could be of great technological interest.

1.5. References

[1] Roco M.C.; Williams R.S.; Alivisatos P., Nanotechnology Research Directions: IWGN Workshop Report, Eds, Kluwer Academic Publishers, Dordrecht Boston London, 2002, 270.

[2] Sugimoto T.; Elsevier, Amsterdam, London, New York, 2001, 792.

[3] Fendler J.H.; Dekany I., Nanoparticles in Solids and Solutions, Eds Kluwer Academic Publishers, Dordrech, Boston, London, 1996, 517.

[4] Efros Al. L.; A. L. Efros, Fizika iTekhnika Poluprovodnikov, 1982, 1209.[Sov. Phys. Semicond., 1982,16, 772 (Engl. Transl.)].

[5] Ekimov A.I.; Onushchenko A.A., Pis´ma v Zhurn. Eksp.i Teor. Fiziki, 1984, 40, 337 [Sov. Phys. JETP Lett.,1984, 40, 1136 (Engl. Transl.)].

[6] Ekimov A.I.; Efros Al. L.; Onushchenko A.A., Solid State Commun., 1985, 56, 921.

[7] Ekimov A.I.; Onushchenko A.A., Fizika i Tekhnika Poluprovodnikov, 1982, 16, 1215 [Sov. Phys. Semicond.,1982, 16, 775 (Engl. Trransl.)].

[8] Huynh W.U.; Dittmer J. J; Alivisatos A.P., Science,2002, 295, 2425.

[9] Yu W.W.; Wang Y.A; Peng X., Chem. Mater., 2003,15, 4300.

[10] Halperin W.P., Rew. Mod.Phys., 1986, 58, 533.

[11] Alivisatos A.P., Science, 1996, 271, 933.

[12] Colvin V.L.; Goldstein A.N.; Alivisatos A.P., J. Am. Chem. Soc., 1992, 114, 5221.

[13] Olshavsky M.A., Goldstein N.A.; Alivisatos A.P., J. Am. Chem. Soc., 1990, 112, 9438.

[14] Labrenz M.; Druschel G.K.; Thomsen_Ebert T.; Gilbert B.; Welch S.A.; Kemner K.M.; Logan G.A.; Summons R.E.; Stasio G.D.; Bond P.L.; Lai B.; Kelly S.D.; Banfield J.F., Science, 2000, 290, 1744.

[15] Li A.; Draine B.T., Astrophys. J., 2002, 564, 803.

[16] Banfield J. F.; Navrotsky A., Washington, DC, USA, Reviews in Mineralogy and Geochemistry, Nanoparticles and the Environment, Eds, 2001, 44, 536.

[17] Eychmuller A., J. Phys. Chem. B, 2000, 104, 6514.

[18] Kouwenhoven L.P.; McEuen P.L., Nanotechnology, Ed. G. Timp, Aip Press, Springer, New York, 1996, 471.

[19] Turton R., The Quantum Dot: A Journey into the Future of Microelectronics, Oxford U. Press, Oxford (UK), 1995.

[20] Yoffe A.D., Adv. Phys., 1993, 42, 173.

[21] Landes C.F.; Link S.; Mohamed M.B.; Nikoobakht B.; Sayed A.E., Pure. Appl. Chem., 2002, 74, 1675.

[22] Peng X.; Manna L.; Yang W.; Wickham J.; Scher E.; Kadavanich A.; and Alivisatos P.A.; Nature, 2000, 404, 59.

[23] Hakimi F.; Bawendi M.G.; Tumminelli R.; Haavisto R.J.; US Patent 5, 1993, 260, 957.

[24] Duonghong D.J.; Ramsden J.; Gratzell M., J. Am. Chem. Soc. 1982, 104, 2977.

[25] Banin U.; Bruchez M.; Alivisatos A.P.; Ha T.; Weiss S.; Chemia D.S., J. Chem. Phys. 1999, 110(2), 1195.

[26] Brust M.; Fink J.; Bethel B.; Schriffren D.J.; Kiely M., J. Chem. Soc. Chem. Commun. (1995), 1655.

[27] Tanori J.; Pileni M.P., Adv. Mater. 1995, 7, 862.

[28] Andrievskii R.A., Russ. Chem. Rev., 1994, 63, 411.

[29] Kittel, C., Quantum Theory of Solids. New York: Wiley, 1987.

[30] Luttinger, J.M., Phys. Rev. B 1956, 102,1030.

[31] Luttinger J.M.; Kohn W. Phys. Rev. 1955, 97, 869.

[32] Bir G.L.; Pikus G.E. ,Symmetry and Strain-Induced Effects in Semiconductors. New York: Wiley, 1974.

[33] Lipari N.O.; Baldereschi A., Phys. Rev. Lett.1973, 42, 1660.

[34] Baldereschi A.; Lipari N.O., Phys. Rev. B 1973, 8, 2697.

[35] Ge'lmont B.L.; D'yakonov M.I., Sov. Phys. Semicond. 1972, 5, 1905.

[36] Kane E.O., J. Phys. Chem. Solids 1957, 1, 249.

[37] Pidgeon C.R.; Brown R.N., Phys. Rev. 1966, 146, 575.

[38] Kane E.O., In Narrow Band Semiconductors, Physics and Applications, Lecture Notes in Physics; Zawadski W, ed. Berlin: Springer-Verlag, 1980; Vol. 133.

[39] Vahala K.J.; Sercel P.C., Phys. Rev. Lett.1990, 65, 239.

[40] Sercel P.C.; Vahala K.J., Phys. Rev. B 1990, 42, 3690.

[41] Efros Al.L.; Rosen M., Phys. Rev. B 1998, 58, 7120.

[42] Nozik A.J.; Micic O.I., MRS Bull.1998, 23, 24.

[43] Petroff P.M.; Mediros-Riberio G., MRS Bull. 1996, 21, 54.

[44] Bimberg D.; Grundmannn M.; Lendkov N.N., MRS Bull.1998, 23, 31.

[45] Peng X.; Wickham J.; Alivisatos A.P., J. Am. Chem. Soc. 1998, 120, 544343.

[46] Borrelli N.F.; Hall D.W.; Holland H.J.; Smith D.W. J. Appl. Phys. 1987,61, 5399.

[47] Alivisatos A.P.; Harris A.L.; Levinos N.J.; Steigerwald M.L.; Brus L.E., J. Chem. Phys. 1988, 89, 4001.

[48] Roussignol P.; Ricard D.; Flytzanis C.; Neuroth N., Phys. Rev. Lett. 1989, 62, 312.

[49] Ekimov A.I.; Efros, Al.L.; Ivanov M.G.; Onushchenko, A.A.; Shumilov S.K., Solid State Commun.1989, 69, 565.

[50] Wang Y.; Herron N., Phys. Rev. B 1990, 42, 7253.

[51] Muller M.P.A.; Lembke, U.; Woggon U.; Ruckmann I. J., Noncrystal. Solids 1992, 144, 240.

[52] Peyghambarian N.; Fluegel B.; Hulin D.; Migus A.; Joffre M.; Antonetti A.; Koch, S.W.; Lindberg, M. IEEE J. Quantum Electronic 1989, 25, 2516.

[53] Esch V.; Fluegel B.; Khitrova G.; Gibbs H.M.; Jiajin X.; Kang K.; Koch S.W.; Liu L.C.; Risbud S.H.; Peyghambarian N., Phys. Rev. B 1990, 42, 7450.

[54] Bawendi M.G.; Wilson W.L.; Rothberg L.; Carroll P.J.; Jedju T.M.; Steigerwald M.L.; Brus L.E., Phys. Rev. Lett.1990, 65, 1623.

[55] Ekimov A.I.; Hache F.; Schanne-Klein M.C.; Ricard D.; Flytzanis C.; Kudryavtsev I.A.; Yazeva T.V.; Rodina A.V.; Efros, Al.L., J. Opt. Soc. Am. B 1993, 10, 100.

[56] Bowen Katari J.E.; Colvin, V.L.; Alivisatos A.P., J. Phys. Chem. 1994, 98, 4109.

[57] Micic O.I.; Sprague J.R.; Curtis C.J.; Jones K.M.; Machol J.L.; Nozik A.J.; Giessen H.; Fluegel B.; Mohs G.; Peyhambarian N. J., Phys. Chem. 1995, 99, 7754.

[58] Hines M.A.; Guyot-Sionnest P. J., Phys. Chem. B 1998, 102, 3655.

[59] Norris D.J.; Yao N.; Charnock F.T.; Kennedy T.A., Nano Lett. 2001, 1, 3.

[60] Peng Z.A.; Peng X., J. Am. Chem. Soc. 2001, 123, 168.

[61] Hines M.A.; Guyot-Sionnest P., J. Phys. Chem. 1996, 100, 468.

[62] Peng X.; Schlamp M.C.; Kadavanich A.V.; Alivisatos A.P., J. Am. Chem. Soc. 1997, 119, 7019.

[63] Pankove, J.I. Optical Processes in Semiconductors; New York: Dover, 1971, 34.

[67] Efros, Al.L.; Efros, A.L. Sov. Phys. Semicond. 1982, 16, 772.

[68] Ekimov, A.I.; Onushchenko, A.A. JETP Lett. 1982, 34, 345.

[69] Brus, L.E. J. Chem. Phys. 1983, 79, 5566.

[70] Ekimov, A.I.; Efros, Al.L.; Onushchenko, A.A. Solid State Commun. 1985, 56, 921.

[71] Brus, L.E. J. Chem. Phys. 1984, 80, 4403.

[72] Murray, C.B.; Norris, D.J.; Bawendi, M.G. J. Am. Chem. Soc. 1993, 115, 8706.

[73] Norris, D.J.; Sacra, A.; Murray, C.B.; Bawendi, M.G. Phys. Rev. Lett. 1994, 72, 2612.

[74] Norris, D.J.; Bawendi, M.G. Phys. Rev. B 1996, 53, 16,338.

[75] Nirmal, M.; Norris, D.J.; Kuno, M.; Bawendi, M.G.; Efros, Al.L.; Rosen, M. Phys. Rev. Lett. 1995, 75, 3728.

[76] Norris, D.J.; Efros, Al.L.; Rosen, M.; Bawendi, M.G. Phys. Rev. B 1996, 53, 16,347.

[77] Guzelian, A.A.; Banin, U.; Kadavanich, A.V.; Peng, X.; Alivisatos, A.P. Appl. Phys. Lett. 1996, 69, 1432.

[78] Banin, U.; Lee, C.J.; Guzelian, A.A.; Kadavanich, A.V.; Alivisatos, A.P.; Jaskolski, W.; Bryant, G.W.; Efros, Al.L.; Rosen, M. J. Chem. Phys. 1998, 109, 2306.

[79] Brus, L. Appl. Phys. A 1991, 53, 465.

[80] Ba´ nyai, L.; Koch, S.W. Semiconductor Quantum Dots. Singapore: World Scientific, 1993.

[81] Alivisatos, A.P. J. Phys. Chem. 1996, 100, 13,226.

[82] Alivisatos, A.P. Science 1996, 271, 933.

[83] Woggon, U. Optical Properties of Semiconductor Quantum Dots. Heidelberg: Springer-Verlag, 1997.

[84] Nirmal, M.; Brus, L.E. Acc. Chem. Res. 1999, 32, 407.

[85] Gaponenko, S.V. Optical Properties of Semiconductor Nanocrystals. Cambridge: Cambridge University Press, 1999.

[86] Eychmuller, A. J. Phys. Chem. B 2000, 104, 6514.

[87] Ashcroft, N.W.; Mermin, N.D. Solid State Physics. Orlando, FL: W.B. Saunders.

[88] Flugge, S. Practical Quantum Mechanics. Berlin: Springer-Verlag, 1971; Vol 1, 155[89] Bastard, G. Wave Mechanics Applied to Semiconductor Heterostructures. New York: Wiley, 1988.

[90] Colvin, V.L.; Schlamp, M.C.; Alivisatos, A.P. Nature 1994, 370, 354.

[91] Dabbousi, B.O.; Bawendi, M.G.; Onitsuka, O.; Rubner, M.F. Appl. Phys. Lett.1995, 66, 1316.

[92] Schlamp, M.C.; Peng, X.; Alivisatos, A.P. J. Appl. Phys. 1997, 82, 5837.

[93] Gao, M.; Lesser, C.; Kirstein, S.; Mohwald, H.; Rogach, A.L.; Weller, H. J. Appl. Phys. 2000, 87, 2297.

[94] Greenham, N.C.; Peng, X.; Alivisatos, A.P. Phys. Rev. B 1996, 54, 17,628.

[95] Huynh, W.U.; Peng, X.; Alivisatos, A.P. Adv. Mater. 1999, 11, 923.

[96] Klein, D.L.; Roth, R.; Lim, A.K.L.; Alivisatos, A.P.; McEuen, P.L. Nature 1997, 389, 699.

[97] Greenham, N.C.; Friend, R.H. In Solid State Physics; Ehrenreich, H. Spaepen, F., Eds; Academic Press: San Diego, CA, 1995; Vol. 49, 1.

[98] Friend, R.H.; Gymer, R.W.; Holmes, A.B.; Burroughes, J.H.; Marks, R.N.; Taliani, C.; Bradley, D.D.C.; dos Santos, D.A.; Bre´das, J.L.; Lo¨ gdlund, M.; Salaneck, W.R. Nature 1999, 397, 121.

[99] Miller, R.D.; McLEndon, G.L.; Nozik, A.J.; Schmickler, W.; Willig, F. Surface Electron Transfer Processes; VCH Publishers: New York, 1995.

[100] Marcus, R.A. Annu.Rev.Phys. Chem. 1964, 15, 155.

[101] Marcus, R.A.; Sutin, N. Biochim.Biophys.Acta 1985, 811, 265.

[102] Brus, L. Phys. Rev. B 1996, 53, 4649.

[103] Schmitt-Rink, S.; Miller, D.A.B.; Chemla, D.S. Phys. Rev. B 1987, 35, 8113.

[104] Shiang, J.J.; Risbud, S.H.; Alivisatos, A.P. J. Chem. Phys. 1993, 98, 8432.

[105] Oshiro, K.; Akai, K.; Matsuura, M. Phys. Rev. B 1998, 58, 7986.

[106] Jortner, J. J. Chem. Phys. 1976, 64, 4860.

[107] Mattoussi, H.; Radzilowski, L.H.; Dabbousi, B.O.; Thomas, E.L.; Bawendi, M.G.; Rubner, M.F. J. Appl. Phys. 1998, 83, 7965.

[108] Borovikov, Y.Y.; Ryltsev, E.V.; Bodeskul, I.E.; Feshchenko, N.G.; Makovetskii, Y.P.; Egorov, Y.P. J. Gen. Chem. USSR 1970, 40, 1942.

[109] Wolfarth, C.; Wohlfarth, B. In Landolt-Bo¨rnstein; Lechmer, M.D., Ed.; Spring-Verlag, Heidelberg, 1996; Vol. 38.A.

[110] Leatherdale, C.A.; Kagan, C.R.; Morgan, N.Y.; Empedocles, S.A.; Kastner, M.A.; Bawendi, M.G. Phys. Rev. B 2000, 62, 2669.

[111] Brus, L.E. J. Chem. Phys. 1983, 79, 5566.

[112] Middleton, A.A.; Wingreen, N.S. Phys. Rev. Lett.1993, 71, 3198.

[113] Scho¨ nherr, G.; Ba¨ ssler, H.; Silver, M. Phil. Mag. B 1981, 44, 47.

[114] Miller, A.; Abrahams, E. Phys. Rev. 1960, 120, 745.

[115] Van der Auweraer, M.; De Schryver, F.C.; Borsenberger, P.M.; Ba¨ ssler, H. Adv. Mater. 1994, 6, 199.

[116] Ginger, D.S.; Greenham, N.C. Phys. Rev. B 1999, 59, 10,622.

[117] Himpsel, F.G.; OrtegaJ.E.; G.J.; Willis R.F, Adv. In Phys. 1998,47,511.

[118] Hernando A., Eds, Nanomagnetism, 247 Series, Dordrecht, Boston, E Kluwer Academic 1993.

[119] Barbara B., J. Mag. Mat.1996, 156, 123.

[120] de Heer W.A., Rev. Mod.Phys.1993, 65, 611.

[121] Speliotis D., J. Mag. Magn. Mat. 1999, 193, 29.

[122] Mee C., The Physics of Magnetic Recording, Nort-Holland, 1994.

[123] Bertram H.; Zhu J.G., Solid State Phys. 1992, 46,271.

[124] Lambeth D.; Velu E.; Bellesis G.; Lee L.; Laughlin D., J. Appl. Phys. 1996, 79, 4497.

[125] Berkowitz, Phys. Rev. Lett.1994, 68, 3745.

[126] Meservey R.; Tedtrow P., Phys. Rep. 1994, 238, 1133.

[127] Crangle J., Solid state magnetism, New York, Van Nostrand Reinhold, 1991.

[128] Mattis D., Theory of magnetism, Springer, 1985.

[129] Rado G.; Suhl H., Eds., Magnetism, New York, academic Press, 1963.

[130] Oda T.; Pasquarello A.; Car R., Phys. Rev. Lett.1998, 80, 3622.

[131] Gunther L.; Barbara B., Eds., Quantum tunnelling of the magnetization, 301, Dordrecht, Boston, Kluwer Academic, 1995.

[132] Sangregorio C.; Ohm T.; Paulsen C.; Sessoli T.; Gatteschi D., Phys. Rev. Lett. 1997, 78, 4645.

[133] Bean C.; Livingston J., J. Appl. Phys. 1958, 30, 120.

[134] Ashcroft N.; Mermin N., Solid State Phys., Forth Worth, Saunders publishing company, 1976.

[135] Kittel C., Introduction to solid state physics, New York, Singapore, John Wiley & Sons, 1996.

[136] Jensen J.; Mackintosh A., Rare earth magnetism, Oxford, New York, Oxford University Press, 1991.

[137] Colvin V.L.; Schlamp M.C.; Alivisatos A., Nature 1994, 370, 354.

[138] Henglein A., Pure Appl. Phys. 1984, 56, 1215.

[139] Rossetti R.; Hull R.; Gibson J.M., J. Chem. Phys. 1985, 82, 552.

[140] Rosetti R.; Ellison J.L; Gibson J.M.; Brus L.E., J. Chem. Phys. 1984, 80, 4464.

[141] Weller H., Adv. Mater.1993, 5, 88.

[142] Weller H.; Fojtik A.; Henglein A., Chem. Phys. Lett.1985, 117, 485.

[143] Haase M.; Weller H.; Henglein A., Ber.Bunsen-Ges.Phys.Chem. 1988, 92, 1103.

[144] Spanhel L.; Henglein A.; Weller H., Ber.Bunsen-Ges.Phys.Chem. 1987, 91, 1359.

[145] Hasselbarth A.; Eychmuller A.; Eichberger R.; Giersi M.; Mews A.; Weller H., J. Phys. Chem. 1993,97, 5333.

[146] Zhou H.S.; Honma I.; Komiyama H.; Haus J.W., J. Phys. Chem. 1993, 97, 895.

[147] Zhou H.S.; Sasahara S.; Honma I.; KomiyamaH.; Haus J.W., Chem. Mater. 1994, 6, 1534.

[148] Eychmuller A.; Hasselbarth A.; Weller H., J. Lumin.1992, 53, 113.

[149] Kortan A.R.; Hull R.; Opila R.L.; Bawendi M.G., Steigerwald M.L.; Carrol P.J.; Brus L.E., J. Am. Chem. Soc. 112, 1327.

[150] Hoener C.F.; Allan K.A.; Bard A.J.; Champion A.; Fox M.A.; Mallouk T.E.; Webber S.E.; White J.M. , J. Phys. Chem. 1992, 96, 3812.

[151] Talapin D.V.; Rogach A.L.; Kornowski A.; Haase M.; Weller H., Nano.Lett.2001, 1, 207.

[152] Wang Y.; Herron N., J. Phys. Chem. 1987, 91, 257.

[153] Cassagneau T.; Hix G.B.; Jones D.J.; Maireles-Torres P.; Rhomari M.; Roziere J., J. Mater.Chem.1994, 4, 189.

[154] Abe T.; Tichibana Y.; Uematsu T.; Iwamoto M., J. Chem. Soc. Chem. Commun.1995, 1617.

[155] Brenchley M.E.; Weller M.T., Angew. Chem. Int. Ed. Engl. 1993, 32, 1663.

[156] Blasse G.; Dirksen C.J.; Brenchley M.E.; Weller M.T., Chem. Phys. Lett.1995, 234, 177.

[157] Watzke H.J.; Fendler J.H., J. Phys. Chem. 1997, 91, 854.

[158] Petit C.; Jain T.K.; Billoudet F.; Pileni M.P., Langmuir, 1994, 10, 4446.

[159] Brigham E.S.; Weisbecker C.S.; Rudzinski W.E.; Mallouk T.E., Chem. Mater.1996, 8, 2121.

[160] Wang Y.; Suna A.; Mahler W.; Kasowski R., J. Chem. Phys. 1987, 87, 7315.

[161] Cao G.; Rabenberg L.K.; Nunn C.M.; Mallouk T.E., Chem. Mater.1991, 3, 149.

[162] Hagatta S.W.; Li X.; Cole-Hamilton D.J.; Fryer J.R., J. Mater.Chem.1996, 6, 1771.

[163] Steigerwald M.L.; Alivisatos A.P.; Gibson J.M.; Harris T.D.; Kortan A.R.; Muller A.J.; Thayer A.M.; Duncan T.M.; Douglass D.C.; Brus L.E., J. Am. Chem. Soc. 1988, 110, 3046.

[164] Kortan R.A.; Hull R.; Opila R.L.; Bawendi M.G.; Steigerwald M.L.; Carrol P.J.; Brus L.E., J. Am. Chem. Soc. 1990, 112, 1327.

[165] Trindade T.; O'Brien P., Adv. Mater.1996, 8, 161.

[166] Trindade T.; O'Brien P.; Zhang X., Chem. Mater.1997, 9, 523.

[167] Trindade T.; O'Brien P.; Zhang X.; Motevalli M., J. Mater.Chem.1997, 7, 1011.

[168] Trindade T.; Monteiro O.C.; O'Brien P.; Motevalli M., Polyhedron 1999, 18, 1171.

[169] Brennin J.G.; Siegrist T.; Carrol P.J.; Stuczynski S.M.; Brus L.E.; Steigerwald M., J. Am. Chem. Soc. 1989, 111, 4141.

[170] Trindade T.; O'Brien P., J. Mater.Chem.1996, 6, 343.

[171] Guzelian A.A.; Katari J.E.B.; Kadavanich A.V.; Banin U.; Hamad K.; Juban E.; Alivisatos A.P.; Wolters R.H., Arnold C.C.; Heath J.R., J. Phys. Chem. 1996, 100, 7212.

[172] Murray C.B.; Norris D.J.; Bawendi M.G., J. Am. Chem. Soc. 1993, 115, 8706.

[173] Guzelian A.A.; Banin U.; Kadavanich A.V.; Peng X.; Alivisatos A.P., Appl. Phys. Lett. 199, 69, 1432.

[174] Olshavski M.A.; Goldstein A.N.; Alivisatos A.P., J. Am. Chem. Soc. 1990, 112, 9438.

[175] Uchida H.; Curtis C.J.; Nozik A.J., J. Phys. Chem. 1991, 95, 5382.

[176] Byrne E.K.; Parkanyi L.K.; Theopold H., Science 1988, 241, 332.

[177] Douglas T.; Teopold K.H., Inorg.Chem.1991, 30, 594.

[178] Goel S.C.; Chiang M.Y.; Buhro W.E., J. Am. Chem. Soc. 1990, 112, 5636

[179] Buhro W.E., Polyhedron 1994, 13, 1131.

[180] Matchett M.A.; Viano A.M.; Adolphi N.L.; Stoddard R.D.; Buhro W.E.; Conradi M.S.; Gibbons P.C., Chem. Mater. 1992, 4, 508.

[181] O'Brien P.; Walsh J.R.; Watson I.M.; Motevalli M., Henriken J.L., J. Chem. Soc. Dalton Trans. 1996, 249.

[182] Lazell M.; O'Brien P., Chem. Commun.1999, 2041.

[183] Revaprasadu N.; Malik M.A.; O'Brien P.; Wakefield G., Chem. Commun.1999, 1573.

[184] Spanhel L.; Haase M.; Weller H.; Henglein A., J. Am. Chem. Soc. 1987, 109, 5649.

[185] Katari J.E.; Colvin V.L.; Alivisatos A.P.,J. Chem. Phys. 1994, 98, 4109.

[186] Noglik H.; Pietro W.J., Chem. Mater. 1994,6, 1593.

[187] Wilson W.L.; Szajowsk P.F.; Brus L.E., Science 1993, 262, 1242.

[188] Danek M.; Jensen J.K.; Murray C.B; Bawendi M.G., Chem. Mater.1996, 8, 173.

[189] Hines M.A.; Guyot-Sionnest P., J. Phys. Chem. 1996, 100, 468.

[190] Peng X.; Schlamp M.C.; Kadavanich A.V.; Alivisatos A.P., J. Am. Chem. Soc. 1997, 119, 7019.

[191] Nair P.S.; Radhakrishnan T.; Revaprasadu N.; Kolawole G.A.; O'Brien P., Polyhedron, 2003, 22, 3129.

[192] Nair P.S.; Radhakrishnan T.; Revaprasadu N.; Kolawole G.A.; O'Brien P., J. Mater. Chem., 2002, 12, 1.

[193] Nair P.S.; Revaprasadu N.; Radhakrishnan T.; Kolawole G.A.; J. Mater.Chem., 2001, 11, 1555.

[194] Sawant P.; Kovalev E.; Klug J.T.; Efrima S., Langmuir, 2001, 18, 2913.

[195] Hirano S.; Somiya S., J. Am. Ceram.Soc.1976, 59, 534.

[196] Burukhin A.A.; Churagulov B.R.; Oleynikov N.N., High Press.Res.2001, 20, 255.

[197] Lu S.W.; Lee B.I.; Wang Z.L.; Guo J.K., J. Cryst.Growth 2000, 219, 269.

[198] Chen C.C.; Jiao X.; Chen D.; Zhao Y., Mater. Res. Bull. 2001,36, 2119.

[199] Maclaren I.; Trusty P.A.; Ponton C.B., Acta Mater. 1999, 47, 779.

[200] Yu S.H.; Shu L.; Wu Y.S.; Qian Y.T.; Xie Y.; Yang L., Mater. Res. Bull. 1998, 33, 1207.

[201] Pamplin B.R., Crystal Growth; Pergamon Press: New York,1975.

[202] Jiang, Y. Forced Hydrolysis and Chemical Co-Precipitation. Handbook of Nanophase and Nanostructured Materials; Wang,

[203] Liu L.Z.; Zhang Y., Eds.; Kluwer Academic: New York, 2003, 59.

[204] Peng Z.A.; Peng X. J,.Am. Chem. Soc. 2001, 123, 183.

[205] Qu L.; Peng Z.A.; Peng X., Nano Lett.2001, 1, 333.

[206] Qu L.; Yu W.W.; Peng X., Nano Lett.2004, 4, 465.

[207] Wang X.; Qu L.; Zhang J.; Peng X.; Xiao M., Nano Lett.2003,3, 1103.

[208] Yu W.W.; Qu L.; Guo W.; Peng X., Chem. Mater.2003, 15, 2854.

[209] Chen X.; Nazzal A.Y.; Xiao M.; Peng Z.A.; Peng X., J. Lumin.2002, 97, 205.

[210] Peng X.; Wilson T.E.; Alivisatos A.P.; Schultz P.G., Angew.Chem., Int. Ed. 1997, 36, 145.

[211] Peng Z.A.; Peng X.J., Am. Chem. Soc. 2002, 124, 3343.

[212] Yen B.K.H.; Stott N.E.; Jensen K.F.; Bawendi M.G., Adv. Mater.2003, 15, 1858.

[213] Liberato M.; Erik C.S.; Alivisatos A.P., J. Am. Chem. Soc. 2000, 122, 12700.

[214] Talapin D.V.; Rogach A.L.; Mekis I.; Haubold S.; Kornowski A.; Haase M.; Weller H., Colloids Surf., A 2002, 202, 145.

[215] Yu W.W.; Qu L.; Guo W.; Peng X., Chem. Mater. 2003, 15, 2854.

[216] Yu W.W.; Peng X., Angew.Chem., Int. Ed. 2002, 41, 2368.

[217] Funnell W.R.; Maysinger D., J. Nanobiotechnol 4, 1.

[218] Peng X., Adv. Mater.2003, 15, 459.

[219] Peng Z. A.; Peng X., J. Am. Chem. Soc. 2001, 123, 1389.

[220] Pellegrino T.; Parak W.J.; Boudreau R. 2003, Differentiation, 71, 542.

[221] Samia A.C.; Dayal S.; Burda C.,Photochem Photobiol 2006, 82, 617.

[222] Lovric J.; Cho S.J.; Winnik F.M.; Maysinger D., Chem Biol, 2005, 12, 1227.

[223] Ipe B.I., Lehnig M., Niemeyer C.M., Small, 2005, 1, 706.

[224] Samia A.C.; Chen X.; Burda C., J. Am. Chem. Soc. 2003, 125, 15736.

[225] Cho S.J.; Maysinger D.; Jain M; Roder B.; Hackbarth S.; Winnik F.M., Langmuir, 2007, 23, 1974.

[226] Maysinger D.; Lovric J.; Eisenberg A.; Savic R., Eur. J. Pharm. Biopharm., 2007, 65, 270.

[227] Choi A.O.; Brown S.E.; Szyf M.; Maysinger D., J. Mol. Med., 2008, 86, 291.

[228] Callinan P.A.; Feinberg A.P., Human Molecular Genetics, 2006, 15 Spec No 1: R95–R101

[229] Sen T.; Sen N.; Tripathi G.; Chatterjee U., Chakrabarti S., Neurochem.Int., 2006, 49, 20.

[230] Ryman-Rasmussen J.P.; Riviere J.E.; Monteiro-Riviere N.A., J. Invest Dermatol., 2007, 127, 143.

CHAPTER 2: SYNTHESES OF MAGNETIC METAL SULFIDE AND SELENIDE NANOPARTICLES FOR POTENTIAL BIOMEDICAL APPLICATIONS

2.1. Introduction

Magnetic nanoparticles have attracted much attention recently due to their potential application in magnetic recording as well as for use in various biological and medical applications such as magnetic separation, hyperthermia treatment, magnetic resonance contrast enhancement and drug delivery [1-4]. Synthesis of magnetic nanoparticles with controlled size, shape, composition and surface chemistry is of great importance. The magnetic properties of these materials are strongly dependent on the above that need to be specifically tuned depending to a desired application. For example, in data storage applications, the particles need to have a stable, switchable magnetic state to represent bits of information, a state that is not affected by temperature fluctuations [5]. For biomedical applications, the particles should present super paramagnetic behaviour at room temperature and of course the stability of the particles in physiological conditions such as water, neutral pH and so on, is critical [6].

Magnetic nanoparticles show phenomena such as super-paramagnetism, high field irreversibility, high saturation field as well as extra anisotropy contributions after field cooling. These phenomena relate to the small size of the nanoparticles and surface effects that dominate the magnetic behaviour of the individual nanoparticles [7]. Frenkel and Dorkman [8] predicted that a particle of ferromagnetic material, below a critical particle size (nanometric), would consist of a single magnetic domain, i.e. a particle that is in a state of uniform magnetization at any field. The magnetization behaviour of these particles above a certain temperature is identical to that of atomic paramagnets except for the extremely large moment and the susceptibilities involved [9]. Herein we report on the synthesis of various types of metal chalcogenide magnetic nanoparticles using the single source precursor method and the reduction method. The optical, structural and magnetic

properties of these new materials are described. These nanoparticles upon further functionalization could find promising applications in biomedical applications.

2.2. Potential biomedical applications

Biomedical applications of magnetic nanoparticles can be classified according to their application inside (*in vivo*) or outside (*in vitro*) the body. *In vivo* applications could be further separated in therapeutic (hyperthermia and drug-targeting) and diagnostic applications (nuclear magnetic resonance (NMR) imaging), while for *in vitro* applications the main use is in diagnostic (separation/selection, and magnetorelaxometry).

2.2.1. In vivo applications

2.2.1.1. Therapeutic applications

Hyperthermia: This is a therapeutic procedure used to raise the temperature of a region of the body affected by malignancy or other growths. The rationale is based on a direct cell killing effect of temperature (>41-42°C). One of the methods used in hyperthermia uses fine iron oxide magnetic particles. The magnetic material can be heated by the loss processes that occur during the reorientation of the magnetization of magnetic materials with low electrical conductivity, induced by the action of an external alternating magnetic field. The advantage of magnetic hyperthermia is that it allows the heating to be restricted to the tumour area. Moreover the use of nanosized magnetic nanoparticles is preferred over bulk materials because the particles absorb much more power at tolerable AC magnetic fields. Importantly, the heating potential is strongly dependent on the particle size and shape.

Drug delivery: Since the pioneering concept proposed by Freeman *et. al.* [10] that fine iron particles can be transported through the vascular system and be concentrated at a particular point in the body with the aid of a magnetic field, the use of magnetic particles for the delivery of drugs or antibodies to organs or tissues altered by diseases has become an attractive field of research [11]. This is shown in Fig. 2-1. The process of drug localization using magnetic delivery systems is based on the competition between forces exerted on the particles by the blood compartment, and magnetic forces generated from the magnet, i.e. an applied field. When the magnetic forces exceed the linear blood flow rates in arteries (10 cm s^{-1}) or capillaries (0.05 cm s^{-1}), the magnetic particles are retained at the target site and

maybe internalized by the endothelial cells of the target tissue [12]. For this application the use of nanoparticles favour the transport through the capillary systems of organs and tissues avoiding vessel embolism.

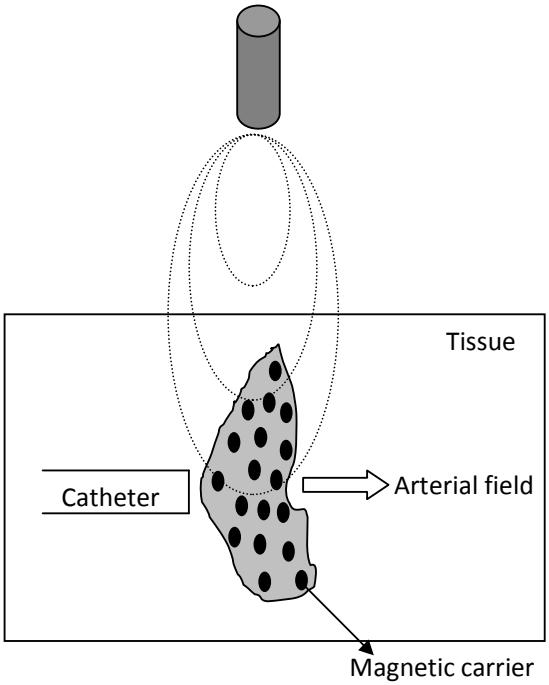

Fig. 2-1: Schematic representation of the magnetically driven transport of drugs to a specific region. A catheter is inserted into a arterial feed to the tumour and a magnetic stand is positioned over the targeted site.

2.2.1.2. Diagnostic applications

NMR imaging: The development of the NMR imaging technique for clinical diagnosis has prompted the need for a new class of pharmaceuticals, so-called magnetopharmaceuticals. These drugs are administered to a patient in order to (1) enhance the image contrast between normal and diseased tissue and/or (2) indicate the status of organ functions or blood flow [13]. A number of different agents have been suggested as potential NMR contrast agents. Most contrast agents used in NMR imaging studies to date have been paramagnetic. Superparamagnetic particles represent an alternative class of NMR contrast agents. Commercial iron oxide nanoparticles of maghemite (Endorem® and Resovit®) have been used as contrast agents in NMR imaging for location and diagnosis of brain and cardiac infarcts, liver lesions or tumours, when magnetic nanoparticles tend to accumulate at higher levels due to the differences in tissue composition and/or endocytotic uptake processes

[14]. Especially promising results have been detected in the improvement of sensitivity of detection and delineation of pathological structures, such as primary and metastic brain tumours, inflammation and ischemia [15]. For this purpose, proteins such as transferrin [16], peptides such as the membrane traslocating tat peptide of the HIV tat protein [17, 18], and oligonucleotides of various sequences [19] have been attached to aminated cross-linked iron oxide nanoparticles in order to obtain specific NMR imaging agents [20].

2.2.2. In vitro applications

2.2.2.1. Diagnostic applications

Separation and selection: Considerable attention has been paid to solid-phase extraction (SPE) as a way to isolate and pre-concentrate desired components from a sample matrix. SPE offers an excellent alternative to the conventional sample concentration methods, such as liquid–liquid extraction [21]. The separation and pre-concentration of a substance from large volumes of solution can be highly time consuming when using standard column SPE, and is in this field where the use of magnetic or magnetizable adsorbents called magnetic solid-phase extraction (MSPE) has been important. In this procedure the magnetic adsorbent is added to a solution or suspension containing the target. This is adsorbed onto the magnetic adsorbent and then the adsorbent with the adsorbed target is recovered from the suspension using an appropriate magnetic separator (Fig. 2-2). The advantage of using magnetic nanoparticles instead of magnetic microparticles is that suspensions can be prepared that are stable against sedimentation in absence of an applied magnetic field. The applicability of magnetic nanoparticles in MSPE is clearly evidenced by the fact that iron oxide nanoparticles already exists in the market (DYNAL Biotech).

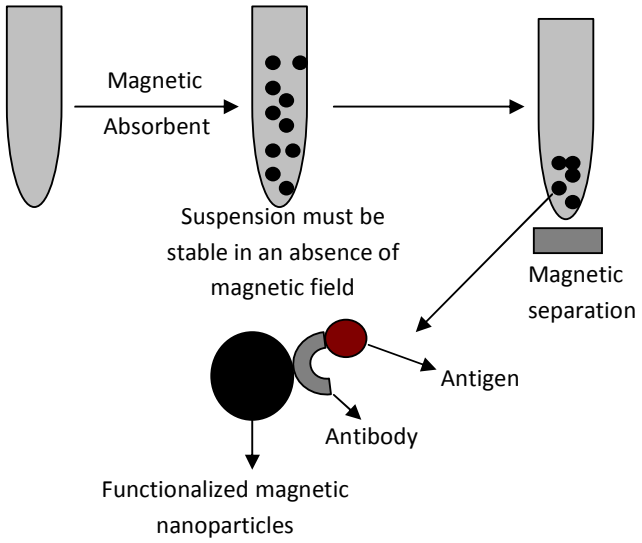

Fig. 2-2: Schematic representation of the magnetically assisted separation of substances. In this case a magnetic nanosphere to which an antibody has been anchored is dispersed in a liquid medium containing the antigen (substance to be analysed).

Magnetorelaxometry: Magnetorelaxometry was introduced as a method for the evaluation of immunoassays [22]. Magnetorelaxometry measures the magnetic viscosity, i.e. the relaxation of the net magnetic moment of a system of magnetic nanoparticles after removal of a magnetic field [23]. There are two different relaxation mechanisms. First, the internal magnetization vector of a nanoparticle can relax in the direction of the easy axis inside the core; this is called N´eel relaxation [24]. Second, particles can accomplish rotational diffusion in a carrier liquid; this is called Brownian relaxation [22]. N´eel and Brownian relaxation can be distinguished by their different relaxation times [24]. Furthermore, Brownian relaxation takes place only in liquids, whereas N´eel relaxation does not depend on the dispersion of the nanoparticles. The fact that magneto-relaxometry depends on the core size, the hydrodynamic size and the anisotropy allows this technique to distinguish between free and bound conjugates by their different magnetic behaviour, and therefore can be used as an analytical tool for the evaluation of immunoassays [22].

2.2.3. Future applications

Magnetically directed microspheres containing radionucleides have been used for internal radiotherapy [11]. However, little work has been done on the use of magnetic nanoparticles in the radiotherapy. One strategy under active investigation is to improve dose localization that of administration of drugs, metabolites, etc that have been labelled with radioactive isotopes in a quantity sufficient to deactivate tumour cells [25]. In this way, the use of surface-activated magnetic nanoparticles could have a tremendous impact in improving the efficiency of cancer treatments. It can be further envisaged that a future in which magnetic particles can be used for the repair of the human body e.g. with prosthetics or artificial replacement parts. In this field the pioneering work of Dailey *et al* [26] who has reported the synthesis of a silicone based magnetic fluid for use in eye surgery deserves mention. Retinal detachment is a major cause of vision loss in adults. It occurs when the retina separates from the choroid, resulting in eventual death of the retina and subsequent loss of vision. Dailey and co-workers have developed an internal tamponade from modified silicone fluid containing sterically stabilized 4–10 nm sized metal particles, which are held in place with an external magnetized scleral buckle.

2.3. Syntheses of magnetic nanoparticles

Metal sulfides and selenides of magnetic metal ions are of particular interest in our study as a result of their dual properties i.e. good optical properties (absorption in: UV for MnS/Se, visible for NiS/Se and IR for CoS/Se and CuS/Se and the ability to emit light) as well as their magnetic properties. The metal centres have shown to have magnetic characteristics due to the unpaired d-electrons. The oxide counterparts of these metals though possessing similar magnetic behaviour rarely luminescent and therefore have limited applications compared to the sulfides and selenides. Metal sulfides and selenides of other metals such as Cd are known to have excellent optical properties and strategies have been developed to dope them with magnetic ions in order to achieve dual applications but these strategies have proved to be challenging and minute amounts of the dopant are usually incorporated into the core metal chalcogenide thus resulting in very small magnetic moments. Other complicated assemblies have also been developed to achieve the same dual properties e.g. simultaneous encapsulation of luminescent nanoparticles such as CdSe and magnetic Fe_2O_3 by a polymer microsphere. These assemblies have disadvantages such as multiple synthesis

steps and large particle sizes. Consequently magnetic metal chalcogenides are far more promising and we therefore embark on synthesizing these nanoparticles and exploring their properties.

Herein we therefore report on the syntheses of MS and MSe (M = Mn, Co, Ni and Cu) semiconductor nanoparticles and probe their optical, structural and magnetic properties. The semiconductor nanoparticles were synthesized via two routes. The MS nanoparticles were synthesized using the single source precursor method. Tetramethylthiuram disulfide metal complexes were used as precursors. The tetramethylthiuram disulfide ligand was used because it has an abundance of sulfur atoms and high affinity for the required metal ions compared to other sulfur containing ligands. The single-source precursor method involves the decomposition of a molecular precursor to form the desired products. The advantage of this method is that the bond between the metal and the chalcogenide already exists and therefore decomposition of the precursor under the right conditions will result in the formation of MS nanoparticles. This approach has been used to produce many metal chalcogenide nanoparticles [27-32]. To our knowledge, after thorough literature surveys, no tetramethylthiuram disulfide complexes of the chosen metals have been reported.

The MSe were formed by the reaction of a metal salt with sodium borohydride reduced selenium. This method offers a good alternative to the synthesis of selenide nanoparticles compared to the single source precursor method where selenium ligands are limited and are rather difficult to form complexes with metal ions. This method also offers advantages such as simplicity, the use of mild conditions and it also allows for easy control of reaction parameters.

2.3.1. Syntheses of MS nanoparticles

2.3.1.1. Materials

Tetramethylthiuram disulfide (TMTD), hexadecylamine (HDA), trioctylphosphine (TOP), manganese acetate tetrahydrate ($Mn(CH_3CHOO)_2.4H_2O$), cobalt chloride hexahydrate ($CoCl_2.6H_2O$), nickel chloride ($NiCl_2.6H_2O$), copper chloride ($CuCl_2.2H_2O$) and methanol were all purchased from Sigma Aldrich and used as purchased.

2.3.1.2. Syntheses of the precursors

A hot solution of tetramethylthiuram disulfide (2.0 mol) in methanol (20 ml) was added into a heated solution of the metal salt (1.0 mol) in methanol (20 ml). The mixture was stirred and refluxed for 1 hour. The resultant precipitate was filtered, washed twice with methanol and dried under vacuum: **$Mn(CH_3CHOO)_2(C_6H_{12}N_2S_4)_2$** – 74.8 % , m. p. 347°C. Calcd. C, 29.55; H, 4.62; N, 8.62. Found: C, 29.07; H 4.56; N 8.78. IR/cm^{-1}: 1504 (s), 1397 (s), 1367 (s), 1227 (s), 1138 (s), 1035 (s), 944 (s), 845 (s), 783 (w), 673 (s), 556 (s), 436 (s) , **$CoCl_2(C_6H_{12}N_2S_4)_2$** Yield 80.2 %; m. p. 363°C. Anal. Calcd. C, 19.49; H, 3.03; N, 7.58. Found: C, 19.46; H 3.27; N 7.57. IR/cm^{-1}: 1387 (s), 1254 (s), 1245 (s), 1124 (s), 1044 (s), 1022 (s), 978 (s), 893 (m), 780 (w), 673 (m), 576 (s), 439 (s).**$NiCl_2(C_6H_{12}N_2S_4)_2$** – Yield 76.2 %; m. p. 383°C. Anal. Calcd. C, 28.29; H, 5.03; N, 6.98. Found: C, 19.46; H 3.27; N 7.57. IR/cm^{-1}: 1384 (s), 1252 (s), 1245 (s), 1124 (s), 1044 (s), 1018 (s), 978 (s), 893 (m), 780 (w), 673 (m), 576 (s), 439 (s).and **$CuCl_2(C_6H_{12}N_2S_4)_2$** – Yield 80.2 %; m. p. 351°C. Anal. Calcd. C, 19.10; H, 3.13; N, 7.58. Found: C, 19.46; H 3.27; N 7.57. IR/cm^{-1}: 1387 (s), 1255 (s), 1245 (s), 1123 (s), 1042(s), 1021 (s), 978 (s), 891 (m), 780 (w), 673 (m), 576 (s), 439 (s).

2.3.1.3. Syntheses of the nanoparticles

In a typical experiment, the precursor was dissolved in TOP (10 – 20 ml). This solution was then injected into 3.125 g of hot HDA at 160 °C. A decrease in temperature of the solution by 20 – 30 °C was observed. The solution was allowed to stabilize at 160 °C and heated for 60 minutes at this temperature. The reaction is quenched and the resultant solution is allowed to cool to about 70 °C, and methanol was added to the solution. A flocculent precipitate forms and this solid product is separated by centrifugation and redispersed in toluene. Toluene was removed by evaporation under reduced pressure to form HDA capped metal sulphide nanoparticles. The particles are washed three times with methanol and redispersed in toluene or dried as powders.

2.3.2. Syntheses of MSe nanoparticles

2.3.2.1. Materials

The metal salts, sodium borohydride ($NaBH_4$) and selenium powder were purchased from Sigma Aldrich and used as received.

2.3.2.2. Syntheses of the nanoparticles

About 12.5 mmol of selenium powder was added together with 26.5 mmol of sodium borohydride in methanol and the mixture was stirred for 60 minutes at room temperature. An amount of 25 mmol of metal chloride was added. This then causes the reaction to give off heat and the temperature rise to 40 °C. The reaction was then allowed to stir for a further 60 minutes. The resultant precipitate was filtered and washed several times with acetone.

2.4. Characterization techniques

A Perkin Elmer Lambda 75S UV-VIS-NIR Spectrophotometer was used to carry out the optical measurements. These were recorded on samples placed in silica cuvettes (1 cm, path length), using toluene as a reference solvent. A Perkin Elmer LS55 with a xenon lamp (150 W) and a 152 P photo multiplier tube as a detector was used to measure the photoluminescence of the particles. The samples were placed in quartz cuvettes (1 cm path length) for spectral analysis. XRD patterns of powdered samples were measured on a PANalytical X'Pert PRO-diffractometer using Cu Kα radiation (wavelength, λ = 1.5406 Å) with variable slits at 45 kV/40 mA. Measurements were taken using a glancing angle of incidence detector at an angle of 2°, for 2θ values in a range 20° – 60° in steps of 0.001° with a scan speed of 0.1°/s.

Cobalt sulfide samples were characterized using FE-SEM (Leo, Zeiss), operated at 3-10 kV electron potential difference and equipped with a semiconductor detector that allows for the detection of energy dispersive X-rays (EDX). The samples were prepared by placing a drop of suspended particles in toluene, onto a carbon tape. The samples were then allowed to dry at room temperature. The TEM images were obtained using a Philips CM 200 compustage electron microscope whilst the HRTEM images were obtained on a Joel JEM-2100 microscopy with a LAB6 filament, all operated at 200 kV. The samples were prepared by placing a drop of a dilute solution of sample in toluene on a copper grid (400 mesh, agar). The samples were allowed to dry completely at room temperature. The ESR spectra of the nanocrystals were recorded on a JEOL JES-FA200 spectrometer under irradiation of a high-pressure mercury lamp (USH-1005D) focusing at the sample cell in the ESR cavity at 298K. The magnitude of modulation was chosen to optimize the resolution and signal-to-noise

ratio of the observed spectra under non-saturating microwave power conditions. The g values were calibrated using a Mn^{2+} marker.

2.5. Results and discussion

2.5.1. Manganese sulfide and manganese selenide nanoparticles

The semiconductor nanoparticles of group VIIB – IB metal chalcogenides have attracted a lot of attention due to their interesting electronic structures and magneto-optical properties. Unlike the conventional II – VI semiconductor such as CdS and CdSe, these semiconductors offer much versatility, i.e. the metal cores are less toxic, the variable oxidation states result in wide range of applications and their magnetic susceptibility offers completely new avenues of applications. Manganese sulfide (MnS) is a wide band gap semiconductor with a bulk band gap of 3.1 eV. It usually exists in three phases, a green stable α-MnS form (alabandite) with a rock salt (RS) structure, a β-MnS and a *γ*-MnS (both pink) metastable modifications with zinc blend (ZB) and wurtzite (W) structures respectively [33-35]. In previous studies considerable interest has been on controlling the crystalline phases and the morphologies. Recently, a variety of novel shapes such as MnS nanorods, hollow spheres, porous networks, coral shaped, and floral-like arrangements have been synthesised by different methods such as hydrothermal, solvothermal, microwave irradiation, spray pyrolysis and chemical bath deposition [36-39].

Just like manganese sulfide, manganese selenide in bulk form is a wide band gap semiconductor of 2.65 eV. It can exist in many forms and posses optoelectronic, transport and magnetic properties. Traditionally molecular beam epitaxy (MBE), organometallic vapor phase epitaxy (OMVPE) and the reaction of metal Mn with elemental selenium at high temperatures in a quartz tube with the existence of I_2 catalyst have been employed to synthesize manganese selenides [40]. Consequently these methods required harsh conditions, expensive equipment as well as toxic materials. Recently, Peng et. *al*. reported that MnSe cubic microcrystals could also be synthesized using a less expensive hydrothermal method but employed a more toxic complex Na_2SeO_3, whilst Wu and co-workers reported on the synthesis of MnSe and $MnSe_2$ nanorods using the same method with $Mn(CH_3COO)_2.4H_2O$, Se and hydrazine hydrate in NaOH to carry-out their reactions [40,41]. Herein we report on the synthesis of manganese sulfide nanoparticles using the single

source precursor method and manganese selenide synthesized by the reaction of manganese chloride with selenium in the presence of a reducing agent sodium borohydride and we report on their optical, morphological and magnetic properties.

The optical spectra of MnS and MnSe nanoparticles are depicted in Fig. 2-3. The absorption spectrum of Fig. 2-3(a) shows an excitonic peak at 371 nm that is blue shifted from bulk MnS band-edge (400nm). This is as a result of the quantization of the energy levels in the valance and conduction bands of the nano-semiconductor causing an increase of the band-gap energy.

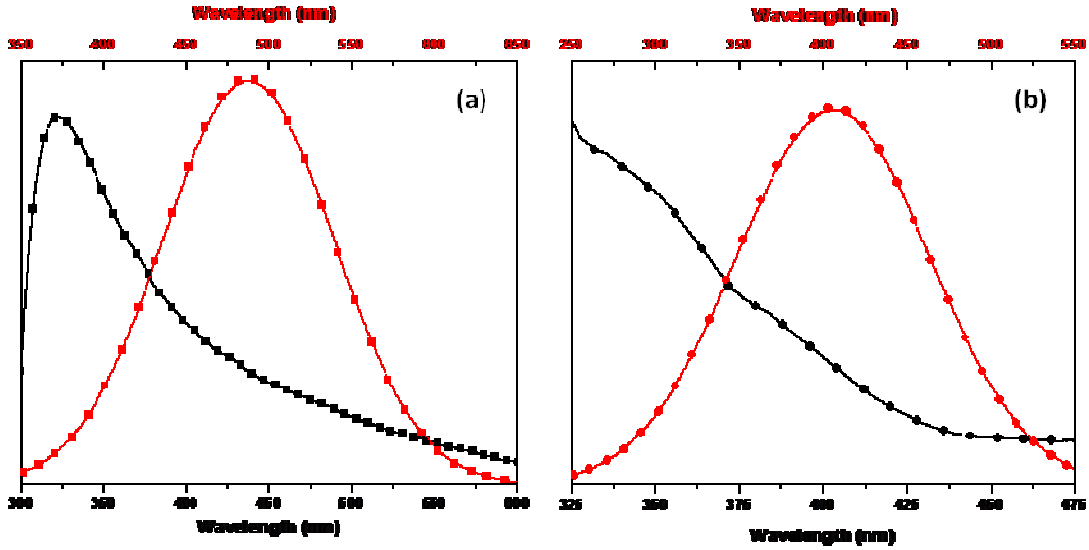

Fig. 2-3: Absorption and photoluminescence spectra (λ_{exc} = 250 nm) of (a) MnS and (b) MnSe.

The photoluminescence spectrum is red-shifted from the absorption band-edge (λ_{max} = 488 nm) as a result of irradiative energy losses. The spectrum is normally distributed, portraying a monodispersed sample as well as good surface passivation of the nanoparticles by the capping agent. The absorption spectrum of the MnSe in Fig. 2-3(b) is characterized by two shoulder peaks with the first peak being associated with the band-edge of the material. The band-edge of 387 nm is blue-shifted from bulk MnSe (468 nm) signifying quantum confinement effects that result from the nanosized particles. This is further validated by the photoluminescence spectrum that shows well passivated nanoparticles evident from the

Gaussian distributed curve. The maximum emission at 407 nm is red-shifted from the absorption band-edge and shows typical features of semiconductor nanomaterials. The optical properties of MnS show some degree of similarities with that of the MnSe, as a result of the similar Mn^{2+} 3d-configuration. The optical properties of these materials offer an alternative for bio-imaging due to their ability to absorb and emit uv-vis light.

The morphological properties of MnS and MnSe nanoparticles are shown in Fig. 2-4. The MnS particles depicted in Fig. 2-4(a) show wire-like structures of approximately 50 nm diameter and various lengths. The high aspect ratio (μ = 4.96) of the particles results in a high surface area that is conducive for bio-medical applications. The corresponding TEM image in Fig. 4(c) confirms the morphology as wire-like. The MnSe nanoparticles (Fig. 2-4(b) and 2-4(d)) also showed rod-like agglomerates (aspect ratio μ = 6.27). The HRTEM also showed crystal fringes as a result of the crystalline nature of the nanoparticles. The formation of 1-dimensional structures for both MnS and MnSe confirms their similarities.

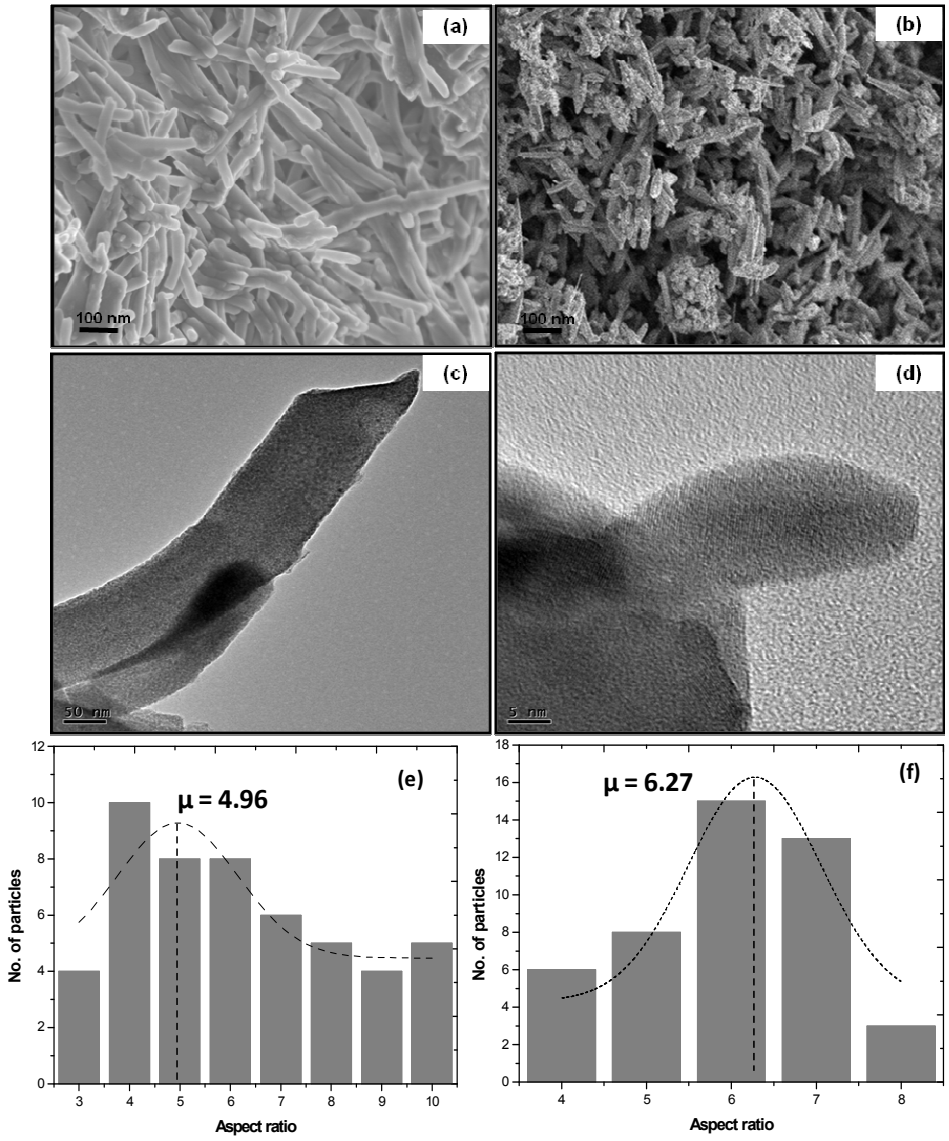

Fig. 2-4: (a, c and e) are the SEM, HRTEM micrographs and size distribution curve of MnS and (b, d and f) are the SEM, HRTEM micrographs and size distribution curve of MnSe.

The crystal phases and crystallinity of both MnS and MnSe nanoparticles were determined by X-ray diffraction, as shown in Fig. 2-5. The MnS nanoparticles in Fig. 2-5(a) could be indexed to a β-MnS phase (JCPDS card no.: 89-3709) with a cubic structure. The diffractogram showed relatively sharp peaks depicting the formation of crystalline nanoparticles. The diffractogram also indicated the presence of HDA (JCPDS card no: 42-1782). The overwhelming presence of the capping agent could to some extent be responsible for the anisotropic morphology of the particles and their phase preference.

HDA has an ability to form anisotropic nanoparticles as the result of selectively coordinating to a preferential facet [42]. This is therefore one of the ways that HDA can influence the properties of the nanoparticles. Because of the size of the nanoparticle and steric hindrance from bulk capping molecules, a finite amount of ligands can attach to the surface of the nanoparticle. In case of excess HDA, this can result in the presence of free HDA ligands in solution (scheme 2-1).

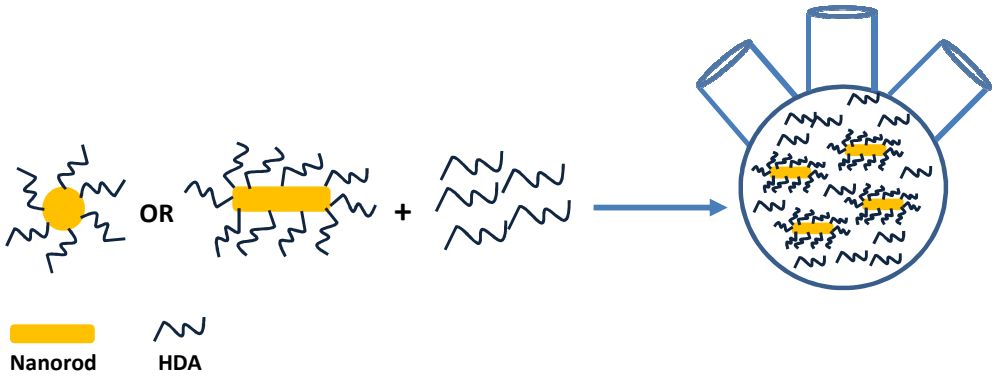

Scheme 2-1: Schematic showing excess HDA ligands.

In the single-source precursor method, the capping agent is usually in excess because it acts as both the capping agent of the nanoparticles as well the solvent for the reaction to occur in. Generally the free excess ligands are removed from the sample by successive methanol washing and centrifugation. Because the ligands on the surface of the nanoparticle are attached through a weak dative bond, harsh treatment on the nanoparticle is generally discouraged and the sample is usually washed three times. This inevitably can result in the remainder of the free uncoordinated ligands. The uncoordinated ligands do not further influence the properties of the nanoparticles but could cause complications in the characterization the nanoparticles e.g. the HDA peaks can contaminate the XRD pattern of the nanoparticles. Determining the exact amount of the capping agent needed to effectively coordinate and protect the surface of a specific size of a nanoparticle has proven to be difficult. Some researchers have attempted to use common characterization techniques such as TGA, absorption spectroscopy, NMR and chromatography to determine the amount of the capping agent. However these techniques suffer from not being able to discriminate between bonded and free ligands [43-46].

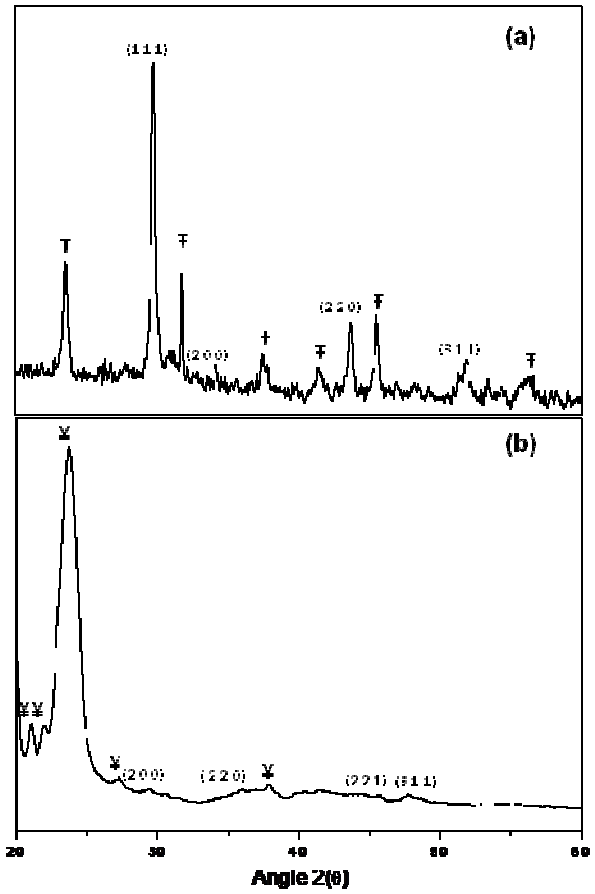

Fig. 2-5: X-ray diffraction patterns of (a) MnS and (b) MnSe (₸ denotes HDA, ¥ denotes elemental Se).

The role of the capping agent in the growth of the nanoparticles is diverse and can affect properties such as solubility, reactivity, stability, melting point and electronic structure. The HDA therefore affects the growth mechanism of the nanocrystals, the excess HDA increases the solubility of the precursor resulting in the formation of small nuclei [42]. The small nuclei behave as magic clusters and prompt the formation of anisotropic nanoparticles. The diffractogram for the manganese selenide nanocrystals was indexed as a cubic MnSe (JCPDS card no.: 00-027-0311). The presence of unreacted selenium was also detected (JCPDS card no.: 06-0362).

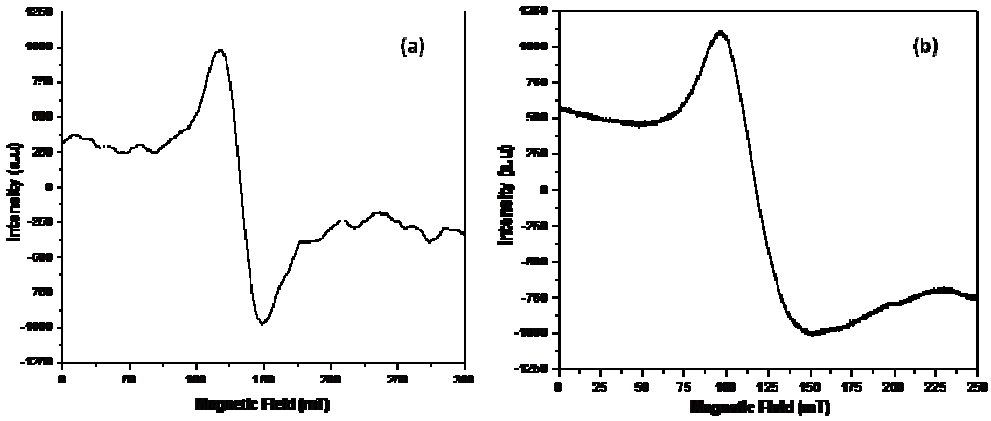

Fig. 2-6: ESR spectra of (a) MnS and (b) MnSe taken at 298 K.

ESR spectroscopy was used to investigate the magnetic properties of manganese sulfide and selenide as shown in Fig. 2-6. From the XRD, it has been established that Mn is in the +2 oxidation state. The Mn^{2+} ion is known to have the isotropic g-factor that is nearly equal to that of a free electron [47]. The ESR spectrum of manganese sulfide nanoparticles shown in Fig. 2-6(a) has a single broad signal with a g-value of 2.0064 and a line width of approximately 75 mT. The observed hyperfine structure is due to the Mn-Mn interactions. This has been readily observed in bulk MnS and DMS with high Mn^{2+} loadings [48]. The small deviation of the g-factor from that of a free electron (g_e = 2.0023) confirms the ESR signal as that of Mn^{2+} ions. The room temperature ESR spectrum of manganese selenide is depicted in Fig. 2-6(b). A single, asymmetric, strong and broad microwave resonance peak was observed at a field of approximately 125 mT, with a large line width of 100 mT and a g-value of 2.0068. Similar properties to that of manganese sulfide were observed. This is consistent since both the ESR signals arise from Mn^{2+} configuration. The small differences in the ESR signals are due to the small differences of the chalcogenides sources.

2.5.2. Cobalt sulfide and cobalt selenide nanoparticles

Semiconductor nanomaterials are an integral part of modern technologies. Various conditions form the basis of these technologies, in the case of biomedical applications, exceptional optical and magnetic properties are desired. Particularly in bio-imaging, materials with longer emission lifetimes as well as big enough magnetic moments are

necessary. Cobalt sulfide and selenide are one of the materials that have tremendous potential for such applications. Due to the size quantization effect at the nanometric level, they posses outstanding optical properties. The valance electrons from the cobalt atom result in the ferromagnetic nature of the cobalt chalcogenides and compared to cobalt doped quantum dots, cobalt sulfide and selenide nanocrystals have an advantage due to its larger magnetic moment. Cobalt sulfide nanocrystals have been previously synthesized using different methods and various morphologies of it has been reported. Chen *et al* reported the hydrothermal synthesis of Co_3S_4 nanotubes based on the Kirendall effect [49]. On the other hand Srouji and co-workers reported the aerosol assisted organic chemical vapour deposition (AACVD) of cobalt sulfide thin film using the n-hexyldithiocarbamato complex as the single-source precursor [50]. Herein we report on the synthesis of cobalt sulfide nanocrystals using the cobalt tetramethylthiuram complex as the single source precursor.

Semiconductor selenides have attracted enormous attention due to their distinctive electrical and magnetic properties and a wide variety of potential applications eg., optical recording materials, solar cells and in biomedicine [51]. Traditionally selenides have been synthesized by solid state reactions, solid state metathesis, solution growth techniques and self-propagating high temperature synthesis [52]. Among these approaches, many are based on high temperature synthesis. In this study, the synthesis of cobalt selenide nanocrystals was carried out at room temperature in an aqueous environment. The optical properties of cobalt sulfide and selenide were investigated using UV-vis and photoluminescence spectroscopy as depicted in Fig. 2-7. The absorption spectrum of cobalt sulfide in Fig. 2-7(a) shows three distinct peaks that are characteristic of cobalt sulfide nanocrystals. These peaks correspond to the electronic transitions that occur within the band structure of nanocrystalline cobalt sulfide. The first excitonic peak is characterized as the band-gap of that material. This is the minimum energy required to excite an electron from the valance band to the conduction band and the subsequent peaks result from the excitation of the irradiated energy from the first transition. This phenomenon is unique to nanomaterials and is dependent on the physical nature of the material.

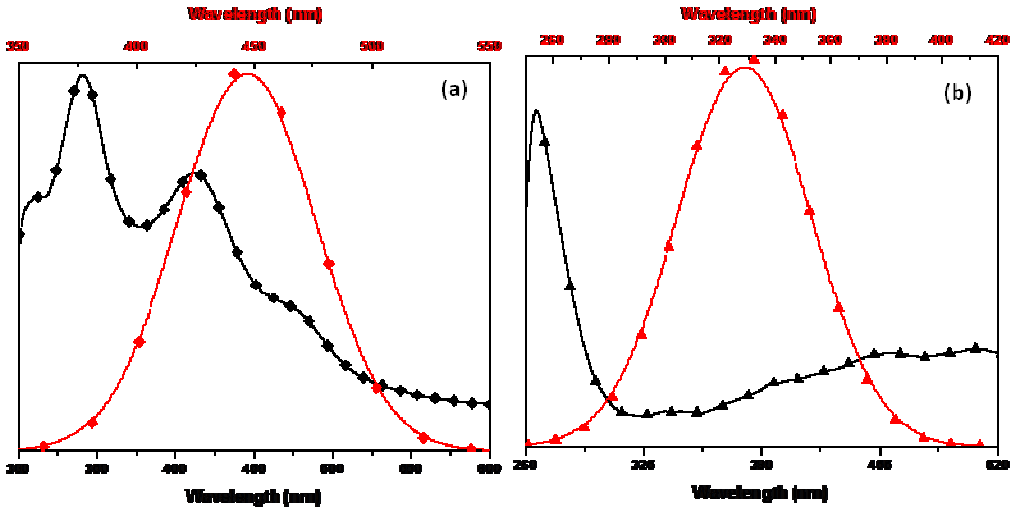

Fig. 2-7: Absorption and photoluminescence spectra (λ_{exc} = 250 nm) of (a) Co_3S_4 and (b) Co_3Se_4.

The bulk band-gap of cobalt sulfide is located at the infra-red region with the wavelength of 1387 nm. Usually nanocrystals show relatively small blue-shifts from the bulk material, due to their intermediate character between molecules and the bulk. However in this case the band-edge of 378 nm is far blue-shifted from the bulk, this could be as a result of the stoichiometry of the resultant cobalt sulfide nanocrystals. Because cobalt sulfide occurs in different stoichiometries, such as CoS, CoS_2, Co_3S_4, Co_9S_8, $Co_{1-x}S$ and etc., it therefore becomes intricate to predict its properties, especially when combined with the nanometric nature.

The photoluminescence properties of cobalt sulfide in Fig. 2-7(a) show a single peak emission with the maximum located at 446 nm. The emission maximum is stoke-shifted from the first excitonic peak by 68 nm. This is a typical behaviour of nanocrystalline materials. The spectrum also depicts relatively monodispersed nanocrystals, indicated by the Gaussian shaped curve and the narrowness of the curve. The location of the emission maximum and the presence of a single peak confirm the 378 nm as the band-edge of the resultant particles and the subsequent peaks in the absorption spectrum are as results of excitonic transition rather than absorption of different sized nanoparticles.

The optical properties of cobalt selenide nanocrystals are shown in Fig. 2-7(b). The absorption spectrum shows a single peak that is blue-shifted from bulk at 264 nm (860 nm). The large blue-shift in this case is due to the small size of the nanocrystals. The synthetic procedure for the cobalt selenide omits the use of the stabilizing agent and the significantly low synthetic temperature result in the formation of small sized nanocrystals. The tailing of the absorption spectrum is due to the sparsely soluble nanocrystals, again as a result of the absence of the surface passivating agent. The photoluminescence spectrum is red-shifted from the absorption band-edge and maximum is located at 330 nm. The large blue-shift from bulk in cobalt selenide nanocrystals is again attributed to the structure of the nanocrystals. The large blue-shifts seen in both cobalt sulfide and selenide and multi-transition absorption observed in the cobalt sulfide nanocrystals offers immense advantage in bio-imaging compared to the traditional organic dyes.

Structural characterizations of both cobalt sulfide and selenide were determined by electron microscopy as well as X-ray diffraction. The electron micrographs are shown in Fig. 2-8. The cobalt sulfide nanocrystals were found to be spherical nanoparticles with a mean diameter of 2.13 nm. The crystals were relatively monodispersed though a small degree of agglomeration was also evident. The monodispersity and the fairly low degree of agglomeration, accordingly come about as a result of the surface passivation of the nanocrystals by HDA. Alternatively the morphology of cobalt selenide is depicted Fig. 2-8(b) and (d). The particles are also spherically shaped but are small compared to the cobalt sulfide nanocrystals (μ = 1.96 nm). A high degree of agglomeration is observed and this undoubtedly is caused by the absence of the capping molecules. The lack of the capping molecules result in smaller particles as the bulky shell covering is not present but on the negative side, the nanocrystals tend to be less stable and therefore opt to clump together in order to attain that stability.

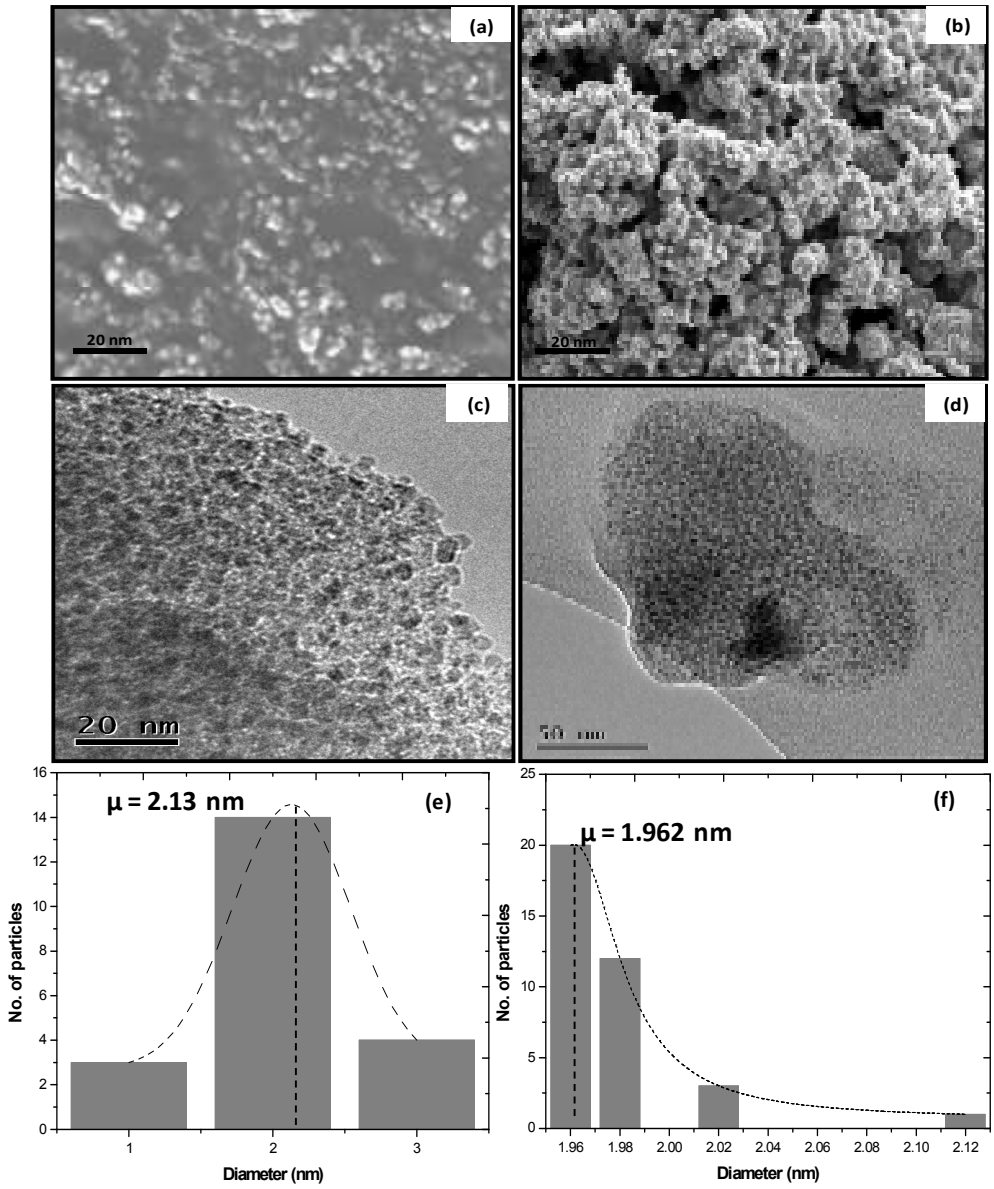

Fig. 2-8: SEM micrographs of (a) Co_3S_4, (b) Co_3Se_4 and HRTEM micrographs of (c) Co_3S_4 and (d) Co_3Se_4.

The X-ray diffractograms of cobalt sulfide and cobalt selenide are shown in Fig. 2-9. The cobalt sulfide nanocrystals were indexed to a cubic phase Co_3S_4 with a space group of Fd3m, whilst the cobalt selenide nanocrystals in Fig. 2-9(b) were indexed to a monoclinic Co_3Se_4. Residual contaminants were detected for both sets of nanocrystals. In the case of cobalt sulfide excess HDA was found and for cobalt selenide, unreacted selenium was detected. The presence of HDA has very little effect on the properties of the cobalt sulfide due to its

nature. On the other hand, selenium is known to have semiconducting properties under favourable conditions and might therefore prove to be interfering with accurate characterization and usability of the cobalt selenide nanocrystals. Nevertheless, one of the interesting things about cobalt chalcogenides is their ability to form varied stoichiometries. This renders them very versatile materials. Co_3S_4 has been known to form various morphologies, from spheres to rods to tubes to even unusual sea urchin morphology [53].
It has been found for both cobalt sulfide and selenide that at this composition, the nanocrystals tend to display antiferromagnetic behaviour under an external magnetic field [54]. These materials therefore have promising applications in biomedical diagnostics.

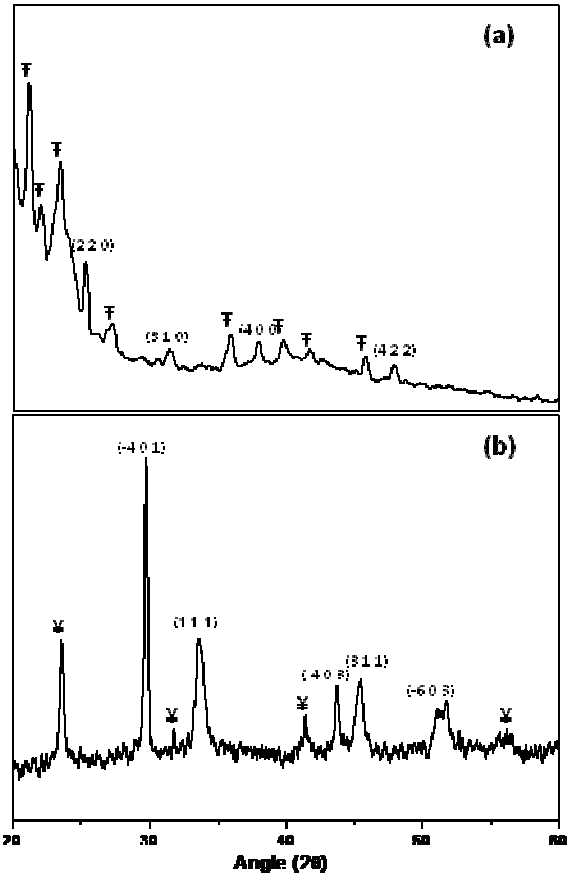

Fig. 2-9: X-ray diffraction patterns of (a) CoS and (b) Co_3Se_4 (₸ denotes HDA, ¥ denotes elemental Se).

The magnetic properties of cobalt sulfide and selenide were determined by ESR spectroscopy. The ESR spectrum of cobalt sulfide in Fig. 2-10(a) shows a strong resonance

peak located at 135 mT as well as the presence of other weak signals. The additional weak peaks arise from the interaction of an unpaired electron by way of its magnetic moment with the nearby nuclear spins, consequently giving rise to additional allowed energy state. The observed g-value for the particles was found to be 1.9987. The deviation of the g factor of the particles from g_e is attributed to the lost of angular momentum through spin orbital coupling. The magnetic properties of cobalt selenide nanocrystals are depicted in ESR spectrum in Fig. 2-10(b). The multi-line resonance spectrum as in the case of cobalt sulfide is as a result of hyperfine coupling through the Fermi contact interaction between the electrons and nuclei within that material. Both the set of nanocrystals show positive response to an externally applied magnetic field at room temperature.

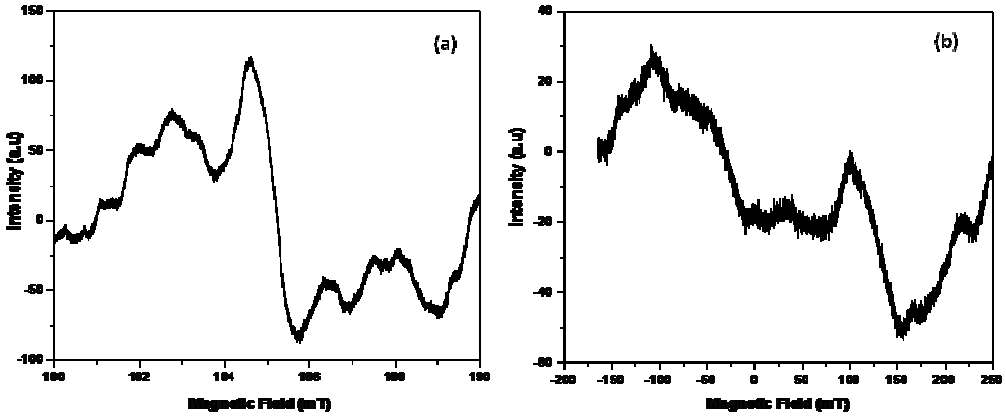

Fig. 2-10: ESR spectra of (a) Co_3S_4 and (b) Co_3Se_4 taken at 298 K.

2.5.3. Nickel sulfide and nickel selenide nanoparticles

Nickel sulfide, as one of the transition metal chalcogenides has attracted considerable attention because of its intrinsic properties such as its unique electromagnetic property involving a first-order phase transition from a low temperature antiferromagnetic semiconductor to a high temperature paramagnetic metal, its toughening effect, and potential applications in solar storage and catalysts for hydrodenitrogenation and hydrodesulfurization [55]. In addition nickel sulfides are a complex system and contain multiple phases and are therefore exciting materials to study. Traditionally nickel sulfides are prepared by high temperature solid state reaction or vapour phase reaction. Recently some soft chemical routes have been used to synthesize nickel sulfides such as nanorods,

nanowhiskers and petal-like nanocrystals [50]. Nickel selenide possesses similar properties with that of nickel sulfide unequivocally as the result of the Ni d-transition metal as well as the location in the same group of the S and Se. Nickel selenides' properties are stoichiometry dependent for example Ni_3Se_2 is a ferromagnet where as $NiSe_2$ is a typical Pauli paramagnet [56]. Various synthetic methods have been reported for the synthesis of nickel selenide nanocrystals. Wang et. al. reported on the synthesis of 1D nickel monoselenides by the reaction of nickel chloride with sodium borohydride and selenium in ethylenediamine [57] whilst Du and co-workers reported on symmetrical six-horn nickel selenide nanostars grown from orientated attachment [58]. Herein, a method similar to Wang's is reported except the synthesis was carried out in aqueous conditions.

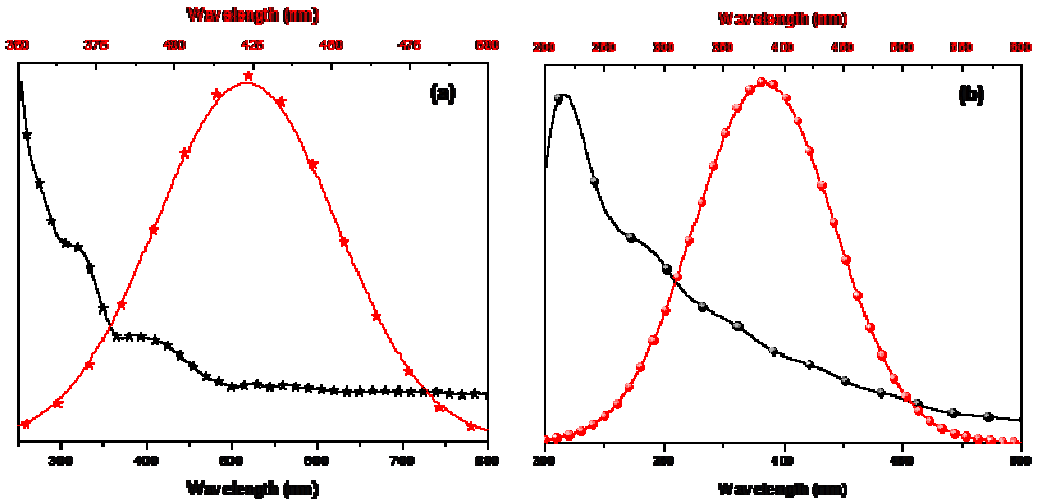

Fig. 2-11: Absorption and photoluminescence spectra (λ_{exc} = 250 nm) of (a) NiS and (b) Ni_3Se_4.

Fig. 2-11 shows the optical properties of both nickel sulfide and selenide. Bulk nickel sulfide has a band gap of approximately 0.5 eV (620 nm) [59]. The absorption spectrum in Fig. 2-11(a) shows multi-peaks arising from different transitions. The band-edge is blue-shifted from bulk and is located in the blue-region of the spectrum. This large blue-shift (330 nm) is associated with the strong quantum confinement effects. As the nanocrystal becomes very small compared to the Bohr exciton radius and approaches the size of the atom, the energy levels within the electronic structure of the nickel sulfide become quantize and result in the blue-shift of the band-gap. The extent of the blue-shift could be contributed to by the

presences of defects. The photoluminescence spectrum is red-shifted from the absorption band-edge and the maximum emission peak is located at 421 nm. The shape of curve signifies a monodispersed sample with particle possessing the same properties thus translating to similar sizes and shapes.

The optical properties of nickel selenide nanocrystals are presented in Fig. 2-11(b). The absorption spectrum of the nickel selenide nanocrystals is blue-shifted from the bulk (620 nm) band-gap, with the first excitonic peak located at 310 nm. The photoluminescence spectrum is red-shifted from the absorption band-edge by a Stokes shift of 57 nm. The nanocrystals are relatively monodispersed indicative by the Gaussian shape curve with the emission maximum located at 367 nm.

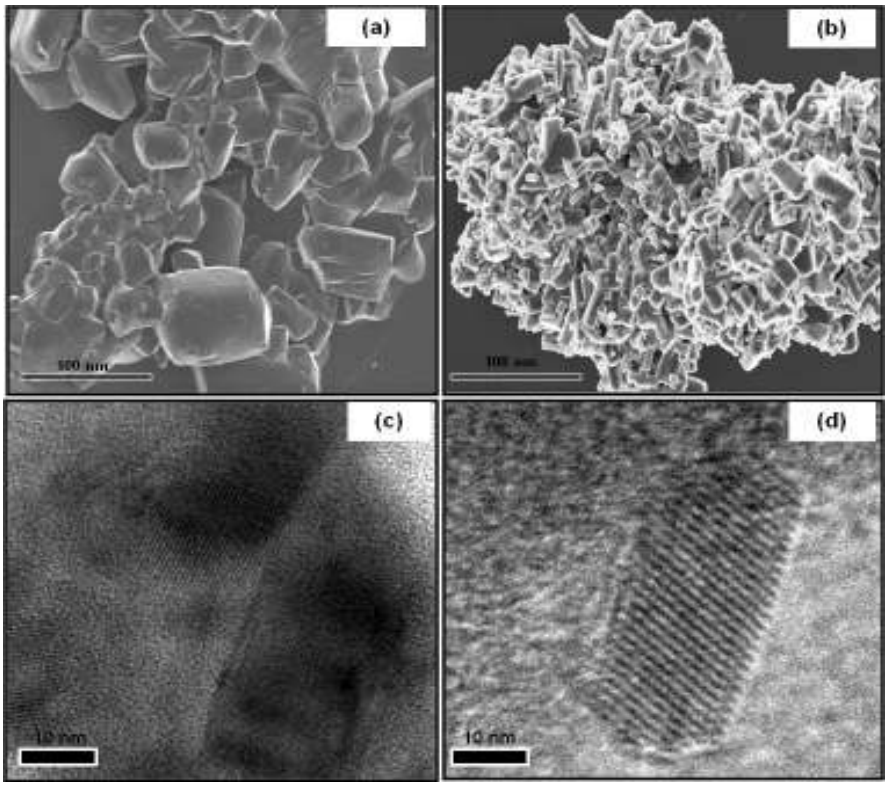

Fig. 2-12: SEM micrographs of (a) NiS, (b) Ni_3Se_4 and HRTEM micrographs of (c) NiS and (d) Ni_3Se_4.

The structural properties of nickel sulfide and selenide are shown in Fig. 2-12 and 2-13. The size and morphology of the nickel sulfide nanocrystals are depicted in Fig. 2-12(a) and (c). The SEM shown in 2-12(a) shows fused cylinderically-shaped nanoparticles with various sizes. The HRTEM shown in 2-12(c) shows two rod-shape crystals with the crystal fringes orientated in different directions. The morphology of nickel selenide nanoparticles is depicted in the micrographs in Fig. 2-12(b) and (d). The particles are rod-shape with the various sizes as shown in the SEM. The HRTEM image shows a single nano-rod with pointed edges that has crystal fringes with a (310) orientation in a monoclinic Ni_3Se_4 system.

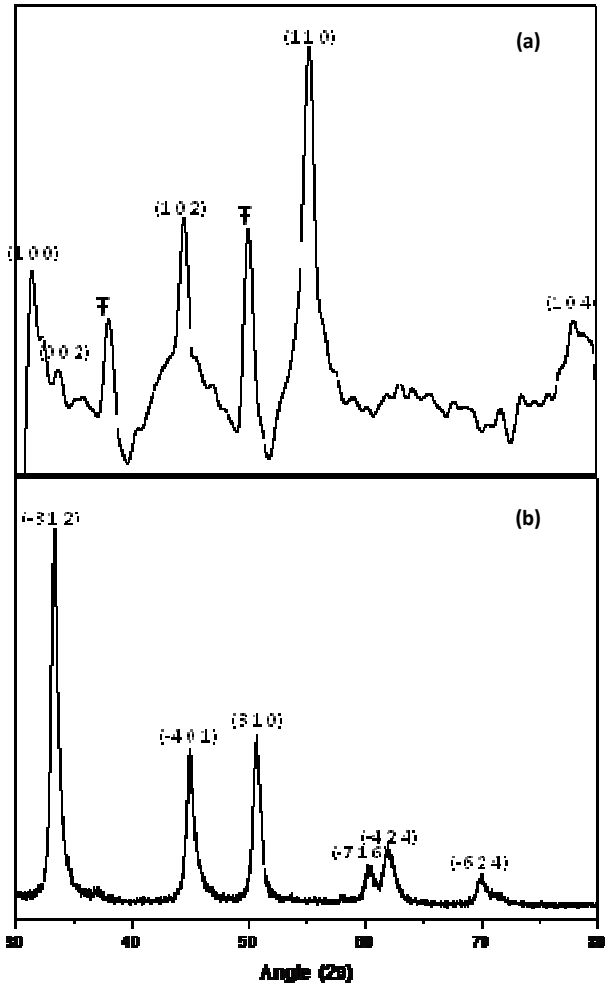

Fig. 2-13: X-ray diffraction patterns of (a) NiS and (b) Ni_3Se_4 (Ŧ denotes HDA).

The phase and the crystallinity of the particle were investigated using X-ray diffraction. The diffractogram of nickel sulfide in Fig 2-13(a) could be indexed to a hexagonal NiS (JCPDS card

no.: 75-0613) with the space group of P63mmc. The broadness of the diffraction peaks is an indication of the presence of small crystallites. The presence of HDA could also be detected. This is also seen in other sample suggests that excessive amounts of the capping agent were used during the synthesis of the metal sulfides. The nickel selenide nanoparticles were indexed as monoclinic Ni_3Se_4 (JCPDS card no.: 65-1220). The diffraction peaks are relatively sharp and broad signifying crystalline nanoparticles.

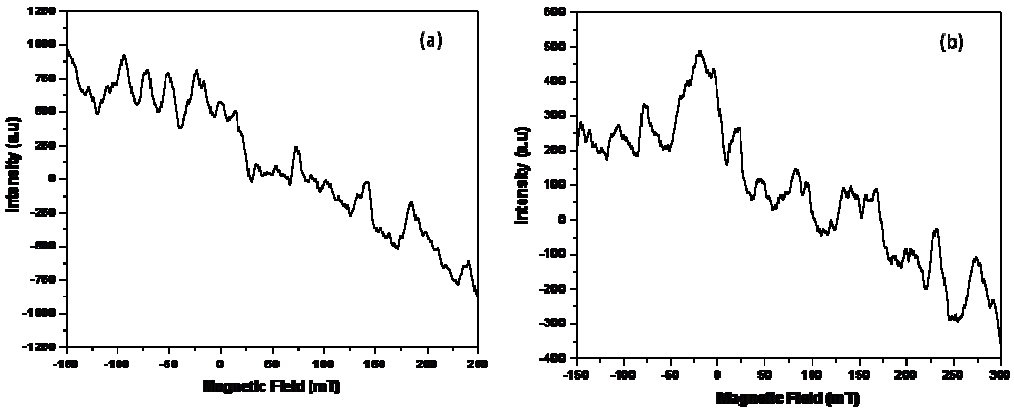

Fig. 2-14: ESR spectra of (a) NiS and (b) Ni_3Se_4 taken at 298 K.

The magnetic properties of nickel sulfide and selenide nanocrystals were probed using ESR spectroscopy. The ESR spectra in Fig. 2-14 show extensive hyperfine splitting of the resonance signal. In both spectra, asymmetrical peaks are observed and these stem from the hyperfine coupling effects. In this contrarily to what is observed for cobalt sulfide and selenide, these arise from dipolar interactions, instead of Fermi contact interactions. The dipolar interactions are highly influenced by the morphology of the nanocrystals, in a sense that the orientation of the nanocrystals in magnetic field becomes increasingly important. In anisotropic particles as seen for both nickel sulfide and selenide (Fig. 2-12), the interaction of the magnetic field is non-homogeneous and therefore gives rise to multi-lined signals.

2.5.4. Copper sulfide and copper selenide nanoparticles

The mineralogy of the Cu-S system is quite interesting. It has many known stable phases from chalcocite (Cu_2S) to sulfur rich covellite (CuS). Depending on the Cu-S ratio, the properties and the application of the material changes for instance, Cu_2S has been used as nanoscale switches whilst CuS has seen application in photocatalysis [60]. Besides its

outstanding optical and electrical properties, copper sulfide has promising function in biomedical fields, magneto-optical devices owing to its magnetic nature. The magnetic properties of copper sulfide arise from the unpaired valance electrons in the d-configuration of the Cu ions. Various methods have been reported for the synthesis of different stoichiometries of copper sulfide. Lu et al synthesized copper sulfide nanowires, nanotubes and nanovesicles by an amine-assisted hydrothermal process [61], whilst Haram and co-workers synthesized copper nanoparticles using Triton-X 100 via a microemulsion method [62].

Copper selenide have been studied extensively due to its interesting properties and application. It is a useful material in photovoltaic cells, in Schottky diodes and a good precursor for the preparation of CIDS (copper indium diselenide), material used for high efficient solar cells [63]. Like copper sulfide, it displays various composition and has been known have good electrical conductivity as well as magnetic properties. As it is usually employed in optoelectronics, it is often grown as thin films. Thin films are quantum wells, confined in one dimension only whereas nanocrystal can exhibit quantum confinement from three dimensions to one dimension depending on the morphology. This will therefore result in distinct properties between the two.

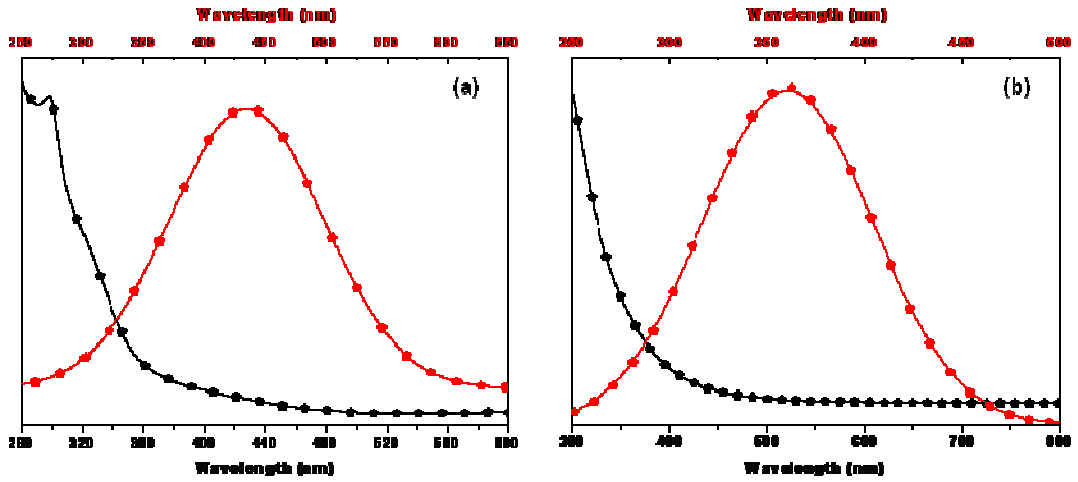

Fig. 2-15: Absorption and photoluminescence spectra (λexc = 250 nm) of (a) CuS and (b) CuSe.

The optical properties of copper sulfide and selenide are shown in Fig. 2-15. The optical properties of copper sulfide are rather fascinating; each stable phase displays its own characteristic properties for example, covellite CuS has a distinctive absorption peak in the near infra-red region at approximately 920 nm and this value decreases as the sulfur content increases from covellite to digenite ($Cu_{1.8}S$) to djurleite ($Cu_{1.96}S$) [64]. On the other hand chalcocite (Cu_2S) has been reported to have no apparent absorption [64].

These features are mainly reported for thin films which are much more similar to bulk materials compared to the nanocrystals. The graph in Fig. 2-15(a) shows an absorption spectrum of the as prepared copper sulfide nanocrystals. Compared to the bulk bang-gap of copper sulfide (1022 nm), the spectrum is blue-shifted and the absorption band-edge is approximately 320 nm. The large blue-shift would first suggest that the particles are very small and will therefore experience stronger confinement and secondly from [65] it would appear that the phase of the crystals would be that of the more sulfur rich composition. The photoluminescence spectrum is red-shifted from the absorption band-edge and has an emission maximum wavelength at 440 nm. This Stoke shift behaviour is typical of nanocrystals and stems from the conventional fluorescence process.

Fig. 2-15(b) illustrates the optical properties of copper selenide. The absorption spectrum is typical of copper chalcogenide nano-semiconductors, with the absence of the excitonic peak. Nevertheless the band-edge can be extrapolated by a tangent through the midpoint of the turning point of the curve. The absence of the excitonic could also be as a result of the formation of bigger particles or perhaps amorphous material. Nonetheless, the absorption band-edge is blue-shifted (350 nm) from the bulk copper selenide (887 nm). The photoluminescence spectrum shows a near band-edge emission peak at 365 nm. This near band-edge arise from the surface defects in the nanocrystal that are electron and hole traps that alter the fluorescence properties resulting in near band-edge emission with reduced lifetimes [66,67]. The presence of surface defects is encouraged by the lack of a capping molecule around the nanocrystal. The capping agent such as HDA passivates the surface of the nanocrystal by bonding using the electron rich entity to the active sites on the nanocrystals. This then limits the formation of trap and overall defects in the nanocrystal.

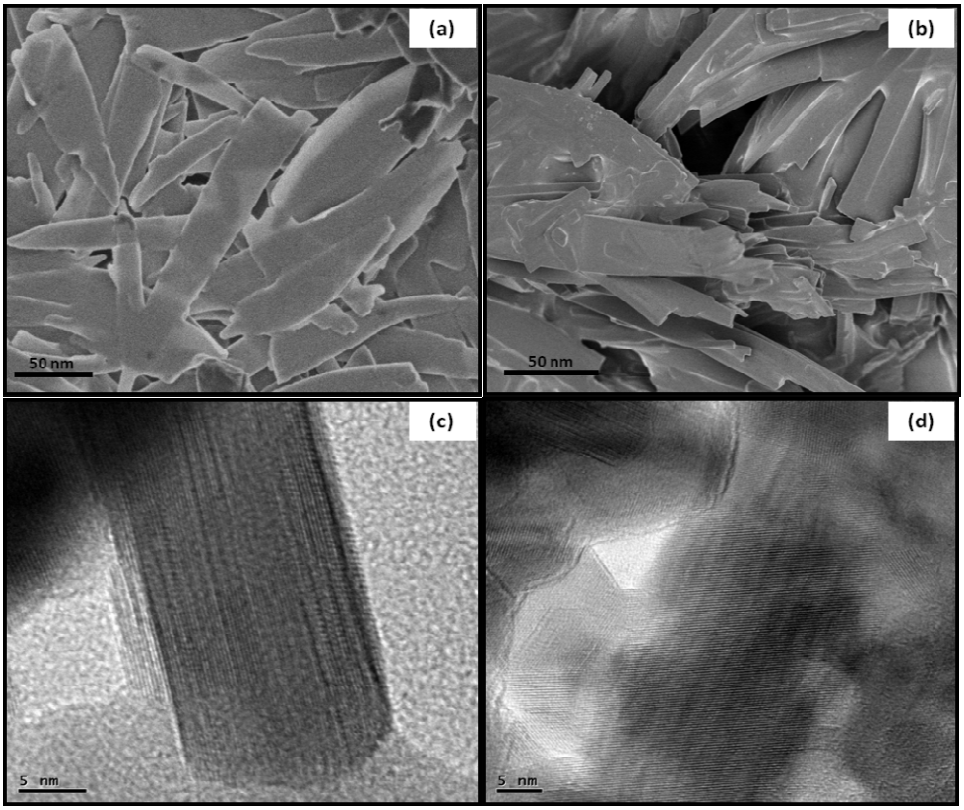

Fig. 2-16: SEM micrographs of (a) CuS, (b) CuSe and HRTEM micrographs of (c) CuS and (d) CuSe.

The structure of the nanocrystals and possible deformations were investigated using SEM and HRTEM as shown in Fig. 2-16. The morphology of copper sulfide as depicted in Fig. 2-16(a) shows the formation of various sized nanosheets. The HRTEM of a single nanosheet in Fig. 2-16(c) shows the crystal fringes signifying good crystallinity. On the other hand, the morphology of the copper selenide shows similar structures with that of copper sulfide with exception that the structures are less defined. Nevertheless, the structures show sharp edges indicative of some ordering and they appear to be agglomerated nanosheets. The HRTEM in 2-16(d) confirms the formation of belts and also shows some degree of agglomeration. The agglomeration could be as a result of the lack of the capping agent. The capping agent usually has long alkyl chains that electro-statically keeps the particles apart, when absent, the nanoparticles tend to clump together to form bigger, energetically favoured particles.

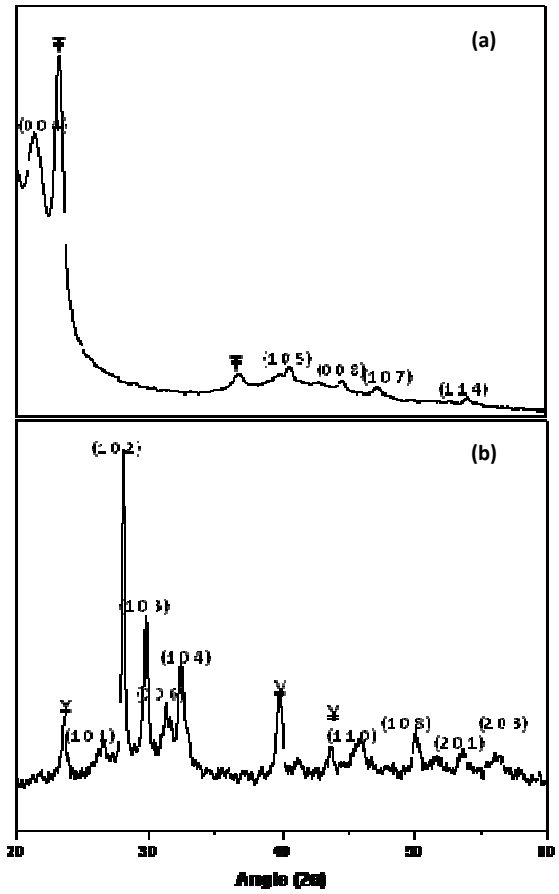

Fig. 2-17: X-ray diffraction patterns of (a) CuS and (b) CuSe (₸ denotes HDA, ¥ denotes elemental Se).

The phase and crystallinity of the copper sulfide and selenide were determined by powder x-ray diffraction as shown in Fig. 2-17. The diffractogram was indexed to a hexagonal CuS (covellite) (JCPDS card no.: 65-3929) and traces of HDA were also detected. The detected copper sulfide to some extent contradicts with the observed optical properties according to reference [64]. As mentioned before, the reported absorption peak was for thin films where the size quantization effects do not necessarily feature. The phase composition of copper selenide was determined in 2-17(b), the diffractogram was indexed to a hexagonal CuSe (JCPDS card no.: 70-8577). The presence of unreacted Se was also detected. The observed diffraction peaks were relatively sharp with some degree of broadening typical of nanocrystals. The similar compositions observed for both copper sulfide and selenide concurs with the observed morphologies.

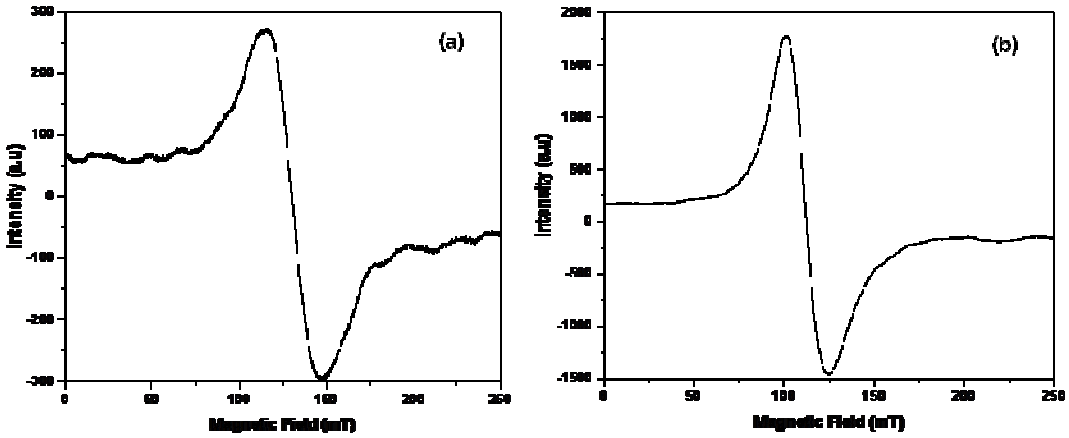

Fig. 2-18: ESR spectra of (a) CuS and (b) CuSe taken at 298 K.

The ESR spectrum of copper sulfide is shown in Fig. 2-18(a). A single symmetrical resonance peak is detected at approximately 125 mT with the line width of 75 mT. The g factor was determined to be 2.0073. The magnetic properties of CuSe (Fig. 2-18(b)) are very similar with the copper sulfide nanocrystals, with a single symmetrical peak also detected at 100 mT. The similarities are not surprising as they concur with the other results.

Table 2-1: Summary of the optical and morphological properties of the nanocrystals.

Particles	Abs. λ (nm)	PL λ (nm)	Phase	Morphology
MnS	371	488	cubic β-MnS	Wire-like (aspect ratio = 4.96
MnSe	389	407	Cubic MnSe	Rods (aspect ratio = 6.27)
Co_3S_4	378	446	Monoclinic Co_3S_4	Spheres (μ = 2.13)
Co_3Se_4	264	330	Monoclinic Co_3Se_4	Spheres (μ = 1.96)
NiS	330	421	Hexagonal NiS	Fused cylindrical nanoparticles (polydispersed)
Ni_3Se_4	310	367	Monoclinic Ni_3Se_4	Rods (polydispersed)
CuS	320	440	Hexagonal CuS	(polydispersed)
CuSe	350	365	Hexagonal CuSe	(polydispersed)

2.6. Conclusions

The metal sulfide nanoparticles were synthesized successfully with the single source precursor method. The presence of excess HDA had no adverse influences on the properties

of the nanocrystals. The optical properties of all the metal sulfides showed astonishing results, with very large blue-shifts in band gap observed. These large blue-shifts were associated with various factors such as the size, shape and phase of nanocrystals as well as the nature of the reactants (synthetic method). Often these factors are studied independently and combined effects are rarely understood. The structural characterization gave insight into the complexity of the metal sulfide due to a variety of stoichiometric compositions. Unique morphologies were observed, from MnS nanowires to spherical Co_3S_4 to rod-shaped NiS and CuS nanobelts. The observed magnetic properties at room temperature render these nanocrystals potential candidates for biomedical applications. Further surface modification of these materials using bio-compactable ligands would ensure realization of real biomedical applications. The metal selenides were synthesized successfully using the as reported method. The intrusion of the unreacted selenium could not be fully ascertained. The optical properties of the selenides were less startling compared to the sulfides. The absorption band-edges were blue-shifted from the reported bulk values, a typical behaviour of semiconductor nanocrystals. The morphologies and structures of the metal nanocrystals were similar to their corresponding sulfides. The particles also showed some level of agglomeration thought to be brought by the lack of use of the capping agent. The magnetic properties were size and shape dependent and room temperature electron spin resonance was achievable. In order for these nanomaterials to be useful in biomedical applications, further modification of the surface should be done such as the addition of ligands that would render the nanoparticles water soluble, addition of bio-molecules that would act as targets and be compactable with the biological system.

2.7. References

[1] LaVan D.A.,Nat. Rev. Drug Discov. 2002, 1(1), 77.

[2] Chan W.C., Curr. Opin.Biotechnol.2002, 13(1), 40.

[3] Niemeyer C M., Angew. Chem. Int. Ed. 2000, 40(22), 4128.

[4] Mitchell G.P., J. Am. Chem. Soc. 1999, 121(35), 8122.

[5] Bangs L.B., Pure Appl. Chem. 1996,68, 1873.

[6] Joubert J.C., Anales de Quimica Int Ed. 1997, 93, S70.

[7] Batlle X. ; Labarta A., J. Phys. D: Apply. Phys. 2002,35, R15.

[8] Frenkel J.; Dorfman J., Nature 1930,126, 27.

[9] Bean C.P.; Livingston J.D., J. Appl. Phys. 1959,30, 1205.

[10] Freeman M.W.; Arrot A.; Watson H.H.L., J. Appl. Phys. 1960, 31, 404.

[11] Joubert J.C., An. Quim. Int. Ed. 1997, 93, S71.

[12] Goodwin S.; Peterson C.; Hoh C.; Bittner C. J. Magn. Magn. Mater. 1999, 194, 132.

[13] Ayant Y.; Belorizky E.; Alizon J.; Gallice J., J. Phys. A 1975, 36, 991.

[14] Freed J.H., J. Chem. Phys. 1978, 68, 4034.

[15] Morales M.P.; Bomati-Miguel O.; P´erez de Alejo R.; Ruiz-Cabello J.; Veintemillas-Verdaguer S.; O'Grady K., J. Magn. Magn. Mater. at press, 2003.

[16] Kim D.K.; Zhang Y.; Kher J.; Klason T.; Bjelke B., Muhammed M, J. Magn. Mater. 2001, 225, 256.

[17] Roberts P.L.; Chuang N.; Roberts H.C. Eur. J. Rad. 2000, 34, 166.

[18] Hogemann D.; Josephson L.; Weissleder R.; Basilion J.P. Bioconjugate Chem. 2000, 11, 941.

[19] Josephson L.; Tung C.H.; Moore A., Weissleder R., Bioconjugate Chem. 1999, 10 186

[20] Lewin M.; Carlesso N.l.; Tung C.H.; Tung X.W.; Cory D.; Scadden D.T.; Weissleder R., Nat. Biotechnol. 2000, 18, 410.

[21] Safarikova M.; Safarik I., 1999 J. Magn. Magn. Mater. 2000, 194, 108.

[22] Weitschies W.; Kotitz R.; Bunte T.; Trahms L., Pharm. Pharmacol. Lett. 1997,7, 5.

[23] Rheinander T.; Kotitz R.; Weitschies W.; Semmler W., J. Magn. Magn. Mater. 2000, 219, 219.

[24] N´eel L., Ann. Geophys. 1949, 5, 99.

[25] Suit H., Int. J. Rad. Onc. Biol. Phys. 2002, 53, 798.

[26] Dailey J.P.; Phillips J.P.; Li C.; Riffle J.S., J. Magn. Magn. Mater. 1999, 194, 140.

[27] Moloto N.; Revaprasadu N.; Moloto M.J.; O'Brien P.; Helliwell M., Polyhedron 2007, 26,3947.

[28] Moloto M.J.; Revaprasadu N.; O'Brien P.; Malik M.A., J. of Mater. Sci.: Mat. In Electr. 2004, 15, 313.

[29] Moloto M.J.; Revaprasadu N.; Kolawole G.A.; O'Brien P.; Malik M.A., S. Afr. J. Sci. 2005, 101, 463.

[30] Moloto N.; Ray S.S.; Moloto M.J.; Journal of Nanoscience and Nanotechnology, 2008, 12(8), 6187.

[31] Nair P.S.; Chili M.M; Radhakrishnan T.; Revaprasadu N.; Christian P.; O'Brien P.,S. Afr. J. Sci. 2005, 101, 466.

[32] Li Y.; Li X.; Yang C.; Li Y., J. Chem. Mater. 2003, 13, 246.

[33] Okajima M.; Ohda T.T., J. Cryst. Growth 1992, 117, 810.

[34] Goede O.; Hermbrodt W.; Einhold V.W., Phys. Status Solidi B 1987, 143, 511.

[35] Kennedy S.W.; Harris K.; Summerville E., J. Solid State Chem. 1980, 31, 355.

[36] Zhang N.; Yi R.; Wang Z.; Shi R.; Wang H.; Qiu G.; Liu X., Mater. Chem.And Phys. 2008, 11, 1.

[37] Wang S.; Li K.; Zhai R.; Wang H.; Hou Y.; Yan H., Mater. Chem.And Phys. 2005, 91, 2.

[38] Lokhande C.D.; Ennaoui A.; Patil P.S.; Giersis M.; Muller M.; Diesner K.; Tributsch H., Thin Solid Films 1998, 330,2.

[39] Jandova J.; Lisa K.; Vu H.; Vranka F., Hydrometallurgy 2005, 77, 1.

[40] Jiang Y.; Meng X.M.; Yiu W.C.; Liu J.; Ding J.X.; Lee C.S.; Lee S.T., J. Phys. Chem. 2004, B 108, 2784.

[41] Li Q.; Brown M.A.; Hemminger J.C.; Penner R.M., Chem. Mater. 2006, 18, 3432.

[42] Jun Y.; Choi J.; Cheon J., Angew. Chem. Int. Ed. 2006, 45, 3414.

[43] Chen Y.; Ding J.; Guo Y.; Kong L.; Li H., Mater. Chem. Phys. 2002, 77, 734.

[44] Moloto N.; Revaprasasu N.; Musetha P.L.; Moloto M.J., J. Nanoscie. And Nanotechnol. 2009, 9(8), 4760.

[45] Zhang J.; Yang X.; Wang D., Adv. Mater. 2000, 12, 1348.

[46] Counio G.; Esnouf S.; Gacoin T.; Boilot J.-P., J. Phys. Chem. 1996, 100(51), 20021.

[47] Nakamura T.; Takeuchi Y.; Mugautu H.; Fujiyasu H.; Nakanishu Y., Appl. Surf. Sci. 1991, 48-49, 478.

[48] Ueda H.; Yonemura M.; Sekine T., Phys. Rev. B 1987, 4602.

[49] Peng X. Adv. Mater. 2003, 15, 459.

[50] Chen X.; Zhang Z.; Qui Z.; Shi C.; Li X., J. of Coll. and Interface Sci. 2007, 308, 271.

[51] Srouji F.; Afzaal M.; Waters J.; O'Brien P., Chem. Vap. Deposition 2005,11,2.

[52] Nath M.; Rao C.N.R., Angew. Chem. 2002, 114, 3601.

[53] Qiao Z.P.; Xie G.; Tao J.; Nie Z.Y.; Lin Y.Z.; Chen X.M., J. Solid State Chem. 2002, 166, 49.

[54] Barrelet C.J., Wu Y.; Bell D.C.; Lieber C.M., J. Am. Chem. Soc. 2003, 125, 11498.

[55] Ghezelbash A.; Sigman M.B.; Korgel B.A., Nano Lett. 2004, 4, 537.

[56] Fan H.J.; Knez M.; Scholz R.; Nielsch K.; Pippel E.; Hesse D.; Zacharias M.; Gösele U., Nature Mater. 2006, 5, 627.

[57] Li Y.; Wang Z.; Ma X.D.; Qian X.F.; Yin J.; Zhu Z.K., J. Solid State Chem. 2004, 177, 4386.

[58] Hagfeldt A.; Gratzel M., Chem. Rev. 1995, 95, 49.

[59] Tatsuya O.; Satoru O.; J. Non-Cryst. Solids 1999, 250, 344.

[60] Wang W.Z.; Geng Y.; Yan P.; Liu F.Y.; Xie Y.; Qian Y.T., J. Am. Chem. Soc. 1999, 121, 4602.

[61] Noue I.; Yasuoka H., Solid State Commun.1979, 30, 341.

[62] Lau Q.; Gao F.; Zhao D., Nano Letters 2002, 2(7), 725.

[63] Noue I.; Yasuoka H.; Ogawa S., J. Phys. Soc. Jpn. 1980, 48, 23.

[64] Haram S.K.; Mahadeshwar A.R.; Dixit S.G., J. Phys. Chem. 1996, 100, 5868.

[65] Wang W.Z.; Geng Y.; Yan P.; Liu F.Y.; Xie Y.; Qian, Y. T., J. Am. Chem. Soc. 1999, 121, 4062.

[66] Shen G.; Chen D.; Tang K; Liu X.; Huang L.; Qian Y., J. Solid State Chem. 2003, 173, 232.

[67] Silvester E. J.; Grieser F.; Sexton B. A.; Healy T.W., Langmuir 1991, 7, 2917.

CHAPTER 3: TIME AND TEMPERATURE DEPENDENCY OF COBALT SULFIDE NANOCRYSTALS: A STABILITY STUDY

3.1. Introduction

Since Gleiter first synthesized nano-structured materials, much interest has been shown on methods to fabricate nanomaterials [1]. Scientists have since developed many synthetic strategies that seek to control the properties and morphology of these materials. An astonishing range of physical and chemical properties of these materials are influenced by their crystallite size and morphology. Approaches frequently utilized in the synthesis of nanomaterials include the sol-gel method, use of microwaves, colloidal procedures, template assisted synthesis and solvothermal methods [2-6].

Fabrication of 3d transition metal chalcogenides has sparked tremendous interest due to their potential use in electronics, optoelectronic devices, and memory devices as well as in solar cell technology [7]. In this study, we report on the synthesis and characterization of nano-sized cobalt sulfide particles. Cobalt sulfide exists in various phases that include Co_4S_3, CoS, Co_3S_4, CoS_2, Co_9S_8, $CoS_{1.97}$, $Co_{1-x}S$, $CoS_{1.035}$, and β'-$CoS_{1.097}$ [8,9]. Because cobalt sulfide can exist in these multiple phases, the synthesis of single phase nanocrystallites poses some serious synthetic challenges. Factors such as concentration, temperature, pH, capping agents as well as the reaction time are critical parameters that influence the size, the morphology and the phase of the synthesized nanoparticles [33].

The stability of nano-structured materials is the key that will ultimately determine their applications. Cobalt sulfide semiconductor nanoparticles have been shown to have good stability over long periods of time under normal room temperature conditions [10-15]. However, it is also of interest to monitor the changes of either the optical or physical properties of the nanoparticles under extreme conditions. Recent work has revealed that electron beam irradiation of nanomaterials can modify an assembly of nanoparticles [16]. It was found that exposing a thin film of alkanethiol passivated gold nanoparticles to an electron beam with energy of 9 KeV resulted in the formation of a carbonaceous network in which gold cores were distributed [17]. Banhart also reported the transformation of

graphitic onions to diamond under electron irradiation in a TEM [18]. Li *et al.* together with Banhart reported the manipulation of hot carbon nanotubes to various structures using a focused electron beam [19]. The main objective of this chapter is to report on the synthesis and characterization of nano-sized cobalt sulfide using the single-source precursor method and to investigate the impact of reaction time on the optical and morphological properties of the synthesized nanoparticles. The stability of the nanocrystals under high energy conditions is also investigated, thus prompting the study of the influence of the synthetic temperature on the properties of the nanoparticles.

3.2. Experimental

3.2.1. Materials

Toluene and methanol were obtained from BDH. Toluene was stored over molecular sieves (40 Å, BDH) before use. HDA (hexadecylamine), TOP (tri-n-octylphosphine), cobalt chloride hexahydrate and tetramethylthiuram disulphide were obtained from Aldrich, and used as received.

3.2.2. Synthesis of the precursor

A hot solution of tetramethylthiuram disulfide (4.16 mmol) in methanol (20 ml) was added into a heated solution of cobalt chloride (2.08 mmol) in methanol (15 ml). The mixture was stirred and refluxed for 1 h. The precipitate was filtered, washed twice with methanol and dried under vacuum. $CoCl_2(SC(N(CH_3)_2)SS(N(CH_3)_2)CS)$: Yield 80.2 %; m. p. 363°C. Anal.Calcd. C, 19.49; H, 3.03; N, 7.58. Found: C, 19.46; H 3.27; N 7.57. IR/cm^{-1}: 1387 (s), 1254 (s), 1245 (s), 1124 (s), 1044 (s), 1022 (s), 978 (s), 893 (m), 780 (w), 673 (m), 576 (s), 439 (s).

3.2.3. Synthesis of cobalt sulfide nanocrystals

3.2.3.1. The reaction time study

In a typical experiment, a known weight (1.0 g) of the cobalt precursor was dissolved in a known volume of TOP (10 ml). This solution was then injected into 3.125 g of hot HDA at 160°C and a decrease in temperature of 20 – 30°C was observed. The solution was allowed to stabilize at 160°C and aliquots of the reaction mixture were collected after different intervals of time (5, 15, 30, 45, and 60 min). The aliquots were then allowed to cool to about 70°C, and methanol was added to dissolve any organic by-products such as TOP and excess

HDA. A flocculent precipitate formed and the solid product was separated by centrifugation and re-dispersed in toluene. Toluene was removed by evaporation under reduced pressure to give HDA capped cobalt sulfide nanoparticles. The particles were washed three times with methanol and were dried at room temperature to form powders.

3.2.3.2. Annealing of the nanoparticles

About 0.5 g of the nanoparticles synthesized after 5 min were placed in a crucible and annealed at 300 °C using a ramp rate of 5 °C/min for 3 h in a Lenton type furnace. Methanol was then added to the resultant paste, this resulted in powder flocculates that were separated through centrifugation. The resultant powder were further washed with methanol and dried at room temperature.

3.2.3.3. Temperature study

A known weight (1.0 g) of the cobalt sulfide precursor was dissolved in 10 ml of TOP. The TOP solution was then injected into 3.125 g of hot HDA. The temperature of the HDA was then varied (120 °C, 160 °C, 200 °C and 240 °C) and the reaction was maintained for 1 h. The reaction mixture was then allowed to cool to about 70°C, and methanol was added to dissolve any organic by-products such as TOP and excess HDA. A flocculent precipitate formed and the solid product was separated by centrifugation and redispersed in toluene. Toluene was removed by evaporation under reduced pressure to give HDA capped cobalt sulfide nanoparticles. The particles were washed three times with methanol and were dried at room temperature to form powders.

3.3. Characterization Techniques

A Perkin Elmer Lambda 75S UV-VIS-NIR Spectrophotometer was used to carry out the optical measurements. These were recorded on samples placed in silica cuvettes (1 cm path length), using toluene as a reference solvent. A Perkin Elmer LS55 with a xenon lamp (150 W) and a 152 P photomultiplier tube as a detector was used to measure the photoluminescence of the particles. The samples were placed in quartz cuvettes (1 cm path length) for spectral analysis. X-ray diffraction (XRD) patterns of powdered samples were measured on a PANalytical X'Pert PRO-diffractometer using Cu Kα radiation (wavelength, λ = 1.5406 Å) with variable slits at 45 kV/40 mA. Measurements were taken using a glancing

angle of incidence detector at an angle of 2°, for 2θ values in a range 20° – 60° in steps of 0.001° with a scan speed of 0.1°/s. Cobalt sulfide samples were characterized using a field-emission scanning electron microscopy (FE-SEM - Leo, Zeiss), operated at 3-10 kV electron potential difference and equipped with a semiconductor detector that allows for the detection of energy dispersive X-rays (EDX). The samples were prepared by placing a drop of suspended particles in toluene, onto a carbon tape. The samples were then allowed to dry at room temperature. The transmission electron microscopy (TEM) images were obtained using a Philips CM 200 compustage electron microscope whilst the high resolution (HRTEM) images were obtained on a Joel JEM-2100 microscope with a LAB6 filament, all operated at 200 kV. The samples were prepared by placing a drop of a dilute solution of sample in toluene on a copper grid (400 mesh, agar). The samples were allowed to dry completely at room temperature. The thermogravimetric analysis (TGA) was carried out on a TGA Q500 from TA Instruments under nitrogen gas with a flow-rate of 15 ml/min.

3.4. Results and Discussion

For the synthesis of cobalt sulfide nanoparticles, a molecular precursor has been used as a starting material. This method offers many advantages over known literature methods. Undoubtedly, the presence of all the elements in the final product within a single-molecule provides some of the advantages [20-23]. The single source molecular precursor method also offers distinct advantages of mild experimental conditions (typical working temperatures, generally between 100 to 300°C), simplified fabrication procedures and experimental set-up [24-29]. Another motivation for the use of this method may be found in the observation of unusual crystal growth selectivity or metastable phase formation of the resultant products, which are sometimes unattainable via the conventional synthetic routes [30-32].

Tetramethylthiuram disulfide (Thiram) as a ligand has been used extensively in the biomedical field [34]. Thiram derivatives have also been employed as an accelerator to speed up vulcanization [35]. Thiram has also been used as a fungicide to protect seeds, fruits, vegetables, ornaments and turf crops from fungal infection [36]. Coordination of thiram with metals such as silver, zirconium and dysprosium has been reported before [37]. Thiram is very cheap, stable and an excellent source of sulfur. However, not much work on

the use of thiram metal complexes as precursors for nanoparticle synthesis has been reported. Nevertheless, Moloto *et al* successfully prepared anisotropic CdS nanoparticles from the cadmium complex [24].

Simple sulfur containing ligands, such as thiourea, thiosemicarbazides, thiols, thioacetimides, and their derivatives have been used extensively to make chalcogenide nanoparticles such as CdS. In this study, the synthesis of cobalt (II) with thiram was undertaken [38-40].Tetramethylthiuram disulphide is a ligand that consists of four atoms of sulfur and as cobalt (II) metal ions have a high affinity for sulfur, this therefore promotes the formation of the Co-S bonds. The chelating ability of the ligand also enhances the binding of the metal through sulfur (Scheme 3-1). Verification and confirmation of the formation of the coordination complex was done using elemental analysis and FTIR spectroscopy. After formation, the complex was decomposed in a controlled manner in a high boiling solvent (HDA) to yield the desired cobalt sulfide nanoparticles.

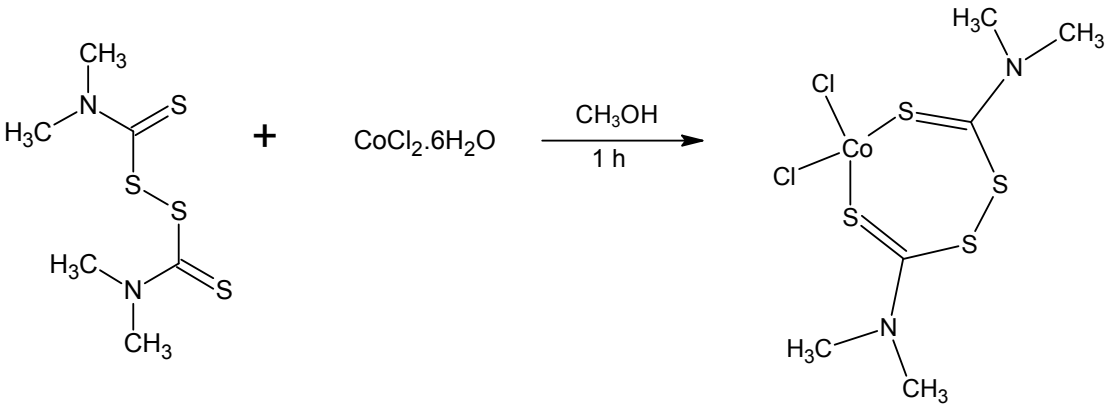

Scheme 3-1: Formation of cobalt chloride tetramethylthiuram disulphide complex.

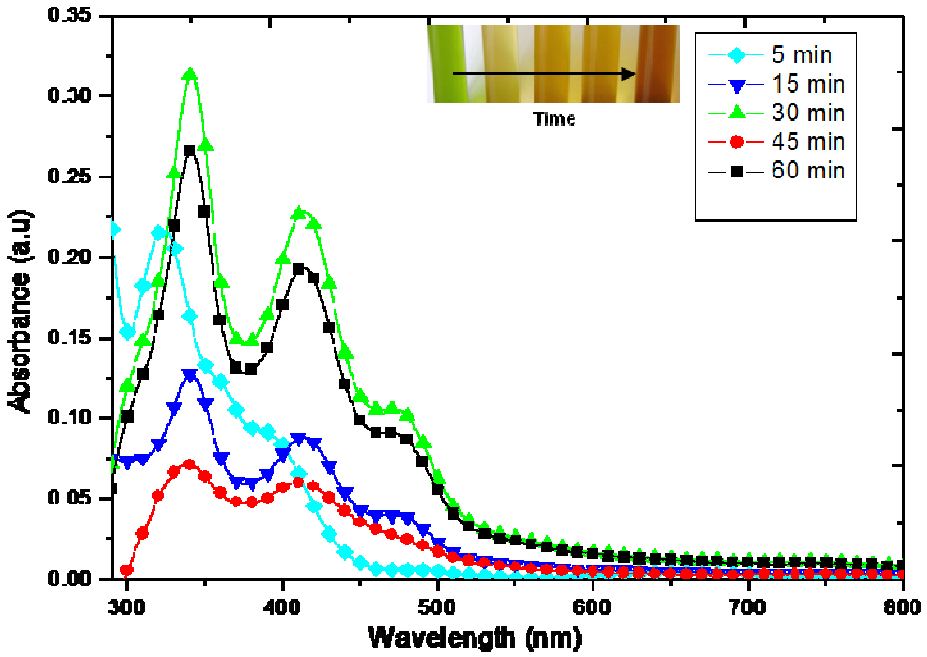

Fig. 3-1: Absorption spectra of cobalt sulfide nanoparticles collected from tetramethylthiuram disulfide at 160 °C in HDA for various times (5 min, 15 min, 30 min, 45 min and 60 min). Inset: colour of the particles dispersed in toluene ranges from green (5 minutes) to dark brown (60 min).

Cobalt sulfide is a VIII-VI semiconductor with bulk band gap energy of 0.9 eV (1378 nm) [30].Fig. 3-1 shows the absorption spectra of the cobalt sulfide after varying the synthesis reaction times viz. 5, 15, 30, 45, and 60 min. The colour of the particles dispersed in toluene ranges from green (5 min) to dark brown (60 min) (inset of Fig. 3-1). The observed three consecutive peaks in the absorption spectra are as a result of quantization. The bulk cobalt sulfide comprises of a continuous valence and conduction band that result in a fixed energy band gap that is characterized by a single absorption peak. As the cobalt sulfide becomes quantized, discrete atomic-like states with energies that are determined by the properties of the nanoparticles arise. The observed three peaks in the absorption spectra of the cobalt sulfide nanoparticles (Fig. 3-1) result from transitions of the 1S, 1P and 1D orbital, with the first excitonic peak categorized as the band-gap of that material.

The onset absorption for the particles prepared after 5 min is 320 nm, a blue-shift from the bulk band-edge. As the reaction time is extended to 15 min, the first exciton peak is shifted to 338 nm. This is further observed at 339 nm, 340 nm and 340 nm for 30, 45, and 60 min, respectively. This behaviour is attributed to the Ostwald ripening effect [41]. Extension of time leads to thermodynamic control of the reaction and therefore results in the growth of the particles. This is due to the fact that molecules at the surface are less stable than the ones that are already ordered in the interior. Larger particles with their lower surface to volume ratio, results in a lower energy state and as a consequence will always be preferred. Particle growth therefore accounts for the slight red-shift in band-edges with prolonged reaction times.

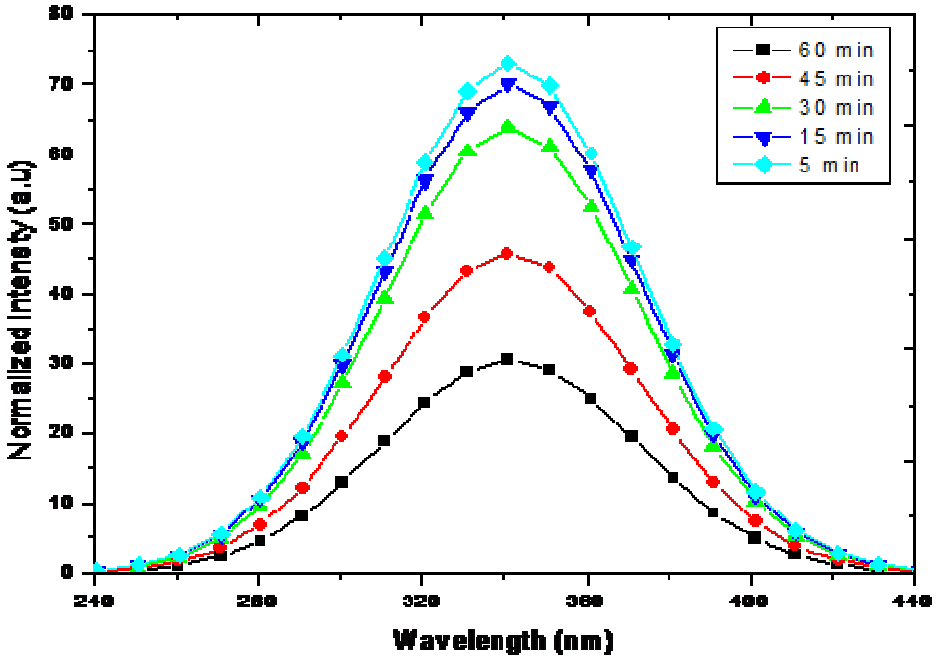

Fig. 3-2: Photoluminescence spectra of cobalt sulfide nanoparticles collected from tetramethylthiuram disulphide at 160°C in HDA for various times (5 min, 15 min, 30 min, 45 min and 60 min).

The photoluminescence properties of cobalt sulfide nanoparticles are shown in Fig 3-2. All the particles were excited with an energy wavelength of 250 nm. Upon excitation with energy larger or equivalent to the absorption onset, an electron from the valence band of

the semiconductor has the ability to be promoted to the conduction band andas a result of relaxation, energy of a wavelength longer than the absorption band-edge will be emitted. All the particles showed a single emission wavelength of 341 nm that was attributed to near band-edge emission. The particles showed a decrease in intensity as the reaction time was prolonged. The decrease in intensity can be related to a decrease in the quantum yield through equation (1).

$$\Phi = \Phi_R \left[\frac{IntA_R \eta^2}{IntA\, \eta_R^{\,2}} \right] \qquad (1)$$

where *Φ* =quantum yield*; Int* = intensity*; A* = area under the curve*; η = Refractive index ; R* = reference.

Quantum yield is a measure of the efficiency of the fluorescence process. In nanomaterials an efficient fluorescence process is a consequence of quantum confinement. Therefore, a change in quantum yield can be used as an indirect estimation of the size or morphology of the nanoparticles. Smaller and spherical particles will possess a higher quantum yield value than bigger or 1-D-structured nanoparticles. The particles are thus becoming bigger with time as noted by the decrease in emission intensities, which concurs with the observation of the red-shift of the absorption spectra.

The structural properties of the cobalt sulfide particles were characterized using powder X-ray diffraction. Parts (a) and (b) of Fig. 3-3, respectively, show the XRD patterns of nanoparticles collected after 5 min and 60 min from the reaction mixture. Both the samples were indexed to a rather less abundant β'-$CoS_{1.097}$ phase under the hexagonal system (JCPDS Card: 19-0366) in the presence of HDA (JCPDS Card: 42-1782). The diffractograms showed some crystallinity with the evidence of peak broadening, suggesting the formation of small crystallites. The size of the crystallites was determined by the Debye-Scherrer equation using an average of three prominent peaks [42]. The particles collected after 5 min showed an average crystallite size of 9.9 nm whilst the particles collected after 60 min showed an average crystallite size of 17.1 nm. This formation of bigger crystallites with time concurs with the red-shift observed in the optical measurements.

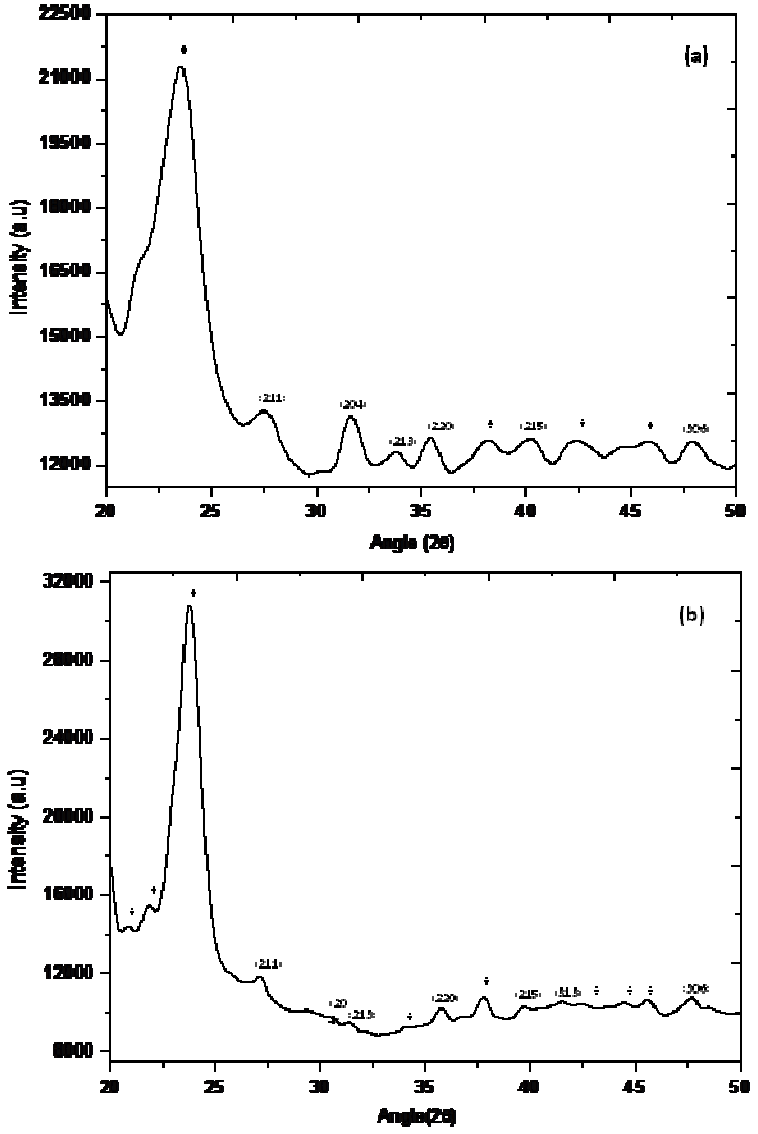

Fig. 3-3: XRD patterns of cobalt sulfide nanoparticles collected from the reaction mixture after: (a) 5 min and (b) 60 min († denote HDA peaks)

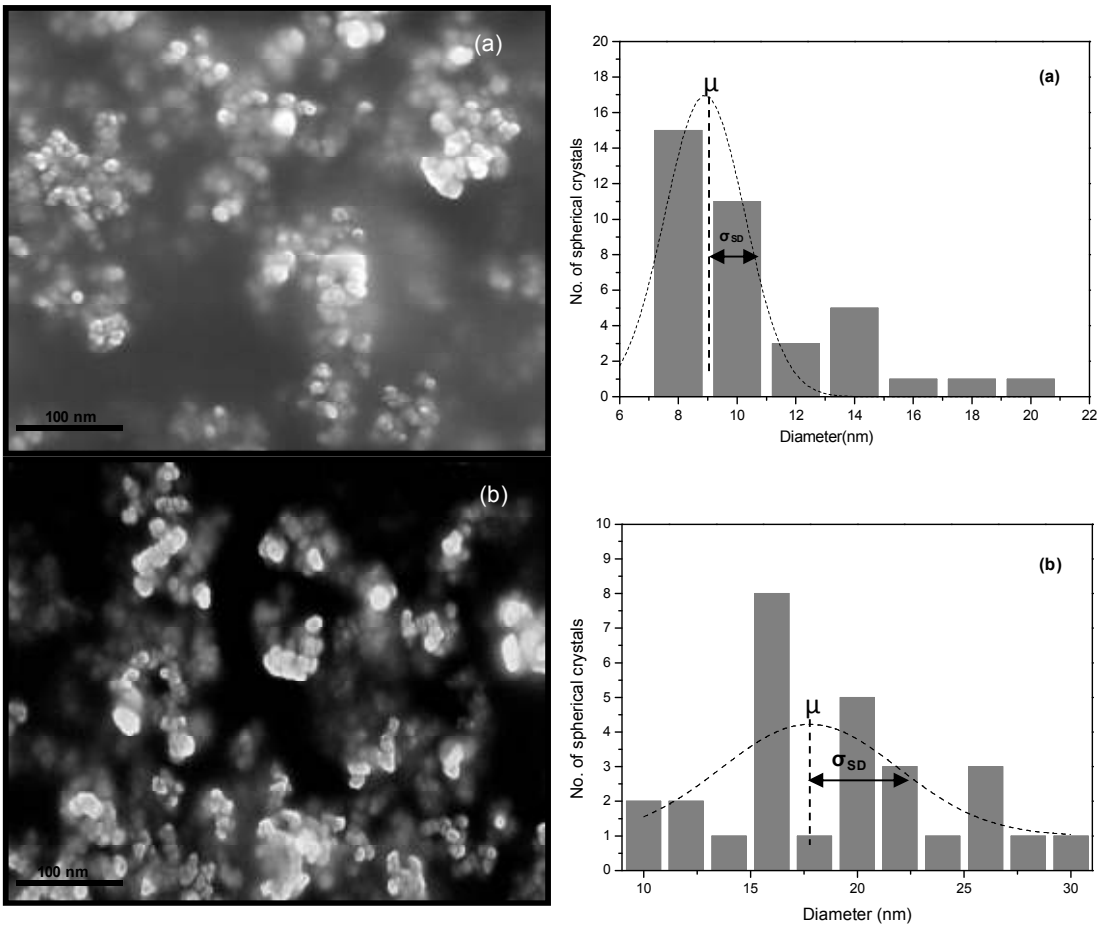

Fig. 3-4: FESEM images (at 5 kV) and size distribution histograms of cobalt sulfide nanoparticles collected from the reaction mixture after: (a) 5 min: μ = 9 ± 1 nm and (b) 60 min: μ = 17 ± 2 nm.

The shape and the size of the particles were investigated and determined by SEM, TEM and HRTEM analyses. Fig. 3-4 (a) and (b), respectively, shows the SEM images of nanoparticles collected after 5 and after 60 min from the reaction mixture. A noticeable increase in size was observed after prolonged reaction time, due to the Ostwald ripening effect. Again this is in agreement with the optical property observations. The particles formed after 5 min had an average size of 9 ± 1 nm whilst those collected after 60 min had an average size of 17 ± 2 nm.

The increment in size increase was consistent with the red-shift observed in the absorption spectra and the estimations of crystallites size obtained from the XRD measurements. To gain more insight into the morphology of the synthesized cobalt sulfide nanoparticles, TEM studies were conducted. TEM images are presented in Fig. 3-5. TEM images of the particles formed after 5 min showed an aggregation of spherical particles as well as wire-like particles with an aspect ratio of approximately 15 ± 4. This was further observed for particles grown after 60 min of the reaction (aspect ratio 16 ± 1). The diameters of the particles observed by TEM were comparable to those observed by SEM and estimated from XRD; however, it is very interesting to note that the shapes of the particles are different.

The observed difference in shapes of the particles is suggested to be related to the applied accelerating voltage used during SEM and TEM measurements. SEM studies were conducted with an accelerated voltage of 5 kV, while for TEM studies the accelerated voltage was 200 kV. As a result of the very high energy used during TEM measurements, anisotropic growth of $CoS_{1.097}$ nanoparticles is promoted and the pre-existing spherical particles eventually act as nucleating agents for the initial growth. The growth eventually starts from the surface of the spherical particles along the direction of one plane.

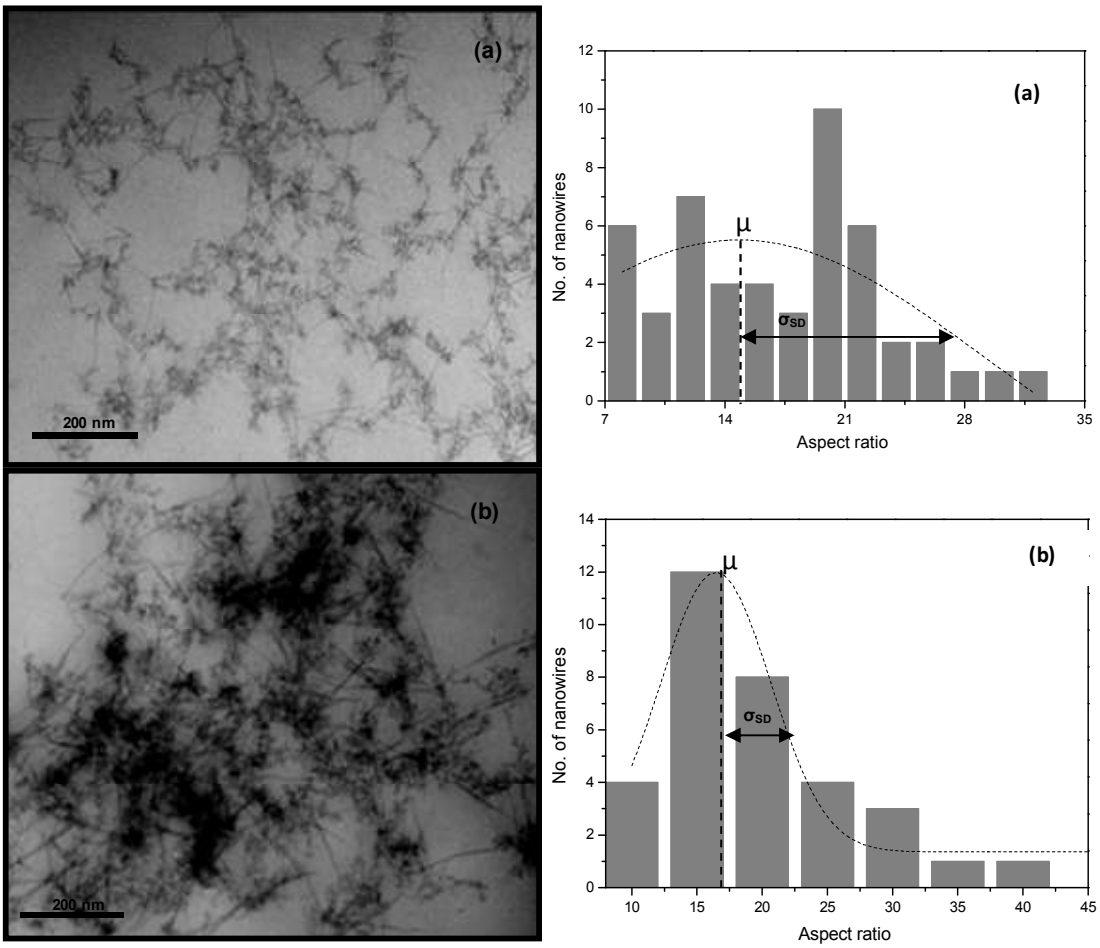

Fig. 3-5: TEM images (at 200 kV) and the size distribution of cobalt sulfide nanoparticles collected from the reaction mixture after: (a) 5 min: μ = 15 ± 4 aspect ratio and (b) 60 min: μ = 16 ± 1 aspect ratio.

Furthermore, HRTEM images were collected to ultimately resolve the shape of the nanoparticles. Initially the HRTEM images showed spherical nanoparticles but as the beam was concentrated on a single particle, an outgrowth from the sphere was observed. Fig. 3-6 shows repetitive shots of a $CoS_{1.097}$ nanoparticle under an electron beam of 200 kV. Fig. 3-6(a) shows the deformation and elongation of the spherical particle. The presence of the lattice fringes confirms the growth as that of the crystalline $CoS_{1.097}$ rather than carbonaceous impurities. Continued exposure of the nanoparticle in the electron beam (Fig. 3-6 b, c, d), gives particle elongation. These results therefore corroborate with the observed morphologies in Fig. 3-5.

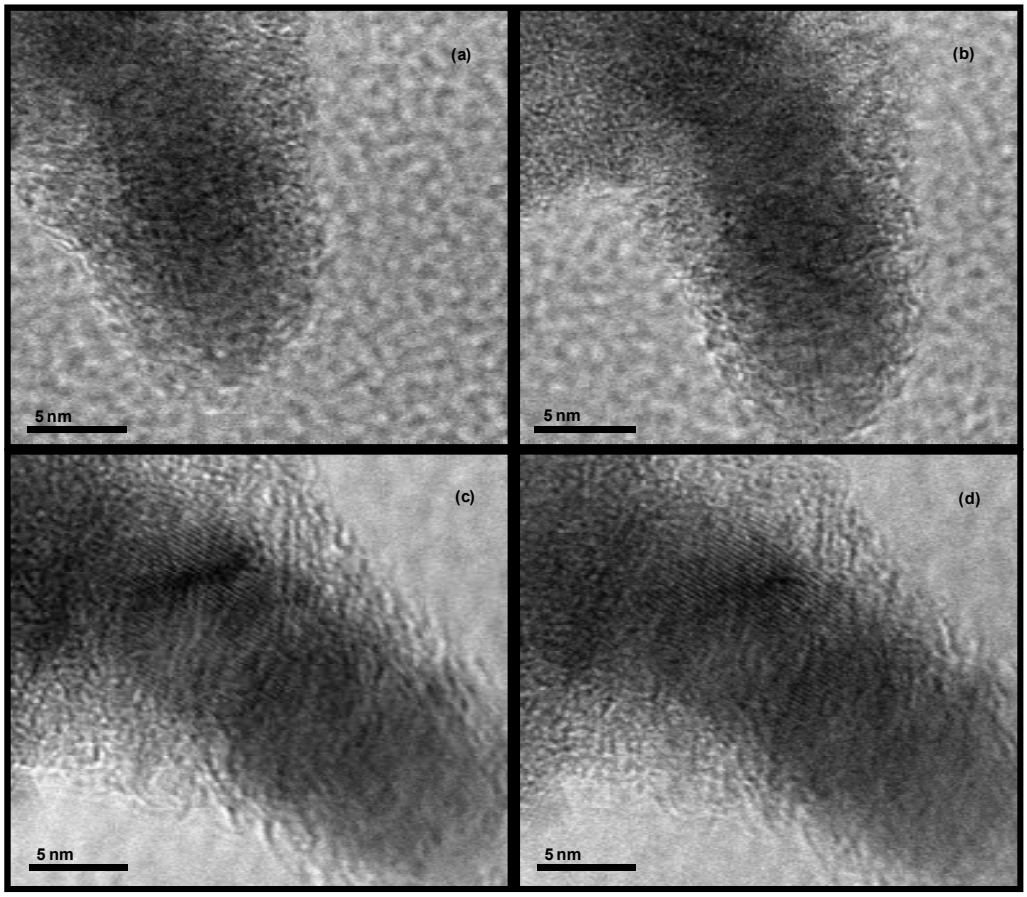

Fig. 3-6: HRTEM micrographs of cobalt sulfide (5 min sample) depicting the growth mechanism of nanowires where the electron beam was focused on a single sphere for (a) 30 sec, (b) 1 min, (c) 5 min and (d) 10 min.

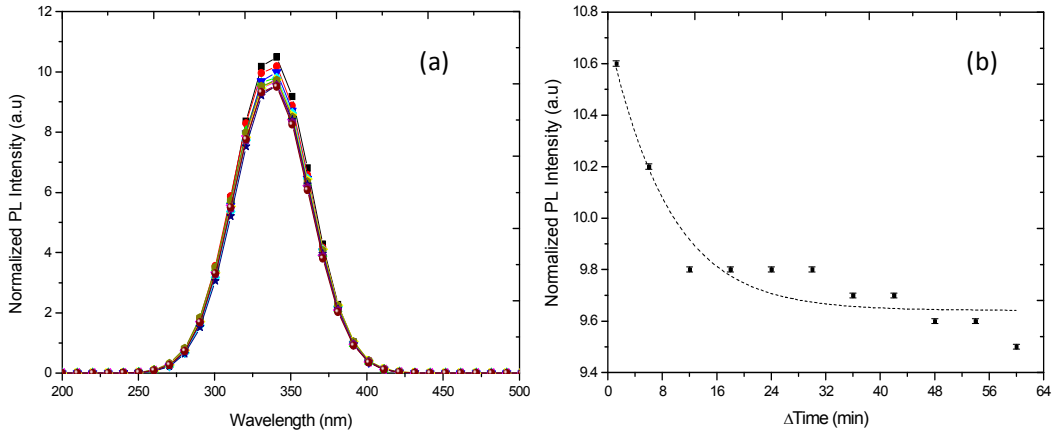

Fig. 3-7: Successive photon bombardment of cobalt sulfide nanoparticles synthesized for 5 min (a), photoluminescence intensity profile with 0.05 % instrument error (b) (curve to guide the eye).

To further support the above growth phenomena of $CoS_{1.097}$ nanowires under high energy irradiation, the optical property of the particles, collected after 5 min, was examined as a function of applied energy. The sample was continually bombarded with photons with a wavelength of 250 nm and 50 scans were collected. Results are summarized in Fig. 3-7. From the photoluminescence spectra, it is observed that as the number of scans increased the intensity of the emission maximum decreased. The decrease in intensity is associated with a decrease in quantum yield. As the shape of the particles changes from spheres to wires, there is a change in confinement from 3-D to 2-D. Theoretically, it has been shown, using the particle in a box model, that 3-D confinement is much stronger than 2-D confinement [31]. Consequently, the luminescence quantum yield decreases with elongation of shape due to an increasing spatial separation of the electron and hole wavefunctions [32]. Reducing the wavefunction overlap results in a decrease in probability of electrons recombining with holes radiatively and this reduces the photoluminescence efficiency. Kan *et. al*. revealed this phenomenon by showing that the lengthening of CdS nanorods caused a decrease in quantum yield [32].

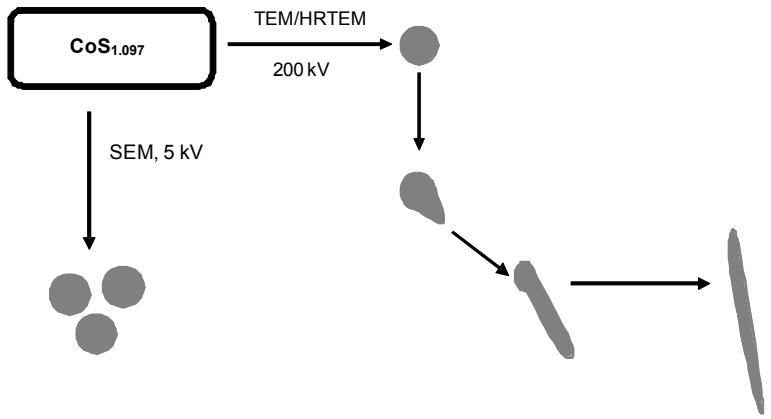

Scheme 3-2: Growth mechanism of high voltage irradiation induced nanowires.

On the basis of the above results we propose a growth mechanism for $CoS_{1.097}$ nanoparticles can be proposed (Scheme 2). The high energy 200 kV electron beam acts in the same way as very high temperature does. The passivating ligand first melts (no agglomeration takes place as the particles are well distributed on the copper grid). This is followed by melting of the core particles to give a kinetic product that has the shape of a rod. The extent of the formation of the nanowires is dependent on the surface energies of the spherical nanoparticles as well as the amount of time the particles are exposed to the electron beam. Therefore a mixture of spherical and wire-like nanoparticles can be expected.

To further validate the proposed mechanism, the thermal property of the nanoparticles synthesized after 5 min was investigated. The particles were heated on a TGA under a nitrogen atmosphere to a maximum temperature of 900 °C. The thermograph in Fig. 3-8, revealed two degradation steps; the first step was correlated to the vaporization and decomposition of the HDA capping agent. The boiling point of HDA is known to be approximately 303 °C, depending on the purity. The second step was assigned to sublimation of cobalt sulfide. The low sublimation temperature of the cobalt sulfide therefore suggests the unstable nature of the nanocrystals under high energy conditions.

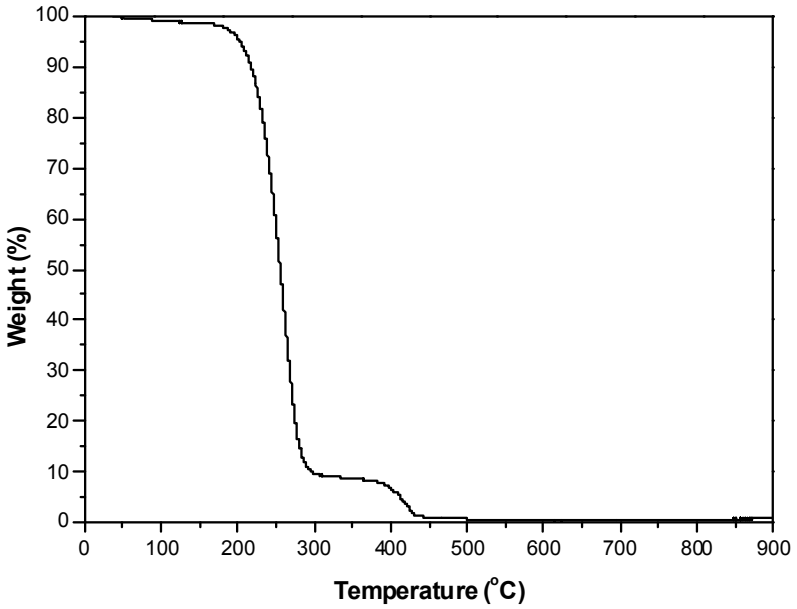

Fig. 3-8: TGA of the cobalt sulfide nanocrystals synthesized after 5 min.

To understand the effect of temperature on the morphology of the nanoparticles, the particles were annealed at 300 °C under nitrogen, in order to remove the HDA and expose the core cobalt sulfide. The resultant particles were then characterized with x-ray diffraction, SEM and HRTEM. The crystal phase of the annealed nanoparticles remained unchanged compared to the original nanoparticles. The morphology of the nanoparticles is shown in Fig. 3-9. The SEM micrographs (a-d) revealed the shape of the nanoparticles to be spheres with variable sizes. The nanoparticles also appeared to coagulate together and form bigger spheres, as clearly depicted in Fig. 3-9(d). The agglomeration undoubtedly resulted from the absence of the capping HDA.

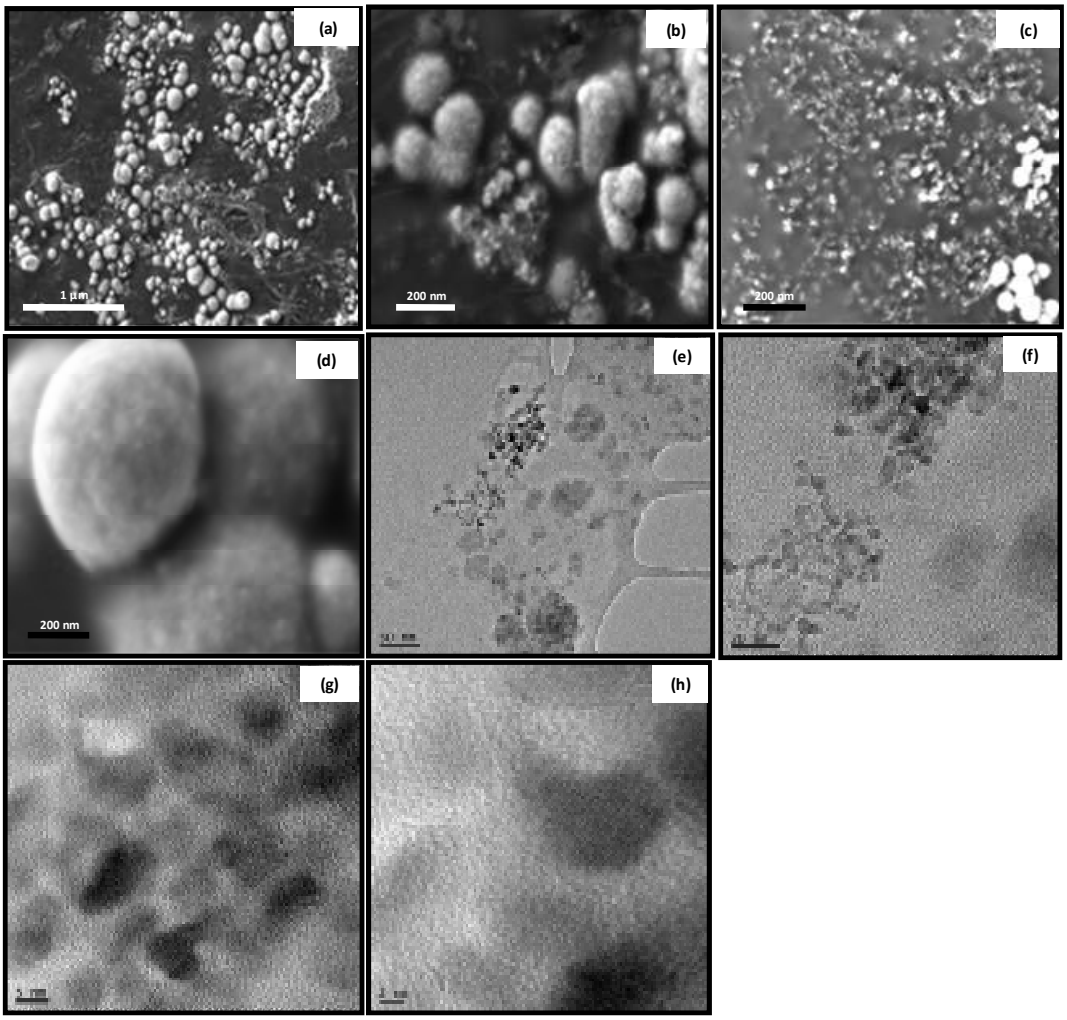

Fig. 3-9: (a) SEM image at low magnification, (b)-(d) SEM images at the same magnification depicting $CoS_{1.097}$ of different sizes, (e)-(f) TEM images showing different sizes of $CoS_{1.097}$ and (g)-(h) HRTEM images at different magnification.

The HRTEM was performed at 120 kV in order to try and minimize the impact of the energy on the ultimate morphology of the nanoparticles. The corresponding HRTEM images confirmed the particles as spheres with some degree of deformity. The HRTEM image in Fig. 3-9(g) confirmed the deviation of the particles from spheres, possibly as a result of the instability of the nanoparticles exacerbated by the absence of the capping agent.

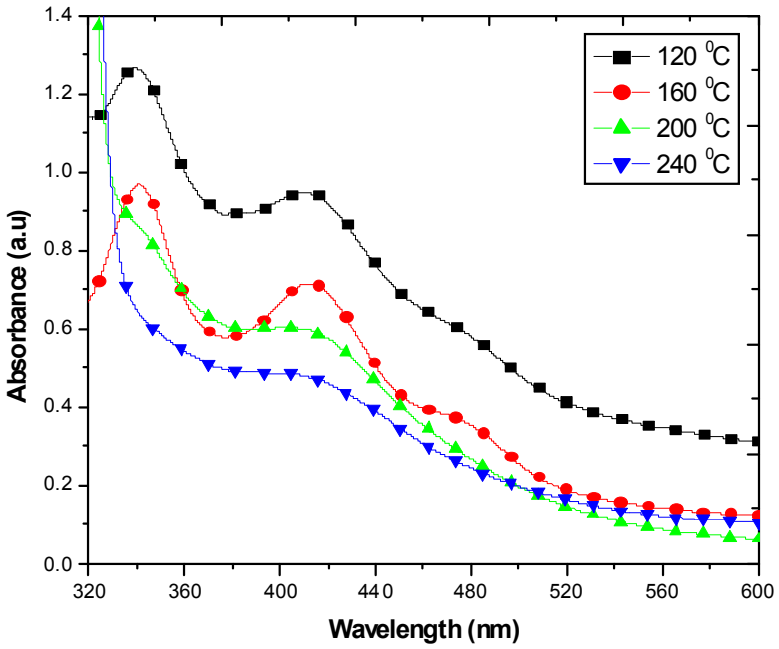

Fig. 3-10: Absorption spectra of cobalt sulfide synthesized for 1hr in HDA at different temperatures.

The study on the effect of the synthetic temperature was then undertaken to ultimately establish its influence on the properties of the nanoparticles. Fig. 10 depicts the profile of the absorption curves with changing synthetic temperatures. One of the advantages of the single source precursor method in the synthesis of nanoparticles is the wide temperature range that could be utilized. This is highly determined by the capping agent. HDA in this case has a melting temperature below 100 °C and a boiling point of 303 °C and can therefore be utilized within this range. In this study, the temperature is varied from 120 °C to 240 °C. The particles synthesized at the lowest temperature shows two distinct peaks and a shoulder (Fig. 3-10). The first excitonic peak (340 nm) is blue-shifted from the bulk absorption band-edge. The first excitonic peak of the absorption curve of the particles synthesized at 160 °C is located at 341 nm, a 1 nm red-shift from the absorption band-edge of the particles synthesized at 120 °C. This suggest that at this stage a temperature difference of about 40 °C has very little effect on the properties of the nanoparticles. As the temperature is increased to 200 °C and ultimately to 240 °C, the first excitonic peak observed in the previous synthetic temperatures, begins to disappear and a narrow shoulder is observed at 347 nm for the particles prepared at 200 °C together with a broader

shoulder at higher wavelengths. The first shoulder is completely absent for the particles synthesized at 240 °C, resulting in a further red-shifted band edge (426 nm) compared to the particles prepared at the other temperatures. The systematic red-shifting of the band-edge with increasing temperature is attributed to the Otswald ripening effect. In the growth mechanism of the nanoparticles, initially the nucleation step occurs followed by the growth of the nuclei. During the growth process, factors such the reaction time as well as the temperature can have an effect on this process. At higher temperatures, the reaction is driven thermodynamically. This therefore translates in such a manner that as the average temperature of the reaction increases, there is an increase in disorder. To overcome this disorder, the particles tend to coagulate together and form bigger, stable particles.

The fluorescence properties are revealed in Fig. 3-11. All the photoluminescence spectra show one major peak and two shoulder peaks. The shoulder peaks are due to the solvent as well as second order excitation. The spectrum of the particles prepared at 120 °C is blue-shifted from the rest; nevertheless it is red-shifted from the corresponding absorption band edge with the emission maximum located at 384 nm.

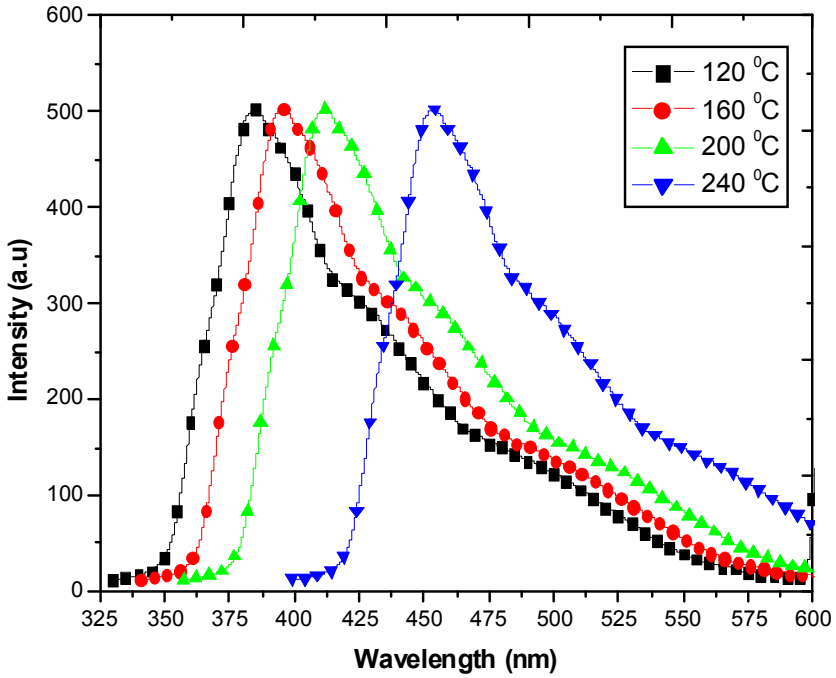

Fig. 3-11: Photoluminescence spectra of cobalt sulfide synthesized for 1hr in HDA at different temperatures.

There is successively a red-shift in the emission maximum as the temperature increases. This is in par with the observed red-shifting of the absorption band-edges with increasing temperature. The emission spectra also showed a narrow distribution consistent with monodispersed samples. The similarities in the observed spectra suggest the likeliness of the particles possibly in morphology.

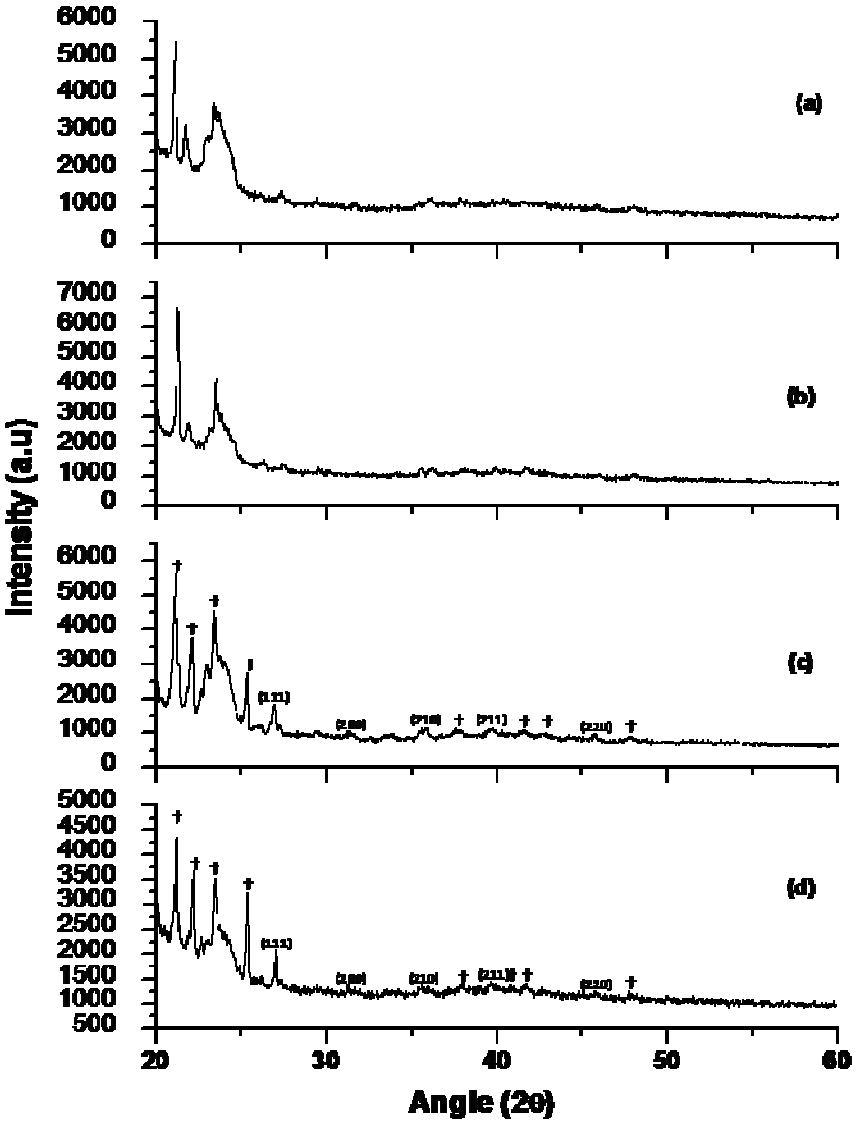

Fig. 3-12: X-ray diffractograms of cobalt sulfide synthesized for 1hr in HDA at (a) 120 °C, (b) 160 °C, (c) 200 °C and (d) 240 °C († denotes HDA).

The structural properties determined by X-ray diffraction are shown in Fig. 3-12. The particles synthesized at temperatures 120 °C and 160 °C were indexed to Co_4S_3 (JCPDS no.: 19-0363). The space group and thus the hkl values are not known due to the rarity of the phase. Cobalt sulfide in its stable bulk form usually exist as a black powder with a CoS stoichiometry. When this material is synthesized and moreover is in the nanosized regime, new trends are observed. The synthesized nanoparticles are brown in colour, which according to the colour spectrum occurs in the lower wavelengths compared to the black bulk cobalt sulfide. This alone therefore suggests a change in the properties of the particles. As substantiated by the optical properties, these particles undergo quantum confinement and subsequently possess novel properties.

As the temperature is increased, the intensity of the colour of the particles increases suggesting a shift towards the black bulk cobalt sulfide. This undoubtedly means that the size of the nanoparticles is increasing as previously validated. As the size of the nanoparticle increases, it stability improves. This is evident from the observed crystal phases of the particles. The particles synthesized at 200 °C and 240 °C are both indexed to a cubic phase CoS_2 (JCPDS no.: 71-4835), which is more stable compared to the Co_4S_3 phase. The diffractograms in Fig 3-12(c) and (d) also show the presence of HDA. The use of HDA in the synthetic method though very useful and essential in stabilizing the nanoparticles, can sometimes if in excess hinder and interfere with the characterization process of the nanoparticles. In the case of XRD, HDA peaks can be overbearing and result in diminished peak intensity of the desire nanoparticle signals. Nonetheless, there appear to be broadening of the peaks signifying that the diffraction is due to small crystallites.

The morphologies of the particles were determined by SEM as shown in Fig. 3-13. The sizes of the particles seem to progressively increase with the increasing temperatures. The shapes of the nanoparticles are spheres and they remained unchanged with varying temperatures. Growth of anisotropic or isotropic particles is largely dependent on factors such as the monomer concentration and the reaction time mainly because they are contributory factors in the nucleation stage of the growth mechanism of the nanoparticles. On the other hand temperature effects dominate the growth stage of the mechanism thus having no influence

on the resultant shape of the particle but primarily controls the size. This therefore explains the observed shapes of the nanoparticles.

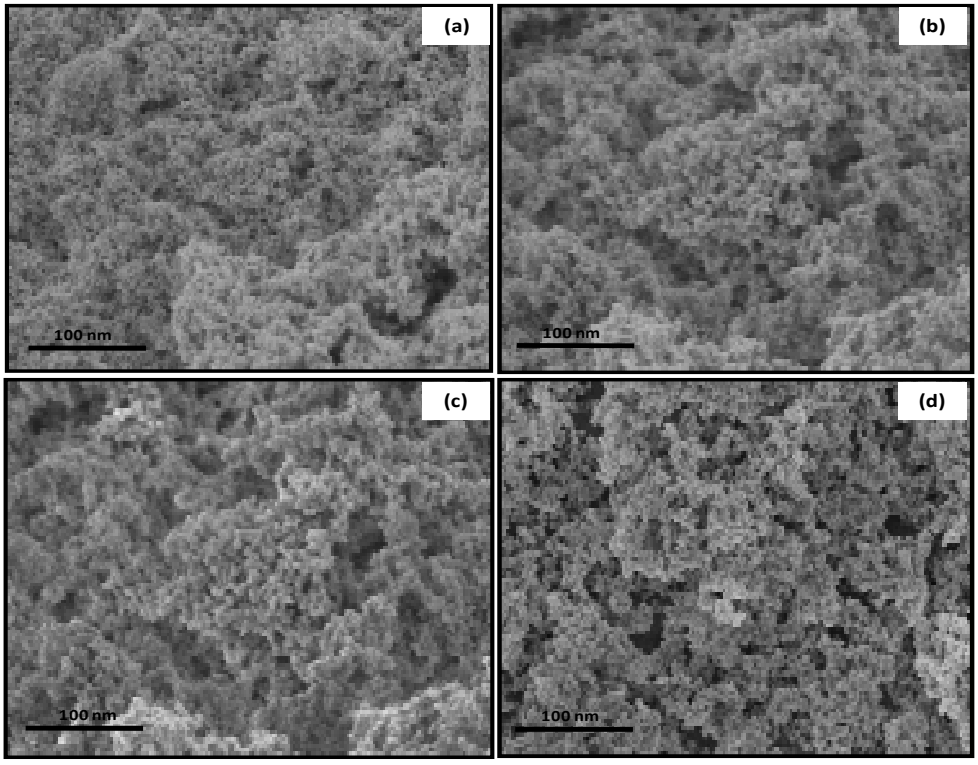

Fig. 3-13: FESEM micrographs of cobalt sulfide synthesized for 1hr in HDA at (a) 120 °C, (b) 160 °C, (c) 200 °C and (d) 240 °C.

3.5. Conclusions

The cobalt sulfide nanoparticles synthesized at different reaction time showed good quantum confinement. The particles collected after 5 min showed the most blue-shifted band-edge and the subsequent samples showed a further red-shift with time. This is due to the Ostwald ripening effect. The synthesized particles showed interesting structural properties with the crystals being indexed to a rather less familiar $CoS_{1.097}$ phase. The morphology of the particles at a low accelerated voltage was spherical. Upon increasing the accelerated voltage to 200 kV during TEM measurements, the shapes of the particles changed from spherical to wire-like nanoparticles, i.e., the morphology was transformed from isotropic to anisotropic. This indicates that the morphology of synthesized $CoS_{1.097}$ nanoparticles is very sensitive to the applied radiation. The stability of the nanoparticles

determined by TGA showed that the synthesized cobalt sulfide degrades at 430 °C, verifying the low stability of the nanoparticles in high energy conditions. The particles were then annealed in order to establish whether there would be any change in morphology. The morphology determined by SEM remained spherical but agglomerated together to form bigger spheres. The TEM showed similar effect with that of the original particles. It is therefore concluded that cobalt sulfide in a $CoS_{1.097}$ phase is susceptible to structural changes when exposed to extreme conditions.The effect of the synthetic temperature on the properties of the nanoparticles was investigated. It was found that the temperature largely influenced the size of the nanoparticles rather than the crystal phase and the morphology. This was attributed to the fact that the temperature usually plays a more prominent role in the growth stage of the nanoparticles rather than in the nucleation stage, meaning it has very little effect on the initial characteristics (phase and shape) of the nanoparticles.

3.6. References

[1] Glieter H., Prog. Mater. Sci. 1989, *33*, 223.

[2] Henish H.K., Crystals in Gel and Liesegang Rings, Cambridge University Press, Cambridge 1988.

[3] Golden J.H.; DiSalvo F.J.; Frechet J.M J.; Silcox, J.; Thomas M.; Elma J., Science 1996, *273*, 782.

[4] Yu S.H. ; Wu Y.S.; Xie Y.; Qian Y.T., Chem. Mater. 1998, *10*, 2309.

[5] Ziegler J.; Merkulov M.; Grabolle M.; Resch-Genger U.; Nann T., Langmuir 2007, *23*, 7751.

[6] Murray C.B.; Norris D.J.; Bawendi M.G., J. Am. Chem. Soc. 1993, *115*, 8706.

[7] Xu J.; Li W.J., Mater. Sci. Lett. 1999, 18, 115.

[8] Wold A.; Dwight K., Solid State Chemistry, Chapman and Hall, Inc., New York, 1993.

[9] Rao C.N.R.; Pisharody K.P.R., Prog. Solid State Chem. 1976, 10, 207.

[10] Pehlke E.; Moll N.; Kley A.; Scheffler M., Appl. Phys. A: Mater. Sci. Pr. 1997, 65, 525.

[11] Grabolle M.; Ziegler J.; Merkulov A.; Nann T.; Resch-Genger U., Annals of the New York Acad. Sci. 2008; 113, 235.

[12] Rene-Boisneuf L.; Scaicino, J. Chem. Mater. 2008, 21, 6638.

[13] Xing B.; Li W.; Dou H.; Zhang P.; Sun K., Chem. Lett. 2007, 36, 1144.

[14] El-Khair M.H.; Xu L.; Chen K.; Zhang Y.; Li M.; Huang X., Chinese Phys. Lett. 2002, 19, 967.

[15] Lee S.; Daruka I.; Kim C.S.; Barabusi A.L.; Merz J.L.; Furdyna J.K., Phys. Rev. Lett. 1998, 81, 3479.

[16] Yan Y.; Liu P.; Wan J.G.; To B.; Al-Jassim M.M., J. Phys. Chem. B 2003, 107, 9701.

[17] Chen Y.; Palmer R.E.; Wilcoxon J.P., Langmuir 2006, 22, 2851.

[18] Banhart F., J. Appl. Phys. 1997, 8, 81.

[19] Li J.; Banhart F., Nano Lett. 2004, 4, 1143.

[20] Tang, Q .; Yoon S M. ; Choi N.L., Langmuir 2006, 22, 2802.

[21] Wada V.; Kaneko M.; Niinobe D., Chem. Lett. 2005, 34, 1618.

[22] Xie Y.; Yan P.; Qian Y., Chem. Lett. 1999, 7, 655.

[23] Moloto N.; Revaprasadu N.; Moloto M. J.; O'Brien P.; Helliwell M., Polyhedron 2007, 26, 3947.

[24] Moloto N.; Revaprasadu N.; Musetha P. L.; Moloto M. J., J. Nanosci. Nanotechnol. 2009, 9(8), 4760.

[25] Moloto M.J.; Revaprasadu N.; O'Brien P.; Malik M.A., J. Mater. Sci. Mater. Elect. 2004, 15, 313.

[26] O'Brien P.; Walsh J.R.; Watson E.M., J. Cryst. Growth 1996, 167, 133.

[27] Nair P.S.; Scholes G.D., J. Mater. Chem. 2006,16, 467.

[28] Hsu X.J.; Lu S.Y., Langmuir 2004, 20, 194.

[29] Gleizes A.N., Chem. Vap. Depos.2006, 6, 155.

[30] Srouji F.; Afzaal M.; Waters J.; O'Brien P., Chem. Vap. Depos. 2005, 11, 91.

[31] Griffiths D.J., Introduction to Quantum Mechanics 2nd Ed., Prentice Hall, 2004.

[32] Kan S.H.; Mokari T.; Rothenberg E.; Banin U., Nature Mater. 2003, 2, 155.

[33] Jun Y.; Choi J.; Cheon J., Angew. Chem. Int. Ed. 2006, 45, 3414.

[34] Contreras J.G.; Gnecco J.G., Ana. de Quimica 1990, 86, 740.

[35] Adamczyk D., Environ. Eng. Sci. 2006, 23, 610.

[36] Victoriano L.I., Bol. Soc. Chil. Quím, 2000, 45, 324.

[37] Victoriano L.I.; Cortes H.B.; Yuseff M.I.S.; Fuentealba L.C., J. Coord. Chem. 1996, 39, 241 .

[38] Sosibo N. M.; Revaprasadu N., Mater. Eng. B 2008,150, 111.

[39] Meteleva Y.V.; Roessner F.; Novikov G.F., J. Photochem. Photobio. A: Chem. 2008, 196, 154.

[40] Yu S.H.; Yang J. ; Qian Y.T.; Yoshimura M., Chem. Phys. Lett. 2002, 61, 362.

[41] Voorhees P W., J. Stat. Phys. 1985, 38, 231.

[42] Cullity D.B., Elements of X-ray Diffraction, Addison Wesley Mass, 1978.

CHAPTER 4: OPTICAL AND STRUCTURAL CHARACTERIZATION OF NICKEL SELENIDE NANOCRYSTALS SYNTHESIZED BY SIMPLE METHODS

4.1. Introduction

The fabrication of size and shape controlled nanoparticles and their self-assembly into materials still poses a challenge in the area of nanosciences. It is well recognized that the shape of nanoparticles plays an important role in determining their properties [1-8]. One of the difficulties in the preparation of zero dimensional (0D - spheres, cubes), 1D (rods, wires) and 2D (discs, prisms, plates) nanoparticles is the control of growth through variation of the reaction parameters [9-14].Factors such as concentration, temperature, pH, capping agent as well as the reaction time are critical parameters that influence the size and the morphology of the nanoparticles. Apart from these factors, altering a synthetic strategy can also introduce surprising results. In this work, we have investigated three different methods used to produce nickel selenide and discuss the advantages and disadvantages of each method.

Owing to its interesting electronic and magnetic properties, nickel selenide has found many applications such as in optical recording materials, solar cells, sensors, laser materials, conductivity fields and optical fibres [15-18]. Due to the valance electronic configuration of nickel ($3d^8 4S^2$) and the small differences between its electronegativity and that of selenium (Ni = 1.9, Se = 2.4), nickel and selenium have an ability to form complexes with varied stochiometries. The physical and chemical properties of these materials as well as their application, is strongly influenced by the composition, phase structure and morphologies of Ni/Se complexes [19]. There are various methods reported for the synthesis of nickel selenide nanoparticles. The solvothermal method is by far the most reported. It involves heating of reactants in a particular solvent in a high pressure system such as an autoclave [20-23]. Bin Li et. al. [25] reported the synthesis of $NiSe_2$ and NiTe nanorods via the solvothermal route at 180 °C for 15 h in ethylenediamine whilst Han and co-workers [24] reported the synthesis of various stochiometries of nickel selenide under assorted

conditions. The challenges associated with these methods, is the lack of manipulation and the inability to monitor the reaction conditions during synthesis. The single source precursor method has been reported for the synthesis of nickel selenide thin films via the CVD method but to our knowledge has not been used for the synthesis of nanopowders [26].

Herein we report on the synthesis of nickel selenide nanoparticles using three different methods such as the single-source precursor method (method 1), the thermolysis of TOPSe and nickel chloride in hexadecylamine (method 2) as well as the reaction of nickel chloride and selenium using sodium borohydride as a reducing agent in methanol and in water (method 3). The physical properties as well as their optical properties of the new materials are reported. This study also describes a comparison of features observed from the various products obtained from each method.

4.2. Experimental

4.2.1. General

Toluene, acetone, ethanol and methanol were obtained from BDH. Toluene was stored over molecular sieves (40 Å, BDH) before use. HDA (hexadecylamine), TOP (tri-n-octylphosphine), nickel chloride hexahydrate, diphenyldiselenide, sodium borohydride, selenium powder were obtained from Aldrich, and used as purchased.

4.2.2. Synthetic Methods

4.2.2.1. Synthesis of $[NiCl_2(SeC_6H_5)_2]$

A hot solution of diphenyl diselenide (1.0 g, 3.20 mmol) and sodium borohydride (0.12 g, 3.20 mmol) in ethanol (20 m1) was added into a heated solution of nickel chloride (0.5 g, 2.10 mmol) in ethanol (20 ml). The mixture was stirred and refluxed for 24 h. The green precipitate was filtered, washed with ethanol and dried under vacuum. Yield 54.3 %; m. p. 383 °C. $[NiCl_2(SeC_6H_5)_2]$: Anal. Calcd. C, 32.66; H, 3.64; Found: C, 32.21; H 3.55. IR /cm^{-1}: 3357(s), 3252(s) 1639(sh), 1473(s), 1375(s), 1269(s), 1071(s), 995 (m) . ^{1}H NMR (δ, $CdCl_3$) ppm 7.2 (m, 5H), 7.6 (m, 5H);^{13}C {^{1}H} NMR (δ, $CdCl_3$) ppm: 129.18 (s, CSe); 77.00 (s, CSe).

4.2.2.2. Synthesis of nickel selenide nanoparticles

(a) Single-source precursor route (method 1)

In a typical experiment, $[NiCl_2(SeC_6H_5)_2]$ (1.0 g) was dissolved in TOP (10 – 20 ml). This solution was then injected into 3.125 g of hot HDA at 160 °C. A decrease in temperature of the solution by 20 – 30 °C was observed. The solution was allowed to stabilize at 160 °C and heated for 60 minutes at this temperature. The solution was then allowed to cool to about 70 °C, and methanol was added to the solution. A flocculent precipitate formed and this solid product was separated by centrifugation and re-dispersed in toluene. Toluene was removed by evaporation under reduced pressure to give greyish-black HDA capped nickel selenide nanoparticles. The particles were washed three times with methanol and re-dispersed in toluene.

(b) Reaction of $NiCl_2$ with TOPSe in HDA: (Method 2)

In a typical reaction, 1.0 g (4.21 mmol) of nickel chloride was dissolved in HDA at a temperature of 160 °C. TOPSe, prepared by the reaction of selenium powder 0.3 g (8.0 mmol) and TOP (5ml), was added to the reaction mixture. Upon the addition of TOPSe, the temperature dropped by ~ 20 °C. The temperature was allowed to rise back to 160 °C and the mixture was heated for 60 minutes at this temperature. The solution was then allowed to cool to about 70 °C, and methanol was added to the solution. A flocculent precipitate formed and this solid product was separated by centrifugation and redispersed in toluene. Toluene was removed by evaporation under reduced pressure to give greyish-black HDA capped nickel selenide nanoparticles. The particles were washed three times with methanol and redispersed in toluene.

(c) Direct reaction of NaSe and $NiCl_2$: (Method 3)

About 1.0 g (12.5 mmol) of selenium powder was added together with 1.0 g (26.5 mmol) of sodium borohydride in either methanol and the mixture was stirred for 60 minutes at room temperature. An amount of 1.0 g (4.21 mmol) of nickel chloride was added. This caused the reaction to give off heat and the temperature to rise to 40 °C. The reaction was then allowed to stir for 60 minutes. The resultant greyish-black precipitate was filtered and

washedseveral times with acetone. This reaction was performed in water as a solvent instead of methanol.

4.3. Characterization techniques

4.3.1. Microanalysis

Microanalysis (C, H, N) was performed on a CARLO ERBA elemental analyzer on the nickel complex.

4.3.2. Nuclear Magnetic Resonance and Fourier Transformed-Infrared spectroscopy

Infrared spectra were recorded on Perkin-Elmer paragon 1000 FT-IR spectrometer using the as prepared solid samples. NMR spectra were recorded on a Varian Associates Inova spectrometer (400 MHz) for both ^{1}H and ^{13}C nuclei using $CDCl_3$.

4.3.3. Optical characterization

A Perkin Elmer Lambda 75S UV-VIS-NIR Spectrophotometer was used to carry out the optical measurements. The powders were dissolved in toluene and placed in quartz cuvettes (1 cm, path length). Perkin Elmer LS55 with a xenon lamp (150 W) and a 152 P photo multiplier tube as a detector was used to measure the photoluminescence of the particles. The samples were dissolved in toluene and placed in quartz cuvettes (1 cm path length) for spectral analysis.

4.3.4. X-ray diffraction

XRD patterns on powdered samples were measured on a Phillips X'Pert materials research diffractometer using secondary graphite monochromated Cu Kα radiation (λ = 1.54060 Å) at 40 kV/50 mA. Samples were supported on glass slides. Measurements were taken using a glancing angle of incidence detector at an angle of 2°, for 2θ values over 10° – 80° in steps of 0.05° with a scan speed of 0.01° 2θ.s^{-1}.

4.3.5. Electron microscopy

Nickel selenide samples were characterized using field emission scanning electron microscopy (FE-SEM)(Leo, Zeiss), operated at 3-10 kV electron potential difference and equipped with a semiconductor detector that allows for the detection of energy dispersive

X-rays (EDX). The samples were prepared by placing a drop of suspended particle in methanol, on a carbon tape. The samples were then allowed to dry at room temperature. The high resolution transmission electron microscopy (HRTEM) and TEM were carried out on a Joel JEM-2100 microscopy with a LAB6 filament. The measurements were carried out at 200 kV with a beam spot size of 20 - 200 nm in TEM mode.

4.4. Results and Discussion

The single-source precursor method (method 1) involves the decomposition of a molecular precursor to form the desired products (scheme 1). The advantage of this method is that the bond between the metal and the chalcogenide already exists and therefore decomposition of the precursor under the right conditions will result in the formation of nickel selenide. The approach has been used to produce many metal chalcogenide nanoparticles [27-32].

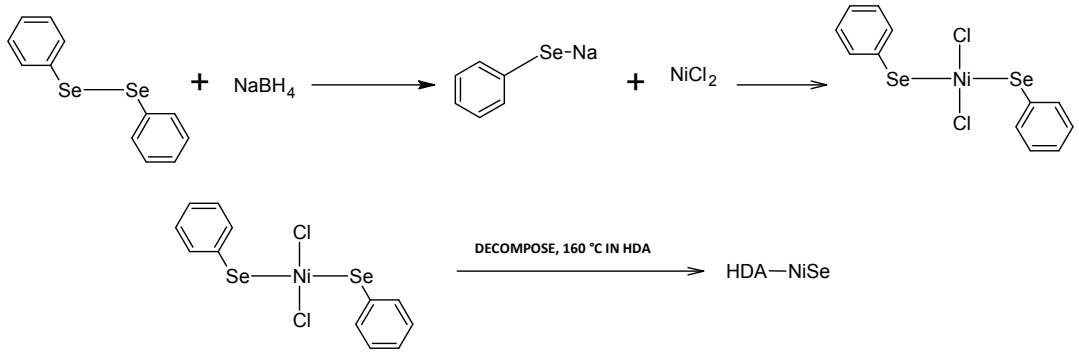

Scheme 4-1: Preparation of nickel selenide using method 1.

This conventional method (method 2) was first reported by Bawendi [33]. The method involves refluxing of a metal salt together with TOPSe in an organic capping solvent under an inert atmosphere (equation 1). It is similar in approach to the single-source precursor method in that both methods use an organic capping agent such as HDA but this method avoids the use of a precursor. This eliminates difficulties associated with the preparation of a starting product. The capping agent plays a crucial and vital role in controlling the growth process, stabilizing the particles and passivating the surface of the semiconductor nanoparticles. The particles formed by this method are nanoscale, and thus render them unstable and necessitate the use of a stabilizing environment. Hexadecylamine (HDA) as a capping agent is versatile and is mobile enough to readily add to monomers but stable

enough to prevent agglomeration. HDA also has a tendency to selectively strongly bind to preferential crystallographic planes, and as a consequence promote the formation of sophisticated morphologies.

$$NiCl_2 + TOPSe \xrightarrow{HDA,\ 160\ ^\circ C} HDA\text{-}NiSe \qquad \textit{equation 1}$$

The third method involves the reduction of elemental selenium to a more reactive species. Most reported methods for the synthesis of nickel selenide utilize the solvothermal method which requires vigorous conditions. The advantage of this method is that it uses relatively simple chemistry under mild conditions and also allows control of reaction parameters. The method reported in this study, initially uses methanol (CH_3OH) as the solvent as seen in equation 2, but the formation of sodium chloride as a by-product, necessitated the change of the solvent to water (H_2O). The salt NaCl, dissolves in H_2O and therefore remains in solution throughout the reaction allowing flocculation of NiSe particles. This permits ready separation of the nickel selenide from the NaCl in water through centrifugation.

$$2\ NaBH_4 + Se + NiCl_2 \xrightarrow{CH_3OH\ /\ H_2O} NiSe + 2\ NaCl + B_2H_6 + H_2 \qquad \textit{equation 2}$$

4.4.1. Optical properties

Nickel selenide is a p-type semiconductor with a band gap of 620 nm (2.0 eV). The optical properties of nickel selenide prepared by the single-source precursor method are shown in Fig. 4-1(a). The absorption spectrum appears as a series of overlapping peaks that get larger at the short wavelengths. Owing to the discreet nature of the electron energy levels in the nanoparticles, each peak corresponds to an energy level. The wavelength of the first excitonic peak and subsequently all the peaks, is a function of the composition and size of the nanoparticles. Smaller particles result in a first excitonic peak at shorter wavelengths. The first excitonic peak (306 nm) is blue-shifted from the bulk nickel selenide (620 nm), an indication of quantum confinement.

One of the impressive features of semiconductor nanoparticles is their ability to emit light. Upon excitation with a wavelength shorter or equivalent to the absorption onset, an electron is promoted from the valance band to the conduction band and upon relaxation a

phonon of light is emitted. The emission spectrum depicted in Fig. 4-1(a), shows a relatively narrow Gaussian distributed curve signifying a monodispersed particle population. The wavelength at maximum emission (400 nm) is red-shifted from the first absorption peak by a Stoke shift of approximately 100 nm. This is a typical feature of well passivated nanoparticles.

The absorption spectrum of nickel selenide prepared by method 2 in Fig. 4-1(b) shows distinct features compared to the spectrum in 1a. There is a disappearance of the absorption peak located at approximately 340 nm. This could be attributed to a probable change in the composition and thus the properties of the as prepared nickel selenide. The particles show very good quantum confinement with the band-edge positioned at 298 nm. The photoluminescence spectrum is red-shifted from the first excitonic peak and shows similar qualities to that displayed in 1a. The similarities in the optical properties of nickel selenide prepared by both method 1 and 2 is not surprising due to the similarities used to synthesis the nickel selenide particles.

Method 3 was expected to produce nickel selenide nanoparticles with properties different from those of the other two methods. The absorption spectrum in Fig. 4-1(c) shows the optical properties of nickel selenide prepared by method 3 with methanol as a solvent. The onset of absorption is at 311 nm and this is followed by tailing indicating the possibility of polydispersity in the sample. The photoluminescence spectrum shows a deviation from a Gaussian curve confirming the uneven distribution of particles, although the particles still show a high degree of quantization. The emission maximum is also more red-shifted (421 nm) compared to the previous two methods. This further confirms the larger variation of particle sizes. This could be attributed to the absence of the organic stabilizing environment such as HDA used in the first two methods. The modification of the solvent from methanol to water helped to eliminate the formation of NaCl as a by-product.

This is evident from the SEM image which shows a large cubic shaped particle. The sodium chloride is thought to further increase the tailing in the absorption spectrum in Fig. 4-1(c) since the absorption spectrum showed no evidence of tailing in Fig. 4-1(d). The photoluminescence spectrum also showed an improvement resulting in a Gaussian

distributed curve with the emission maximum of 387 nm.The large blue-shifts in the optical band-gaps observed for all the samples (approximately 300 nm) compared to the bulk nickel selenides can be attributed to strong confinement. A stronger confinement leads to a larger separation of the energetic levels; as a result a higher energy is required to promote an electron from the valance band to the conduction band.

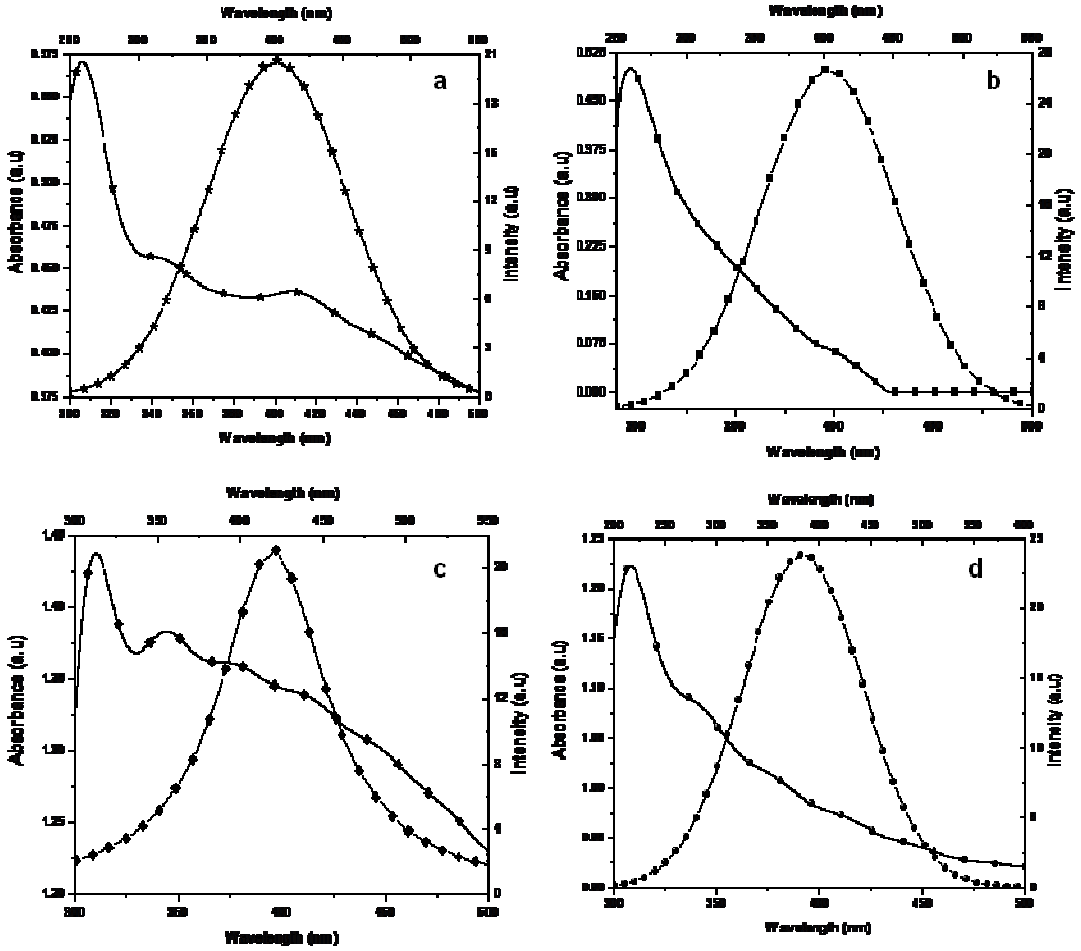

Fig. 4-1: Absorption and photoluminescence spectra of nickel selenide prepared by method 1 - a, 2 - b, 3 - c in CH_3OH and 3 - d in H_2O.

4.4.2. Structural properties

Optical characterization does not definitively define the physical attributes of the nanoparticles and therefore structural characterization was performed on the samples. X-ray diffraction can establish the composition, phase and crystallinity of the particles.XRD patterns in Fig. 4-2(a) shows particles of nickel selenide obtained from method 1 indexed to

a $NiSe_2$ cubic phase (JCPDS card 65-1843). The sharp peaks in Fig. 4-2(a) signify good crystallinity. The XRD pattern of nickel selenide prepared by method 2 shows peaks that are rather broad correlating to the smaller particle sizes. This agrees with the observation made from the optical properties obtained from method 2 with peaks slightly blue-shifted compared to the nickel selenide produced in method 1. These crystallites can be indexed to an orthorhombic NiSe (JCPDS card 29-0935).

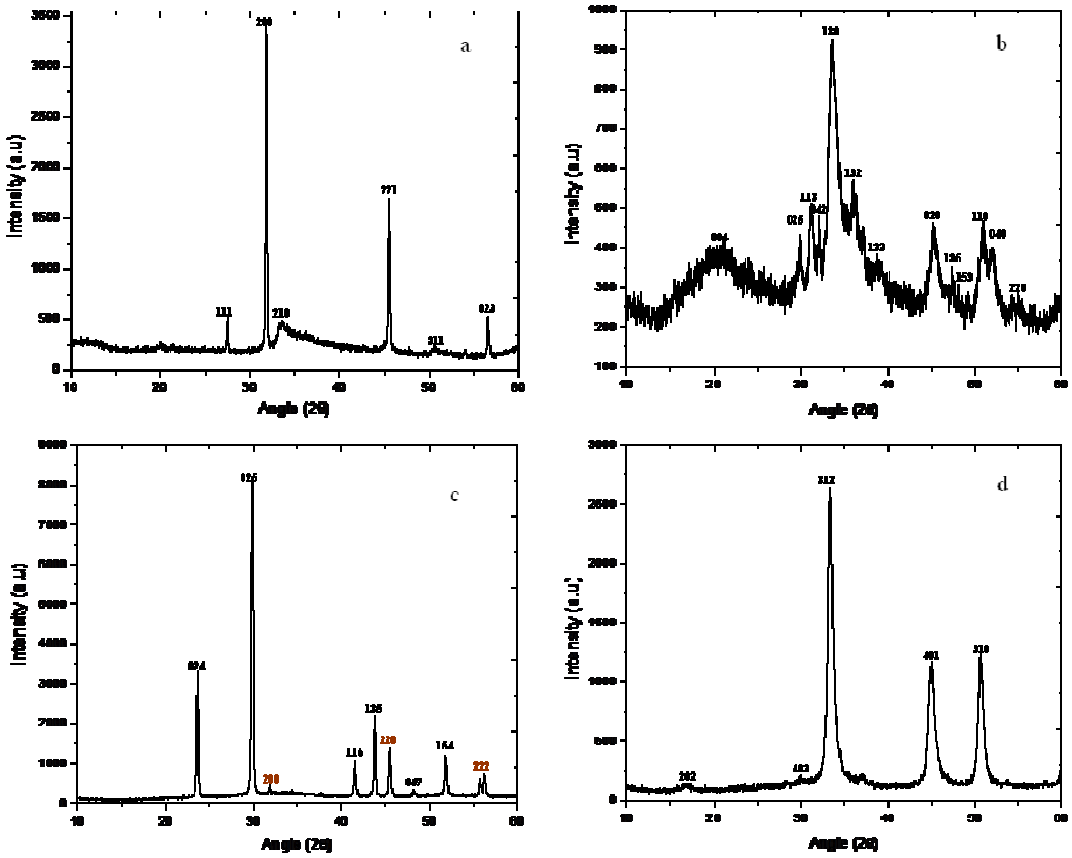

Fig. 4-2: X-ray diffraction patterns of nickel selenide prepared by method 1 - a, 2 - b, 3 – c in CH_3OH and 3 – d in H_2O.

The particles prepared by method 3, yielded sharp peaks that were indexed to cubic NaCl (JCPDS card 89-3615), one of the by-products of the reaction and orthorhombic NiSe. The X-ray diffraction pattern in Fig. 4-2(d), shows the presence of nickel selenide that can be indexed to monoclinic Ni_3Se_4 (JCPDS card 65-1220). The peaks are slightly broader compared to the ones shown in Fig. 4-2(c).

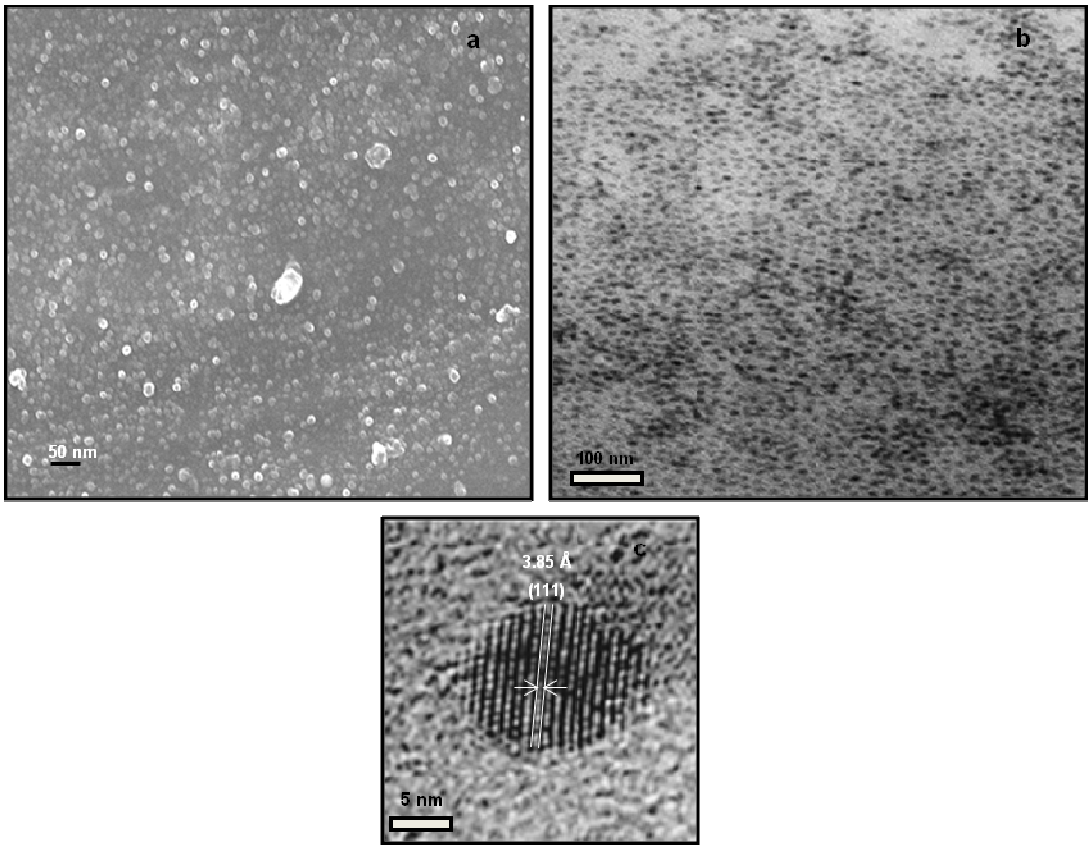

Fig. 4-3: FE-SEM micrographs (a), TEM (b) and HRTEM (c) of nickel selenide prepared by method 1.

The structural properties of the nickel selenide samples were further characterized by FE-SEM, TEM and HRTEM in order to establish the size, morphology and the crystallinity of the particles. The SEM micrograph from nickel selenide produced in method 1 (Fig. 4-3(a)) shows nearly monodispersed spherical particles with diameters in the range of approximately 10-15 nm. The TEM and HRTEM shown in Fig. 4-3(b) and 4-3(c) respectively confirm the size and the spherical morphology of the nanoparticles. The lattice fringes signifies good crystallinity of the particles as previously observed in the XRD and the lattice orientation corresponds to the (111) plane of a cubic $NiSe_2$ with a lattice spacing of 3.85 Å. It has been previously reported that the single source precursor method gives particles with relatively good dispersity with standard deviation of no more than 5% [34] and this concurs with the observations noted in this study.

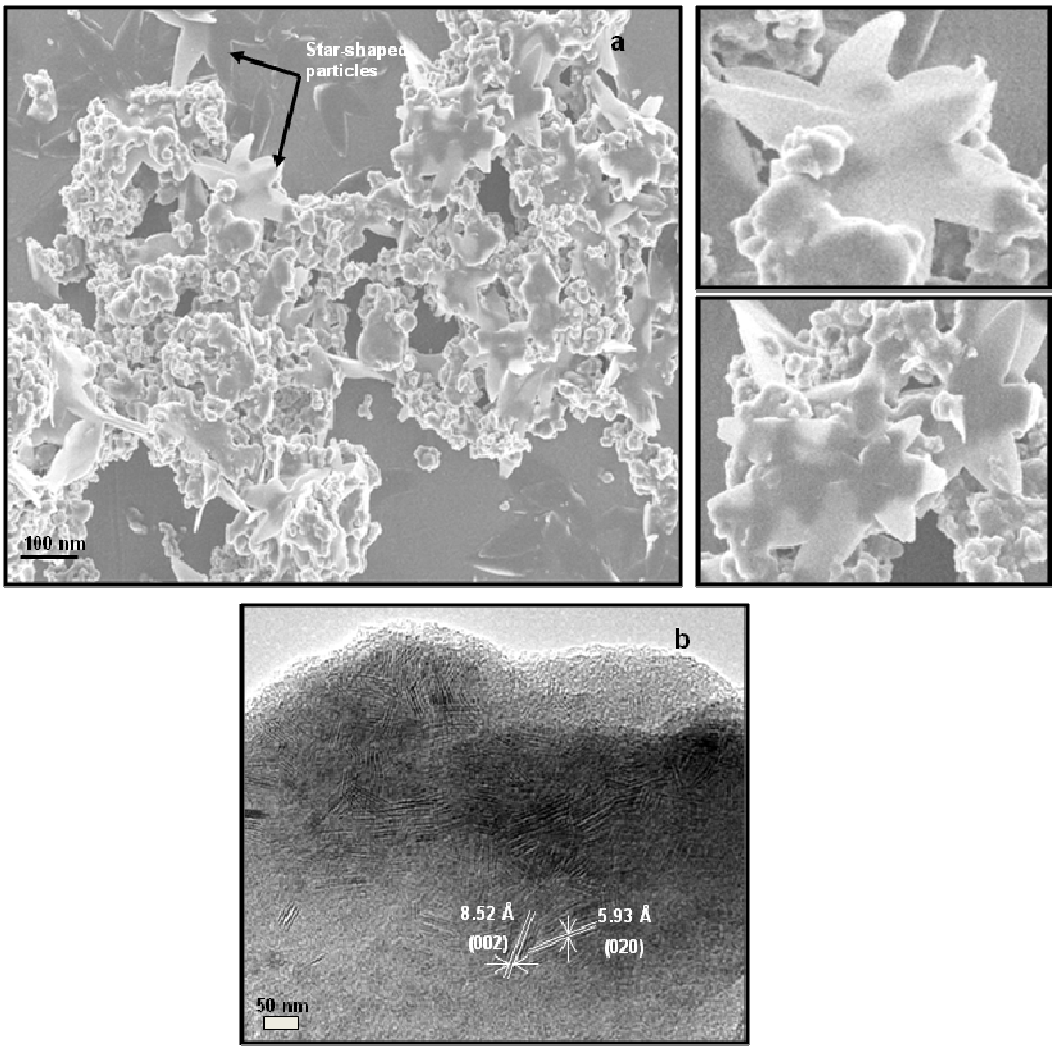

Fig. 4-4: FE-SEM micrographs (a), and HRTEM (b) of star-shaped nickel selenide prepared by method 2.

The SEM image (Fig. 4-4(a)) for particles prepared by method 2 shows two types of morphologies; an amorphous nickel selenide deposit as well as star shaped particles. The existence of only one phase in the XRD, confirms the amorphous nature of the deposit. The star shaped particles have platelet morphology with four horns, with a thickness in the nanometric size as seen in the enlarged SEM images. The HRTEM study was carried out in order to establish the crystallinity and the crystallographic make up of the star-shape particles. It revealed two types of crystallographic planes intersecting to form a horn or an apex as seen in Fig. 4-4b. These planes correspond to a (002) plane with a d-spacing of 8.52 Å and (020) plane with the lattice spacing of 5.93 Å both from the orthorhombic NiSe

system. This then suggests that the HDA binds strongly along both these planes resulting in the deviation of the morphology from spherical and further growth along both the planes continue until they intersect forming a horn or an apex.

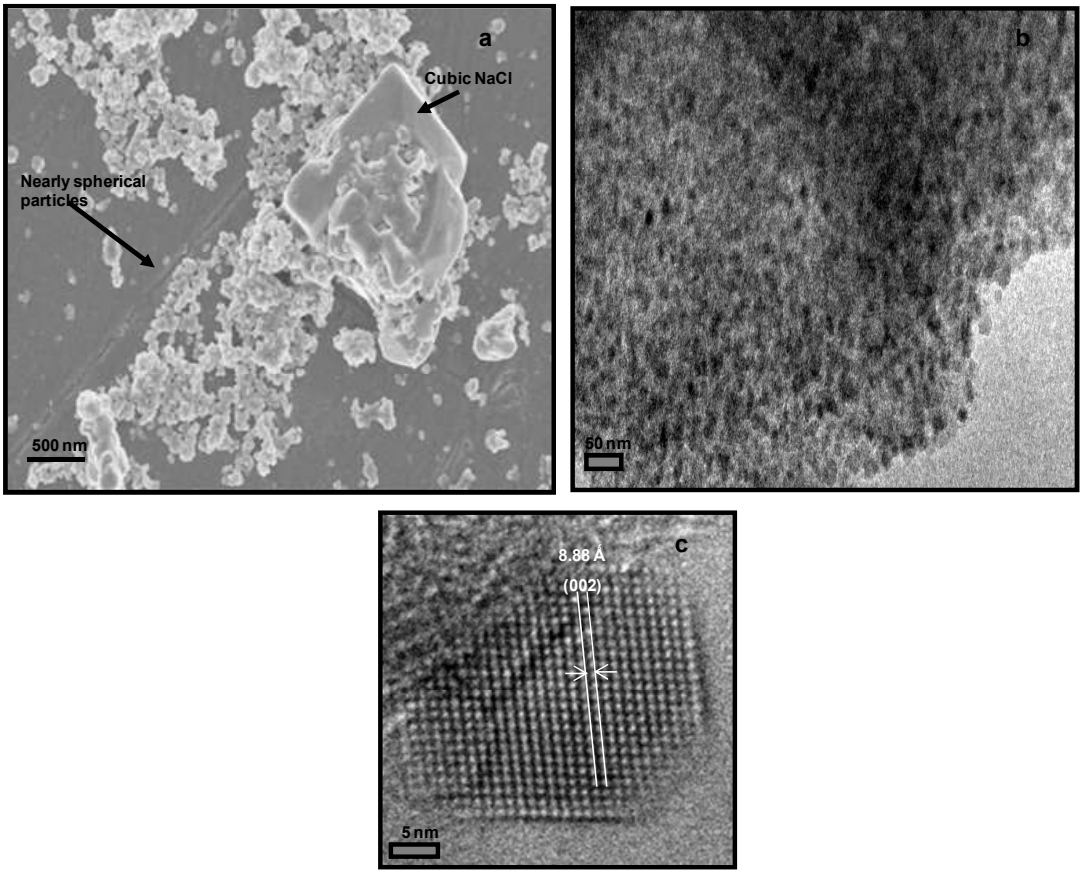

Fig. 4-5: FE-SEM micrographs (a), TEM (b) and HRTEM (c) of nickel selenide prepared by method 3 in CH_3OH.

The micrograph in Fig. 4-5a shows nearly spherical nickel selenide particles in the range 20-40 nm as well as a huge cubic crystal. EDX analysis verified the composition of the small particles as well as the large particle (Fig. 4-6). The EDX analysis of the small particles confirmed the presence of nickel and selenium. The big crystal was identified by EDX as sodium chloride. This observation correlates with the XRD as well as the optical results. The TEM and HRTEM were carried out to give better resolution of the morphology are shown in Fig. 4-5(b) and 4-5(c) respectively. The HRTEM showed the morphology to be hexagonally shaped nanoparticles with a lattice plane corresponding to the (002) plane with a lattice spacing of 8.88 Å for the orthorhombic NiSe.

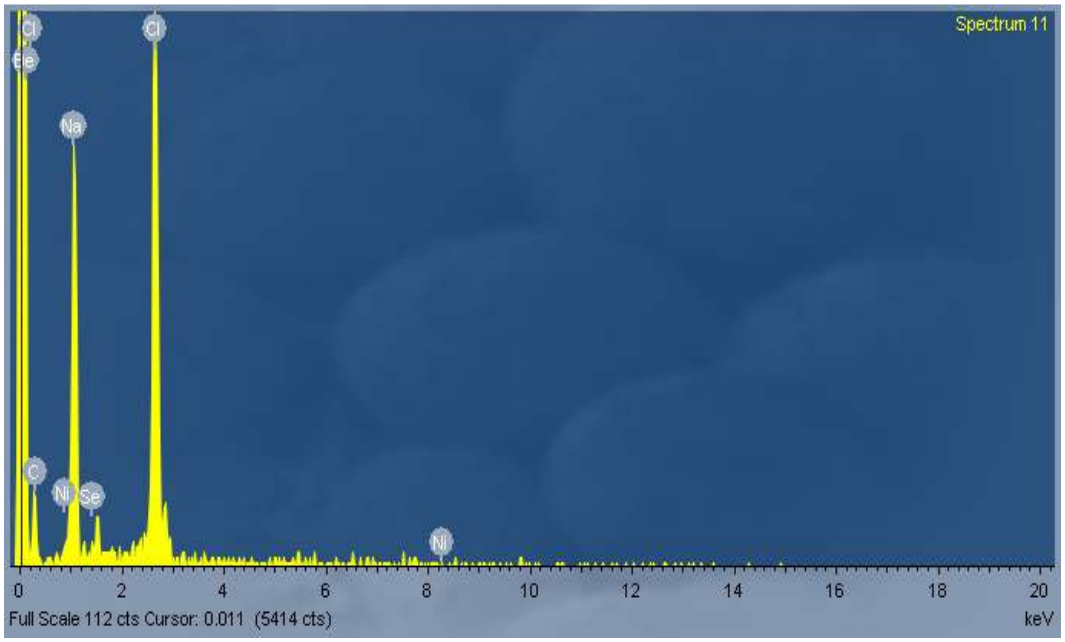

Fig. 4-6: EDX spectrum of particles prepared by method 3 in CH_3OH.

Particles prepared by the modified method 3, showed very good crystallinity, with clearly defined morphology. The particles as observed in Fig. 4-7(a) and 7(b) were of various sizes with rod-shaped morphologies. No presence of sodium chloride was observed (SEM and EDX). The HRTEM image in Fig. 4-7(c) shows an interesting atomic arrangement which can be said to be zigzagging with two atoms at the base (same plane) and one at the top (another plane).

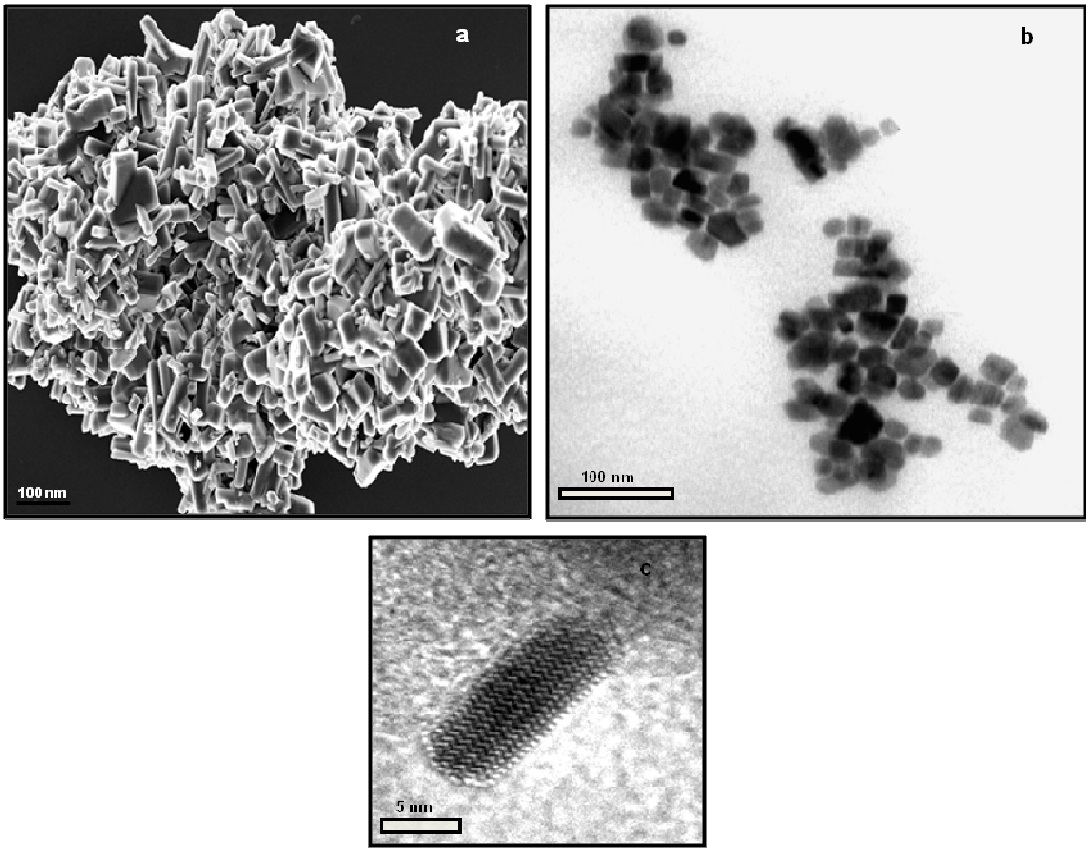

Fig. 4-7: FE-SEM micrographs (a), TEM (b) and HRTEM (c) of nickel selenide prepared by method 3 in H_2O.

The different morphologies yielded by these different synthetic methods is related to the reaction conditions and the growth mechanism. Method 1 is a one-pot synthesis carried out at 160 °C where all the constituents of the final product are present within the precursor. The decomposition of the precursor (which is faster because of the temperature) promotes the nucleation process, followed instantaneously by the growth of the nuclei. This rapid growth minimizes the incorporation of impurities and defects, thus resulting in the formation of low energy spherical particles that are well passivated by HDA. On the hand, method 2 requires separate introduction of the nickel and the selenium source. This then slows down the nucleation and the growth process and thus giving enough time for the surfactant (HDA) to selectively bind on certain crystallographic planes. This eventually results in an anisotropic morphology. For nickel selenide, method 3 is very different from the two previous methods and therefore follows a different growth mechanism.

The difference in morphology of the particles prepared in methanol compared to the particles prepared in water is solely attributed to the reaction conditions. The presence of the impurities in the methanol synthesis (NaCl) hinders the aspect ratio of the particles and the opposite is seen for the synthesis in water due to the absence of the impurities.Table 4-1 summarises the properties of the nickel selenide prepared by the different methods. The optical properties of all the samples show relatively good quantum confinement that varies from 0D to 1D (method 1 – 0D, method 2 – 1D, method 3(CH_3OH) – 0D and method 3(H_2O) – 1D). From the results, the more blue-shifted samples (298 nm and 297 nm) result in more remarkable morphologies. The XRD data revealed that the NiSe orthorhombic phase is usually favoured when there are impurities in the samples, as validated by the presence of an amorphous nickel selenide deposit in method 2 and sodium chloride in method 3 (methanol).

Table 4-1: Summary of nickel selenide particle's data from all methods

Method	**1**	**2**	**3 in CH_3OH**	**3 in H_2O**
Absorption, λ (nm)	306	298	311	297
Emission, λ (nm)	400	400	421	387
XRD patterns	Cubic $NiSe_2$	Orthorhombic NiSe	Orthorhombic NiSe	Monoclinic Ni_3Se_4
Morphology	Spherical 10-15 nm	Star shaped and amorphous	hexagonal and cubic NaCl 20-40 nm	Rod shaped, polydispersed

4.5. Conclusions

In summary method 1 produced particles with good optical and structural properties that are near monodisperse. Method 2 yielded star shaped particles that could find good application in solar cell technology because of large surface area. Method 3 was the easiest method to employ and it produced hexagonal nanoparticles when using methanol as a solvent and rod shaped particles when using water as a solvent. Due to the versatility of the methodsthe role of pH, temperature and reactant ratios will certainly impact on the optical properties and morphology of NiSe.

4.6. References

[1] Yu S.; Yang J.; Qian Y.; Yoshimura M., Chem. Phys. Lett. 2002, 361, 362 .

[2] Yang J.; Zeng J.; Yu S.; Yang L.; Zhou G.; Qian Y., Chem. Mater. 2000, 12, 3259.

[3] Zhan J.; Yang X.; Wang D., Adv. Mater. 2000, 12, 1348 .

[4] Chen Y.; Ding J.; Guo Y.; Kong L.; Li H., Mater. Chem. Phys. 2002, 77, 734 .

[5] Jun Y.; Choi J.; Cheon J., Angew. Chem. Int. Ed. 2006, 45, 3414.

[6] Li Y.; Feng J.; Daniels S.; Pickett N.; O'Brien P. J., Nanosci. Nanotechnol. 2007, 7, 2301.

[7] Viswanatha R.; Sapra S.; Amenitsch H.; Sartori B.; Sarma D.D., J. Nanosci. Nanotechnol. 2007, 7, 1726.

[8] Nag A.; Sapra S.; Chakraborty S.; Basu S.; Sarma D.D., J. Nanosci. Nanotechnol. 2007, 7, 1965.

[9] He Y.P.; Miao Y.M.; Li C.R.; Wang S.Q.; Cao L.; Xie S.S.; Yang G.Z.; Zou B.S; Burda C., Phys. Rev. 2005, B71, 125411.

[10] Burda C.; Chen X.B.; Narayanan R.; El Sayed M.A., Chem. Rev. 2005, 105, 1025.

[11] Empedocles S.A.; Neuhauser R.; Shimizu K.; Bawendi M.G., Adv. Mater.1999, 11, 1243.

[12] Empedocles S.; Bawendi M.G., Acc. Chem. Res. 1999, 32, 389.

[13] Hyeon T., Chem. Commun. 2003, 8, 927.

[14] Puntes V.F.; Krishnan K.M.; Alivisatos A.P., Science 2001, 291, 2115.

[15] Wang X.; Zhuang J.; Peng Q.; Li Y.D., Nature 2005, 437, 121.

[16] Mongeliaz F.; Fillot A.; Griot R.; De Lallee J., Proc. SPIE-Int. Soc. Opt. Eng. 1994, 56, 2227.

[17] Lakshmikvmar S.T., Sol. Energy Mater. Sol. Cells 1994, 32, 7.

[18] Korzhuev A.A., Fiz. Khim. Obrab. Mater. 1991, 3, 131.

[19] Wang W.Z.; Geng Y.; Yan P.; Liu F.Y.; Xie Y.; Qian Y.T., J. Am. Chem. Soc. 1999, 121, 4602.

[20] Xie Y.; Qian Y.T.; Zhang W.Z.; Zhang S.Y.; Zhang Y.H, Science 1996, 272, 1926.

[21] Zhuang Z.; Peng Q.; Zhuang J.; Wang X.; Li Y., Chem. Eur. J. 2006, 12, 211.

[22] Li Y.D.; Wang Z.Y.; Ding Y., Inorg. Chem. 1999, 38, 4737.

[23] Liu X.; Zhang N.; Yi R.; Qiu G.; Yan A.; Wu H.; Meng D.; Tang M., Materials Science and Engineering B 2007, 140, 38.

[24] Han Z.H.; Yu S.H.; Li Y.; Zhao H.Q.; Li Q.; Xie Y.; Qian Y.T., Chem. Mater. 1999, 11, 2302.

[25] Li B.; Xie Y.; Huang J.; Su H.; Qian Y., Nanostructured Materials 1999, 11, 1067.

[26] Panneerselvam A.; Malik M.A.; Afzaal M.; O'Brien P.; Helliwell M., J. Am. Chem. Soc. 2008, 130, 2420.

[27] Moloto N.; Revaprasadu N.; Moloto M.J.; O'Brien P.; Helliwell M, Polyhedron 2007, 26, 3947.

[28] Moloto N.; Sinha Ray S; Moloto M.J., J. Nanosci. Nanotechnol. 2008, 8, 10.

[29] Moloto M.J.; Revaprasadu N.; Kolawole G.A., O'Brien P., Malik M.A., SAJS, 101(2005) 463.

[30] Nair P.S.; Chilli M.M.; Radhakrishnan T.; Revaprasadu N.; O'Brien P.; Malik M.A., J. Mater. Science. Mater. Electr.2004, 15, 313.

[31] Moloto M.J.; Malik M.A.; O'Brien P.; Motevalli M.; Kolawole G.A., Polyhedron 2003, 22, 595.

[32] Nair P.S.; Radhakrishnan T.; Revaprasadu N.; Kolawole G.A., O'Brien P., J. Mater. Chem. 2002, 12, 1.

[33] Bawendi M.G.; Kortan A.D.; Steigerwald M.; Brus L.E., J. Chem. Phys. 1989, 91, 7282.

[34] Murray C.B.; Norris D.J.; Bawendi M.G., J. Am. Chem. Soc. 1993, 115, 8706.

CHAPTER 5: SYNTHESIS AND CHARACTERIZATION OF NICKEL SELENIDE NANOPARTICLES: SIZE AND SHAPE DETERMINING PARAMETERS

5.1. Introduction

In a nanoscale system, chemical and physical properties of inorganic crystals are highly dependent on geometrical factors such as size and shape [1-3]. Precise control of these factors allows one not only to observe unique nanocrystal properties but also to tune their chemical and physical properties as desired. Over the past years, researchers have sought out synthetic methods for the preparation of well defined inorganic nanocrystals with controllable size and shape. Gas-phase syntheses such as the vapor-liquid-solid (VLS) method and thermal evaporation methods have been utilized for the controlled fabrication of nanoparticles. Advanced nanoparticle structures with interesting geometries that include wires, tubes, ribbons, and more sophisticated shapes are good examples of the successful utilization of the gas-phase approaches [4-12].

Alternatively, the colloidal approach in liquid media provides convenient and reproducible routes for the fabrication of nanoparticles with controlled sizes and shapes [13]. This enables the resulting nanoparticles not only to be precisely tuned at the sub-10 nm scale but also to be easily dispersed in organic or aqueous media for the numerous potential applications in electronic and biological systems. For example, the size of CdSe nanospheres can be tuned from 1 to 12 nm with one nanometer resolution by controlling growth parameters. The surface capping molecules can influence the solubility of nanocrystals in typical organic or aqueous media. Along with such size controllability, anisotropic shape controllability of nanocrystals has also been attained through liquid methods [14].

High pressure solvothermal methods have been utilized to makenickel selenide [15-17]. The solvothermal method unlike most colloidal routes, avoids the use of complicated precursors. Typically a metal salt together with the chalcogenide source in the presence of a reducing agent react in a high pressure system such as an autoclave to produce the desired materials.

This method has resulted in the synthesis of various morphologies such as sea-urchin cobalt selenide, star-shaped and octahedral nickel selenide [18,19].

Unfortunately the solvothermal method lacks the ability to control particle size and has limited adaptability compared to the traditional colloidal synthetic methods. Herein we report on the synthesis of nickel selenide nanoparticles using a modified solvothermal method. The modified method excludes the use of an expensive high pressured vessel and therefore allows for the reaction to take place at atmospheric pressure. This in turn results in a highly adaptable setup that can be easily modified. The desire to have size and shape control of nanocrystals is motivated by the link between properties and potential applications. For instance, rod shaped nanoparticles in self assembled arrays are known to transfer electric charge better than spherical particles and therefore would function more efficiently in photoelectronic devices [18]. Factors such as the temperature, the monomer or precursor concentration, the solvent and etc are known to have an effect on size and shape of the nanoparticles [19].

5.2. Experimental

5.2.1. Materials

Acetone, toluene, nickel chloride, selenium, sodium borohydride, sodium hydroxide (NaOH), hydrochloric acid (HCl), ethylenediamine (en) and pyridine (py) were all purchased from Sigma-Aldrich and used as they were obtained.

5.2.2. Synthesis of the nickel selenide nanocrystals

About 12.5 mmol of selenium powder was added together with 26.5 mmol of sodium borohydride in deionized water and the mixture was stirred for 60 min at room temperature. An amount of 4.2 mmol of nickel chloride was then added. This caused an exothermic reaction and the temperature rose to 40 °C. The reaction was then allowed to stir for a further 60 min with the temperature maintained at 40 °C. The resultant precipitate was separated through centrifugation and washed several times with water and acetone and eventually allowed to dry at room temperature. The reaction parameters such as the nickel salt to selenium ratio, the time after the addition of $NiCl_2$, pH and the solvent were varied as shown in Table 5-1 – 5-4. The pH variation was carried out by the drop-wise

addition of either sodium hydroxide or hydrochloric acid to the reactant solution. The resultant precipitates were washed several times with deionized water to remove any excess ions. The solvents were also varied from water to ethylenediamine and pyridine.

Table 5-1: Reaction parameters for the molar ratio experiments

Sample	Ni:Se ratio	Temperature	Time	pH	Solvent
A_{11}	1:1	40 °C	1h	6	H_2O
B_{12}	1:2	40 °C	1h	6	H_2O
C_{13}	2:1	40 °C	1h	6	H_2O
D_{14}	1:3	40 °C	1h	6	H_2O

Table 5-2: Reaction parameters of the time experiments

Sample	Ni:Se ratio	Temperature	Time	pH	Solvent
A_{21}	1:2	40 °C	1h	6	H_2O
B_{22}	1:2	40 °C	3 h	6	H_2O
C_{23}	1:2	40 °C	6 h	6	H_2O
D_{24}	1:2	40 °C	24 h	6	H_2O

Table 5-3: Reaction parameters for the pH experiments

Sample	Ni:Se ratio	Temperature	Time	pH	Solvent
A_{31}	1:2	40 °C	1h	6	H_2O
B_{32}	1:2	40 °C	1h	7	H_2O
C_{33}	1:2	40 °C	1h	8	H_2O
D_{34}	1:2	40 °C	1h	14	H_2O
D_{44}	1:2	40 °C	1h	1	H_2O

Table 5-4: Reaction parameters for the solvent experiments

Sample	Ni:Se ratio	Temperature	Time	pH	Solvent
A_{41}	1:2	40 °C	1h	6	H_2O
B_{42}	1:2	40 °C	1h	6	en[a]
C_{43}	1:2	40 °C	1h	6	py[b]

[a]ethylenediamine, [b]pyridine

5.3. Characterization techniques

5.3.1. Optical characterization

A Perkin Elmer Lambda 75S UV-VIS-NIR Spectrophotometer was used to carry out the optical measurements. The powders were dissolved in toluene and placed in quartz cuvettes (1 cm, path length). A Perkin Elmer LS55 with a xenon lamp (150 W) and a 152 P photo multiplier tube as a detector was used to measure the photoluminescence of the particles. The samples were dissolved in toluene and placed in quartz cuvettes (1 cm path length) for spectral analysis.

5.3.2. X-ray diffraction

XRD patterns on powdered samples were measured on a Phillips X'Pert materials research diffractometer using secondary graphite monochromated Cu Kα radiation (λ = 1.54060 Å) at 40 kV/50 mA. Measurements were taken using a glancing angle of incidence detector at an angle of 2°, for 2θ values over 10° – 80° in steps of 0.05° with a scan speed of 0.01° 2θ.s^{-1}.

5.3.3. Electron microscopy

Nickel selenide samples were characterized using a field emission scanning electron microscope (FE-SEM)(Leo, Zeiss), operated at 3-10 kV electron potential difference and equipped with a semiconductor detector that allows for detection of energy dispersive X-rays (EDX). The samples were prepared by placing a drop of suspended particle in methanol, on a carbon tape. The samples were then allowed to dry at room temperature. The high resolution transmission electron microscopy (HRTEM) measurements were carried out on a Joel JEM-2100 microscope with a LAB6 filament. The measurements were carried out at 200 kV with a beam spot size of 20 - 200 nm in TEM mode.

5.4. Results and discussion

5.4.1. The effect of molar ratio on the size and shape of nickel selenide nanocrystals

The band-gap is an important characteristic of a semiconductor. In semiconductors of macroscopic sizes, the width of this gap is a fixed parameter, which is determined by the material's identity. However, in semiconductor nanoparticles the band-gap is a function of the particle size. As the nanocrystal size decreases, the band-gap increases, leading, in particular, to a blue shift of the absorption wavelength. The size of the nanocrystal is therefore crucial in determining the properties of the material, and it is for this reason that control of this feature is studied. Size control is hugely dependent on the growth mechanism of the nanocrystal. Each growth stage can be controlled and manipulated to yield a certain size. Generally, the growth mechanism of the nanocrystal is understood in terms of La Mer and Dinegar's studies of colloidal particle nucleation and growth [20]. The nucleation stage of the growth process is usually fast, followed by the slow growth stage. Both these stages are susceptible to the reaction environment. Therefore in this study factors that affect the reaction environment are monitored and their influences on the properties of the nanoparticles are investigated.

Nickel selenide is a p-type semiconductor with a bulk energy band-gap of 2.0 eV (620 nm). Because it is a Pauli magnet a much of interest has been directed to the synthesis of nickel selenide [21]. The nickel selenide reported in this study was synthesized by reacting nickel chloride with sodium borohydride reduced selenium. This method previously reported by us provides a robust and quick route for the formation of nickel selenide nanoparticles [22]. It has long been established that concentration has an effect on the resultant properties of nanomaterials. Various studies especially of CdS nanoparticles have shown that at higher monomer concentrations anisotropic morphologies are favored and these result in different electronic spectra compared to isotropic morphologies [19,23]. Hydrothermal syntheses of metal selenides with varying reactant ratios have also been conducted and these have resulted in rather big particles with unusual morphologies [24]. Because nickel can exhibit different oxidation states, it is of particular interest to explore, in a controlled manner the preferred stoichiometries of nickel selenide. Synthesis of nickel selenide with varying molar concentrations of nickel and selenium are hereby reported herein.

The optical properties of nickel selenide prepared at different reactant ratios are shown in Fig. 5-1. The particles with the 1:1 Ni:Se ratio in Fig. 5-1(a) shows two absorption shoulders and has an energy band-edge located at 528 nm. The band-edge is blue-shifted from the bulk band-edge of 620 nm. This is indicative of quantum size effects. The second shoulder is attributed to agglomerated particles and it is not as prominent as the first shoulder. The corresponding emission spectrum shows a single Gaussian peak centered around 590 nm. The symmetric shape of the curve is indicative of a relatively monodispersed sample. The particles synthesized with 1:2 molar ratio shows similar features to those synthesized with 1:1 Ni:Se ratio. The absorption band-edge is also blue-shifted and located at 525 nm whilst the emission maximum is located at 582 nm. The further blue-shift of both the absorption and emission spectra is indicative of smaller particle sizes compared to the 1:1 ratio sample. The absorption and emission spectra of particles synthesized from a 2:1 and 1:3 Ni:Se ratios are shown in Fig. 5-1(c) and (d) respectively. The absorption spectra of both samples show multiple shoulder peaks and tailing which is indicative of poly-dispersed samples. The emission spectra have a similar shape that deviates from a Gaussian distribution confirming the poly-dispersity of the samples. The maxima are located at 600 nm.

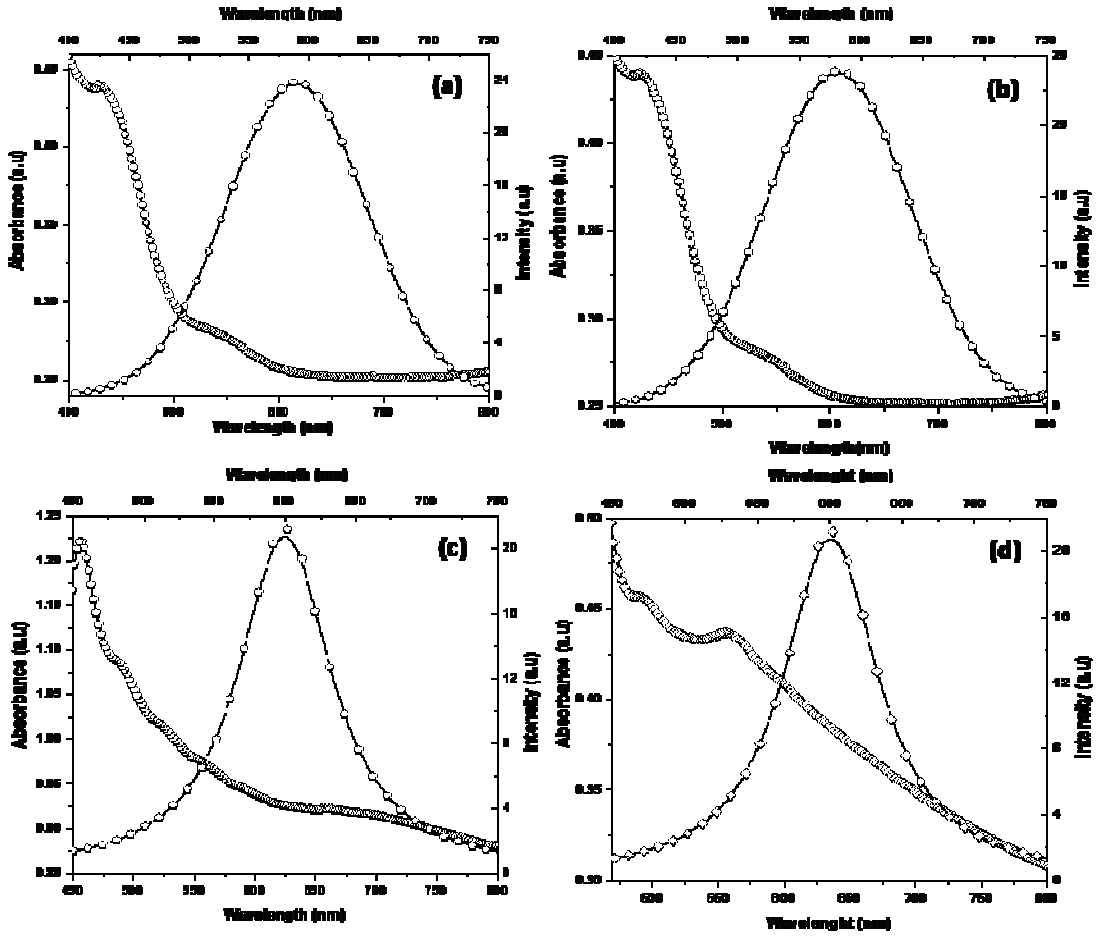

Fig. 5-1: Absorption and photoluminescence spectra of nickel selenide nanoparticles synthesized at various times.

The morphologies of the particles were established by SEM and HRTEM studies. The results are depicted in Fig. 5-2. The particles synthesized from a 1:1 Ni:Se ratio are elliptic in shape (μ= 7 nm) and show some degree of agglomeration. The crystal fringes seen in the HRTEM images are indicative of a crystalline sample. The particles synthesized from a 1:2 molar ratio are similar in shape to those synthesized using 1:1 ratio. Though similar, the particles synthesized from a 1:2 ratio are smaller (μ = 3 nm) and well dispersed. This is in agreement with the optical results. The particles synthesized from a 2:1 ratio shows bigger quasi-spherical particles together with smaller spheres resembling the one reported from 1:1 and 1:2 ratios.

It appears that high doses of nickel ions favour the formation of larger particles; this could be as a result of the excess nickel forming another nickel selenide core on top of an existing nickel selenide particle. In that case, the crystal phase of the particles is expected to remain the same. However the particles synthesized from 1:3 Ni:Se molar ratio show two distinct particle populations. The excess selenium could result in generating samples containing selenium as inpurity. The solubility of selenium in water is low. The EDX analysis performed on the sample could not differentiate whether the presence of selenium was due to elemental selenium or nickel selenide.

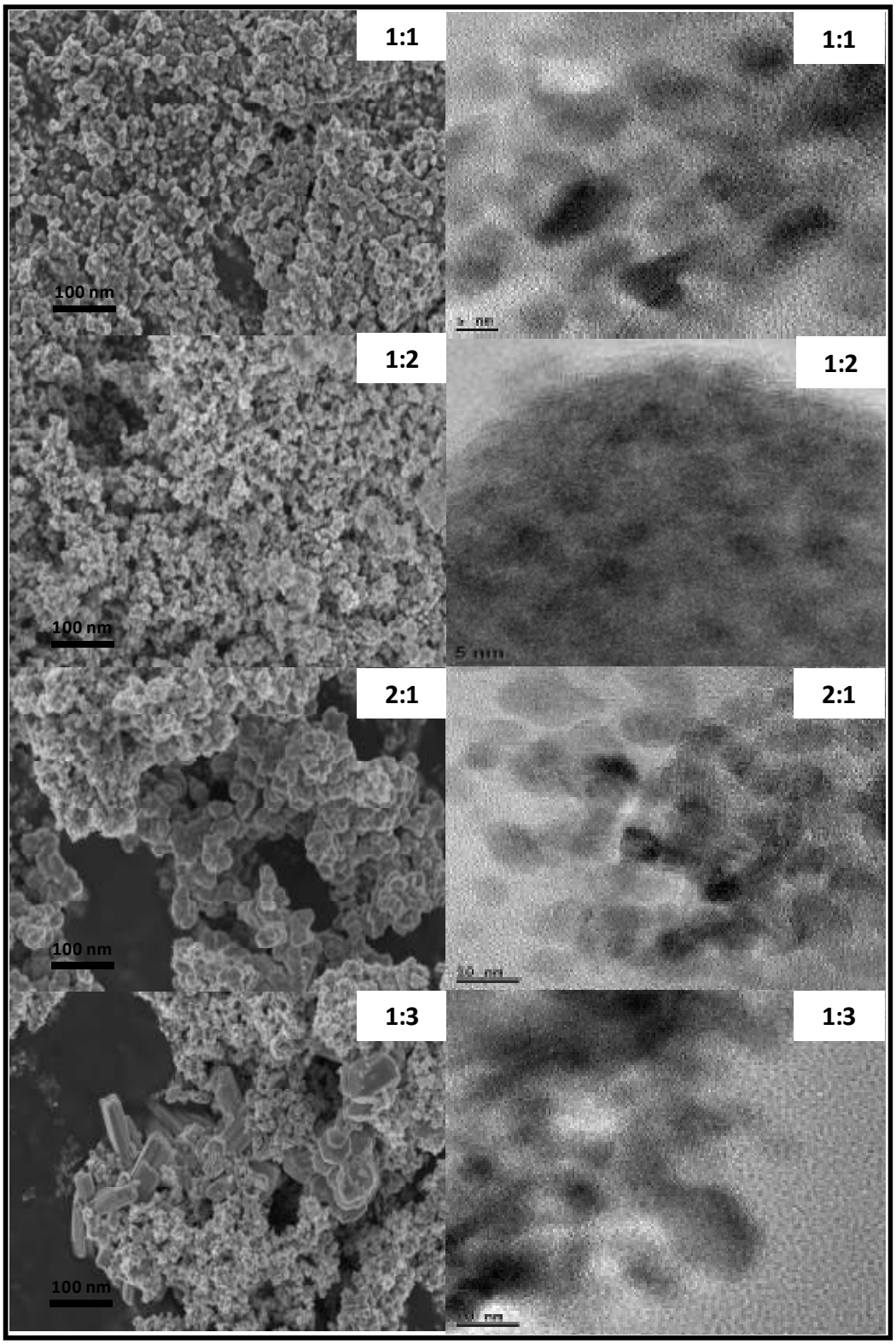

Fig. 5-2: SEM and HRTEM micrographs of nickel selenide particles synthesized in a 1:1, 1:2, 2:1 and 1:3 Ni:Se ratio respectively.

The particles were then characterized by XRD to establish their crystal phase as well as to consolidate the SEM and HRTEM results. The XRD patterns are shown in Fig. 5-3. The 1:1, 1:2 and 2:1 ratios resulted in particles with a hexagonal $Ni_{0.95}Se$ phase (JCPDS card: 72-2546). The small differences observed in the optical results and morphologies between the 1:1 and 1:2 ratios are attributed to the possible electrostatic attraction for the 1:1 ratio particles due to insufficient selenium ions ultimately resulting in some agglomeration of the particles. The particles synthesized from a 1:3 Ni:Se ratio were indexed to a monoclinic Ni_3Se_4 phase (JCPDS card: 89-2020). The peaks at $2\theta = 23.3°$ and 29.8° with the hkl values (100) and (101) respectively were established as that of selenium (JCPDS card: 06-0362). The presence of selenium could then ascertain the rod shape particles as that of selenium. As a result of the quality of the particles synthesized with a 1:2 Ni:Se molar ratio being better than the other ratios, subsequent preparations were carried out at this ratio.

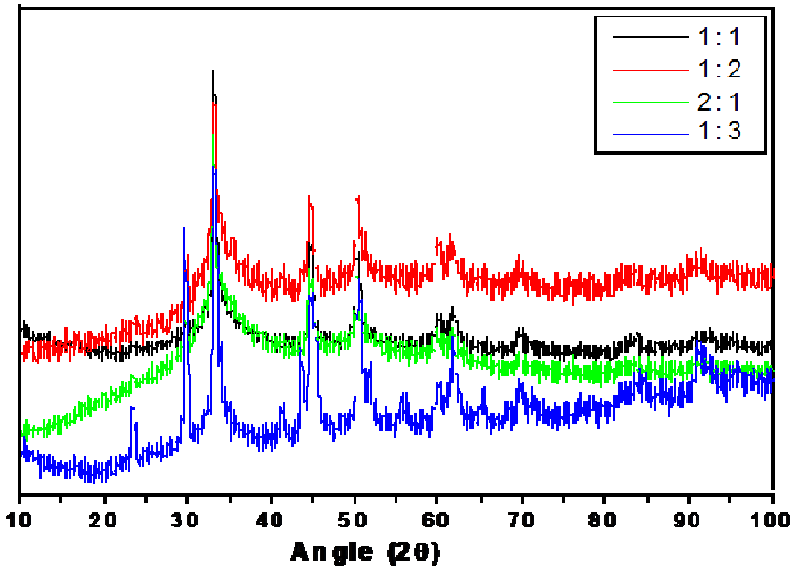

Fig. 5-3: XRD patterns of nickel selenide synthesized at different Ni:Se molar ratios.

5.4.2. The effect of reaction time on the size and shape of nickel selenide nanocrystals

The effect of time on the properties of CdS quantum dots has been well studied. It has been reported that longer reaction times yield larger particles due to the facilitation of the Ostwald ripening process [23]. However, to our knowledge no work has been reported on the influence of time on the properties of nickel selenide especially using the above mentioned method. The absorption and photoluminescence spectra of nickel selenide

synthesized at various times are depicted in Fig. 5-4. The absorption spectrum of particles synthesized after 1h shows a single absorption peak that is blue-shifted from the bulk bang-edge to 525 nm. The blue-shift in the band-edge is indicative of the size being in the nano-scale size regime. The photoluminescence spectrum of the particles synthesized after 1 h shows an emission peak with a maximum located at 582 nm. The emission Gaussian shape and the narrow size distribution show no indication of surface defects. This has been established in Fig. 5-1 as well.

As the synthetic time is prolonged to 3 h, there are changes in the observed features of the absorption spectrum. There is a noticeable presence of two peaks which is possibly as the result of either the internal optical transitions or from the presence of two particle populations. The first absorption peak is located at 520 nm, which is similar to the observed wavelength for the particles synthesized after 1h. The second peak is more red-shifted and located at approximately 625 nm. The photoluminescence spectrum is consistent with the absorption spectrum by also depicting two peaks.

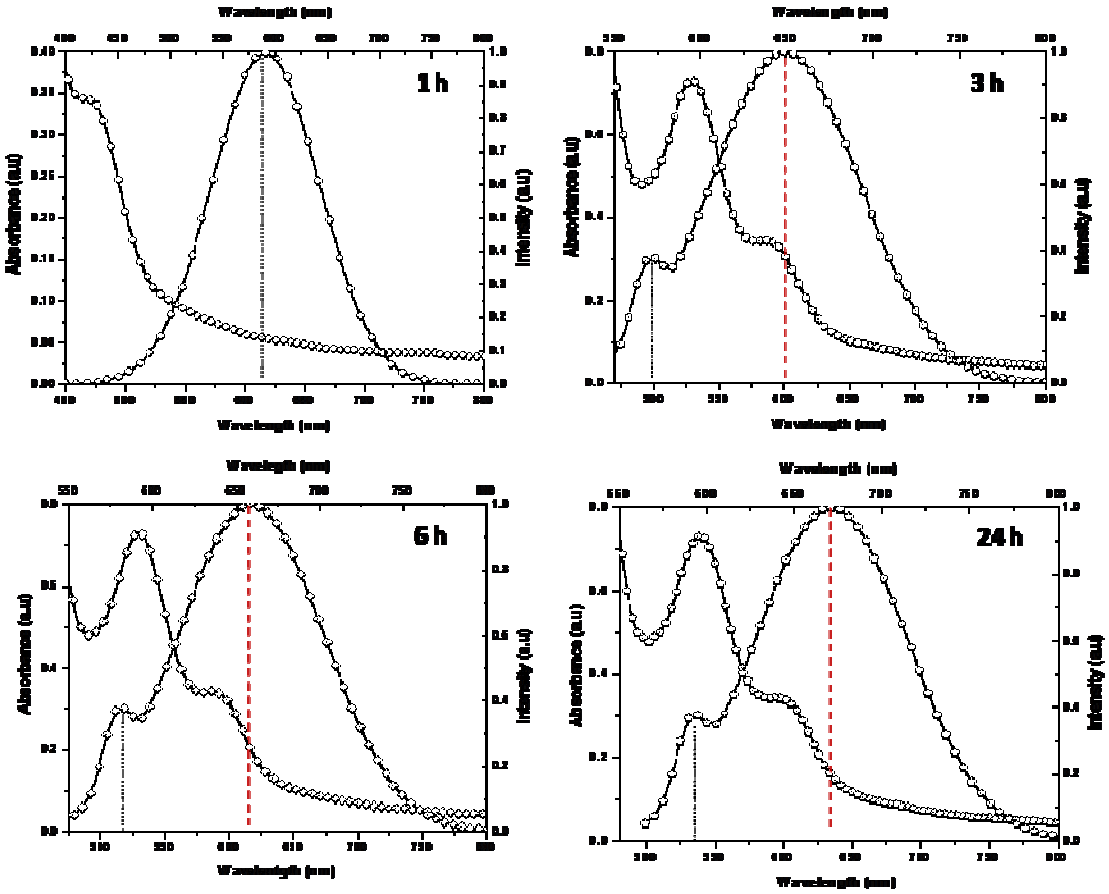

Fig. 5-4: Absorption and photoluminescence spectra of nickel selenide nanoparticles synthesized at various times.

The first emission peak located at 562 nm is associated with the first population of the nanoparticles and is red-shifted from the corresponding absorption band-edge by a Stoke shift of 42 nm. This is a readily observed phenomenon. The second emission peak located at 650 nm validates the existence of two populations of particles. It further eludes that the size of the particles is larger than the first population and that the size is approaching that of the bulk. The area under the photoluminescence peaks also suggests that there is more prevalence of the bigger particles in the sample compared to the smaller ones. As the time is extended to 6h and 24h, the same trend is observed. There is a slight red-shift of the absorption peaks with time. This is expected as the elongation of time result in the formation of larger particles. Prolonged reaction times enable further addition of the

monomers to the existing nuclei and facilitate growth through the Ostwald repining process. The summary of the optical properties is shown in Table 5-5.

The morphology and the crystal phase of the particles were investigated with SEM, HRTEM and XRD. The SEM and HRTEM micrographs of the particle synthesized at different times are shown in Fig. 5-5. The SEM micrograph of the particles synthesized within 1 h shows agglomerates of small spherical nanoparticles. The particles show a very narrow size distribution which is in agreement with the corresponding optical properties. The HRTEM confirms the observed morphology and depict crystal fringes that are indicative of the crystalline nature of the material. As the time is extended to 3 h, two populations of particles are observed, as predicted by the absorption and photoluminescence properties. The first population constitutes of small spherical particles similar to those observed in the 1 h synthesis. The second population consists of larger fused cylindrical particles as shown on the SEM and HRTEM. The position of the second absorption peak is justified as the fused particles are well over 100 nm in size. Similarly the particles synthesized after 6 h shows two sets of particles with the first particles resembling the one synthesized after 1 h. The second set of particles depicts a unique morphology that seems to be self-assembling to form "stem with nodes" like morphologies. The same trend of two populations is continued for the particles synthesized after 24 h, though the observed morphology is different. The morphology of the second population appears to be a coagulation of very small particles that assembly to form roundish towers and these towers in turn join to form pillars. The EDX was performed on the individual population for all the samples and they portrayed the presence of both nickel and selenium.

Table 5-5: Summary of the optical properties observed at different reaction time.

Time	*Abs λ_1 (nm)*	*Abs λ_2 (nm)*	*PL λ_1 (nm)*	*PL λ_2 (nm)*
1 h	525	-	582	-
3 h	520	625	562	650
6 h	525	614	580	670
24 h	535	630	585	674

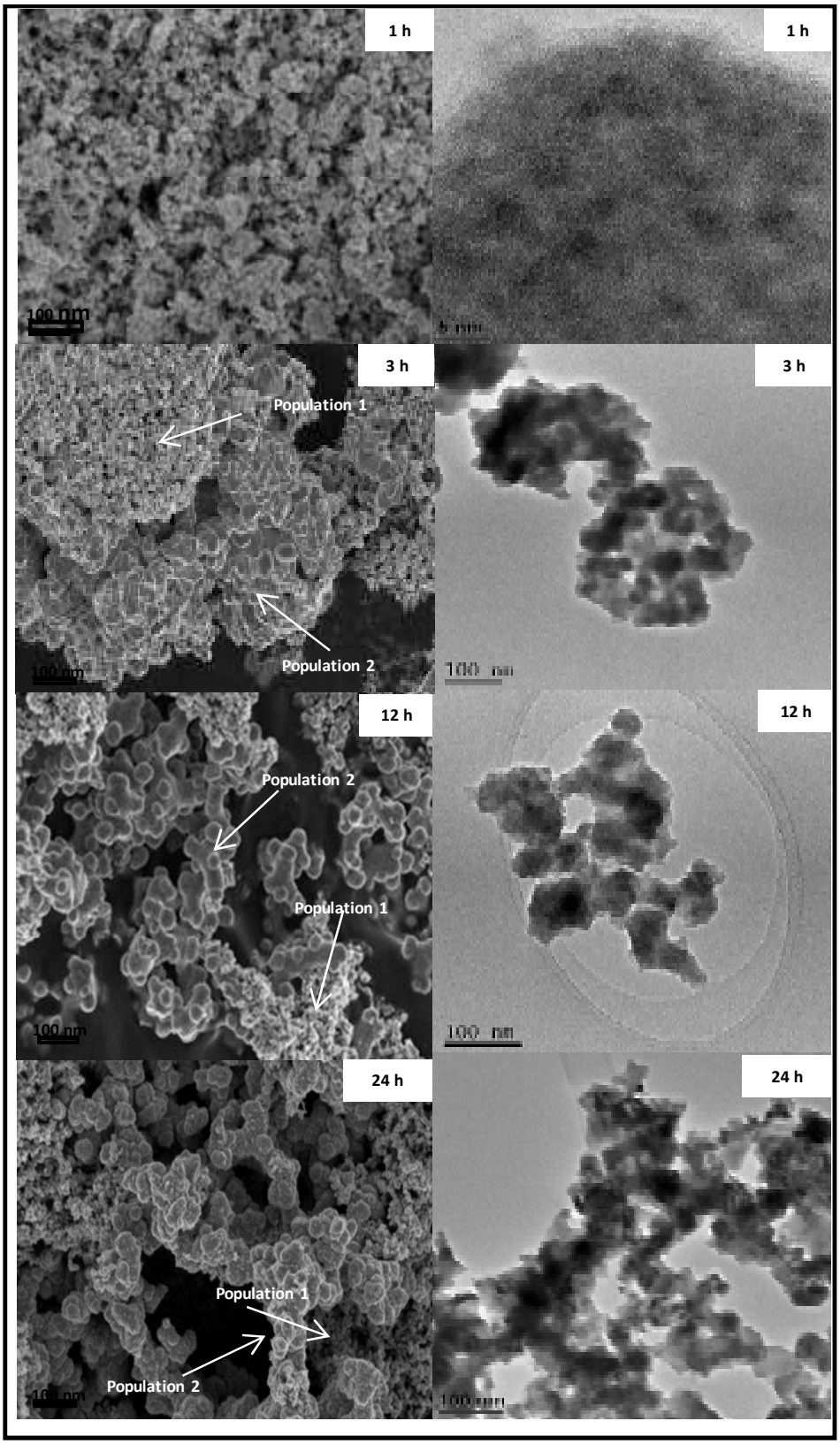

Fig. 5-5: SEM and HRTEM micrographs of nickel selenide particles synthesized after 1h, 3h, 6h and 24h respectively.

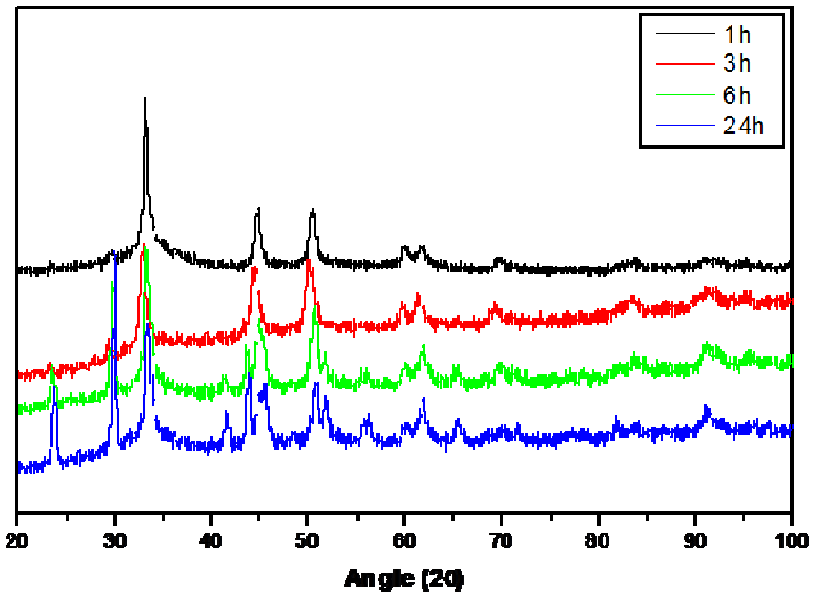

Fig. 5-6: XRD patterns of nickel selenide synthesized at different times.

The X-ray diffraction studies were conducted to ascertain the crystal phases of the particles. The XRD patterns for the corresponding samples are shown in Fig. 5-6. The samples synthesized after 1 h and 3 h have a similar XRD pattern and they are indexed to a hexagonal $Ni_{0.95}Se$ phase (JCPDS card: 72-2546). The particles synthesized for 6 h and 24 h were indexed to a slightly more complex system of monoclinic Ni_3Se_4 (JCPDS card: 89-2020). The peaks at $2\theta = 23.3°$ and 29.8° correspond to the selenium diffraction planes of (100) and (101) respectively (JCPDS card: 06-0362). The amount of selenium appears to be low for particles synthesized for 1 h and 3 h as validated by the small peak heights and the reverse can be said for the particles synthesized after 6 h and 24 h. From the observed diffractograms in Fig. 5-6, it can be concluded that there is a direct relationship between the amounts of residual selenium and the crystal phases. At shorter reaction times, almost all of the reactants are converted to products. On the other hand, at longer reaction times the reaction equilibrium shifts to the right resulting in the precipitation of selenium.

$$2NaBH_4 + Se + NiCl_2 \rightleftharpoons NiSe + 2NaCl + B_2H_6 + H_2$$

5.4.3. The effect of pH on the size and shape of nickel selenide nanocrystals

The pH of the solution plays a major role in the synthesis of semiconductor nanoparticles because it can influence the rate of the formation of the nuclei during the nucleation stage. Depending on the pH, the solubility of the monomers can be affected. This can therefore have an effect on the resultant properties of the nanoparticles. The effects of pH on the optical and morphological properties of the as-prepared nickel selenide are reported herein.

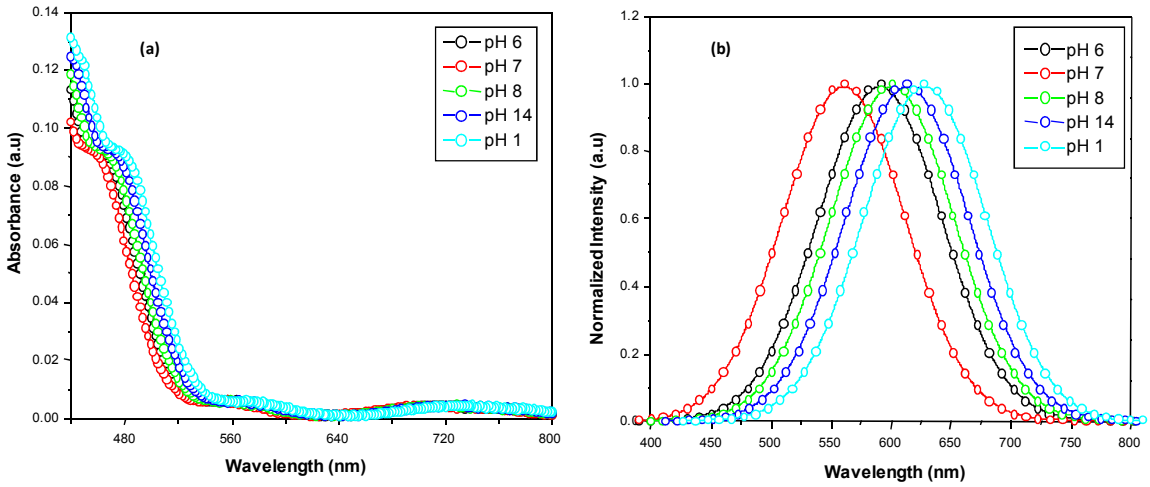

Fig. 5-7: Absorption and photoluminescence spectra of nickel selenide nanoparticles synthesized at differentpH values.

The results from the absorption and photoluminescence spectroscopy study are shown in Fig. 5-7. The synthesis of nickel selenide reported above prior to any addition of either NaOH or HCl occurs at pH 6. At this pH the resultant particles absorb the radiation at 525 nm which is blue-shifted from the bulk band-edge of 620 nm as earlier established (Fig. 5-1). As the pH is increased to a neutral pH 7, the absorption band-edge is blue-shifted from that of pH 6 and the same trend is observed for the emission spectrum. When the pH is varied from pH 8 to pH 14 and pH 1, there is a progressive red-shifting of the absorption band-edge and the emission maximum compared to the nanoparticles synthesized at pH 7. It has been reported that synthesis of metal selenide nanoparticles involving the use of elemental selenium is highly pH dependent and often results in the selenium being very reactive in the pH range of 7-10. At pH values outside this range non-reacted selenium precipitates from solution [25]. As the pH falls out of this ideal range, the formation of larger nuclei is

favoured due to the decrease in monomer concentration that is limited by the amount of available selenium ions. Larger nuclei in turn result in the formation of larger particles during the growth stage of the particles thus explaining the observed red-shift.

The morphological properties are shown in Fig. 5-8 and Fig. 5-9. The XRD diffraction patterns for particles synthesized at pH 6, 7, 8 and 14 are all indexed to a $Ni_{0.95}Se$ phase (JCPDS card: 72-2546) whilst the particles synthesized at pH 1 are indexed to amonoclinic Ni_3Se_4 (JCPDS card: 89-2020). The XRD pattern of particles synthesized at pH 1 show evidence of selenium being present as depicted by the peaks at 2θ = 23.3° and 29.8°. It appears that the method of synthesis is rather pH tolerant as the deviation from the preferred phase is only observed at pH 1 which is 6 pH units outside the preferred pH range.

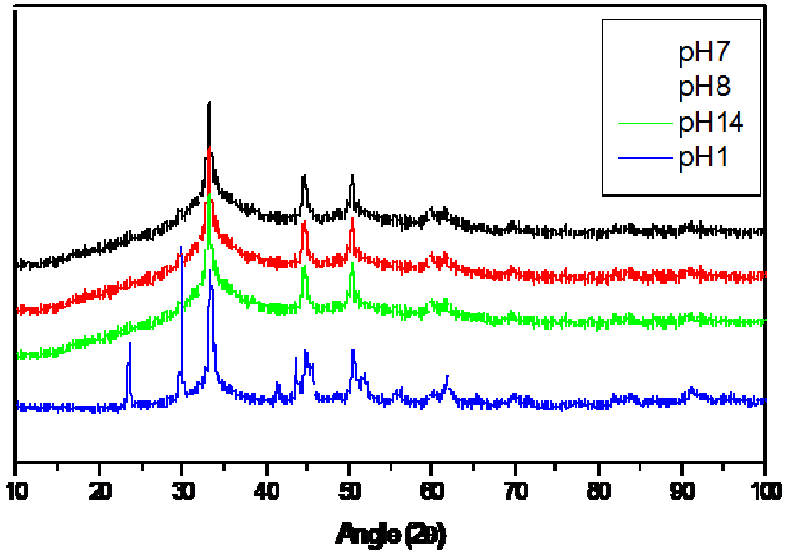

Fig. 5- 8: XRD patterns of nickel selenide synthesized at different pH values.

The morphologies of the particles are shown in Fig. 5-9. The particles synthesized at pH 6, pH 7 and pH 8 form spheres. It is evident from the SEM images that the particles synthesized at pH7 are smaller in size and have a higher degree of mono-dispersity compared to those synthesized at pH 6 and pH 8. This is consistent with the data from the observed absorption and photoluminescence wavelengths. The particles synthesized at pH 14 are highly agglomerated and show some degree of facet formation. At pH 1 the particles

show a cubic morphology. The TEM micrographs (not shown) look similar and have indistinguishable features. It emerges and it can be concluded, that the pH has an influence on the resultant nanoparticles but the influence is not so drastic compared to changes imposed by other reaction parameters such as time, temperature, etc.

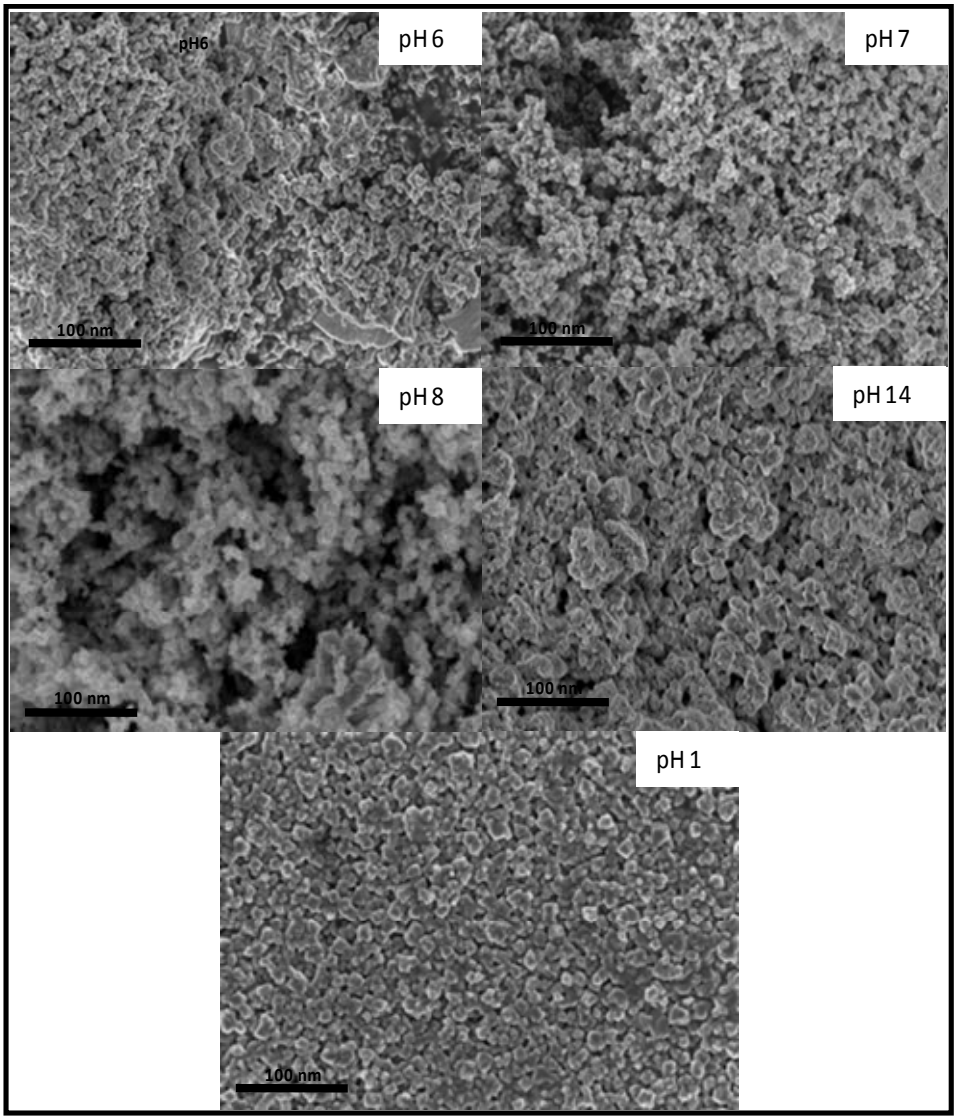

Fig. 5-9: SEM micrographs of nickel selenide nanocrystals synthesized at different values of pH.

5.4.4. The effect of solvent on the size and shape of nickel selenide nanocrystals

In the synthesis of colloidal semiconductor nanocrystals, the solvent usually plays a dual role. Firstly it solvates the reactants in order for sufficient collisions to occur between the reactants to ultimately result in the formation of the desired products. Secondly it can coordinate around the nanoparticles thus preventing agglomeration and stabilizing the particles. The optical properties of the nickel selenide synthesized in water, ethylenediamine and pyridine are shown in Fig. 5-10. The particles synthesized in water (Fig. 5-10(a)) show a single absorption peak that is blue-shifted from bulk nickel selenide and shows a characteristic emission curve as earlier indicated from Fig. 5-1. Alternatively when the synthesis occurs in ethylenediamine, the absorption and photoluminescence spectra depicted in Fig. 5-10(b) have significantly different features from those in Fig. 5-10(a). The absorption spectrum has multiple peaks possible arising from the presence of amines. Amines are known to absorb UV radiation at wavelengths below 350 nm. Nevertheless, the absorption band-edge is still blue-shifted (420 nm) and the size of the nanoparticles is expected to be smaller than those synthesized in water as a result of the further blue-shift of the band-edge.

The photoluminescence spectrum shows a single peak that has a slight deviation from the Gaussian distribution. The presence of impurities can be caused by the scattering of light that can ultimately affect the peak shape. The optical properties of particles synthesized in pyridine are shown in Fig. 5-10(c). The absorption spectrum shows multiple shoulder peaks and a very broad peak centered on 550 nm. This is attributed to the poly-dispersity of the sample. The photoluminescence spectrum also portrays a shoulder peak at 450 nm and an intense peak centered on 650 nm. This therefore signifies that the emission stems from nanoparticles of different sizes. The area under the peaks is an indication of the size population distribution.

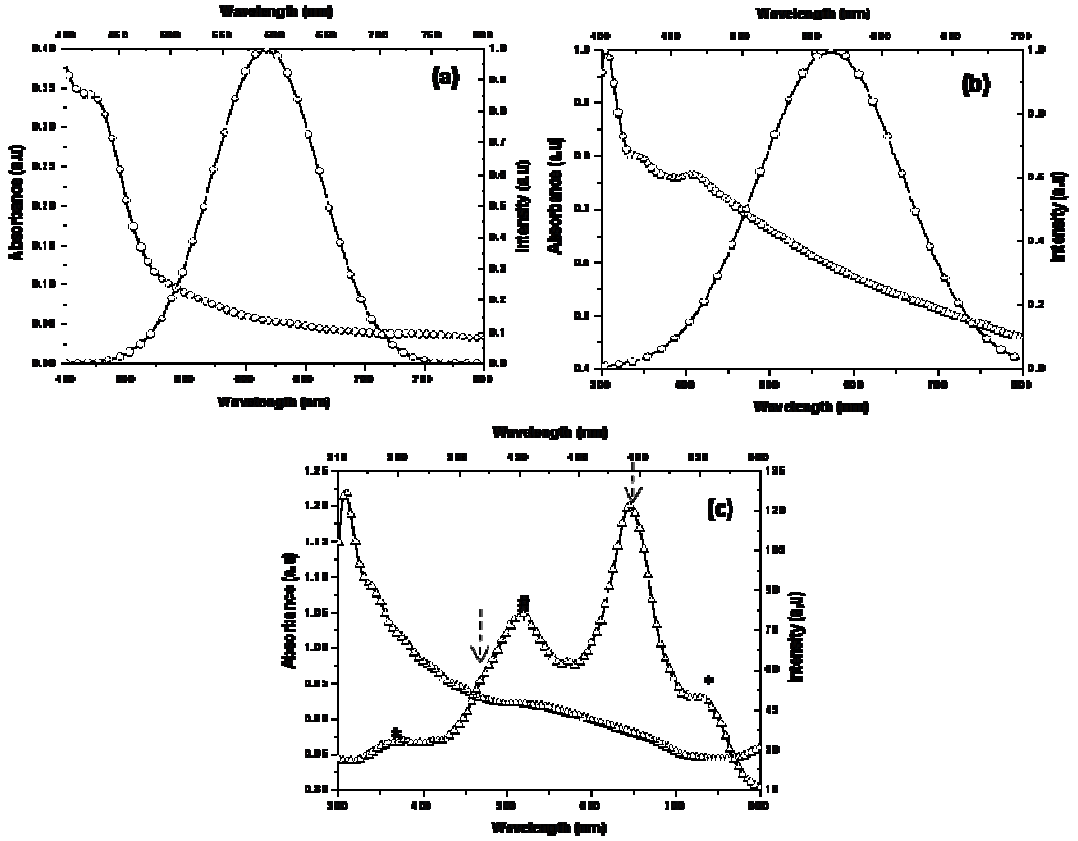

Fig. 5-10: UV-Vis absorption and photoluminescence spectra of nickel selenide synthesized using different solvents; (a) water, (b) ethylenediamine and (c) pyridine. *Toluene and #second order excitation.

Structural characterization was undertaken to establish the crystal make-up of the nanoparticles as well as their morphologies. The SEM and HRTEM micrographs are shown in Fig. 5-11. The particles synthesized in water are spheres with diameters of approximately 5 nm. The ethylenediamine synthesis yielded very small particles that are embedded in an organic layer as shown in the SEM micrograph. The HRTEM image shows an agglomerate of particles covered with an amorphous carbon layer. On the other hand, the pyridine synthesized particles show a mixture of spherical and cubic shaped particles of various sizes. The presence of particles with various dimensions and shapes concurs with observed optical properties. The lattice fringes shown on HRTEM are indicative of the crystalline nature of the particles.

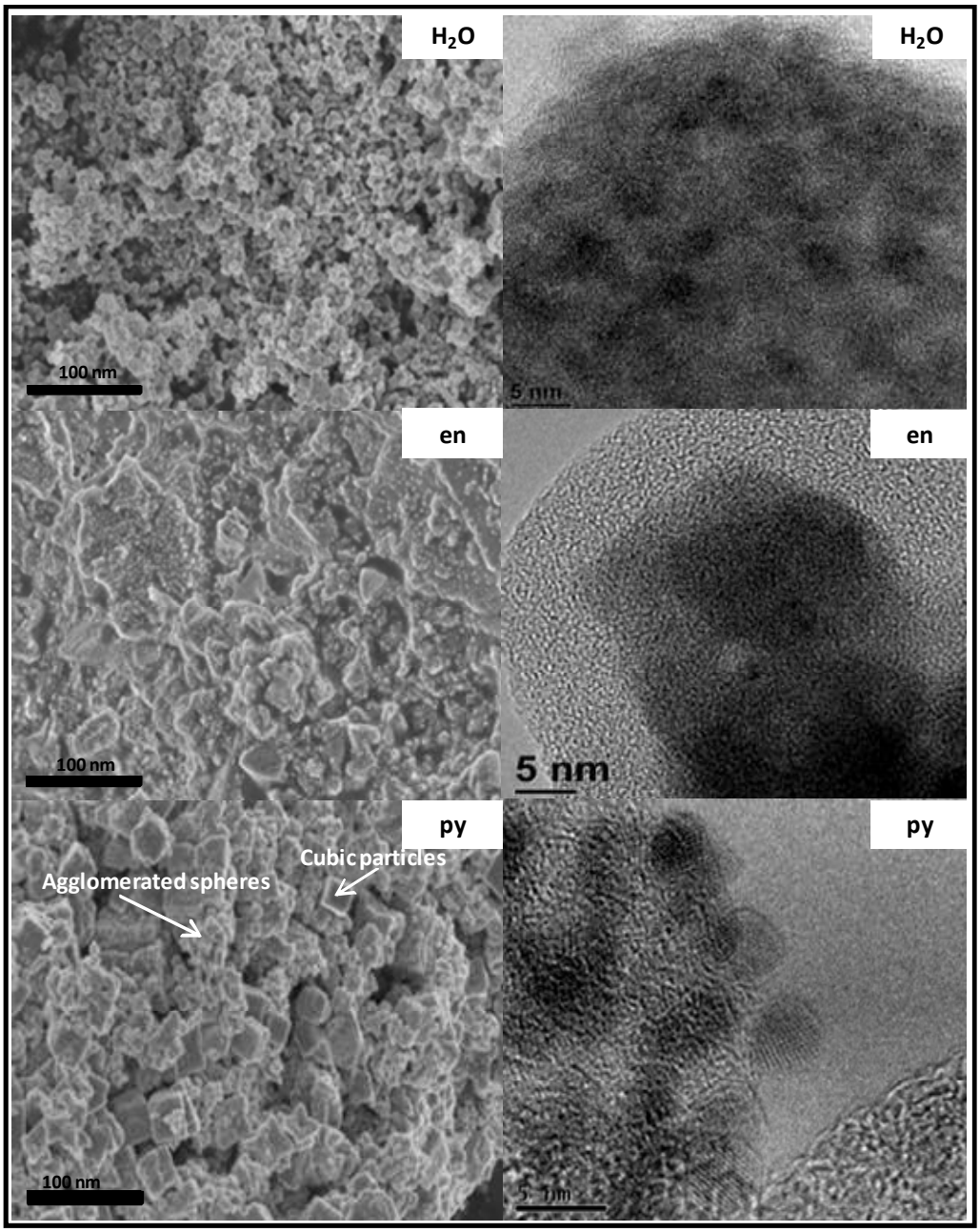

Fig. 5-11: SEM and HRTEM micrographs of nickel selenide nanocrystals synthesized in different solvents.

The difference in morphologies of the particles in different solvents relate to the nucleophilic strength of each solvent. During the nucleation phase of the nanocrystal growth, it has been reported that the solvent has a tendency to absorb to the surface of the growing nuclei and form a corresponding complex $Ni_xSe_y(L)_n$ where L= solvent molecules [26] Zhang et al. reported that complex ions with bidentate ligands such

ethylenediamine could be linked through hydrogen bonds in the polyamine donor solvents, and self-assembled to a chain structure. The steric hindrance, limitation of spatial structure and the chain structure of the intermediate molecular building blocks could influence the preferential growth towards nanorods and dendrites [26-28]. When single-dentate nucleophiles such as pyridine and water are substituted for the bidentate solvents, the ability of forming the intermediate molecular building blocks via hydrogen bonds between 'N' ofone amine molecule and 'H' of another amine molecule for example, become greatly weaker, and hence only quasi-spherical or other irregular aggregates of nanoparticles are formed. In this study it appears that the chelating ability of the ligand results in the ethylenediamine binding with both ends to the surface of the nanocrystals thus yielding quasi-spherical particles. The extra coating around the particles results from the excess solvent.

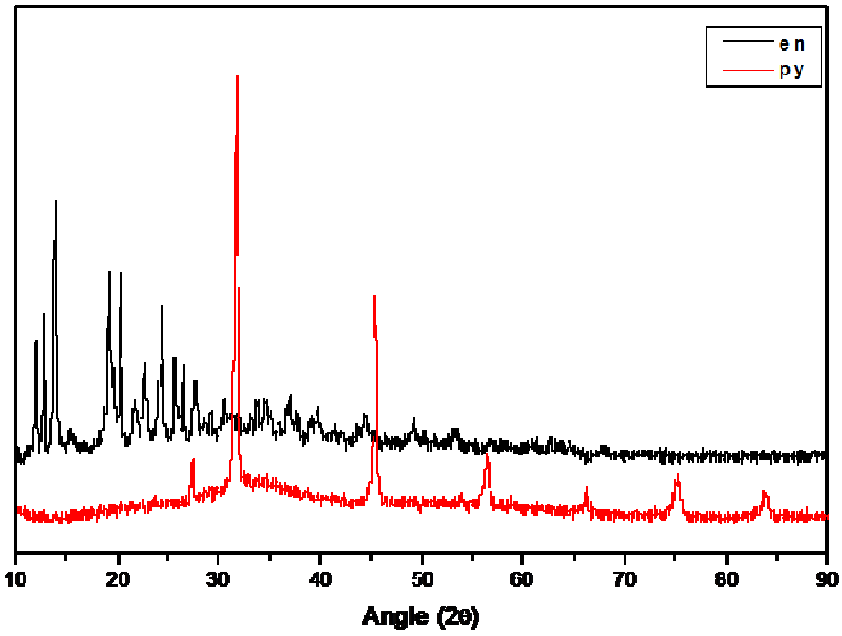

Fig. 5-12: XRD patterns of nickel selenide nanoparticles synthesized in ethylenediamine and pyridine.

X-ray diffraction analysis was done on the particles in order to establish their crystallinity, the phase composition of the particles as well as any presence of impurities. The XRD diffractograms are shown in Fig. 5-12. The particles synthesized in water as previously discussed exist in a hexagonal $Ni_{0.95}Se$ phase.The ethylenediamine synthesized nickel

selenide was indexed to an orthorhombic Ni_6Se_5 phase (JCPDS card: 19-0842). The diffraction peaks 2θ = 11.48°, 19.28°, 20.17°, 21.63°, 25.59°, 30.50°, 33.74°, 34.65° and 36.64° were indexed to (002), (022), (004), (023), (024), (025), (114), (130) and (132) respectively. The non-indexed peaks are the diffraction of impurities. The composition of the impurities could not be resolved. The diffraction pattern of the particles synthesized in pyridine show no evidence of impurities. The diffraction peaks are slightly broader signifying small crystallite sizes. The particles were indexed to an orthorhombic Ni_5Se_5 phase (JCPDS card: 71-2279) with the positions 2θ = 27.24°, 31.77°, 45.15°, 56.18°, 66.13°, 75.17° and 84.04° corresponding to the hkl values of (111), (006), (028), (0210), (244), (263) and (1512) respectively. Both the ethylenediamine and the pyridine synthesized nanoparticles exist in rare forms of nickel selenide. This could be as the result of the solubility of the precursor in these solvents being enhanced or their nitrogen binding modes.

5.5. Conclusions

Varying the reaction parameters such as concentration, time, pH and solvent had enormous influences on the properties of nickel selenide nanoparticles. The optical properties, size, shape and phase of the particles showed some degree of dependence on the Ni:Se molar ratio. The amount of selenium present was the determining factor. Lack of selenium as in the 1:1 ratio resulted in a buildup of partial-charge on the surface of the dots thus causing them to agglomerate. Alternatively excess selenium resulted in the precipitation of rod-shaped selenium particles together with spherical $Ni_{0.95}Se$ nanoparticles. The size and shape of the nickel selenide nanoparticles varied with time. The short reaction times yielded smaller mono-dispersed nanoparticles whilst an increase in times resulted in two populations of particles being formed with various morphologies. The variation of pH resulted in particles with similar properties, although at pH 1, the high acidity of the reaction resulted in the formation of fairly faceted particles. The effect of solvent was also investigated. The synthesis in water resulted in mono-dispersed spherical shaped particles whilst the ethylenediamine synthesized particles resulted in very small particles coated with an external carbon layer. The particles synthesized in pyridine on the other hand resulted in poly-dispersed particles with spherical and cubic morphologies.

5.6. References

[1] Alivisatos A.P., Science 1996, 271, 933.

[2] Brus L.E., J. Chem. Phys. 1984, 80, 4403.

[3] Markovich G.; Collie C.P.; Henrichs S.E.; Remacle F.; Levine R.D., J.R. Heath, Acc. Chem. Res.1999, 32, 415.

[4] Hu J.; Odom T.W.; Lieber C.M., Acc. Chem. Res. 1999, 32, 435.

[5] Yang P., MRS Bull. 2005, 30, 85.

[6] Law M.; Goldberger J.; Yang P., Annu. ReV. Mater. Res. 2004, 34, 83.

[7] Bakkers E.P.A.M.; Verheijen M.A., J. Am. Chem. Soc. 2003, 125, 3440.

[8] GoldbergerJ.; He R.R.; Zhang Y.F.; Lee S.W.; Yan H.Q.; Choi H.J.; Yang P.D., Nature 2003, 422, 599.

[9] Pan Z.W.; Dai Z.R.; Wang Z.L., Science 2001, 291, 1947.

[10] Kong X.Y.; Ding Y.; Yang R.S.; Wang Z.L., Science 2004, 303, 1348.

[11] Saito Y.; Matsumoto T., Nature 1998, 392, 237.

[12] Gao P.X.; Wang Z.L., J. Phys. Chem. B 2004, 108, 7534.

[13] Murray C.B.; Norris D.J.; Bawendi M.G., J. Am. Chem. Soc. 1993, 115, 8706.

[14] Trentler T.J.; Goel S.C.; Hickman K.M.; Viano A.M.; Chiang M.Y.; Beatty A.M.; Gibbons P.C.; Buhro W.E., J. Am. Chem. Soc. 1997, 119, 2172.

[15] Xie Y.; Qian Y.T.; Zhang W.Z.; Zhang S.Y.; Zhang Y.H., Science1996, 272, 1926.

[16] Zhuang Z.; Peng Q., Zhuang J.; Wang X.; Li Y., Chem. Eur. J.2006, 12, 211.

[17] Li Y.D.; Wang Z.Y.; Ding Y., Inorg. Chem. 1999, 38, 4737.

[18] Liu X.; Zhang N.; Yin R.; Qui G.; Yan A.; Wu H.; Meng D.; Tang M., Mater Sci. & Eng. B 2007, 140, 38.

[19] Moloto N.; Moloto M.J.; Coville N.J.; Ray S.S., J. of Cryst. Growth 2009, 311, 3924.

[20] Lamer K.V.; Dinegar R.H., Am. Chem. Soc. 1950, 72, 4847.

[21] Wang X.; Zhuang J.; Peng Q.; Li Y.D., Nature 2005, 437, 2115.

[22] Moloto N.; Revaprasadu N.; Musetha P.L.; Moloto M.J., J. Nanosc. Nanotech. 2009, 9, 4760.

[23] Jun J.; Lee S.M.; Cheon N.J., J. Am. Chem. Soc. 2001, 123, 5150.

[24] Liu X.; Zhangi N., Qui G.; Yan A.; Wu H.; Meng D.; Tang M., Mat. Sci. and Eng. B 2007, 140, 38.

[25] Matsai Y.; Polsky R.; Koltypin Y.; Gedanken; Hodes G., J. Am. Chem. Soc. 1999, 121, 10047.

[26] Zhang Y.C.; Wang G.Y.; Hu X.Y., J. Alloys and Comp. 2007, 437, 47.

[27] Gorai S.; Ganguli D., Chaudhuri S., Cryst. Growth Des. 2005, 5, 875.

[28] Li B.; Xie Y.; Huang J., Nanostruct. Mater. 1999, 11, 1067.

CHAPTER 6: SYNTHESES AND CHARACTERIZATION OF QD-POLYMER NANOCOMPOSITES FOR POTENTIAL OPTO-ELECTRONIC APPLICATIONS

6.1. Introduction

Over the last few years, there has been a great deal of research interest in the synthesis of quantum dots (QDs) incorporated in polymers. It has been alleged that only the creation of QDs as assemblies uniformly distributed in the polymer matrix and segregated from one another, can help the realization of their prospectively unique optical properties [1–4]. Quantum confined nanoparticles have therefore been employed as fillers for polymer matrices to improve their intrinsic properties. Due to quantum confinement in all dimensions, QDs offer inimitable properties over the other nanostructures that are 1D, 2D or 3D [5-9]. Incorporation of semiconductor nanocrystals within polymeric materials, also offer advantages compared to nanocrystals in solution, such as retainment of shape and retention of the properties of the nanocrystals. Further-more, polymers are easily processable materials and can therefore be of incredible value in the fabrication of new devices [10].

Semiconductor nanocrystals of the group II–VI elements with Mn doping such as (ZnS, Mn) and (CdS, Mn) are the most studied dilute magnetic semiconductors (DMS) [11-12]. These materials display new and original magnetic and optical properties, due to the s, p-d and Mn^{2+}3d electron states [13]. In these materials there is also an antiferromagnetic correlation between the Mn^{2+}(S = 5⁄2) spins due to d-p-d super-exchange interaction [14-15]. These novel properties have thus stimulated an interest in the fabrication of metal chalcogenide DMSs, such as MnS, CoS and NiS for various applications.MnS usually exists in three phases, α-MnS, a green stable form (alabandite) with rock salt (RS) structure, with β-and γ-MnS pink metastable modifications with zinc blend (ZB) and wurtzite (W) structures respectively.All the three phases are antiferromagnetic with the Neel temperature of 152 K for the RS and 90 K for both ZB and W phases [16-20].

On the other hand, PNVC (poly(vinylcarbazole)) is a well-studied polymer with outstanding photo-physical properties and thermal stability [21]. Further, PNVC is a hole transport material (with the hole mobility, μ_h larger than electron mobility, μ_{el}) exhibiting an emission spectrum that owing to the carbazole groups, covers the whole blue region [22]. For this reason, PNVC is used in optoelectronic systems, such as organic electroluminescence devices, solar cells, etc. [23,24].

Considering the usefulness of PNVC and the outstanding magneto-optical properties of MnS nanocrystals, in this study we therefore investigate the impact of incorporation of MnS QDs on the properties of PNVC, with the hope that good results will promise new devices.Therefore the main objective of this work was to find a simplistic route for the synthesis of MnS QDs / PNVC nanocomposite and to study the morphology, optical and electrical properties of the synthesized nanocomposites.

6.2. Application of QD/PNC in opto-electronic devices

6.2.1. Photovoltaics based on quantum dots-polymer nanocomposites

Hybrid solar cells combine advantages of both inorganic and organic semiconductors. Hybrid photovoltaics have organic materials that consist of conjugated polymers that absorb light as the donor and transport holes [25]. Inorganic materials i.e. the QDs in hybrid cells are used as the acceptor and electron transporter in the structure. Hybrid photovoltaic devices have significant potential for not only roll-to-roll processing but also scalable solar power conversion. In hybrid solar cells, an organic material is mixed with high electron transport material to form the photoactive layer [26]. The two materials are assembled together in a hetero-junction type photoactive layer. By placing one material into contact with each other, the power conversion efficiency can be greater than a single material [27]. One of the materials acts as the photon absorber and exciton donor, and the other facilitates exciton dissociation at the junction by charge transfer, this is illustrated in Fig. 6-1.

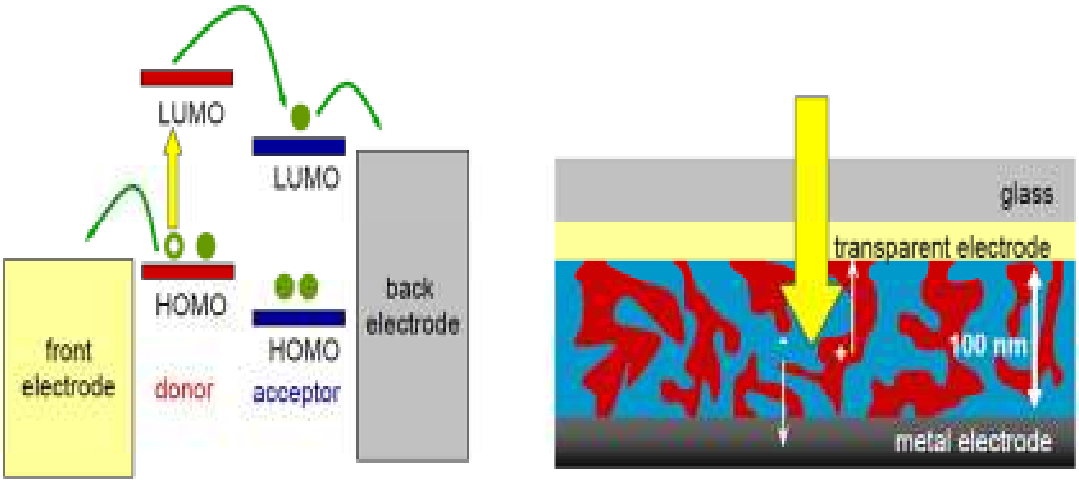

Fig. 6-1: Illustration of the bulk hetero-junction hybrid solar cells and the charge transfer mechanism [27].

6.2.2. Light emitting diodes based on the quantum dots-polymer nanocomposites

There are numerous efforts to increase the efficiency of light emitting diodes, solid state light and displays. Polymer light emitting diodes have attracted much attention because of their ease of preparation and assembly. This therefore renders them cheap to manufacture and widely applicable. Unfortunately thus far their commercial application has been limited as result of their low stability, susceptibility to moisture and poor brightness [28]. To curb these problems researchers have been fabricating quantum dots doped polymer light emitting diodes. These are perceived to result in longer life-time and brighter colours [29]. A typical configuration of a hybrid polymer light emitting diode is shown on Fig.6-2. It is very similar to the hybrid solar cell in Fig. 6-1 except it operates using a reverse mechanism. Consequently an external AC source is required to excite the electroluminescence layer.

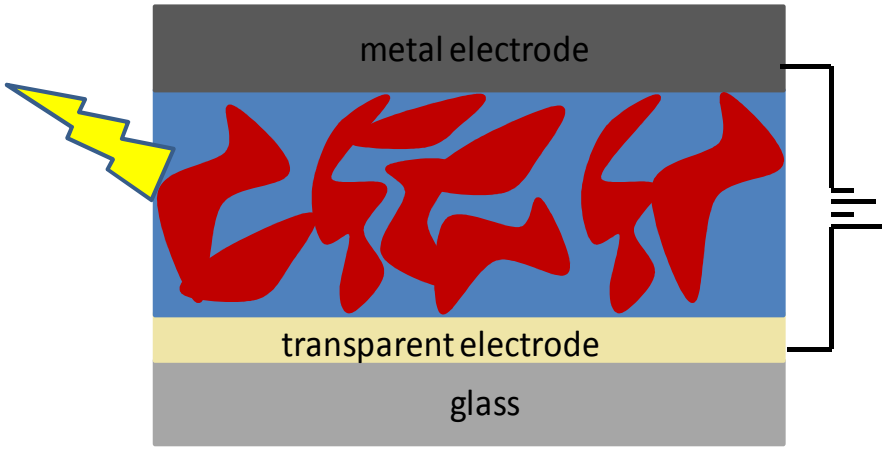

Fig. 6-2: Typical configuration of a hybrid polymer light emitting diode.

Table 1 illustrates some of the practical examples of devices employing quantum dots polymer nanocomposite materials. The complexity and the configuration differ widely depending on the desired application.

Table 6-1: Practical examples of QD-polymer devices

E.g.	Materials	Application	Ref.
1	ZnO, CdSe and MEH-PPV	Nanowire-QD-polymer solar cells	[30]
2	InAs and MEH-PPV	InAS QD-polymer solar cells	[31]
3	CdSe, ZnS.Cu and PIB	Inkjet printed QD-polymer AC-driven electroluminescence devices	[32]
4	PbSe and MEH-PPV	QD-polymer photodectetors	[33]
5	CdSe/CdS/ZnS, PEDOT:PSS, TFB and TiO_2	QD light emitting diodes	[34]

6.3. Experimental

6.3.1. Materials

Hexadecylamine (HDA) and trioctylphosphine (TOP), tetrahydrate manganese acetate, tetramethylthiuram disulfide, ethanol (analytical grade), pyridine and PNVC, Mw 100 k $g.ml^{-1}$were purchased from Sigma-Aldrich SA. Toluene and methanol were obtained from BDH. Chloroform was stored over molecular sieves (40 Å, BDH) before use.All other samples were used as received.

6.3.2. Synthesis of the precursor

A hot solution of tetramethylthiuram disulfide (2 mol) in methanol (20 ml) was added into a heated solution of the metal salt (1 mol) in methanol (20 ml). The mixture was stirred and refluxed for 1 hour. The resultant precipitate was filtered, washed twice with methanol and dried under vacuum: **$Mn(CH_3CHOO)_2(C_6H_{12}N_2S_4)_2$**: Yield 74.8 % , m. p. 347.1 °C. Calcd. C, 29.55; H, 4.62; N, 8.62. Found: C, 29.07; H 4.56; N 8.78. IR/cm^{-1}: 1504 (s), 1397 (s), 1367 (s), 1227 (s), 1138 (s), 1035 (s), 944 (s), 845 (s), 783 (w), 673 (s), 556 (s), 436 (s).

6.3.3. Synthesis of MnS nanoparticles

The precursor was dissolved in TOP (10 – 20 ml). This solution was then injected into 3.125 g of hot HDA at 160 °C. A decrease in temperature of the solution by 20 – 30 °C was observed. The solution was allowed to stabilize at 160 °C and heated for 60 minutes at this temperature. The solution was then allowed to cool to about 70 °C, and methanol was added to the solution. A flocculent precipitate forms and this solid product was separated by centrifugation and dispersed in toluene. Toluene was removed by evaporation under reduced pressure to form HDA capped MnS nanoparticles. The particles are washed three times with methanol and re-dispersed in toluene or dried as powders.

6.3.4. Synthesis of the nanocomposites

6.3.4.1. Route 1

In this route, 0.5 g of PNVC was dissolved in 10 ml of CH_3Cl by stirring for 15 min at room temperature. MnS nanoparticles solution was obtained by stirring 3 wt. % MnS in 10 ml of CH_3Cl at room temperature in another conical flask. The MnS solution was added to the PNVC solution drop-wise and stirred for 3 h at room temperature. Then, about 250 ml of CH_3OH was added to the MnS/PNVC solution to flocculate the resultant nanocomposites. The resultant mass was filtered and dried at 100 ˚C under vacuum for 6 h.

6.3.4.2. Route 2

A solution of 0.5 g of PNVC in 10 ml of CH_3Cl was prepared by stirring for 15 min at 70 ˚C. MnS powder (3 wt. %) was then dissolved in 10 ml of CH_3Cl and stirred for 15 min at 70 ˚C. The MnS solution was added to the PNVC solution drop-wise and refluxed for 1 h at 70 ˚C. Then, about 250 ml of CH_3OH was added to the MnS/PNVC solution to flocculate the

resultant nanocomposite. The resultant mass was filtered and dried at 100 ˚C under vacuum for 6 h.

6.3.4.3. Route 3

About 3 wt. % of MnS powder was dissolved in 10 ml of pyridine and stirred for 15 min at 70 ˚C. CH_3OH was then added to precipitate the particles. The particles were recovered through centrifugation and dried at room temperature. The dried powder was then dissolved in 10 ml of CH_3Cl and the MnS chloroform solution was added to a 10 ml PNVC chloroform solution drop-wise and refluxed for 1 h at 70 ˚C. Then 250 ml of CH_3OH was added to the MnS/PNVC solution to flocculate the resultant nanocomposite. The resultant mass was filtered and dried at 100 ˚C under vacuum for 6 h.

6.3.4.4. Route 4

The tetramethylthiuram disulfide precursor was dissolved in TOP (10 – 20 ml). This solution was then injected into 3.125 g of hot PNVC at 120 °C. A decrease in temperature of the solution by 20 – 30 °C was observed. The solution was allowed to stabilize at 120 °C and heated for 60 minutes at this temperature. The solution was then allowed to cool to about 70 °C, and methanol was added to the solution. A flocculent precipitate formed and this solid product was separated by centrifugation and dispersed in toluene. Toluene was removed by evaporation under reduced pressure to form HDA capped MnS nanoparticles. The particles were washed three times with methanol and re-dispersed in toluene or dried as powders.

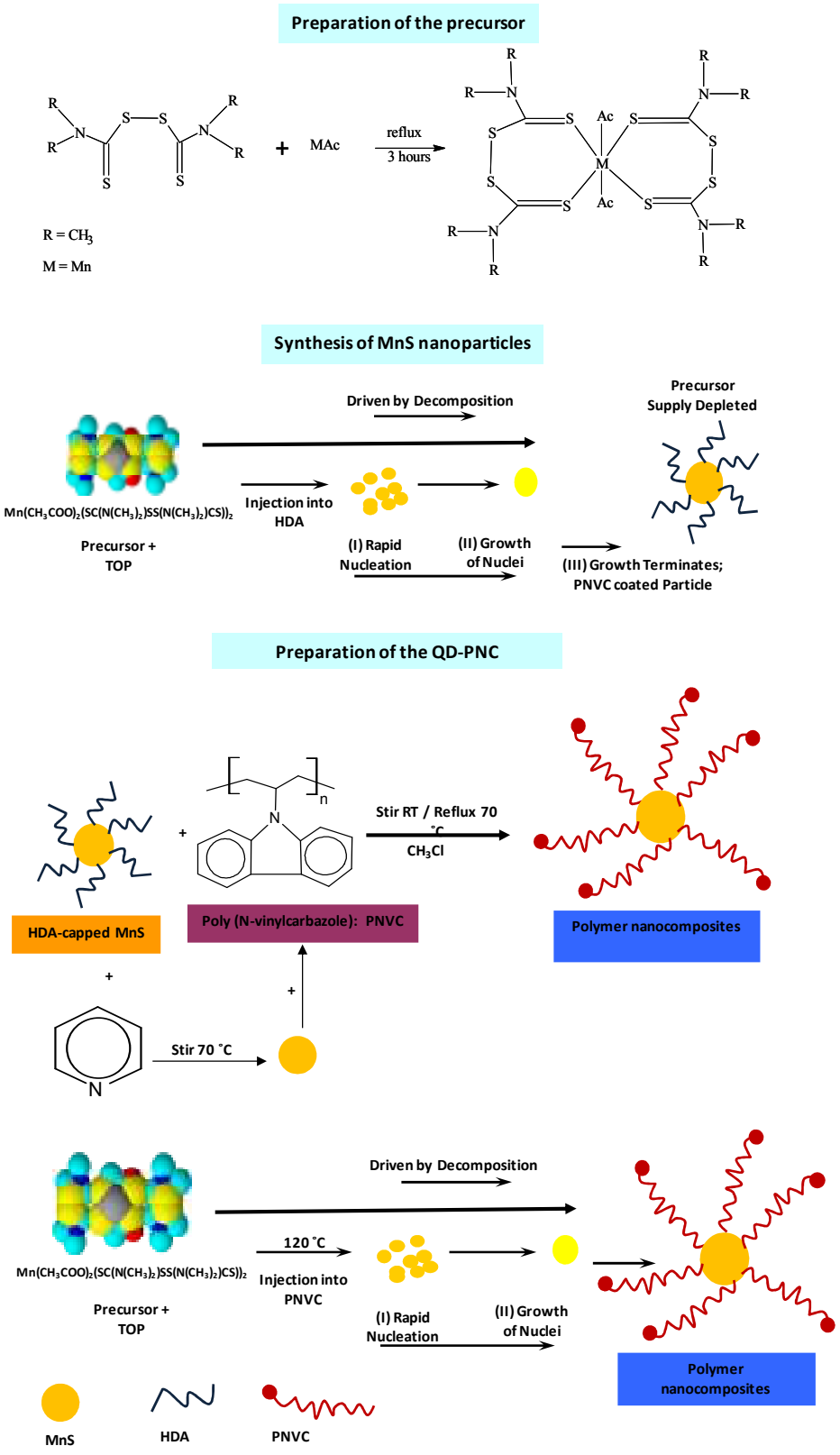

Scheme 6-1: Schematic diagram of the synthetic routes of MnS/PNVC nanocomposites.

6.4. Characterization

The morphology of pure MnS nanoparticles and PNVC/MnS nanocomposites was characterized by FE-SEM (Leo, Zeiss), operated at 3-10 kV electron potential difference and equipped with a semiconductor detector that allows for detection of energy dispersive X-rays (EDX). The samples were prepared by placing a drop of suspended particle in methanol, on a carbon tape. The samples were then allowed to dry at room temperature. The surface topography of nanocomposite samples was studied by means of Atomic Force Microscope (AFM, Veeco NanoScope IVa microscope) using tapping mode with a tip model RTESP equipped with 0.5 – 0.2 Ωcm phosphorous (n) – doped Si at a scanning rate of 1 Hz utilizing a phase data type. A Perkin Elmer Lambda 20 UV-Vis Spectrophotometer was used to carry out the optical measurements and the samples were placed in quartz cuvettes (1 cm, path length), using chloroform as a reference solvent. A Jobinyvon-spex-Fluorolog-3-Spectrofluorimeter with a xenon lamp (150 W) and a 152 P photo multiplier tube as a detector was used to measure the photoluminescence of the particles. The samples were placed in quartz cuvettes (1-cm path length). The FT-IR spectra were taken using a Perkin Elmer spectrum 100 series with spotlight 400 FT-IR imaging system. The electrical properties of the MnS quantum dots and the composites were measured using the set-up shown in scheme 6-2. A known weight of the powdered sample (A) was placed in a cylindrical tube with a 1 cm diameter between two stainless steel pistons (B) of the same diameter. The powder sample was then compressed at a known constant pressure to form a pellet and the density of the powder was measured. The resistance of the powder was then measured using a micrometer (E). The apparatus was made in our lab.

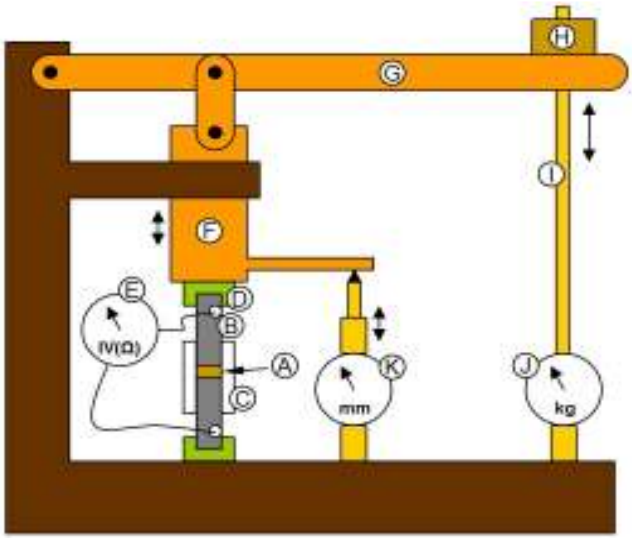

Scheme 6-2: Schematic diagram of the set-up for the electrical measurements of the powders, (A) sample holder, (B) stainless steel pistons,(C, D) stainless steel casings, (E) micrometer, (J) weight, (K) Pressure gauge, (I, F, G, H) iron metal pieces.

6.5. Results and discussion

The MnS nanocrystals were prepared via the single source precursor method, [36–37] with tetramethylthiuram disulfide (a sulphur abundant ligand), the chalcogenide source and manganese acetateas the metal source. The manganese complex of tetramethylthiuram disulphide was characterized by microanalysis and infrared spectroscopy. The microanalysis revealed that the manganese salt reacted with the ligand in a 2:1 mol ratio. The infra-red spectral data confirmed the binding of the ligand to the metal centre. The change in the spectral values of the complex associated with especially CN and CS bonds signified the bonding of the ligand to the metal centre wasthrough the sulphur atoms. The resultant MnS nanocrystals were characterized by XRD to establish their phase. The diffractogram shown in Fig. 6-3 was indexed to a γ-MnS phase(27.32°–100, 29.68°–002, 31.39°–101, 37.42°–102, 45.72°–110, 48.40°–103 and 54.70°–112).

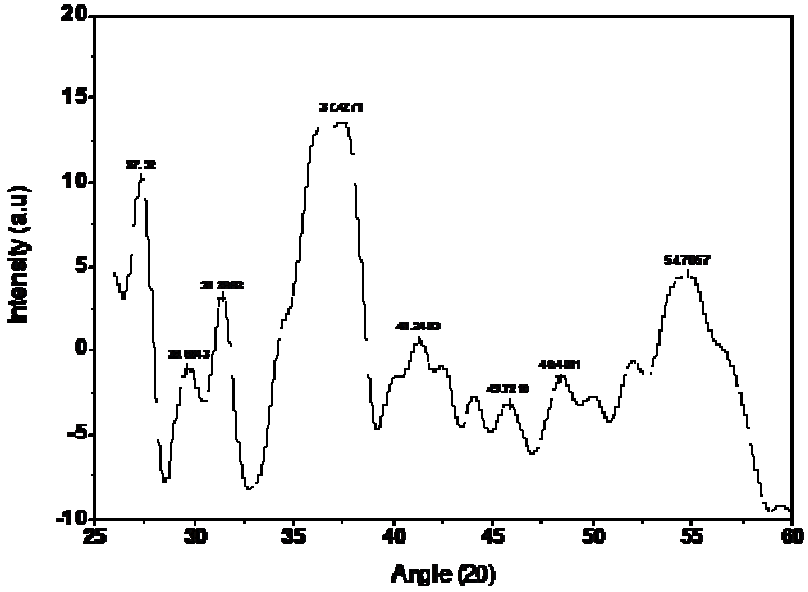

Fig. 6-3: XRD pattern of MnS quantum dots.

The optical properties were also investigated and are shown in Fig. 6-4(a). The band-edge was blue-shifted (367 nm) from its bulk counterpart of 388 nm.The nanocrystals were sufficiently passivated by the stabilizing hexadecylamine (HDA) and showed a Gaussian distributed photoluminescence spectrum with an emission maximum of 600 nm. The particles were spherical in shape with a mean diameter of approximately 50 nm as shown in Fig. 6-5(a). In order for MnS nanocrystals to be integrated into thepolymer matrix, an understanding of the surface chemistryof the nanocrystal is essential. There are various reported methods for the incorporation of nanostructured materials into polymer matrices. For example, Guo et. al. synthesized ZnS/PMMA nanocomposites hybrids by *in situ* polymerization of MMA (Methyl methacrylate) with MPS (Methacryloxypropyltrimethoxysilane) functionalized ZnS nanocrystals [40]. Lansalot and co-workers successfully encapsulated individual CdSe-ZnS/TOPO nanocrystals in polystyrene beads by a mini-emulsion approach [41] whilst O'Brien and co-workers produced CdSe labelled polymer beads by suspension polymerization [42]. Some of the methods reported above can be very complex. On the other hand, spin casting is one of the simplest approaches. It involves the casting of the pre-prepared nanoparticles together with the polymer in a suitable solvent, into a thin film [43].

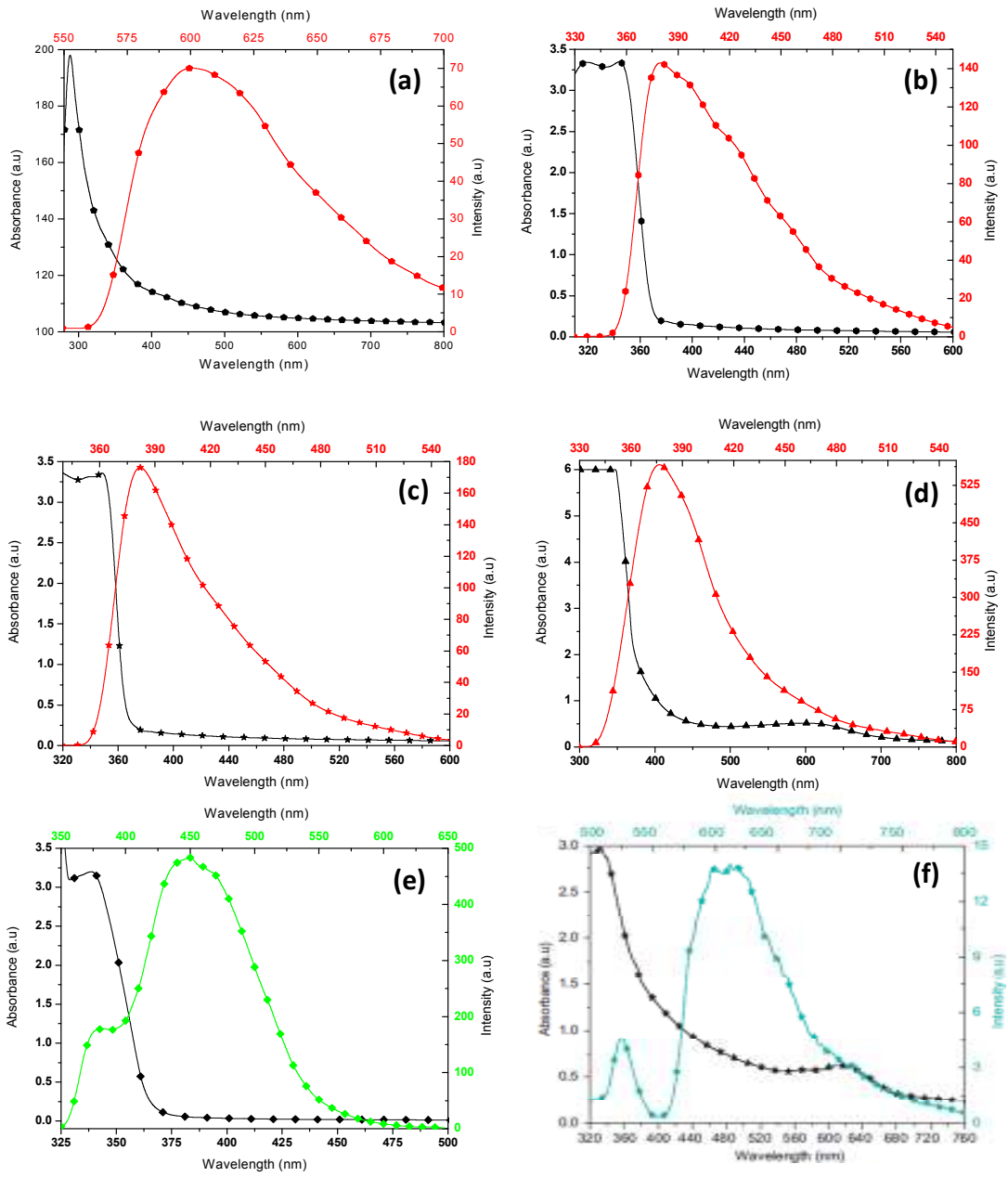

Fig. 6-4: Absorption and photoluminescence spectra of (a) MnS nanoparticles, (b) pure PNVC, (c) MnS/PNVC prepared by route 1, (d) MnS/PNVC prepared by route 2, (e) MnS/PNVC prepared by route 3 and (f) MnS/PNVC prepared by route 4.

However, this method results in the incorporation of the capping molecules of the pre-prepared nanoparticles into the composite. There are therefore mainly two routes that have been recognized in polymer nanocomposite formation i.e. the preparation of the

nanocrystals in the presence of the polymer and the dispersion of the pre-prepared nanocrystals into the polymer matrix. In this work, both methods were used. The pre-prepared HDA-capped MnS nanoparticles were integrated into the polymer matrix via route 1, 2 and 3. Route 1involved the use of very mild conditions in order to retain the structure and hence the properties of the nanocrystals. Previously it has been reported that temperature can influencethe properties of nanoparticles [44] and consequently the reaction was carried out at room temperature. The optical properties of the QD/PNC synthesized by route 1 (Fig. 6-4(c)) showed no distinguishable features when compared from those of the pure PNVC (Fig.6- 4(b)). This resulted in the conclusion that no chemical interaction was taking place between the polymer and the nanocrystals. This was further reiterated by the SEM micrograph in Fig.6-5(c) that showed MnS quantum dots dispersed separately from the PNVC.This then prompted the modification of route 1toroute 2.In route 2the temperature was kept just under the boiling point of the solvent and this was low enough so as not to alter the properties of the MnS nanocrystals.A noticeable change in the optical properties was observed after the adjustment of the temperature.

The absorption spectrum shown in Fig. 6-4(d) showed two excitonic peaks, the first peak was similar to that observed in the polymer and the second broad peak was attributed to the MnS nanoparticles. The location of the second excitonic peak was red-shifted (excitonic peak: 600 nm) from that of the nanocrystals. This was to be expected due to the aggregation of the MnS nanoparticles within the polymer, see (Fig.6-5(d)). The photoluminescence spectrum showed similar features with that of the polymer, but had a considerable increase in intensity. FT-IR spectroscopy was used to further verify the extent of interaction between the polymer and the MnS nanoparticles, prepared by route 2.The slight shift in frequencies in Fig. 6-6(b) from that of the pure PNVC (Fig.6-4(a)) suggested that there was some form of interaction between the polymer and the MnS nanoparticles. The morphology of the resultant nanocomposite (route 2) was then investigated by two microscopy techniques, i.e., SEM and AFM. An SEM image shown in Fig. 6-5(d) illustrates some of the MnS nanocrystals embedded within a film of PNVC whilst others are trapped in the holes of the film.

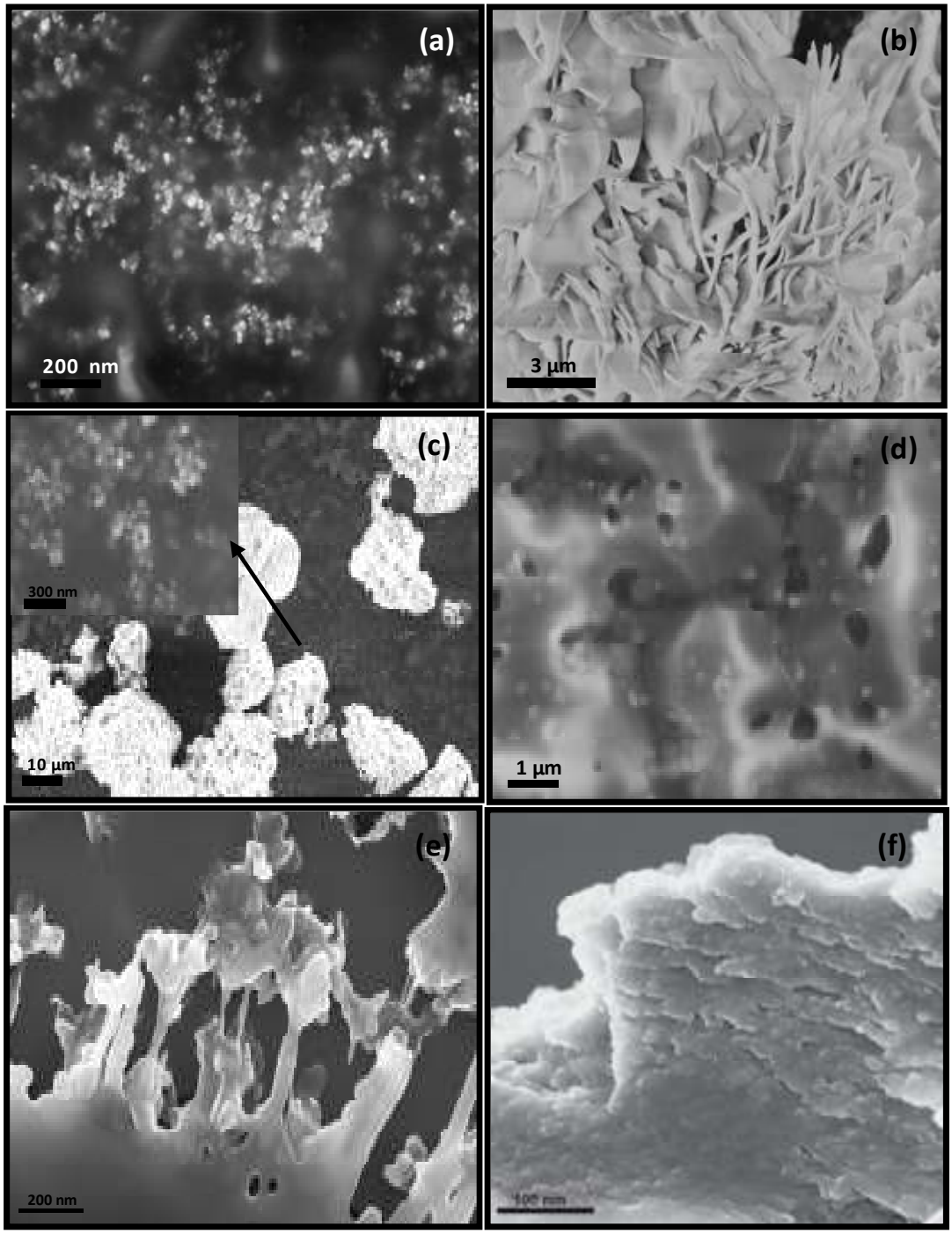

Fig. 6-5: SEM micrographs of (a) MnS quantum dots, (b) PNVC, (c) MnS/PNVC synthesized by route 1, (d) MnS/PNVC synthesized by route 2, (e) MnS/PNVC synthesized by route 3 and (f) MnS/PNVC synthesized by route 4.

The film like structure of the polymer was due to surface tension. The MnS nanocrystals were poly-dispersed, compared to those in Fig. 6-5(a), the introduction of polymer

molecules caused other smaller particles to agglomerate and thus yielded a wide range of particle diameters. This was in agreement with the presence of the second broad excitonic peak observed in the absorption and photoluminescence spectra in Fig. 6-4(d). The reason for the effectiveness of route 2 compared to route 1 relates to the elevated temperature promoting the departure of some of the HDA molecules on the surface of the nanocrystals thus creating vacancies for the polymer molecules to interact.

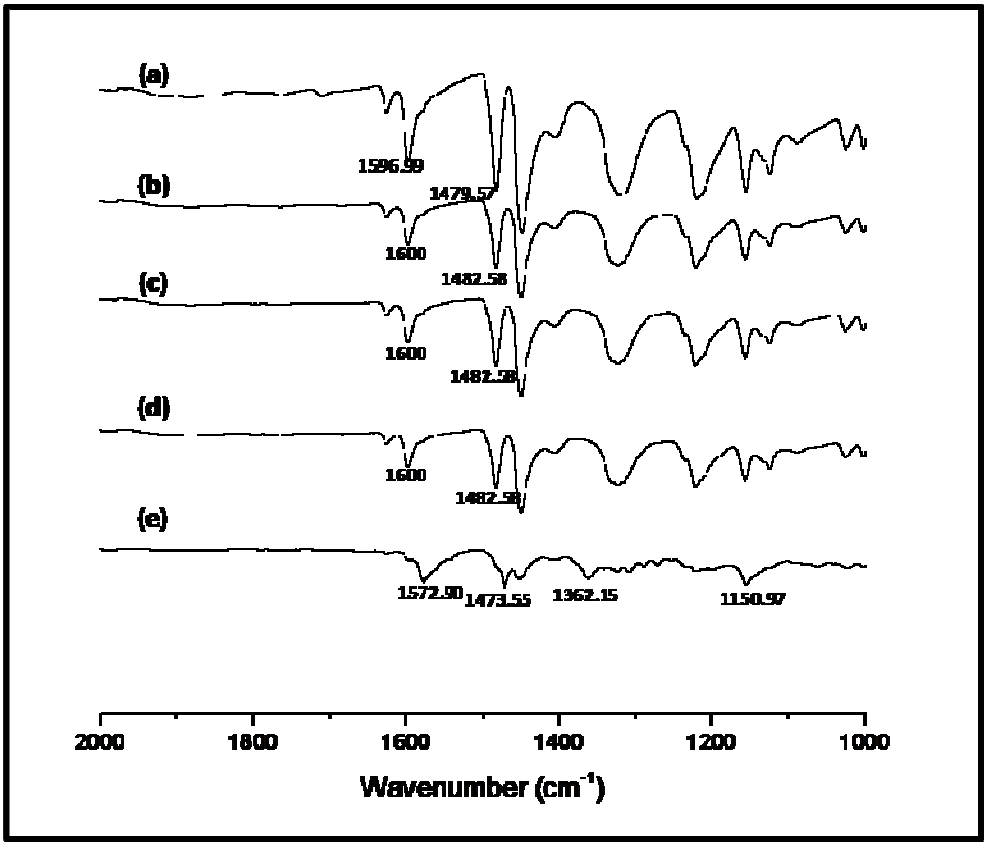

Fig. 6-6: FT-IR spectra of (a) pure PNVC, (b)MnS/PNVC synthesized by route 1, (c) MnS/PNVC synthesized by route 2, (d) MnS/PNVC synthesized by route 3 and (e)MnS/PNVC synthesized by route 4.

The extent of interaction was further investigated using AFM.A drop or two of the MnS/PNVC nanocomposite, suspended in methanol, was placed on a sample disc and allowed to dry and form a film. An AFM top view image in Fig. 6-7(a) showed mounds that represented the embedded nanocrystals. This was clearly shown in the 3D view in Fig. 6-

7(b). The diameter of the mounds ranged from 50 to 100 nm from (Fig. 6-7(c)). The wide size distribution was in agreement with the results obtained from the SEM and the optical measurements.

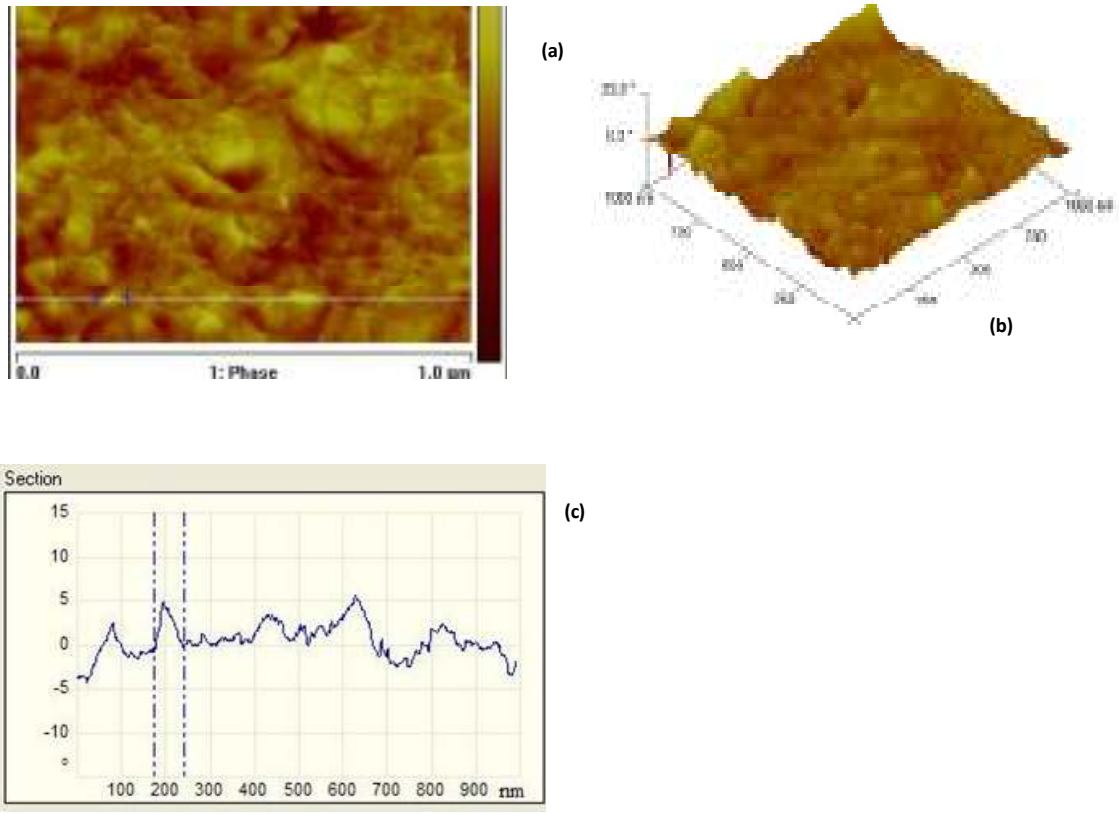

Fig. 6-7: AFM images of a MnS/PNVC synthesized by route 2, (a) cross-section, (b) 3D view and (c) line scan.

Route 2 revealed that the interaction between the polymer and the nanocrystals was still hindered by the presence of HDA. Consequently route 3 involved the stripping of the HDA molecules from the surface of the QD by pyridine. The pyridine molecules bind very weakly to the surface of the QD and can therefore be easily substituted by the polymer. The optical properties of the PNC synthesized by route 3 are shown in Fig. 6-4(e). The absorption spectrum shows no particular differences when compared with that of the pure polymer (Fig. 6-4(a)) whilst the PL shows two distinct peaks at image378 and 460 nm, attributed to the emission of PNVC and MnS nanoparticles, respectively. The blue-shifting of the emission maximum of the MnS nanoparticles could be as the result of the absence of HDA. FT-IR

spectroscopy was used to further verify the formation of the polymer nanocomposites. The spectrum of the nanocompositesprepared by route 3 (Fig. 6-6(d)) showed similar features withthat of the possible interaction betweenthe MnS and PNVC.The morphology and the extent of the interaction or dispersityof the MnS quantum dots into the PNVC matrix was studied using SEM and is depicted in Fig. 6-5(e). The SEM micrograph showed spherical particles embedded inside the polymer. The SEM also showed evidenceof strong interfacial interaction between the polymer and thequantum dots. Route 2 due to presence of HDA, resulted in a higher degree of agglomeration of the incorporated MnSquantum dots due to steric hindrance occurring between the bulky HDA molecules and the polymer chains. The removal of theHDA capping molecules in route 3 encouraged the direct interactionbetween the polymer and the nanoparticles, therefore preventing agglomeration.

Having discovered the importance of the surface ligands in the preparation of the QD/PNC, route 4 looked to exploit the synthetic method of quantum dots and thus involved the direct substitution of HDA with PNVC during the synthesis of the nanoparticles as illustrated in scheme 6-1.

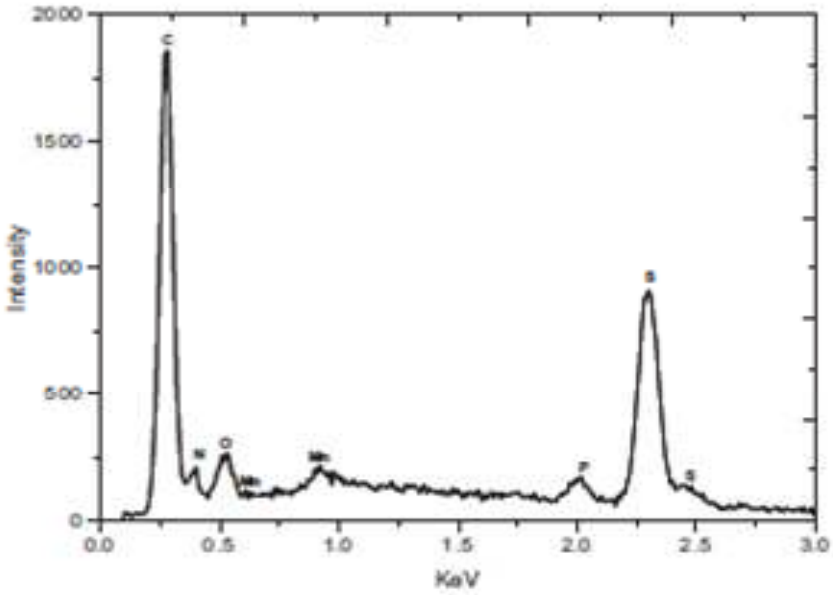

Fig. 6-8: EDX spectrum of MnS/PNVC nanocomposites synthesized by route 4.

Theabsorption spectrum shown in Fig. 6-4(f) showed two excitonic peaks, onelocated at 320nm which was attributed to PNVC and another broadpeak located at 620nm arising

potentially from MnSnanoparticles; similar to what was observed in PNC synthesized by route 2. The PL spectrum also showed two peaks confirmingthe existence of the excess PNVC and MnS.The SEM micrograph (Fig. 6-5(f)) of MnS/PNVCnanocomposite obtained using route 4 showed sphericalaggregates that appeared to be coated with the polymer. The composition of the aggregates was thereforeverified through EDX (Fig. 6-8). The EDX confirmed the presence of theMn, S (from MnS particles), N, C (from polymer) and O (fromthe solvent) and P (from TOP). Also evident was thatroute 4 resulted in theincorporation of impurities.FT-IR was also done to further ascertain the presence of the polymer. The spectrum in Fig. 6-6(e) showed disappearance of some peaks when compared to the pure polymer. This was attributed tothe role that the PNVC plays during the synthetic method. Thepolymer assumed the role of HDA and capped the nanoparticles thusforming a core-shell like structure while all the other routes resulted in ahomogeneous mixture of the MnS and the polymer.

Table 6-1: Electrical properties of the QD and QD/PNC.

Sample	Mass (g)	Density (gcm^{-3})	R (Ω)	σ(Sm^{-1})
MnS	0.2018	1.433	9.33×10^{-5}	0.41×10^{-3}
PNVC	0.2016	1.321	64.1978	6.64×10^{-10}
PNC (route 1)	0.2038	1.297	56.9917	7.72×10^{-10}
PNC (route 2)	0.2008	1.263	42.6992	9.71×10^{-10}
PNC (route 3)	0.2004	1.301	20.3196	2.11×10^{-9}
PNC (route 4)	0.2030	1.319	7.4088	5.78×10^{-9}

The electrical conductivity of the pristine MnS and the different composites was measured in order to establish their potential in opto-electronic devices (Table 6-1). The conductivity was derived from the measured data using the following equations:

$$\sigma = \frac{\left(\frac{1}{R}\right) l}{A} \qquad (1)$$

$$V = \frac{m}{d} \qquad (2)$$

Since the sample holder is cylindrical, it follows:

$$V = \pi r^2 l \qquad (3)$$

$$A = 2\pi r^2 + 2\pi r l \qquad (4)$$

where$l$ is the length, V is the volume, m is the mass, d is the density, r is the radius and A is the area.

The conductivity of the nanocomposites showed improvement compared to the pure polymer. The nanocomposites synthesized via route 4 showed the highest conductivity compared to the ones synthesized by the other routes. This is probably due to the homogeneity of the sample. The core-shell structure appeared to harness the properties of the quantum dots better than the other morphologies.

6.6. Conclusions

Four different methods were used to prepare MnS/PNVC nanocomposites. The PNC synthesized via route 1 showed no interaction between the quantum dots and the polymer thus the properties of the PNC showed little improvement compared tothe pure polymer. The route 2 synthesized PNC showed a dispersion of MnS quantum dots within the PNVC matrix. The elevated temperature in route 2 compared to route 1 allowed for interfacial interaction between the quantum dots and the polymer to occur. This resulted in improved optical and electrical properties.The nanocomposites prepared by route 3 showed stronginteraction between the MnS nanoparticles and the PNVC asevident from the SEM and FT-IR. The optical properties of thecomposites showed features associated with the quantum dots.The in situ prepared PNC (route 4) showed both thepresence of MnS and PNVC as validated by the EDX and FT-IR. Thisroute resulted in MnS nanoparticles capped with thePNVC polymer. The electrical properties for all the PNC showed enhancement compared to the pure polymer. This was attributed to the presence of MnS quantum dots. Uniformly distributed MnS nanoparticles in polymer resulted in much better conductivity compared to the agglomerated nanoparticles.

6.7. References

[1] Caseri W., Macromol. Rapid Commun.2000, 21, 705.

[2]Beecroft L.L.; C.K.Ober, Chem. Mater.1997, 9, 1307.

[3]Erskine L.; Emrick T.; Alivisatos A.P.; Frechet J.M.J., Polym. Prepr. 2000, 41, 593.

[4]Radhakrishnan T.; Georges M.K.; Nair P.S.; Luyt A.S.; Djokovic V., J. Nanosci. Nanotechnol. 2007, 7, 986.

[5]Viswanatha R.; Sapra S.; Amenitsch H.; Sartori B.; Sarma D.D., J. Nanosci. Nanotechnol. 2007, 7, 1726.

[6]Sharma H.; Sharma S.N.; Singh G.; Shivaprashad S.M., J. Nanosci. Nanotechnol. 2007, 7, 1953.

[7] Xin S.H.; Wand P.D.; Aie Y.; Kim C.; Dobrowolsku M.; Merz J.L.; Furdyna J.K., Appl. Phys. Lett.1998, 69, 3884.

[8]Heun S.; Biasiol G.; Grillo V.; Carlino E.; Sorba L.; Golinelli G.B.; Locatelli A.; Mentes T.O.;Guo F.Z., J. Nanosci. Nanotechnol. 2007, 7, 1721.

[9]Lowisch M.; Kabe M.; Stegemann B.; Henneberger F.;Grundmann M.; Turck V.;Bimbers D., Phys. Rev. B 1996,54, R11074.

[10]Dabbaousi B.O.; Bawendi M.G.; Onitsuka O.; Rubner M.F. , Appl. Phys. Lett.1995, 66, 1316.

[11]Furdyna J.K., J. Appl. Phys. 1998, 64, R29.

[12]Goede O.; Heimbrodt W., Phys. Status Solidi B 1988, 146, 11.

[13]Haas K.C.; Ehrenreich H., J. Cryst. Growth 1988, 86, 8.

[14]Larson B.E.; Haas K.C.; Ehrenreich H.; Carlsson A.E., Solid State Commun. 1985, 56, 34.

[15]Gunshor R.L.; Nurmikko A.V., Semiconductors and Semimetals, Academic, New York 1997, Vol.44.

[16]Okajima M.; Tohda T., J. Cryst. Growth 1992, 117, 810.

[17]Goede O.; Hermbrodt W.; Weinhold V., Phys. Status Solidi B 1987, 143, 511.

[18]Kennedy S.W.; Harris K.; Summerville E., J. Solid State Chem. 1980, 31, 355.

[19]Kan S.H.;Felner i.; Banin U., Isr. J. Chem. 2001, 41, 55.

[20]Pramanik P.; Akhter M.A. ,Thin Solid Films 1988, 158, 271.

[21]Maity A.; Sinha Ray S.;Pillai S.K., Macromol. Rapid Commun.2007, 28, 2224.

[22]Shi M.M.; Chen H.Z.; Wang M.; Ye J., Synth. Mat.2003, 137, 153.

[23]Winiarz J.G.; Zhang L.; Lal M.; Friend C.S.;Prasad P.N., Chem. Phys. 1999, 121, 5287.

[24]Winiarz J.G.; Zhang L.; Lal M.; Friend C.S.; Prasad P.N., Chem. Phys. 1999, 245, 417.

[25]Milliron D.J., MRS Bulletin 2005, 30, 41.

[26]Shaheen S.E., MRS Bulletin 2005, 30, 15.

[27]Saunders B.R.; Turner M.L., Advances in Colloid and Interface Sc. 2008, 138(1), 1.

[28]Burroughes J.H.; Bradley D.D.C.; Brown A.R.; Marks R.N.; Mackay K.; Friend R.H.; Burns P.L.; Holmes A.B., Nature 1990, 347, 539.

[29] Ginger D.S.; Greenham N.C.,Phys. Reviews B 1999, 59, 624.

[30]Nadurajah A.; Robert Word C.; Vasant K.; Korenkamp R., Phys Stat. Sol. B 2008, 245(9), 1834.

[31]Anctil A.; Landi B.; Wolman J.; Raffaelle R., Mater. Res. Soc. Symp. Proc. 2007, 1013, 1013-207-30.

[32]Wood V.; Chen J.; Panzer M.J.; Bradley M.S.; Halpert J.E.; Bawendi M.G.; Bulovic V., MIT 2007.

[33]Qi D.; Fischbein M.; Dirdic M.; Selmic S., Appl. Phys. Letters 2005, 86, 093103.

[34]Cho K-S.; Lee K.E.; Joo W-J.; Jang E.; KimT-H.; Lee S.J.; Kwon S-J.; Han J.Y.; Kim B-Ki,Choi B.L.; Kim M.J., Appl. Phys. Lett. 2006, 89, 253531.

[35]Moloto N.; Moloto M.J.; Sinha Ray S., J. Cryst. Growth 2009, 305, 2305..

[36]Trindade T.; O'Brien P., Adv. Mater.1996, 8, 161.

[37] Trindade T.; O'Brien P., Chem. Mater.1997, 9, 523.

[38]Pearton S.J.; Abernathy C.R.; Norton D.P.; Herbad A.F.; Park Y.D.; Boatner L.A.;Budai J.D., Mater. Sci. Eng. 2003,40, 137.

[39]Pearton S.J.; Abernathy C.R.; Overberg M.E.;Thaler G.T.; Norton D.P.;Theodorpoulou N.; Herbad A.F.; Ren F.; Kim J.; Boatner L.A., J. Appl. Phys. 2003, 93, 1.

[40]Guo L.; Chen S.; Chen L., Colloid Polym. Sci. 2007, 285, 1593.

[41]Jouma N.; Lansalot M.; Theretz A.; Elaissar A.; Sukhanova A.; Artemyer M.; Nabiev I, Cohen M., Langmuir 2006, 22, 1810.

[42]O'Brien P.; Cummins S.S.;Darcy D.; Dearden A.; Masala O.; Pickett N.L.; Ryle S.; Sutherland A.J., Chem. Commun.2003, 2532.

[43] Wang S.; Yang S.; Yang C.; Li Z.; Wang J.; Ge W., J. Phys. Chem. B 2000, 104, 11853.

[44]Moloto N.; Revaprasadu N.; Moloto M.J.; O'Brien P.; Helliwell M., Polyhedron 2007, 26, 3947.

CHAPTER 7: CONCLUSIONS AND RECOMMENDATIONS

7.1. Conclusions

Dilute magnetic semiconductors are probably the most attractive of the quantum dots because of their multifunctional properties. Thus far much of the research has been centred on doping well known quantum dots systems (CdS, CdSe, ZnS and etc) with magnetic ions such Mn and Co [1]. The problem associated with these kinds of dilute magnetic semiconductors is the low success rate of doping and even if doping is achieved, the dopant concentrations are usually very low thus resulting in very small magnetic moments. Another complication arises from the characterization of the presences and the location of the dopants. The characterization techniques employed are usually limited. The research has therefore migrated to two types of materials i.e. the synthesis of multi-component nanoparticles where typically the magnetic entity is Fe_2O_3 and the photoluminescent entity is either a dye or quantum dots [2]. This approach results in complex systems that require tedious synthetic routes and sophisticated instrumentation for characterization. The second approach is presented in this thesis where metal chalcogenides of magnetic metals (MnS, CoS and etc.) are synthesized. Some of the issues that have limited the widespread synthesis and utilization of these materials are the difficulty in synthesis, the difficulty in synthesizing small sizes that are sub 100 nm as well as controlling the stoichiometries.

In this thesis, we therefore embarked on solving some of the stipulated challenges. Elaboration on the syntheses and characterization as well as highlights of some possible applications of these nanoparticles was done over six chapters. Chapter 2 described the syntheses and characterization of metal chalcogenide nanoparticles and their possible application in the biomedical fields. The syntheses of metal (Mn, Co,Ni and Cu) sulfides and selenides using the single-source precursor method and a modified hydrothermal method was reported. Particular focus was placed on the optical, structural and magnetic properties of these nanomaterials. The interest of exploration of these nanomaterials came from their inherent properties as semiconductors in the nanometric system as well as that they have potential to perform better than dilute magnetic semiconductors as a result of the magnetic ions not being dopants rather they form the bulk crystal structure. The optical properties of

all the metal sulfides studied showed large blue-shifts in band gap indicative of quantum confinement effects. These large blue-shifts were associated to arise from influences such as the size, shape and phase of nanocrystals as well as the nature of the reactants (synthetic method). The structural characterization gave insight into the complexity of the metal sulfide due to a variety of stoichiometric compositions. Unique morphologies were observed, from MnS nanowires to spherical Co_3S_4 to rod-shaped NiS and CuS nanobelts. The nanoparticles displayed magnetic character at room temperature. Frequently semiconductor nanocrystals do not display any magnetic character at room temperature thus requiring ESR measurements to be performed at very low temperatures consequently rendering them inapplicable in the biomedical fields. The optical properties of the selenides were less startling compared to the sulfides. The absorption band-edges were blue-shifted from the reported bulk values, a typical behaviour of semiconductor nanocrystals. The morphologies and structures of the metal nanocrystals were similar to their corresponding sulfides. The particles also showed some level of agglomeration thought to be brought by the lack of use of the capping agent. The magnetic properties were size and shape dependent and room temperature electron spin resonance was achievable.

The chapters following chapter 2 were derived from the conclusions drawn in chapter 2. For example, cobalt sulfide synthesized from tetramethyl thiuram disulfide showed distinct and prominent absorption features compared to other chalcogenides and therefore in chapter 3, systematical studies were done in order to understand the evolution of these absorption features whether they were inherent to cobalt sulfide or stemmed from the reaction conditions. Time and temperature being the easiest of parameters to monitor were varied and the optical and morphological characteristics of the material were then examined. The cobalt sulfide nanoparticles synthesized at different reaction time showed good quantum confinement and the excitonic features were similar to those described in chapter 2. The particles collected after 5 min showed the most blue-shifted band-edge and the subsequent samples showed a further red-shift with time. This was due to the Ostwald ripening effect. The synthesized particles showed interesting structural properties with the crystals being indexed to a rather less familiar $CoS_{1.097}$ phase. The morphology of the particles using an SEM (low accelerated voltage) resulted in spherical shaped nanoparticles. Upon increasing the accelerated voltage to 200 kV during TEM measurements, the shapes of the particles

changed from spherical to wire-like nanoparticles, i.e., the morphology was transformed from isotropic to anisotropic. This indicated that the morphology of the synthesized $CoS_{1.097}$ nanoparticles was very sensitive to the applied radiation. The stability of the nanoparticles determined by TGA showed that the synthesized cobalt sulfide degrades at 430 °C, verifying the low stability of the nanoparticles in high energy conditions. The particles were then annealed in a nitrogen atmosphere in order to establish whether there would be any change in morphology. The morphology determined by SEM remained spherical but agglomerated together to form bigger spheres. The TEM showed similar effect as the SEM. It was therefore deduced that the cobalt sulfide in a $CoS_{1.097}$ phase was susceptible to structural changes when exposed to extreme conditions. The effect of the synthetic temperature on the properties of the nanoparticles was investigated. It was found that the temperature largely influenced the size of the nanoparticles rather than the crystal phase and the morphology. This was attributed to the fact that the temperature usually plays a more prominent role in the growth stage of the nanoparticles rather than in the nucleation stage, meaning it has very little effect on the initial characteristics (phase and shape) of the nanoparticles.

In-depth studies of nickel selenide nanoparticles were done in chapter 4 and 5. In chapter 4, a series of nickel selenide ($NiSe_2$, NiSe and Ni_3Se_4) nanoparticles were synthesized by three different methods, i.e. the single-source precursor (method 1), the thermolysis of trioctylphosphine selenide (TOPSe) and nickel chloride in hexadecylamine (method 2) as well as the reaction of nickel chloride and selenium using sodium borohydride as a reducing agent in methanol and in water (method 3). The optical properties of nickel selenide synthesized from all the methods showed good nanometric characteristics with an observed blue-shift in the absorption band-edge from bulk nickel selenide.

The structural characteristics varied with the methods employed, with method 1 producing 10 nm spherical $NiSe_2$ particles, method 2 star-shaped NiSe particles, while method 3 produced hexagonal NiSe nanoparticles in methanol and rod-shaped Ni_3Se_4 particles in water. Chapter 4 elaborated the variability in stoichiometries of these materials and therefore showing their versatility that could perhaps be exploited and used in wider applications. In chapter 5, method 3 discussed in chapter 4 was used to synthesize nickel

selenide nanoparticles. The reaction parameters such as time, concentration, temperature, pH and solvent were systematically varied and their effects on the optical and structural properties were studied. All these parameters had an influence on either the size or morphology of the nanoparticles. This then unavoidably had an influence on the optical properties. Nickel selenide also displayed susceptibility to the formation of unusual morphologies with high reproducibility.

Chapter 6 gave a brief review on the application of quantum dots/polymer nanocomposites in optoelectronic devices. Experimental work on the preparation and characterization of polymer nanocomposites was also discussed in this chapter. A variety of synthetic strategies were employed in order to achieve well dispersed semiconductor nanoparticles into the polymer matrix. In route 1 a chloroform solution of HDA capped MnS dots was added to a chloroform solution of PNVC at room temperature, in route 2 the temperature was elevated to 70 °C whilst route 3 involved the initial step of removal of HDA by pyridine form the HDA capped MnS nanoparticles and route 4 was an in situ synthesis of PNVC capped MnS using the single source precursor method. The PNC synthesized via route 1 showed no interaction between the quantum dots and the polymer thus the properties of the PNC showed little improvement compared to the pure polymer. The route 2 synthesized PNC showed a dispersion of MnS quantum dots within the PNVC matrix. The elevated temperature in route 2 compared to route 1 allowed for interfacial interaction between the quantum dots and the polymer to occur. This resulted in improved optical and electrical properties. The nanocomposites prepared by route 3 showed stronginteraction between the MnS nanoparticles and the PNVC asevident from the SEM and FT-IR. The optical properties of thecomposites showed features associated with the quantum dots.The in situ prepared PNC (route 4) showed both thepresence of MnS and PNVC and was validated by EDX and FT-IR. This route resulted in MnS nanoparticles capped with the PNVC polymer. The electrical properties for all the PNC showed enhancement compared to the pure polymer. This was attributed to the presence of MnS quantum dots. Uniformly distributed MnS nanoparticles in polymer resulted in much better conductivity compared to the agglomerated nanoparticles.

7.2. Future work and Recommendations

- **Syntheses and characterization of the dilute magnetic metal chalcogenide:** Further synthetic strategies of the QD should be employed that would result in more controlled morphologies and stoichiometries. The precursors in the single source precursor method can be easily modified and ligands such as thiols, thiosemicarbazides and other sulphur containing ligands can be employed. Different surface ligands can also be used. The avenues are endless for perfecting these materials to the standard similar to the II-VI semiconductors. Further characterization especially of the magnetic properties can be done using techniques such SQUID.

- **Surface functionalization for biomedical applications:** Further functionalization of the particles with ligands that would render the particles water soluble is essential. Bio-molecules such as PEG or BIOTIN should be added on the surface of the dots to make them bio-compactable. Multifunctional compact polymers with all the important components have recently been used to passivate the surface of dots and employed in biomedical applications [3].

- **Application in polymer nanocomposites:** The quantum dots can be combined with different polymers for different applications. They could be used to enhance the refractive index of the polymers and could therefore be employed in opto-electronic devices such as in making optical lenses. Combined with polymers the applications are numerous.

- **Fabrication of LEDs and PVs:** Because these QDs are solution based, LEDs and PVs can be easily processed. Different device architects and QD active layers can be employed.

7.3. References

[1] Levy N.; Hochepied J.F.; Pileni M.P., J. Phys. Chem. 1996, 100(47), 18322.

[2] Insin N.; Tracy J.B.; Lee H.; Zimmer J.P.; Westervelt R.M.; Bawendi M.G., ACS Nano 2008, 2(2), 197.

[3] Liu W.; Howarth M.; Greytak A.B.; Zhang Y.; Nocera D.G.; Ting A.Y.; Bawendi M.G., J. Am. Chem. Soc 2008, 130(4), 1274.[i]

[i] Chapter 3: J. Nanosci. and Nanotech., 2010, 10(9), 5594.
Chapter 4: J. Cryst. Growth, 2009, 311, 3924.
Chapter 6: J. Nanosci. and Nanotech., 2009, 9(8), 4760 and Physica B, 2009, 404, 4461.